molecules

Special Issue Reprint

Two-Dimensional Materials

From Synthesis to Applications, 2nd Edition

Edited by
Sake Wang, Nguyen Tuan Hung and Minglei Sun

mdpi.com/journal/molecules

MDPI

Two-Dimensional Materials: From Synthesis to Applications, 2nd Edition

Two-Dimensional Materials: From Synthesis to Applications, 2nd Edition

Guest Editors

Sake Wang
Nguyen Tuan Hung
Minglei Sun

MDPI

Basel • Beijing • Wuhan • Barcelona • Belgrade • Novi Sad • Cluj • Manchester

Guest Editors

Sake Wang
College of Science
Jinling Institute of Technology
Nanjing
China

Nguyen Tuan Hung
Frontier Research Institute for Interdisciplinary Sciences
Tohoku University
Sendai
Japan

Minglei Sun
Department of Physics
University of Antwerp
Antwerp
Belgium

Editorial Office
MDPI AG
Grosspeteranlage 5
4052 Basel, Switzerland

This is a reprint of the Special Issue, published open access by the journal *Molecules* (ISSN 1420-3049), freely accessible at: https://www.mdpi.com/journal/molecules/special_issues/VY337364WE.

For citation purposes, cite each article independently as indicated on the article page online and as indicated below:

Lastname, A.A.; Lastname, B.B. Article Title. *Journal Name* **Year**, *Volume Number*, Page Range.

ISBN 978-3-7258-7088-2 (Hbk)
ISBN 978-3-7258-7089-9 (PDF)
https://doi.org/10.3390/books978-3-7258-7089-9

Contents

About the Editors

Sake Wang

Sake Wang earned his Ph.D. in physics at Southeast University, China, in 2016. During this period, he was awarded the national scholarship for doctoral students. Since 2021, he has been an Associate Professor at the Jinling Institute of Technology, China. He was a Visiting Scientist at Tohoku University, Japan, from 2019 to 2021. His current interests focus on theoretical studies of spin and valley transport, as well as valley-optoelectronic devices in two-dimensional materials. He is the PI of the National Science Foundation for Young Scientists of China and the Natural Science Foundation of Jiangsu Province. He has published one book (first author, IOP Publishing) and 71 papers with more than 4,500 citations; for 33 of these papers, he was the first or corresponding author. Four of his first-authored and corresponding-authored papers are in the top 1% of ESI highly cited papers. He was ranked in the World's Top 2% most-cited scientists from 2021 to 2025 by Stanford University. He has also served as an Associate Editor of the *Journal of Superconductivity and Novel Magnetism* (Springer Publishing) since 2020 and as an Editorial Board Member of *Discover Physics* (Springer Publishing) since 2025, and was an outstanding reviewer of five SCI journals.

Nguyen Tuan Hung

Nguyen Tuan Hung has been an Assistant Professor since 2019 and a Prominent Research Fellow since 2021 at Tohoku University, Japan. He was also a Visiting Scholar at the Massachusetts Institute of Technology, USA, in 2023–2024. His research focuses on theory-driven energy materials, with an interdisciplinary emphasis on solid-state theory, simulation, and machine learning.

Minglei Sun

Minglei Sun is a research scientist at the Department of Materials Science and Engineering at the University of Texas in Dallas. His research focuses on first-principles studies of nanomaterials and their applications, particularly in energy conversion and storage. He is actively engaged in exploring the theoretical design and optimization of advanced materials for sustainable energy solutions and electronic devices. Currently, he is working on Bayesian optimization and nonlinear physics.

Preface

Building on our previous edition, "Two-Dimensional Materials: From Synthesis to Applications", this reprint gathers a curated selection of contributions that map the evolving landscape of low-dimensional materials science. The subject of this volume is intentionally broad: it spans fundamental theory and modeling, materials synthesis and processing, heterostructure and device engineering, electrochemical energy storage, catalytic and environmental applications, and advanced spectroscopic characterization. It aims to present not only individual advances, but also the links that unite seemingly disparate approaches into a coherent, multidisciplinary research program that is accelerating both discovery and technological translation.

The scope of this reprint reflects the field's current dynamics. At one end, atomically thin crystals and their one-dimensional derivatives reveal new quantum, magnetic, and transport phenomena that require rigorous first-principles description and careful experimental validation. At the other end, practical architectures—composites, doped nanowires, supported nanoparticles, and multifunctional heterojunctions—demonstrate how low-dimensional motifs can be embedded into devices for sensing, energy conversion, and remediation. Between these poles, method development (simulation, synthetic routes, and characterization techniques) provides the connective tissue that turns conceptual ideas into robust, reproducible science.

We produced this reprint for several reasons. First, two-dimensional materials remain a fertile ground for both fundamental questions and translational impact; documenting current best practices and emerging strategies is invaluable for researchers entering or pivoting into the field. Second, the accelerating pace of cross-disciplinary work—combining computational design, thin-film growth, nano-fabrication, electrochemistry, and environmental engineering—means that insights produced in one subdomain often enable progress elsewhere. Finally, this collection is intended to serve as a reference and a stimulus, both to consolidate lessons learned and to provoke creative thinking about future directions.

This volume addresses a broad audience: graduate students and postdoctoral researchers seeking an entry point into contemporary 2D research; experimentalists and theorists wanting to compare approaches across subfields; and applied scientists and engineers interested in incorporating low-dimensional components into devices and systems. We hope the articles will be useful for course reading lists, research group seminars, and as inspiration for collaborative proposals.

The reprint brings together contributions from many dedicated scientists and collaborators; we are grateful to our authors from Bulgaria, China, Poland, Russia, and the USA for choosing this Special Issue to publish their excellent science. We are thankful to the anonymous referees whose constructive critiques strengthened the manuscripts, to the editorial team at *Molecules* for their professional handling of submissions and proofs, and to colleagues who provided technical advice, experimental samples, computational resources, and thoughtful discussions. Special acknowledgment goes to laboratory staff and funding agencies whose support made the underlying research possible.

It has been a privilege to assemble this collection and to witness the creativity and rigor of our community. We hope you find the articles as enlightening and inspiring as we did and that you contribute to the next edition of the Special Issue "Two-Dimensional Materials: From Synthesis to Applications, 3rd Edition".

Sake Wang, Nguyen Tuan Hung, and Minglei Sun
Guest Editors

molecules

MDPI

Editorial

Two-Dimensional Materials: From Synthesis to Applications, 2nd Edition

Sake Wang [1,*], Nguyen Tuan Hung [2] and Minglei Sun [3]

[1] College of Science, Jinling Institute of Technology, 99 Hongjing Avenue, Nanjing 211169, China
[2] Frontier Research Institute for Interdisciplinary Sciences, Tohoku University, Sendai 980-8578, Japan; nguyen.tuan.hung.e4@tohoku.ac.jp
[3] NANOlab Center of Excellence and Department of Physics, University of Antwerp, Groenenborgerlaan 171, 2020 Antwerp, Belgium; minglei.sun@uantwerpen.be
* Correspondence: isaacwang@jit.edu.cn

1. Introduction

Two-dimensional materials continue to redefine modern materials science by offering a unique combination of atomic-scale thickness, tunable electronic structures, and highly accessible surfaces [1]. Since the emergence of graphene, the field has expanded dramatically to include elemental 2D materials, transition-metal dichalcogenides, nitrides, oxides, and a wide variety of hybrid and composite systems [2]. These materials have enabled conceptual and technological breakthroughs across nanoelectronics, optoelectronics [3], energy storage, catalysis, sensing, and environmental remediation [4].

Building upon the first edition [5], the second edition of the Special Issue "Two-Dimensional Materials: From Synthesis to Applications" in *Molecules* captures this breadth and maturity of the field. The contributions span theoretical modeling, controlled synthesis, heterostructure engineering, device design, catalytic mechanisms, and advanced characterization methodologies [6]. Collectively, the papers illustrate how fundamental understanding at the atomic and electronic levels translates into real-world applications.

Notably, the contributors to this Special Issue come from Bulgaria, China, Poland, Russia, and the USA, highlighting the global and collaborative nature of contemporary research in low-dimensional materials.

2. Scope and Thematic Organization of the Special Issue

To provide a coherent overview, the eight contributions can be broadly classified into four interrelated thematic categories:

1. Fundamental Physics and Electronic Structure of 2D Materials (Paper [7]).
2. Two-Dimensional Materials and Heterostructures for Optoelectronic and Electromagnetic Devices (Papers [8,9]).
3. Energy Storage and Conversion Enabled by 2D and 2D-Derived Materials (Papers [10,11]).
4. Catalysis, Environmental Remediation, and Advanced Characterization (Papers [12–14]).

Table 1 summarizes the thematic classification, material systems, and targeted applications of each contribution.

Table 1. Overview and categorization of contributions in this Special Issue.

Ref.	Material System	Dimensionality/Structure	Main Focus	Key Application
[7]	α-Borophene nanoribbons	1D ribbons from 2D sheet	Edge-dependent electronic and magnetic properties	Nanoelectronics, spintronics
[8]	ZnO–MoS_2 heterostructure	2D/2D p–n junction	Ultra-broadband photodetection	Optoelectronics, internet of things sensing
[9]	Graphene + Dirac semimetals	Hybrid layered structures	Tunable THz absorption	Electromagnetic devices
[10]	ZnS/2D carbon films	2D carbon-supported nanocomposites	Lithium storage mechanisms	Li-ion batteries
[11]	Co-doped GaN nanowires	1D/2D hybrid architecture	Doping-enhanced electrochemistry	Li-ion batteries
[12]	ZnO, ZnO/Eu_2O_3	Nanostructured oxide catalysts	Tribocatalysis driven by mechanical energy	Environmental remediation
[13]	Pt–SnS_2 nanosheets	2D semiconductor/metal hybrids	LSPR-assisted photocatalysis	Water purification
[14] (review)	Zeolites	Micro-/mesoporous frameworks	NMR relaxation characterization	Catalysis, porous materials

3. Fundamental Physics and Electronic Properties of Low-Dimensional Systems

A defining strength of 2D materials lies in their sensitivity to reduced dimensionality, edges, defects, and external perturbations. Rakshit et al. [7] present a comprehensive first-principles investigation of α-borophene nanoribbons, a 1D derivative of a metallic 2D boron sheet. Their work demonstrates how edge geometry (armchair vs. zigzag), ribbon width, and edge termination collectively determine electronic conduction and magnetism.

Of particular significance is the emergence of edge magnetism and spin-polarized transport in zigzag nanoribbons, with spin filtering efficiencies exceeding 40%. Such findings place borophene-based nanostructures at the forefront of spintronic interconnects, where metallic conductivity and tunable magnetism must coexist. This study exemplifies how theoretical modeling can guide the rational design of low-dimensional components for future nanoelectronic circuits.

4. Two-Dimensional Materials for Optoelectronic and Electromagnetic Devices

The integration of 2D materials into functional devices is strongly represented in this Special Issue. Zhou et al. [8] report a ZnO–MoS_2 type-II heterostructure [15,16] photodetector with an exceptionally broad operational range spanning from ultraviolet to MIR wavelengths (365 nm–10 µm). The combination of experimental device fabrication and DFT calculations reveals how defect engineering—specifically Mo vacancies—reduces the effective bandgap to ~0.20 eV, enabling MIR detection.

Equally compelling is the demonstration of self-powered operation, fast response times, and light-controlled hysteresis, which opens avenues for optical memory and neuromorphic computing. This work highlights the versatility of 2D heterostructures in multifunctional optoelectronic platforms [3].

https://doi.org/10.3390/molecules31020215

Complementing photodetection, Zhou et al. [9] explore THz absorption using hybrid systems composed of graphene and bulk Dirac semimetals. Through electromagnetic simulations and impedance-matching analysis, they demonstrate broadband absorption exceeding 80% in the 7.7–9.2 THz range. The dual tunability arising from graphene and Dirac semimetals underscores how 2D materials can be engineered for adaptive electromagnetic environments, relevant to sensing, communication, and stealth technologies.

5. Energy Storage: 2D Materials in Lithium-Ion Batteries

Energy storage remains a central challenge for sustainable technologies, and several contributions address this domain. Wei et al. [10] introduce a general synthesis route to ZnS nanoparticles embedded in 2D carbon films, derived from the thermal decomposition of organic zinc salts. The resulting ZnS/C composites show excellent lithium storage performance, benefiting from enhanced electrical conductivity and effective buffering of volume changes during lithiation.

Wu et al. [11] further advance this theme by designing Co-doped GaN nanowires grown directly on carbon paper. By combining experimental electrochemical measurements with DFT calculations, the authors reveal how Co^{2+} substitution modifies the electronic structure of GaN, lowers ion diffusion barriers, and significantly improves cycling stability. The work exemplifies how doping strategies and hierarchical architectures can transform traditionally inert semiconductors into high-performance battery electrodes.

Together, these studies demonstrate that 2D and quasi-2D materials are not merely passive hosts but active participants in charge storage and transport processes.

6. Catalysis, Environmental Remediation, and Surface Phenomena

Catalytic and environmental applications are another strong pillar of this Special Issue. Ivanova et al. [12] introduce an innovative tribocatalytic approach using ZnO and ZnO/Eu_2O_3 sol–gel catalysts, where mechanical friction replaces light as the driving energy source. The ability to degrade paracetamol under dark conditions highlights a promising pathway for green chemistry and sustainable pollutant removal, leveraging ubiquitous mechanical energy in natural environments.

In a complementary photocatalytic context, Feng et al. [13] investigate Pt-decorated SnS_2 nanosheets for tetracycline degradation. The synergy between sheet-like SnS_2 morphology and the LSPR of Pt nanoparticles leads to enhanced light absorption, efficient charge separation, and high degradation efficiency. This work reinforces the importance of metal–2D semiconductor interfaces in solar-driven environmental remediation.

7. Advanced Characterization and Conceptual Expansion Beyond Strictly 2D Systems

While this Special Issue focuses on 2D materials, Shelyapina [14] provides a timely and insightful review on NMR relaxation techniques for probing zeolites. Although zeolites are not strictly 2D materials, their hierarchical porosity, surface chemistry, and confined diffusion phenomena resonate strongly with concepts central to 2D materials science.

The review highlights how 2D NMR relaxation methods (T_1–T_2 and T_2–T_2 correlations) enable unprecedented insight into molecular mobility, surface acidity, pore size distribution, and connectivity. These techniques are increasingly relevant for characterizing 2D-based catalysts, membranes, and hybrid porous systems, thereby broadening the methodological toolkit available to the community.

https://doi.org/10.3390/molecules31020215

8. Outlook and Perspectives

The contributions collected in this second edition collectively demonstrate that the field of 2D materials has progressed from isolated material discovery toward system-level integration, multifunctionality, and real-world relevance [17]. From edge-engineered borophene nanoribbons and defect-tuned heterostructures to mechanically driven catalysis and advanced spectroscopic characterization, the Special Issue reflects both depth and diversity.

This edition will stimulate continued interdisciplinary collaboration, inspiring both curiosity and application-driven exploration in materials science, which we sincerely hope will contribute to the next edition of this Special Issue, "Two-Dimensional Materials: From Synthesis to Applications, 3rd Edition".

Funding: S.W. was funded by the China Scholarship Council (No. 201908320001), the Natural Science Foundation of Jiangsu Province (No. BK20211002), and Qinglan Project of Jiangsu Province of China. N.T.H. was funded by financial support from the Frontier Research Institute for Interdisciplinary Sciences, Tohoku University, Japan. M.S. was supported by funding from Research Foundation-Flanders (FWO; no. 12A9923N).

Acknowledgments: The authors would like to thank all the staff in MDPI Publishing and the editors of Molecules for establishing and running this Special Issue, as well as reviewers around the globe who spent their valuable time thoroughly reviewing and improving the articles published in this Special Issue. We also feel grateful to all the authors from Bulgaria, China, Poland, Russia, and the USA for choosing this Special Issue to publish their excellent science.

Conflicts of Interest: The authors declare no conflicts of interest.

Abbreviations

The following abbreviations are used in this manuscript:

1D	one-dimensional
2D	two-dimensional
DFT	density functional theory
LSPR	local surface plasmon resonance
MIR	mid-infrared
NMR	nuclear magnetic resonance
THz	terahertz

References

1. Sharma, R.; Raghav, S. (Eds.) *2D Materials: Fundamentals, Fabrication, and Applications*; Engineering Materials; Springer: Singapore, 2025. [CrossRef]
2. Deshmukh, K.; Pandey, M.; Hussain, C.M. (Eds.) *Hexagonal Boron Nitride: Synthesis, Properties, and Applications*; Micro and Nano Technologies; Elsevier: Amsterdam, The Netherlands, 2024. [CrossRef]
3. Wang, S.; Tian, H. *Two-Dimensional Valleytronic Materials: From Principles to Device Applications*; IOP Publishing: Bristol, UK, 2025. [CrossRef]
4. Mokashi, S.S. *Applications of Nano Materials in Engineering*; Geh Press: Lucknow, India, 2025.
5. Wang, S.; Hung, N.T.; Sun, M. Two-Dimensional Materials: From Synthesis to Applications. *Molecules* **2025**, *30*, 741. [CrossRef] [PubMed]
6. Wu, X.; Yan, Q.; Wang, H.; Wu, D.; Zhou, H.; Li, H.; Yang, S.; Ma, T.; Zhang, H. Heterostructured Catalytic Materials as Advanced Electrocatalysts: Classification, Synthesis, Characterization, and Application. *Adv. Funct. Mater.* **2024**, *34*, 2404535. [CrossRef]
7. Rakshit, S.; Sun, F.; Gonzalez Szwacki, N.; Yakobson, B.I. α-Borophene Nanoribbons: Edge-Dependent Metallic and Magnetic Properties for Low-Dimensional Nanoelectronics. *Molecules* **2025**, *30*, 4177. [CrossRef]
8. Zhou, B.; Peng, X.; Chu, J.; Malca, C.; Diaz, L.; Zhou, A.F.; Feng, P.X. Type II ZnO-MoS_2 Heterostructure-Based Self-Powered UV-MIR Ultra-Broadband p-n Photodetectors. *Molecules* **2025**, *30*, 1063. [CrossRef]

9. Zhou, J.; Sun, X.; Xu, J.; Wu, S.; Jin, K.; Tang, Y.; Yi, Z.; Yi, Y. Versatile Tunable Terahertz Absorption Device Based on Bulk Dirac Semimetals and Graphene. *Molecules* **2025**, *30*, 999. [CrossRef] [PubMed]
10. Wei, D.; Wang, T.; Jiao, R.; Qu, L.; Zeng, S. Two-Dimensional Carbon Film-Supported ZnS Nanocomposites Obtained from Thermal Decomposition of Organic Zinc Salts and Sulfidation Reactions for Lithium Storage. *Molecules* **2025**, *30*, 893. [CrossRef] [PubMed]
11. Wu, P.; Wang, X.; Wang, D.; Wang, Y.; Zheng, Q.; Wang, T.; Sun, C.; Liu, D.; Chen, F.; Wang, S. High-Quality Epitaxial Cobalt-Doped GaN Nanowires on Carbon Paper for Stable Lithium-Ion Storage. *Molecules* **2024**, *29*, 5428. [CrossRef] [PubMed]
12. Ivanova, D.; Kolev, H.; Mladenova, R.; Stefanov, B.I.; Kaneva, N. Harvesting Friction Energy on Zinc Oxide and Zinc Oxide/Europium Oxide Sol-Gel Catalysts for Tribocatalytic Paracetamol Degradation. *Molecules* **2025**, *30*, 2265. [CrossRef] [PubMed]
13. Feng, M.; Zhou, T.; Li, J.; Cao, M.; Cheng, J.; Li, D.; Qi, J.; You, F. Insight into the Local Surface Plasmon Resonance Effect of Pt-SnS_2 Nanosheets in Tetracycline Photodegradation. *Molecules* **2024**, *29*, 5423. [CrossRef] [PubMed]
14. Shelyapina, M.G. NMR Relaxation to Probe Zeolites: Mobility of Adsorbed Molecules, Surface Acidity, Pore Size Distribution and Connectivity. *Molecules* **2024**, *29*, 5432. [CrossRef] [PubMed]
15. Wang, S.; Ren, C.; Tian, H.; Yu, J.; Sun, M. MoS_2/ZnO van der Waals heterostructure as a high-efficiency water splitting photocatalyst: A first-principles study. *Phys. Chem. Chem. Phys.* **2018**, *20*, 13394–13399. [CrossRef] [PubMed]
16. Wang, S.; Tian, H.; Ren, C.; Yu, J.; Sun, M. Electronic and optical properties of heterostructures based on transition metal dichalcogenides and graphene-like zinc oxide. *Sci. Rep.* **2018**, *8*, 12009. [CrossRef] [PubMed]
17. Rogdakis, K.; Psaltakis, G.; Fagas, G.; Quinn, A.; Martins, R.; Kymakis, E. Hybrid chips to enable a sustainable internet of things technology: Opportunities and challenges. *Discov. Mater.* **2024**, *4*, 4. [CrossRef]

molecules

MDPI

Article

α-Borophene Nanoribbons: Edge-Dependent Metallic and Magnetic Properties for Low-Dimensional Nanoelectronics

Subrata Rakshit [1,2], Favian Sun [2], Nevill Gonzalez Szwacki [1] and Boris I. Yakobson [2,*]

[1] Faculty of Physics, University of Warsaw, Pasteura 5, PL-02093 Warszawa, Poland; srakshit@fuw.edu.pl (S.R.); gonz@fuw.edu.pl (N.G.S.)
[2] Department of Materials Science and NanoEngineering, Rice University, Houston, TX 77005, USA; fs67@rice.edu
* Correspondence: biy@rice.edu

Abstract: We present a comprehensive first-principles study of nanoribbons made from the α-borophene sheet. This study looks at how edge shape, ribbon width, and magnetic ordering affect their structural, electronic, and transport properties. Ribbons cut along armchair (ac) and zigzag (zz) directions with various edge designs—armchair (a), single (s), and double (d) chains—are all stable. The double chain "dd" edges have the highest binding energies and the lowest edge energies, which aligns with near-bulk coordination. Our analysis of electronic structure and ballistic transport shows strong metallic characteristics in almost all configurations. Only the narrowest "3-ad" ribbon shows a small energy gap that disappears as the width increases. Zigzag ribbons ("zz") display edge magnetism that depends on width, changing from non-magnetic to antiferromagnetic and finally to ferromagnetic states. Their spin-resolved transmission demonstrates clear spin filtering with polarization exceeding about 40%. Edge passivation affects these properties: hydrogen and fluorine reduce the "zz" edge magnetic moments and spin transport, while oxygen maintains finite magnetism. Near the Fermi level, many ribbons allow for multiple conducting channels. This feature supports low-resistance charge flow even for widths below 10 nm, while higher-energy transmission shows greater dependence on width. These findings position α-borophene nanoribbons as promising one-dimensional components for nanoelectronic connections and spintronic devices, combining high stability, adjustable edge magnetism, and strong metallic conduction.

Keywords: borophene nanoribbons; DFT; electronic properties; electronic transport

1. Introduction

Low-dimensional materials continue to reveal unique physical phenomena and hold promise for nanoscale electronics, energy applications, and sensing technologies. Among them, boron—a neighbor of carbon in the periodic table—has emerged as an especially versatile element for constructing low-dimensional nanostructures due to its electron deficiency, multicenter bonding, and polymorphism [1,2]. The possibility of boron-based analogs to carbon structures, including fullerenes [3,4], nanotubes [5], and two-dimensional (2D) borophene sheets [6], has opened a rich frontier in boron nanoscience [7,8].

Borophene, a single-atom-thick sheet of boron, has been synthesized on metallic substrates such as Ag(111) and Ag(110) using physical vapor deposition methods under ultrahigh vacuum conditions [9,10]. Unlike graphene, borophene is not a single-phase material but comprises several polymorphic phases, including α, β_{12}, χ_3, and δ_6, characterized by a mixture of triangular and hexagonal motifs [11]. These polymorphs exhibit

anisotropic bonding networks, high flexibility, and metallic behavior, making borophene and its derivatives highly attractive for applications in flexible electronics, batteries, and energy storage [12,13].

A natural variety of borophene's two-dimensional (2D) structure is the formation of borophene nanoribbons (BNRs, an analog of extensively studied GNR–graphene nanoribbon [14,15]), which are quasi-one-dimensional (1D) strips characterized by controlled edge morphology and tunable widths. Conceptually, BNRs can be constructed by cutting a borophene sheet along defined crystallographic directions, resulting in edge-dependent properties [16]. Previous first-principles calculations show that hydrogen passivation of zigzag boron nanoribbon (BNRs) edges stabilizes the structures and opens semiconducting gaps that oscillate with ribbon width [17]. Transport calculations further indicate a pronounced width dependence in BNRs devices, with wider ribbons delivering substantially higher conductance [18]. In terms of structural origin, nanoribbons obtained from the α-boron sheet are energetically favored over those from triangular or reconstructed sheets, and their stability increases with width; while most BNRs are metallic, semiconducting cases have also been reported [19]. Complementary NEGF/TB calculations on α-BNRs FM/NM/FM junctions predict pure spin currents and spin voltages under thermal gradients, with perfect spin filtering and diode-like response at low temperatures. The spin figure of merit grows with stronger exchange fields and decreases with ribbon width, underscoring the promise of narrow α-BNRs for spin-thermoelectric devices [20]. Recent DFT studies indicate that nitrogen termination of zigzag α-BNRs edges stabilizes the ribbons and can open a band gap. Subsequent Cr or Mn doping induces robust ferromagnetism with Curie temperatures above 700 K, resulting in a magnetic metal for Cr and a diluted magnetic semiconductor for Mn [21]. 1D boron chains undergo a transition from metallic to semiconductor, driven by the formation of spin density waves [22]. Recent advances in topological and mechanochemical design have enabled the fabrication of complex ribbon architectures, including rectangular and bi-trapezium-shaped motifs derived from β_{12} and χ_3 borophene phase [23]. These designs provide powerful handles for tuning the band structure, electronic transport and bonding networks of BNRs [24,25]. Furthermore, advanced many-body computational methods such as thermally assisted-occupation density functional theory (TAO-DFT) have revealed that large BNRs exhibit pronounced size-dependent electronic properties and strong static correlation effects due to their inherent multiradical character [26]. Previous studies have shown that the presence of double- or triple-chain edge structures enhances the stability of borophene nanoribbons [27].

Experimental efforts have succeeded in synthesizing BNRs with widths in the range of 10–100 nm and lengths up to several micrometers using various vapor-phase techniques, including chemical vapor deposition and magnetron sputtering [28,29]. Structural analyses indicate that these nanoribbons may adopt tetragonal crystalline cores with amorphous surface layers. Meanwhile, scanning tunneling microscopy (STM) and first-principles simulations have confirmed the atomic-scale periodicity and polymorphism in epitaxial BNRs grown on Ag surface [30].

In the present work, we investigate boron nanoribbons derived from the α-sheet borophene polymorph, characterized by a hexagonal hole density of $\eta = 1/9$, where η denotes the ratio of hexagonal vacancies to total atomic sites in the ideal triangular lattice. This particular configuration is chosen because both theoretical predictions and experimental observations identify α-borophene ($\eta = 1/9$) as one of the most stable borophene phases [1,6]. We construct nanoribbons by trimming the α-sheet along two principal crystallographic directions: armchair (ac) and zigzag (zz). For the ac-oriented nanoribbons, we design multiple edge configurations by combining distinct motifs—namely "a" (armchair chain), "s" (single chain), and "d" (double chain)—to explore the impact of

edge geometry on electronic behavior. To further investigate the influence of passivation, borophene nanoribbons (BNRs) edges are passivated with hydrogen (H), oxygen (O), and fluorine (F). Using density functional theory (DFT) calculations, we systematically examine the structural stability, binding energies, electronic band structures, magnetic properties, and ballistic transport characteristics of selected ribbon types. Our results demonstrate the persistence of metallicity across a wide range of edge configurations and reveal clear structure–property correlations. These findings offer valuable insight into the tunability of α-borophene nanoribbons and their potential as functional one-dimensional components in future nanoelectronic and spintronic devices.

2. Computational Methods

All first-principles calculations were carried out within the framework of DFT using the Perdew–Burke–Ernzerhof (PBE) exchange–correlation functional and norm-conserving pseudopotentials from the PseudoDojo library [31], as implemented in the Quantum ESPRESSO (QE) package (v7.2) [32]. The plane-wave kinetic energy cutoff was set to 80 Ry. Structural relaxations were performed by optimizing both atomic positions and cell parameters until the forces on all atoms were below 0.3 meV/Å and the total energy change per self-consistent cycle was less than 10^{-5} Ry. Spin polarization effects were included, and the systems were sampled using a Γ-centered $1 \times 16 \times 1$ Monkhorst–Pack k-point mesh along the periodic direction. To simulate isolated 1D systems, we employed vacuum regions of 12 Å. The electronic structures were obtained on dense k-point grids of $1 \times 48 \times 1$ along periodic direction to ensure accurate interpolation of the electronic bands. Visualization of atomic structures was performed using the VESTA software (v3.5.8) [33].

Ballistic transport calculations were performed using the TranSIESTA (v5.2.1) [34,35] code under the Non-Equilibrium Green's Function (NEGF) formalism. Without relaxing the structures in SIESTA, the transmission steps have good agreement with the band structures computed in QUANTUM ESPRESSO. The electrodes were sampled using 101 k-points in the periodic direction, while the scattering region was sampled with only the gamma point. Eigenchannel wavefunctions are computed using the Inelastica package (v1.3.7) [36,37]. Current under a finite voltage was computed using the Landauer–Büttiker equation,

$$I(V) = \frac{e}{h}\int T(E,V)[f(E,\mu + V/2) - f(E,\mu - V/2)]dE \quad (1)$$

where $T(E,V)$ is the mode-weighted transmission value under a bias V, $f(E,\mu)$ is the Fermi distribution function at a chemical potential μ, e is the charge of an electron, and h is Planck's constant.

3. Results

We classify the borophene nanoribbons (BNRs) into seven distinct categories (as shown in Figure 1): six derived from the armchair (ac) direction and one from the zigzag (zz) direction. The adopted nomenclature is defined as follows: "aa" indicates ribbons whose edges both consist of armchair chains; "as" denotes ribbons with one armchair edge and one single chain edge; "ad" represents ribbons with one armchair edge and one double chain edge. Similarly, "ss", "ds", and "dd" denote ribbons whose edges consist, respectively, of single–single, double–single, and double–double chain combinations. The "zz" refers to ribbons oriented along the zigzag direction. The parameter N specifies the number of chains spanning the ribbon width. In addition to the pristine BNRs, the "zz" BNRs are further investigated by edge passivation using hydrogen (H), oxygen (O), and fluorine (F) atoms on their structural and magnetic properties. The "zz" BNRs are specifically chosen because they exhibit magnetism at the zigzag edges. This makes it an ideal candidate to

explore how different passivating atoms influence the stability and edge magnetism, in contrast to non-magnetic configurations such as "dd" BNRs.

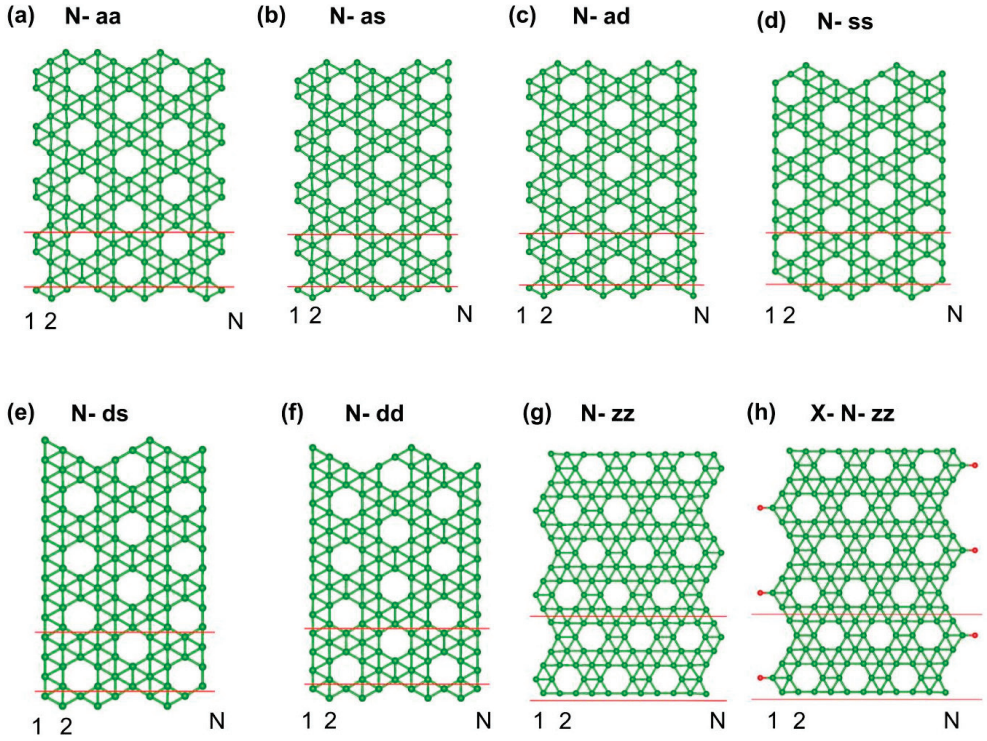

Figure 1. (**a**) N-aa (both edges are armchair chain), (**b**) N-as (one edge armchair chain and another edge single chain), (**c**) N-ad (one edge armchair chain and another edge double chain), (**d**) N-ss (both edges are single chain), (**e**) N-ds (one edge double chain and another edge single chain), (**f**) N-dd (double chain at both edges), (**g**) N-zz, and (**h**) X-N-zz (edges are passivated with X, where X = H-, O-, F-, shown as red dots). The red lines delineate the unit cell.

Figure 2 provides a systematic illustration of how the binding energy E_b varies with nanoribbon width and edge shape. The binding energy is used to evaluate the stability of the BNRs. It is calculated using the formula: $E_b = (n \times E_n - E)/n$, where E_b is the binding energy per atom, n is the number of atoms, E_n is the energy of one single boron atom, E is the energy of one BNR. A higher (more positive) binding energy indicates greater stability of the BNRs. A general and consistent trend observed across all edge types is that the binding energy E_b increases monotonically with ribbon width (i.e., with the number of chains N). This indicates that wider ribbons are more energetically favorable. For instance, in "aa", E_b increases from 5.386 eV/atom for "4-aa" to 5.798 eV/atom for "16-aa". Similar monotonic increase is evident for "ss" (from 5.379 to 5.816 eV/atom), "ds" (from 5.645 to 5.858 eV/atom), and "dd" (from 5.80 to 5.895 eV/atom) edge families. This trend is the same for all types of edges, reflecting a general tendency toward bulk-like stability as the ribbon width increases and edge effects weaken, supporting the potential feasibility of synthesizing such nanoribbons experimentally.

While width plays an important role, the edge structure shows an even more pronounced effect on the stability. Among the seven categories of BNRs considered, the double chain edge ("dd") consistently exhibits the highest binding energy for any given width. For example, at comparable widths (~12 Å), binding energy E_b = 5.870 eV/atom for the "11-dd" ribbon, closely approaching the cohesive energy of the α-boron sheet, whereas the "10-aa" ribbon yields 5.707 eV/atom. The higher stability of "dd" edges can be attributed to their enhanced structural uniformity and minimal edge reconstruction. The double chain termination effectively saturates most of the dangling bonds at the boundary, reducing electronic

localization and strain, which leads to higher binding energy. Moreover, the smaller edge energy ($\varepsilon \approx 0.20 - 0.21$ eV/Å) observed for "dd" ribbons confirms that "dd" edges are more favorable. In contrast, the armchair—armchair chain ("aa") configuration has the lowest E_b values (5.386–5.798 eV/atom), corresponding to the largest edge energy ($\varepsilon \approx 0.58$ eV/Å). The armchair chain edges host a large number of under-coordinated atoms and irregular bond lengths ranging from 1.52 Å to 1.94 Å (Table 1), signifying enhanced local stress and substantial bond-length variation. This geometric diversity introduces strain energy and localized electronic states, both of which destabilize the structure. Therefore, the "aa" BNRs are the least stable among all edge terminations. Between these extremes, there are several intermediate edge configurations that bridge the stability gap. The single chain ("ss" and "as") and double chain ("ad" and "ds") ribbons show progressively increasing E_b values. For instance, "ad" BNRs exhibit $E_b = 5.367 - 5.837$ eV/atom with $\varepsilon \approx 0.41 - 0.45$ eV/Å, while "ds" shows $E_b = 5.645 - 5.858$ eV/atom and $\varepsilon \approx 0.33 - 0.35$ eV/Å. The edge energies follow the trend as "dd" < "ds" < "ad" < "ss" < "as" ≈ "aa". This systematic decrease in edge energy (ε) confirms the energetic hierarchy deduced from the binding energy (E_b) trends. The E_b follows the order "aa" < "as" < "ss" < "ad" < "ds" < "dd", which clearly shows an increasing stabilization as edge atoms become more coordinated. These trends correspond to a gradual reduction in the number of unsaturated valences and dangling bonds along the edge.

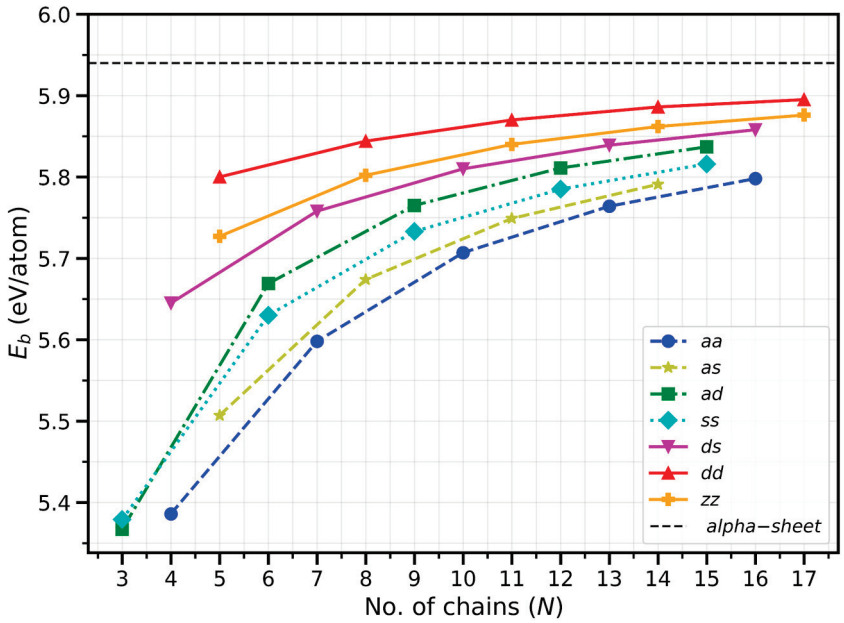

Figure 2. Binding energy vs. the number of boron chains. The value for the α-borophene phase is $E_b = 5.94$ eV/atom. All follow closely an analytical relation $E = E_b - \varepsilon/N$, where ε values reflect the energies of the edges.

A complementary understanding arises from examining bond-length variation at the ribbon edges. Edge atoms in "aa" BNRs display the broadest bond-length range (1.52–1.94 Å), indicating significant structural distortions and local stress accumulation. But "dd" edges maintain a narrower and more uniform distribution (1.64–1.73 Å), suggesting nearly bulk-like coordination and reduced edge reconstruction. This structural homogeneity translates directly to improved binding energy, highlighting that uniform bonding environments at the edges are a key factor governing nanoribbon stability. The more regular the bond pattern, the lower the total energy, since localized distortions and under-coordination are minimized.

Table 1. Geometric, energetic, magnetic, and electronic transport properties of α-borophene nanoribbons (BNRs) with various edge configurations and widths. For each structure, we report the ribbon width (in Å), binding energy per atom (E_b, in eV/atom), edge energy (ε, in eV/Å), minimum and maximum bond lengths (d_{min} and d_{max}, respectively), total magnetic moment (M, in μ_B), and the number of transmission channels T at the Fermi level (E = E_F), (up/down) is transmission channels of up spin and down spin of "zz" BNRs. Structures are grouped by edge type: "aa", "as", "ad", "ss", "ds", "dd", and "zz", as defined in the text.

Name	Width (Å)	E_b (eV/atom)	ε (eV/Å)	d_{min} (Å)	d_{max} (Å)	M ($\mu_B/atom$)	T (E = E_F) (up/down)
4-aa	4.11	5.386	0.52	1.54	1.94	0.012	3
7-aa	8.56	5.599	0.59	1.53	1.79	0.028	3
10-aa	12.96	5.707	0.59	1.52	1.80	0.017	3
13-aa	17.34	5.764	0.58	1.52	1.80	0.003	3
16-aa	21.73	5.798	0.58	1.52	1.80	0.001	3
5-as	5.79	5.507	0.56	1.51	1.79	0.019	4
8-as	10.18	5.674	0.55	1.51	1.79	0.006	3
11-as	14.55	5.749	0.55	1.51	1.79	0.004	3
14-as	18.94	5.791	0.55	1.51	1.79	0.000	4
3-ad	2.94	5.367	0.45	1.54	1.78	0.000	0
6-ad	7.28	5.669	0.43	1.52	1.79	0.000	4
9-ad	11.67	5.765	0.42	1.52	1.80	0.000	4
12-ad	16.06	5.811	0.41	1.52	1.79	0.000	4
15-ad	20.45	5.837	0.41	1.52	1.79	0.003	5
3-ss	2.98	5.379	0.46	1.60	1.70	0.015	3
6-ss	7.41	5.630	0.50	1.60	1.72	0.000	6
9-ss	11.77	5.733	0.50	1.61	1.71	0.000	4
12-ss	16.17	5.785	0.50	1.62	1.71	0.000	4
15-ss	20.53	5.816	0.49	1.62	1.74	0.000	4
4-ds	4.45	5.645	0.33	1.61	1.75	0.011	3
7-ds	8.87	5.758	0.35	1.62	1.74	0.019	4
10-ds	13.27	5.810	0.35	1.61	1.73	0.004	5
13-ds	17.65	5.839	0.35	1.62	1.73	0.003	5
16-ds	22.05	5.858	0.35	1.62	1.74	0.002	4
5-dd	5.98	5.800	0.20	1.64	1.72	0.009	3
8-dd	10.38	5.844	0.21	1.64	1.72	0.005	3
11-dd	14.78	5.870	0.21	1.65	1.73	0.000	4
14-dd	19.13	5.886	0.21	1.65	1.72	0.003	4
17-dd	23.52	5.895	0.21	1.66	1.72	0.002	5
5-zz	9.03	5.727	0.34	1.60	1.86	0.005	4
8-zz	14.13	5.802	0.35	1.62	1.83	1.335	3/6
11-zz	19.18	5.840	0.34	1.62	1.82	1.335	2/5
14-zz	24.24	5.862	0.34	1.62	1.82	1.325	3/6
17-zz	29.29	5.876	0.34	1.62	1.81	1.30	3/6

The "zz" BNRs obtained from zigzag directions show remarkably high binding energies (E_b = 5.727 − 5.876 eV/atom), exceeded only by the "dd" ribbons. The corre-

sponding edge energies ($\varepsilon \approx 0.34$ eV/Å) make them one of the most stable terminations. This suggests that the zigzag-type edges allow efficient reconstruction and electron delocalization, which effectively saturate edge bonds. Overall, both energetic and structural analyses show a clear stability trend among all investigated BNRs. Based on edge energy (ε) and binding energy (E_b), the order of thermodynamic favorability follows: "dd" (most stable) < "zz" < "ds"< "ad" < "ss" < "as" < "aa" (least stable).

Since passivation with different atoms can enhance the stability of pristine BNRs by saturating dangling bonds and lowering edge energy, we further investigated the role of edge passivation on the stability of the "zz" BNRs with hydrogen (H), Oxygen (O), and Fluorine (F) at the edges. In Table 2, the formation energy of passivation per unit length is presented. The formation energy of passivation per unit length is calculated using the formula $E_f = (E_{BNR+X} - n_X \times E_X - E_{BNR})/L$; E_{BNR+X} energy of passivated BNRs, E_{BNR} is the energy of pristine BNRs, n_X is no of passivated X (X = H-, O-, F-) atom, E_X is the energy of an isolated X atom, and L is the length of the unit cell. As shown in Table 2, all the passivated "X-N-zz" BNRs exhibit negative formation energies, which confirms that H-, O-, and F- passivation processes are energetically favorable. Among them, fluorine-passivated BNRs show the highest negative formation energy (E_f = −1.415 to −1.429 eV/Å), indicating the strongest stabilization, followed by oxygen and hydrogen passivations. The formation energy E_f oscillates with ribbon width. This peculiar behavior indicates a stronger electronic correlation between the edge passivated atoms and the inner boron atoms in the "zz" BNRs.

Table 2. For passivated "zz" structure, we report the formation energy per unit length (E_f, in eV/Å), bond lengths between B and X atom (X = H-, O-, F-), total magnetic moment (M, in μ_B), and the number of transmission channels T at the Fermi level (E = E_F), (up/down) is transmission channels of up spin and down spin of passivated BNRs.

	E_f (eV/Å)	$d_{B\text{-}X}$ (Å)	M ($\mu_B/atom$)	T (E = E_F) (up/down)
H-5-zz	−0.916	1.189	0.0	3
H-8-zz	−0.931	1.189	0.0	5
H-11-zz	−0.935	1.189	0.0	2
H-14-zz	−0.936	1.189	0.0	2
H-17-zz	−0.937	1.189	0.0	2
O-5-zz	−1.342	1.283	0.855	3/5
O-8-zz	−1.338	1.283	0.791	4/6
O-11-zz	−1.349	1.283	0.845	6/4
O-14-zz	−1.347	1.283	0.855	2/6
O-17-zz	−1.345	1.283	0.87	2/6
F-5-zz	−1.415	1.339	0.0	3
F-8-zz	−1.428	1.339	0.0	4
F-11-zz	−1.429	1.339	0.0	2
F-14-zz	−1.428	1.339	0.0	2
F-17-zz	−1.428	1.339	0.0	2

The calculated electronic band structure and density of states (DOS) for all the BNRs are shown in Figure 3 (and in Supplementary Figure S1). The results reveal that most of the BNRs are metallic, with multiple bands crossing the Fermi level. Only "3-ad" BNR

has an indirect band gap of 0.165 eV. This gap closes with increasing BNR width. There is no evidence of Peierls-type distortions. Even after edge passivation with hydrogen (H), oxygen (O), and fluorine (F) atoms, all BNRs retain their metallic character. This indicates band structure is robust against passivation, highlighting their potential for nanoscale electronic and spintronic applications.

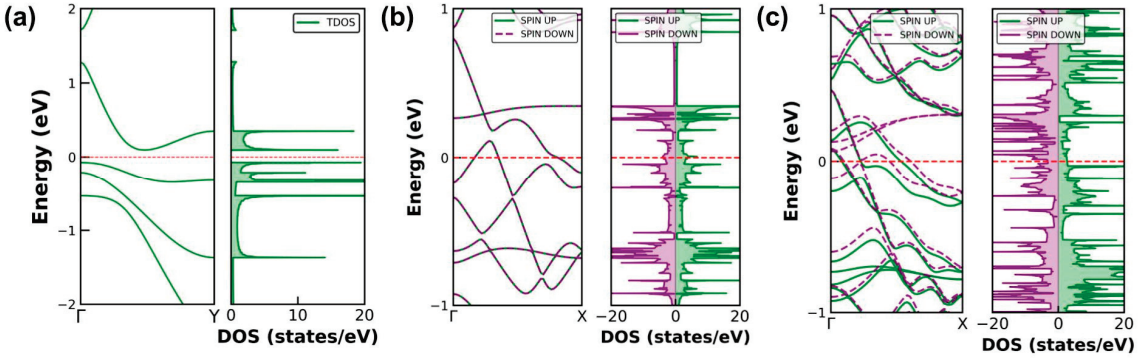

Figure 3. (**a**) Electronic band structure and total density of states of the "3-ad" nanoribbon, showing a finite band gap. (**b**,**c**) Spin-resolved band structure and DOS of the "8-zz" and "17-zz" nanoribbons, respectively, symmetric and asymmetric DOS show AFM and FM behavior of the BNRs.

Magnetic moments indicate that ribbons cut along the armchair(ac) direction are predominantly non-magnetic or only weakly magnetic. In contrast, zigzag-edge boron nanoribbons ("zz"-BNRs) display a pronounced width-dependent anisotropy. As summarized in Table 1, the narrow "5-zz" ribbon is non-magnetic, consistent with earlier reports [21]. With increasing width, "zz" BNRs develop magnetic ground states: "8-zz", "11-zz", and "14-zz" show ferromagnetic alignment along each edge with antiferromagnetic coupling between opposite edges (i.e., AFM across the ribbon, as shown in Figure 4), whereas "17-zz" is ferromagnetic both along and across the edges. The total magnetic moment per atom is largest for "8-zz" (1.335 $\mu_B/atom$) and decreases slightly with width, reaching 1.30 $\mu_B/atom$ for "17-zz". Edge passivation of hydrogen (H) and fluorine (F) suppresses the magnetism on edges, and "zz" BNRs become non-magnetic. In contrast, passivation of oxygen (O) at the edges retains finite magnetism. Pristine "5-zz" is non-magnetic, but it becomes magnetic with O-passivation ("O-5-zz") with a magnetic moment are 0.855 $\mu_B/atom$. The magnetic moment for other O-passivated "zz" are shown in Table 2 and magnetic alignments are the same as pristine "zz" BNRs.

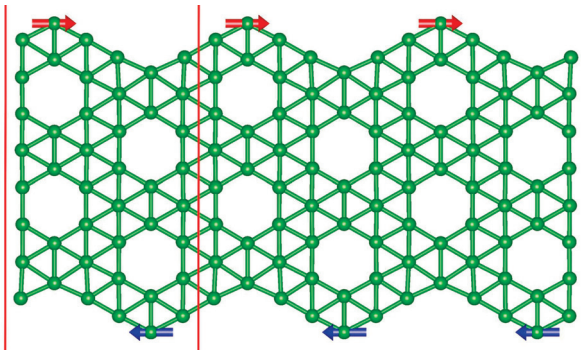

Figure 4. Magnetic ordering in "8-zz" BNRs. The red and blue arrow shows antiferromagnetic spin alignment at the opposite edges. The red line shows the unit cell.

To quantify the inter-edge exchange, we evaluate $\Delta {E_b}^{AFM-FM} = {E_b}^{AFM} - {E_b}^{FM}$. The energy differences are 0.8 meV ("8-zz"), 0.172 meV ("11-zz"), 0.015 meV ("14-zz") and -0.02 meV ("17-zz"). The progressive reduction of $\Delta {E_b}^{AFM-FM}$ signifies a gradual

weakening of AFM inter-edge coupling with greater width, and a crossover to a slightly FM-favored state at "17-zz". For the passivated "zz" BNRs, the corresponding energy differences are 0.3 meV ("O-5-zz"), 3.2 meV ("O-8-zz"), −0.01 meV ("O-11-zz"), 0.005 meV ("O-14-zz") and 0.003 meV ("O-17-zz"). These results confirm that all O-passivated BNRs except "O-11-zz" favor AFM inter-edge coupling.

These findings highlight the tunability of both electronic and magnetic properties in boron nanoribbons by controlling their width and edge geometry. The emergence of magnetism in zigzag (zz) nanoribbons with decreasing width, along with the ability to transition between AFM and FM orderings, points to their potential utility in nanoscale spintronic devices.

The electronic transport properties of α-BNRs were studied in the ballistic regime since mean free paths in similar BNRs are predicted to be on the order of ~30–100+ nm [20,38], exceeding the nanowire dimension. Under the ballistic transport assumption, the ribbon's conductance is determined by the number of conducting channels at or near E_F. For a single conducting channel, the conductance is $G_0 = \frac{2e^2}{h} = 7.748 \times 10^{-5}\ S$, accounting for spin degeneracy. With the exception of the semiconducting "3-ad", all nanoribbons have at least three spin-degenerate channels at $E = E_F$, as shown in Table 1, which can support ~1 μA under a small bias of 4 mV. The "zz" BNRs show different numbers of open channels depending on spin. Due to the high conductivity of these nanoribbons, they can operate as low-contact resistance [39] interconnects for 2D electronics with very little power loss.

Since bulk borophene is metallic, the number of transmission channels is expected to scale linearly with width. However, as shown in Table 1, the BNRs in this study do not show any strong width dependence of $T(E = E_F)$, indicating the dominance of confinement or edge effects on the transmission of low-energy carriers in α-BNRs. As the nanoribbons increase in width, we expect the transmission to return to a linear dependence on width, independent of edge structure. At energies away from E_F, the transmission depends strongly on the width.

The transmission plots for "dd" and "ss" BNRs of increasing widths are shown in Figure 5. In the "dd" edge nanoribbons, a weak dependence on width at E_F is shown. However, in the "ss" BNRs, the second-smallest ("6-ss" BNR) has the highest transmission near E_F. Notably, the "6-ss" BNR has double the transmission at E_F compared to ribbons almost 3× its width. Careful selectivity of ribbon width and edge construction may be necessary for optimized and consistent BNRs for electronic devices. It is apparent from Figures 5a and 6c that the transmission away from E_F is more dependent on width, owing to more total electrons, and thus channels, in the wider ribbons. Transmission plots for other edge configurations are shown in Supplementary Figures S2–S5.

The spatial distribution of transmission channels was analyzed using Inelastica [36,37]. Several edge-localized transmission channels at $E = E_F$ were identified and are shown in Figures 6 and S6. The "s" and "d" edge channels persist independently of the structure of the opposite edge. The "a" edge shows transmission channel wavefunctions with higher magnitude on the edges, but not fully localized. These edge channel observations agree with previous studies suggesting electron density build-up at other BNRs edges [16]. In the thinnest ribbons, it is difficult to separate the edge orbitals from the non-edge orbitals from differences in magnitude of the wavefunctions. However, the stability of transmission at widths even under 0.5 nm indicates promising applications of these BNRs as ultrathin 1D wires.

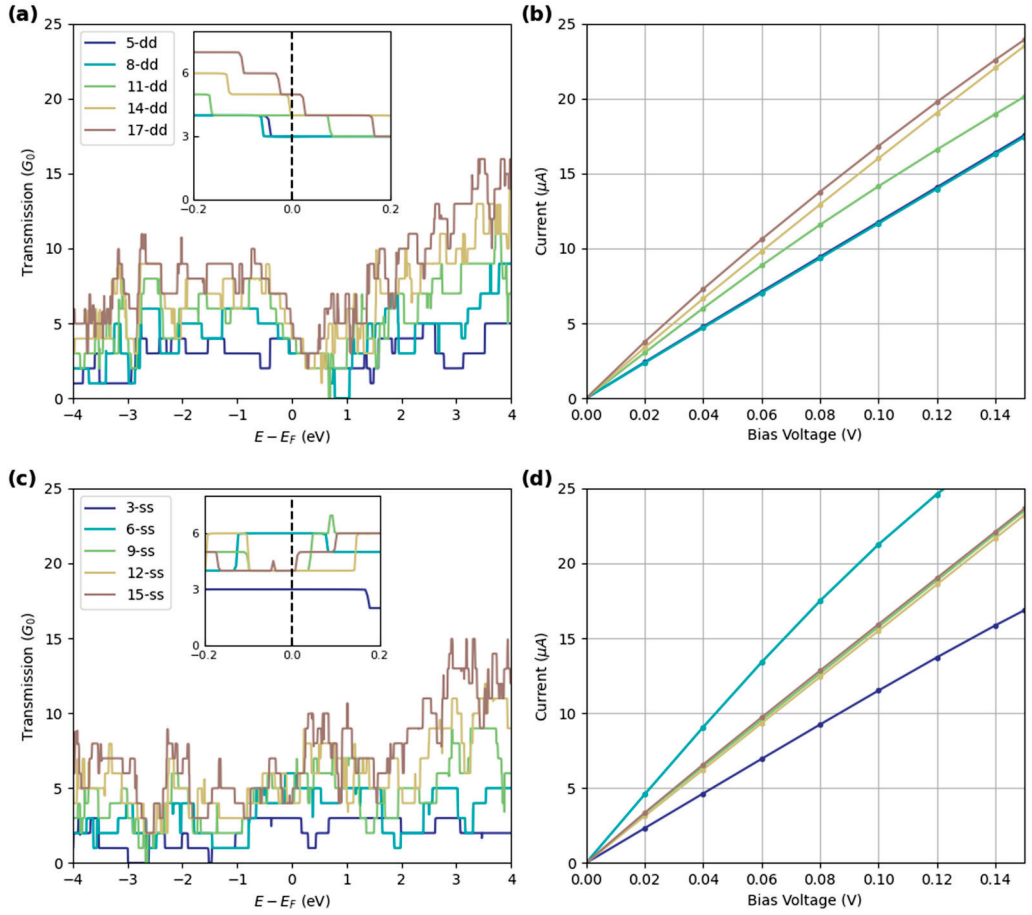

Figure 5. (**a**) Transmission at V = 0 for various "dd" BNRs. Inset shows transmission close to E_F. Within the "dd" edge nanoribbons structures, T(E = E_F) slightly increases with width. (**b**) I-V characteristics of "dd" edge nanoribbons. (**c**) Transmission at V = 0 for various "ss" BNRs. slightly increases with width. (**d**) I-V characteristics of "ss" edge nanoribbons.

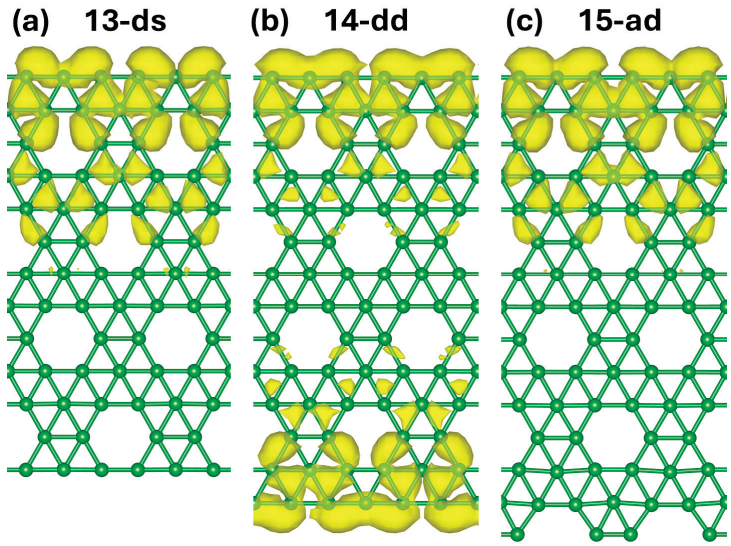

Figure 6. Magnitude of the "d" edge state wavefunction on (**a**) "13-ds", (**b**) "14-dd", and (**c**) "15-ad" nanoribbons.

Note that these edge states are a result of hybridized orbitals of under-coordinated edge atoms and are by no means topologically protected. This is to say that disorder or substrate interactions can disrupt these edge channels. Additionally, many of the transmission channels, especially in the thinner nanoribbons, correspond to wavevectors

in the middle of the Brillouin zone, with real space wavelengths of a few nanometers. In such cases, the coherence across the channel may easily be disrupted by finite length nanoribbons and imperfect coupling across junctions. Careful mode-matching at interfaces may be necessary to fully utilize the conducting channels of BNRs.

Spin-polarized transport calculations were performed for the "zz" BNRs structures. Due to the magnetization on the edges, the transmission curves show clear spin dependence. Interestingly, the minority spin carrier (spin down) has increased transmission at E_F. These magnetic nanoribbons show promise for use as a spin filter with polarization magnitude up to 42.8% at E = E_F, quantified as follows:

$$P(E) = \frac{T_{\uparrow}(E) - T_{\downarrow}(E)}{T_{\uparrow}(E) + T_{\downarrow}(E)} \tag{2}$$

where $T_{\uparrow}(E)$ and $T_{\downarrow}(E)$ are the majority (spin up) and minority (spin down) transmissions.

Figure 7 below shows the spin-resolved transmission across "zz" BNRs widths. Again, there is no strong dependence of width on the total transmission at E_F. The spin-dependent transport in magnetic BNRs has shown promise in spintronics applications [38,40]. Although the spin polarization is moderate in the intrinsic nanoribbons, external modulations, including gate control, doping, and phase junctions, offer promising methods to tune the electronic and spin transport properties [20,40,41]. Looking at the spin polarization of the thinnest magnetic ribbon, "8-zz", we observe a swing from 100% to −60% polarization within +/−0.25 eV of the intrinsic Fermi level. The wider nanoribbons also show a similar flip of the polarization, but no half-metallic region characterized by +/−100% polarization. This suggests that spin filtering effects can be dynamically modulated or flipped using finite bias or gating, opening up applications for BNRs spintronic devices.

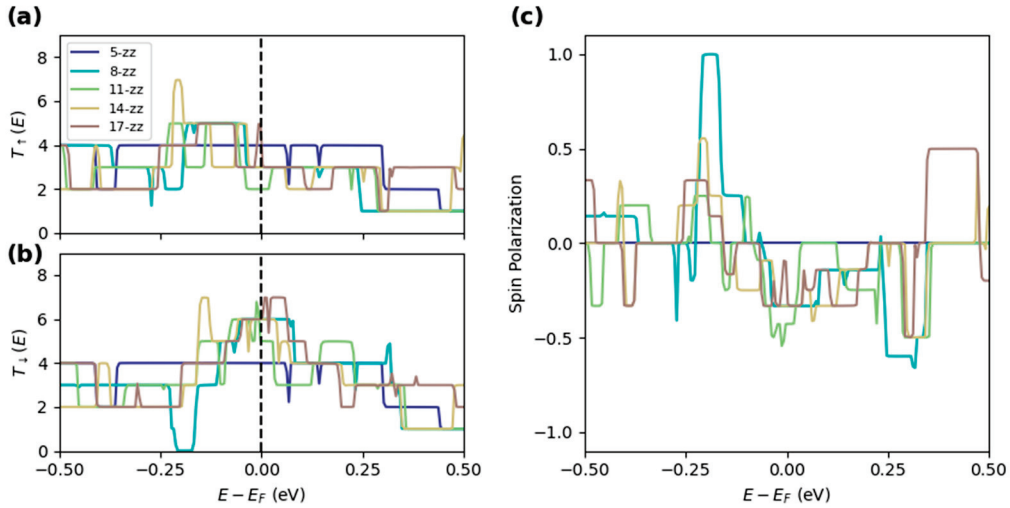

Figure 7. Transmission function for (**a**) spin up and (**b**) spin down channels for "zz" BNRs of increasing width. (**c**) Spin polarization, per Equation (2), as a function of energy.

Upon passivation of the "zz" BNRs with hydrogen or fluorine, the ribbons become non-magnetic and thus lose spin transport properties, as shown in Table 2. Additionally, the transmission of the wider is suppressed to only two spin-degenerate channels near the Fermi level, which is less conductive than all of the unpassivated BNR structures except the insulating "3-ad" BNR. On the other hand, the "O-zz" BNR structures are all magnetic.

4. Summary and Conclusions

In this work, we conducted a thorough investigation of α-borophene-based nanoribbons. We revealed how their structural, electronic, magnetic, and transport properties

depend on edge shape and ribbon width. Our detailed analysis across seven edge families shows a clear energetic trend: "dd" > "zz" > "ds" > "ad" > "ss" > "as" > "aa". This trend corresponds to lower edge stress and better coordination. The double chain "dd" edges have the highest binding energies (up to 5.90 eV/atom) and the lowest edge energies ($\approx$0.20 eV Å^{-1}). This confirms their strong thermodynamic stability and consistent structural uniformity. The steady increase in binding energy with ribbon width suggests that wide α-BNRs can be made with good stability, especially under conditions that promote self-saturation of dangling bonds. Electronic structure calculations show that metallic behavior is stable across all edge types. Even after hydrogen, oxygen, or fluorine passivation, the α-BNRs still have delocalized conduction channels at the Fermi level. The narrowest "3-ad" ribbon does open a small 0.165 eV gap, but this quickly disappears as the width increases. This enduring metallicity, along with edge-localized conduction states, explains the low resistance of α-BNRs and provides a simple way to understand their adjustable conductance. Magnetic analyses reveal width-dependent magnetism in zz nanoribbons. Narrow "zz" BNRs do not show magnetism, but as the width increases, localized edge moments appear. These moments shift from antiferromagnetic coupling between opposite edges to ferromagnetic alignment at both edges. The magnetic moment per atom ($\approx$1.3 μ_B) and the small differences between AFM and FM energy (less than 1 meV) suggest that the magnetic order can be easily switched using external fields or strain. Edge passivation has a strong impact on magnetism. Hydrogen and fluorine atoms reduce local moments, while oxygen termination secures finite magnetic states, allowing for chemical control of spin order. Ballistic transport calculations show that most α-BNRs have at least three conduction channels at $E = E_F$, leading to conductance values of $G \approx 2$–$3\ G_0$ ($G_0 = 2e^2/h$). The transmission spectra show little change with width near E_F but show significant variation at higher energies, indicating that both edge and bulk-like channels exist. Spin-resolved transport for magnetic "zz" BNRs shows polarization above 40%, confirming their spin filtering ability and suggesting potential applications as spin valves or thermospintronic devices.

Overall, these findings position α-borophene nanoribbons as an appealing option for one-dimensional metallic interconnects and spintronic components. Their strong intrinsic stability, controllable edge magnetism, and strong metallicity combine the benefits of graphene nanoribbons with the chemical flexibility of boron. Future research should examine how substrates, strain engineering, and heterostructure design influence their transport and magnetic properties. Creating α-BNRs with controlled edge chemistry could lead to advanced nanoscale conductors, spin filters, and quantum devices built on light, flexible boron structures.

Supplementary Materials: The following supporting information can be downloaded at the following: https://www.mdpi.com/article/10.3390/molecules30214177/s1, Figure S1: (a) Electronic band structure and density of states (DOS) of "aa" BNRs, (b) Electronic band structure and density of states (DOS) of "as" BNRs, (c) Electronic band structure and density of states (DOS) of "ad" BNRs, (d) Electronic band structure and density of states (DOS) of "ss" BNRs, (e) Electronic band structure and density of states (DOS) of "ds" BNRs, (f) Electronic band structure and density of states (DOS) of "dd" BNRs, (g) Electronic band structure and density of states (DOS) of "zz" BNRs, (h) Electronic band structure and density of states (DOS) of H-passivated "zz" BNRs, (i) Electronic band structure and density of states (DOS) of O-passivated "zz" BNRs, (j) Electronic band structure and density of states (DOS) of F-passivated "zz" BNRs; Figure S2: (a) Transmission at V = 0 for various "aa" edge nanoribbons. Inset shows no width dependence for transmission near E_F; $T(E = E_F) = 3$ for all 5 "aa" edge nanoribbons. (b) I-V characteristics of aa-BNRs. "7-aa" and "10-aa" show non-linear I-V due to the existence of band edges near E_F. The equilibrium T(E) of "10-aa" shows a spike near E_F due to a flat region in the band structure near E_F, but it does not play any role in the transport at finite voltages; Figure S3: (a) Transmission at V = 0 for various "as" edge nanoribbons. Inset shows transmission

near E_F. (b) I-V characteristics of "as" edge nanoribbons; Figure S4: (a) Transmission at V = 0 for various "ad" edge nanoribbons. Inset shows transmission near E_F. (b) I-V characteristics of "ad" edge nanoribbons; Figure S5: (a) Transmission at V = 0 for various "ds" edge nanoribbons. Inset shows transmission near E_F. (b) I-V characteristics of "ds" edge nanoribbons; Figure S6: Edge-localized transmission channels for "ss" edge nanoribbons shown as absolute (left) and real (right) parts of the wavefunction. Transmission channels (b) and (c) have identical absolute wavefunctions, but their phases are symmetric/anti-symmetric across the ribbon width. When changing one edge, only one of (b) and (c) exists.

Author Contributions: Conceptualization, S.R., F.S., N.G.S. and B.I.Y.; methodology, S.R. and F.S.; software, S.R. and F.S.; validation, S.R. and F.S.; investigation, S.R. and F.S.; writing—original draft preparation, S.R. and F.S.; writing—review and editing, S.R., F.S., N.G.S. and B.I.Y.; visualization, S.R. and F.S.; supervision, B.I.Y. All authors have read and agreed to the published version of the manuscript.

Funding: This research was funded by the Polish National Agency for Academic Exchange under the Preludium Bis NAWA 3 Programme, decision no. BPN/PRE/2023/1/00039/DEC/1 and the National Science Centre, Poland, under grant number 2021/43/O/ST3/03280. Work at Rice (F.S., B.I.Y.) was supported by the Office of Naval Research grant N00014-22-1-2753.

Institutional Review Board Statement: Not applicable.

Informed Consent Statement: Not applicable.

Data Availability Statement: The original contributions presented in this study are included in the article. Further inquiries can be directed to the authors.

Acknowledgments: Computer resources were provided by the National Science Foundation ACCESS program under allocation DMR100029. S.R. is grateful to the Polish National Agency for Academic Exchange for the financial support and to the Rice University for hospitality.

Conflicts of Interest: The authors declare that they have no known competing financial interests or personal relationships that could have appeared to influence the work reported in this paper.

References

1. Penev, E.S.; Bhowmick, S.; Sadrzadeh, A.; Yakobson, B.I. Polymorphism of Two-Dimensional Boron. *Nano Lett.* **2012**, *12*, 2441–2445. [CrossRef]
2. Zhang, Z.; Yang, Y.; Gao, G.; Yakobson, B.I. Two-Dimensional Boron Monolayers Mediated by Metal Substrates. *Angew. Chem.* **2015**, *127*, 13214–13218. [CrossRef]
3. Gonzalez Szwacki, N.; Sadrzadeh, A.; Yakobson, B.I. B 80 Fullerene: An Ab Initio Prediction of Geometry, Stability, and Electronic Structure. *Phys. Rev. Lett.* **2007**, *98*, 166804. [CrossRef] [PubMed]
4. Zhai, H.-J.; Zhao, Y.-F.; Li, W.-L.; Chen, Q.; Bai, H.; Hu, H.-S.; Piazza, Z.A.; Tian, W.-J.; Lu, H.-G.; Wu, Y.-B.; et al. Observation of an All-Boron Fullerene. *Nat. Chem.* **2014**, *6*, 727–731. [CrossRef]
5. Singh, A.K.; Sadrzadeh, A.; Yakobson, B.I. Probing Properties of Boron α-Tubes by Ab Initio Calculations. *Nano Lett.* **2008**, *8*, 1314–1317. [CrossRef]
6. Tang, H.; Ismail-Beigi, S. Novel Precursors for Boron Nanotubes: The Competition of Two-Center and Three-Center Bonding in Boron Sheets. *Phys. Rev. Lett.* **2007**, *99*, 115501. [CrossRef]
7. Liu, X.; Li, Q.; Ruan, Q.; Rahn, M.S.; Yakobson, B.I.; Hersam, M.C. Borophene Synthesis beyond the Single-Atomic-Layer Limit. *Nat. Mater.* **2022**, *21*, 35–40. [CrossRef]
8. Li, Q.; Aklile, E.B.; Tsui, A.; Hersam, M.C. Progress and Future Directions in Borophene Research. *Nat. Chem.* **2025**, *17*, 642–652. [CrossRef]
9. Mannix, A.J.; Zhou, X.-F.; Kiraly, B.; Wood, J.D.; Alducin, D.; Myers, B.D.; Liu, X.; Fisher, B.L.; Santiago, U.; Guest, J.R.; et al. Synthesis of Borophenes: Anisotropic, Two-Dimensional Boron Polymorphs. *Science* **2015**, *350*, 1513–1516. [CrossRef] [PubMed]
10. Feng, B.; Zhang, J.; Zhong, Q.; Li, W.; Li, S.; Li, H.; Cheng, P.; Meng, S.; Chen, L.; Wu, K. Experimental Realization of Two-Dimensional Boron Sheets. *Nat. Chem.* **2016**, *8*, 563–568. [CrossRef] [PubMed]
11. Zhang, Z.; Penev, E.S.; Yakobson, B.I. Polyphony in B Flat. *Nat. Chem.* **2016**, *8*, 525–527. [CrossRef]

12. Zhang, Z.; Penev, E.S.; Yakobson, B.I. Two-Dimensional Boron: Structures, Properties and Applications. *Chem. Soc. Rev.* **2017**, *46*, 6746–6763. [CrossRef]
13. Li, D.; Gao, J.; Cheng, P.; He, J.; Yin, Y.; Hu, Y.; Chen, L.; Cheng, Y.; Zhao, J. 2D Boron Sheets: Structure, Growth, and Electronic and Thermal Transport Properties. *Adv. Funct. Mater.* **2020**, *30*, 1904349. [CrossRef]
14. Yang, X.; Dou, X.; Rouhanipour, A.; Zhi, L.; Räder, H.J.; Müllen, K. Two-Dimensional Graphene Nanoribbons. *J. Am. Chem. Soc.* **2008**, *130*, 4216–4217. [CrossRef]
15. Son, Y.-W.; Cohen, M.L.; Louie, S.G. Energy Gaps in Graphene Nanoribbons. *Phys. Rev. Lett.* **2006**, *97*, 216803. [CrossRef] [PubMed]
16. Izadi Vishkayi, S.; Bagheri Tagani, M. Edge-Dependent Electronic and Magnetic Characteristics of Freestanding β_{12}-Borophene Nanoribbons. *Nano-Micro Lett.* **2018**, *10*, 14. [CrossRef] [PubMed]
17. Ding, Y.; Yang, X.; Ni, J. Electronic Structures of Boron Nanoribbons. *Appl. Phys. Lett.* **2008**, *93*, 043107. [CrossRef]
18. Li, G.Q. The Transport Properties of Boron Nanostructures. *Appl. Phys. Lett.* **2009**, *94*, 193116. [CrossRef]
19. Saxena, S.; Tyson, T.A. Insights on the Atomic and Electronic Structure of Boron Nanoribbons. *Phys. Rev. Lett.* **2010**, *104*, 245502. [CrossRef]
20. Ghasemzadeh, F.; Farokhnezhad, M.; Esmaeilzadeh, M. Thermal Spin Filtering and Spin-Dependent Seebeck Effect in α-Borophene Nanoribbons. *J. Phys. Chem. C* **2024**, *128*, 21108–21116. [CrossRef]
21. Vatankhahan, A.; Movlarooy, T. DFT Study of High-Curie-Temperature Ferromagnetism in A-borophene Nanoribbons for Spintronic Applications. *Adv. Theory Simul.* **2023**, *6*, 2200925. [CrossRef]
22. Liu, M.; Artyukhov, V.I.; Yakobson, B.I. Mechanochemistry of One-Dimensional Boron: Structural and Electronic Transitions. *J. Am. Chem. Soc.* **2017**, *139*, 2111–2117. [CrossRef] [PubMed]
23. Gonzalez Szwacki, N.; Tarkowski, T.; Majewski, J.A. Structure and Energetics of Fragments of the Planar α and β Boron Sheets. *Acta Phys. Pol. A* **2016**, *129*, A-148–A-149. [CrossRef]
24. Hu, P.-J.; Liang, Z.-R.; Sun, J.-W.; Fang, T.-F.; Guo, A.-M.; Sun, Q.-F. Contact Effects on Electron Transport along Disordered Borophene Nanoribbons with Line Defects. *Phys. Rev. B* **2024**, *109*, 165437. [CrossRef]
25. Hu, P.-J.; Wang, S.-X.; Chen, X.-F.; Liang, Z.-R.; Fang, T.-F.; Guo, A.-M.; Xu, H.; Sun, Q.-F. Resonant Tunneling in Disordered Borophene Nanoribbons with Line Defects. *Npj Comput. Mater.* **2022**, *8*, 131. [CrossRef]
26. Seenithurai, S.; Chai, J.-D. Electronic Properties of Linear and Cyclic Boron Nanoribbons from Thermally-Assisted-Occupation Density Functional Theory. *Sci. Rep.* **2019**, *9*, 12139. [CrossRef]
27. Qiu, L.; Mu, Y.; Kim, S.Y.; Ding, F. Self-Termination of Borophene Edges. *JACS Au* **2024**, *4*, 116–124. [CrossRef]
28. Tian, J.; Xu, Z.; Shen, C.; Liu, F.; Xu, N.; Gao, H.-J. One-Dimensional Boron Nanostructures: Prediction, Synthesis, Characterizations, and Applications. *Nanoscale* **2010**, *2*, 1375. [CrossRef]
29. Xu, T.T.; Zheng, J.-G.; Wu; Nicholls, A.W.; Roth, J.R.; Dikin, D.A.; Ruoff, R.S. Crystalline Boron Nanoribbons: Synthesis and Characterization. *Nano Lett.* **2004**, *4*, 963–968. [CrossRef]
30. Li, Q.; Wang, L.; Li, H.; Chan, M.K.Y.; Hersam, M.C. Synthesis of Quantum-Confined Borophene Nanoribbons. *ACS Nano* **2024**, *18*, 483–491. [CrossRef]
31. Van Setten, M.J.; Giantomassi, M.; Bousquet, E.; Verstraete, M.J.; Hamann, D.R.; Gonze, X.; Rignanese, G.-M. The PseudoDojo: Training and Grading a 85 Element Optimized Norm-Conserving Pseudopotential Table. *Comput. Phys. Commun.* **2018**, *226*, 39–54. [CrossRef]
32. Giannozzi, P.; Baroni, S.; Bonini, N.; Calandra, M.; Car, R.; Cavazzoni, C.; Ceresoli, D.; Chiarotti, G.L.; Cococcioni, M.; Dabo, I.; et al. QUANTUM ESPRESSO: A Modular and Open-Source Software Project for Quantum Simulations of Materials. *J. Phys. Condens. Matter* **2009**, *21*, 395502. [CrossRef]
33. Momma, K.; Izumi, F. *VESTA 3* for Three-Dimensional Visualization of Crystal, Volumetric and Morphology Data. *J. Appl. Crystallogr.* **2011**, *44*, 1272–1276. [CrossRef]
34. Brandbyge, M.; Mozos, J.-L.; Ordejón, P.; Taylor, J.; Stokbro, K. Density-Functional Method for Nonequilibrium Electron Transport. *Phys. Rev. B* **2002**, *65*, 165401. [CrossRef]
35. Papior, N.; Lorente, N.; Frederiksen, T.; García, A.; Brandbyge, M. Improvements on Non-Equilibrium and Transport Green Function Techniques: The next-Generation Transiesta. *Comput. Phys. Commun.* **2017**, *212*, 8–24. [CrossRef]
36. Paulsson, M.; Brandbyge, M. Transmission Eigenchannels from Nonequilibrium Green's Functions. *Phys. Rev. B* **2007**, *76*, 115117. [CrossRef]
37. Frederiksen, T.; Paulsson, M.; Brandbyge, M.; Jauho, A.-P. Inelastic Transport Theory from First Principles: Methodology and Application to Nanoscale Devices. *Phys. Rev. B* **2007**, *75*, 205413. [CrossRef]
38. Norouzi, F.; Farokhnezhad, M.; Esmaeilzadeh, M.; Szafran, B. Controllable Spin Filtering and Half-Metallicity in B12-Borophene Nanoribbons. *Phys. Rev. B* **2021**, *104*, 245431. [CrossRef]
39. Huang, Y.; Yu, H.; Sun, F.; Ruan, Q.; Yakobson, B.I. Electron Transport in Borophene–Graphene Lateral Edge–Edge Junctions. *ACS Nano* **2025**, *19*, 11675–11683. [CrossRef] [PubMed]

40. Xing, E.-F.; Niu, Z.-H.; Zhang, G.-P.; Wang, C.-K.; Chen, G.; Song, Y. First Principles Design of Multifunctional Spintronic Devices Based on Super Narrow Borophene Nanoribbons. *Sci. Rep.* **2025**, *15*, 2602. [CrossRef]
41. Ghasemzadeh, F.; Farokhnezhad, M.; Esmaeilzadeh, M. Ultrafast Switching in Spin Field-Effect Transistors Based on Borophene Nanoribbons. *Phys. Chem. Chem. Phys.* **2024**, *26*, 13061–13069. [CrossRef] [PubMed]

molecules

MDPI

Article

Type II ZnO-MoS_2 Heterostructure-Based Self-Powered UV-MIR Ultra-Broadband p-n Photodetectors

Badi Zhou [1], Xiaoyan Peng [2], Jin Chu [2], Carlos Malca [3], Liz Diaz [3], Andrew F. Zhou [1,*] and Peter X. Feng [4,*]

[1] Department of Chemistry, Biochemistry, Physics, and Engineering, Indiana University of Pennsylvania, Indiana, PA 15705, USA; badi.zhou@pm.me
[2] College of Artificial Intelligence, Southwest University, Chongqing 400715, China; pengxy2015@swu.edu.cn (X.P.); chujin@swu.edu.cn (J.C.)
[3] Department of Chemistry, University of Puerto Rico, San Juan, PR 00936, USA; carlos.malca@upr.edu (C.M.); liz.diaz2@upr.edu (L.D.)
[4] Department of Physics, University of Puerto Rico, San Juan, PR 00936, USA
* Correspondence: fzhou@iup.edu (A.F.Z.); peter.feng@upr.edu (P.X.F.)

Abstract: This study presents the fabrication and characterization of ZnO-MoS_2 heterostructure-based ultra-broadband photodetectors capable of operating across the ultraviolet (UV) to mid-infrared (MIR) spectral range (365 nm–10 μm). The p-n heterojunction was synthesized via RF magnetron sputtering and spin coating, followed by annealing. Structural and optical analyses confirmed their enhanced light absorption, efficient charge separation, and strong built-in electric field. The photodetectors exhibited light-controlled hysteresis in their I-V characteristics, attributed to charge trapping and interfacial effects, which could enable applications in optical memory and neuromorphic computing. The devices operated self-powered, with a peak responsivity at 940 nm, which increased significantly under an applied bias. The response and recovery times were measured at approximately 100 ms, demonstrating their fast operation. Density functional theory (DFT) simulations confirmed the type II band alignment, with a tunable bandgap that was reduced to 0.20 eV with Mo vacancies, extending the detection range. The ZnO-MoS_2 heterostructure's broad spectral response, fast operation, and defect-engineered bandgap tunability highlight its potential for imaging, environmental monitoring, and IoT sensing. This work provides a cost-effective strategy for developing high-performance, ultra-broadband, flexible photodetectors, paving the way for advancements in optoelectronics and sensing technologies.

Keywords: two-dimensional materials; transition-metal dichalcogenides; photonics; ZnO-MoS_2 heterostructure; p-n heterojunction; photovoltaic mode; photoconduction mode; ultra-broadband photodetectors; UV-MIR spectral range; vacancy defects; bandgap tuning; Internet of Things (IoT) sensing

1. Introduction

Photodetectors play a vital role in modern optoelectronic systems by converting light into electrical signals, enabling applications in optical communication, imaging, environmental monitoring, medical diagnostics, and real-time Internet of Things (IoT) sensing [1]. The increasing demand for high-performance photodetectors with broadband sensitivity, capable of detecting light from the ultraviolet (UV) to the infrared (IR) and terahertz (THz) regions, has driven extensive research into novel materials and advanced device architectures. Among the wide array of broadband photodetectors, molybdenum disulfide (MoS_2)-based devices have emerged as highly promising due to their unique

optoelectronic properties, including a tunable bandgap, high carrier mobility, and strong light–matter interaction [2]. Recent advancements in MoS_2-based photodetectors have focused on leveraging heterostructures, doping, and plasmonic enhancement to extend their detection capabilities across a broad spectral range, enhancing their sensitivity and response times. Integrating MoS_2 with other two-dimensional (2D) materials or nanostructures has led to devices with an improved performance, as summarized in Table 1. However, challenges remain in achieving a wide spectral response, high responsivity, fast response times, and low power consumption [3–5].

A key strategy for addressing these challenges is the development of heterostructure-based photodetectors that exploit the complementary properties of different materials through bandgap engineering [6]. Although ZnO is a wide-bandgap semiconductor with strong UV absorption only while MoS_2 is sensitive to visible light, theoretical studies have shown that vacancies and defects in ZnO-MoS_2 heterostructures can significantly alter their electronic and optical properties, possibly enabling efficient broadband absorption up to the THz range [7–9]. Despite these predicted advantages, ZnO-MoS_2 heterostructure-based broadband photodetectors have scarcely been tested. Apart from theoretical studies, further efforts are needed to investigate the fabrication methods and characterize the performance of ZnO-MoS_2 heterostructure-based broadband photodetectors, with a focus on addressing key performance limitations in the spectral response range.

Table 1. State-of-the-art performance of MoS_2-based broadband photodetectors.

Active Material	Wavelength λ (μm)	Bias Voltage (V)	Responsivity (mA/W)	Response Time [1] (ms)	Ref.
MoS_2	0.4–1.1		1.4×10^7 (@700 nm)	2.5	[10]
MoS_2	0.445–2.717		50.7		[11]
MoS_2 + Si	0.405–0.98	1 V	74.6	t_r = 0.178, t_d = 0.198	[12]
MoS_2 2D/0D	0.365–0.78		12.8 (@554 nm)		[13]
MoS_2 + ZnS	0.365–0.78		0.0179 (@554 nm)		[14]
MoS_2 + CuInSe$_2$-QDs	0.355–1.064	5 V	74.8×10^3 (@1064 nm)		[15]
MoS_2 + PDPP3T	0.38–0.98		12.4 (@380 nm)		[16]
MoS_2 + Ga_2O_3	0.254–1.2	5 V	171×10^3 (@900 nm)	t_r = 0.097, t_d = 0.114	[17]
MoS_2 + P(VDF-TrFE)	0.375–10	5 V	140 (@2.76–10 μm)	5.5 (@2.76–10 μm)	[18]
MoS_2 + V_2O_5	0.365–0.78	−1 V	65.1 (@554 nm)	~40,000 (@554 nm)	[19]
MoS_2 + SnS$_2$-QD	0.365–0.78	1 V	435×10^3 (@554 nm)	t_r = ~100	[20]
MoS_2 + CdS	0.365–0.7	1 V	5.5×10^3 (@700 nm)	t_r = 100 (@610 nm)	[21]
Graphene + MoS_2 + graphene	0.405–2	−1 V	414×10^3 (@532 nm) 376×10^3 (@2 μm)	692.5 (@532 nm)	[22]
ZnO + MoS_2	0.365–10	0 V 0.5 V	0.17 (@940 nm) 1.46 (@940 nm)	t_r = 140, t_d = 100	This work

[1] t_r = rise time; t_d = decay time.

This paper describes the fabrication of ZnO-MoS_2 heterostructure-based broadband photodetectors through a two-step process aimed at enhancing MoS_2's optical absorption properties. ZnO films were first deposited onto a silicon wafer via RF magnetron sputtering, followed by the spin coating of MoS_2 nanosheets. Multiple MoS_2 layers were deposited to ensure a uniform distribution, and the heterostructures were annealed to improve the integration and material properties. Platinum electrodes were added to complete the photodetector prototypes, which featured a simple and cost-effective design. The devices were subsequently characterized to assess their performance, and the impact of Mo vacancies on the ZnO-MoS_2 bilayer's band structure was also simulated.

2. Properties of ZnO and MoS_2 Heterostructures

As reported, ZnO nanostructures can be 0D, 1D, 2D, or 3D [23], depending on the growth techniques and conditions. Hence, the surface morphologies of the prepared ZnO and MoS_2 samples were analyzed in their composition using a JEOL 6480LV scanning electron microscope (SEM) (JEOL, Tokyo, Japan) equipped with energy-dispersive X-ray spectroscopy (EDX). Figure 1a shows the SEM images of a ZnO sample before and after MoS_2 spin coating. The synthesized ZnO nanoparticles (Figure 1a inset) have smooth surfaces and diameters of 100 nm. The layer's thickness was estimated to be approximately 1 μm [24]. In contrast, the ZnO-MoS_2 heterostructures exhibit larger diameters and rougher surfaces due to the MoS_2 nanosheets coated onto the surface of the ZnO nanoparticles. An average continuous MoS_2 sheet has an estimated thickness of ~5 nm and a lateral size of approximately 4 μm^2, with the total MoS_2 thickness reaching about 500 nm due to the stacking of multiple randomly oriented MoS_2 clusters [25].

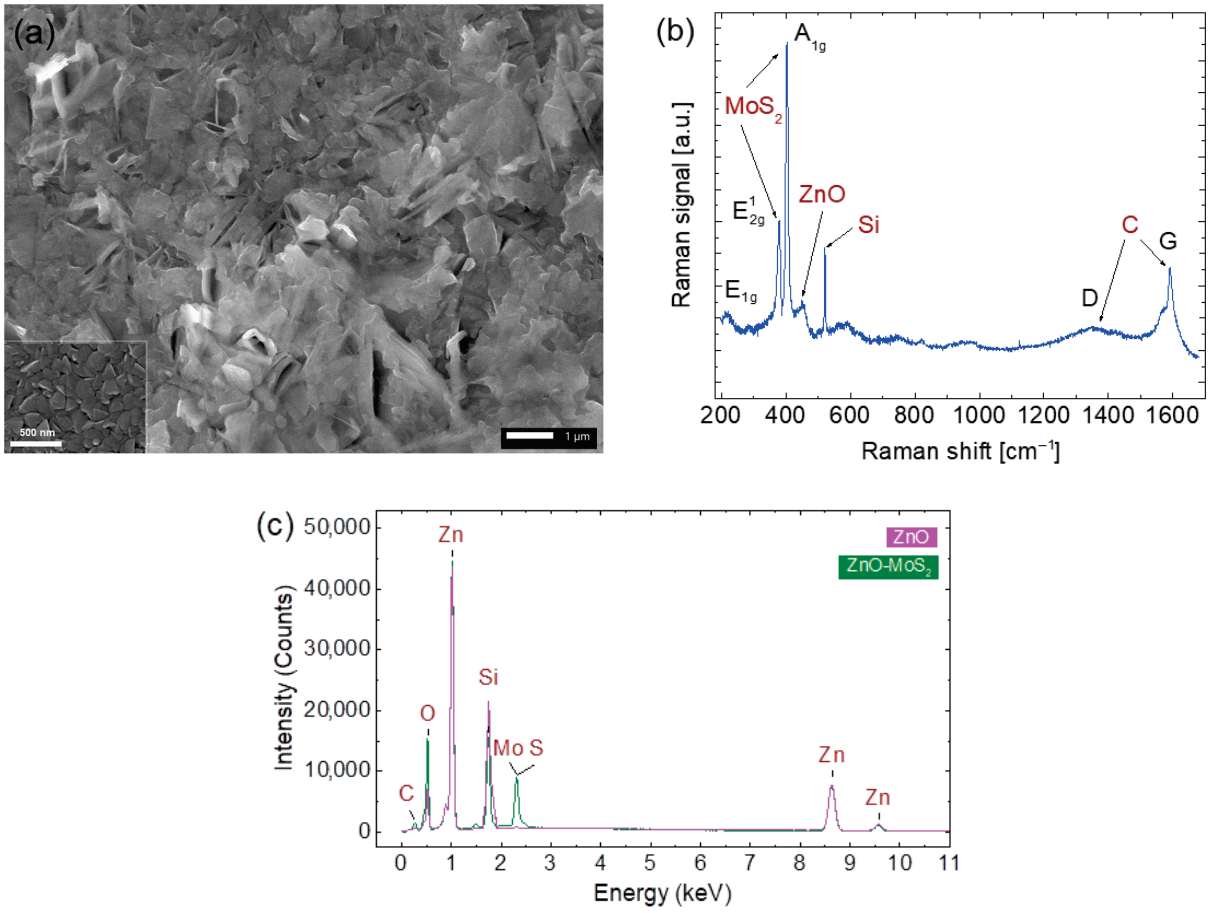

Figure 1. (**a**) SEM image of ZnO coated with MoS_2, with a scale bar of 1 μm. Inset: ZnO nanoparticles; scale bar: 500 nm. (**b**) Raman spectrum of the ZnO-MoS_2 sample. (**c**) EDX spectra of ZnO and ZnO-MoS_2 after annealing.

Micro-Raman scattering measurements were performed using a Jobin-Yvon T64000 Triplemate system (Horiba Jobin-Yvon, Edison, NJ, USA), with 514.5 nm (2.41 eV) radiation from a coherent argon laser as the excitation source. The scattered data were collected and processed using a liquid-nitrogen-cooled charge-coupled device (CCD) system, as shown in Figure 1b. The MoS_2 layer exhibited characteristic MoS_2 Raman modes at 379 and 402 cm^{-1} corresponding to the E^1_{2g} and A_{1g} modes, respectively, with an interval of 23 cm^{-1}, which indicated that the MoS_2 nanosheets were predominantly multilayer [26],

while the peak at ~200 cm^{-1}, marked as E_{1g}, most likely corresponded to the in-plane vibrational mode of MoS_2, activated due to the interlayer van der Waals interactions [27].

The Raman results show that the formation of the ZnO-MoS_2 heterojunction led to both band broadening and band shifting compared to these values in the individual materials, indicating that the combination of MoS_2 and ZnO in a heterostructure led to changes in the electronic structure and enhanced the photoelectric performance compared to that of single-material-based prototypes [28]. While defects and doping can influence the Raman spectra, no significant peak shifts or additional defect-related features were observed in our data, suggesting that these factors were not the primary contributors to the 200 cm^{-1} peak. However, we acknowledge the possibility of ZnS's formation at the interface due to a chemical reaction between ZnO and MoS_2, particularly during thermal annealing. The weak and broad nature of the ~200 cm^{-1} peak may be linked to ZnS, as reported in previous studies [29].

The Raman signal from the ZnO nanoparticles was weak and broad, attributed to the lower degree of crystallinity due to the room-temperature deposition, as well as the overcoating of the MoS_2 layers. The peak at 520 cm^{-1}, corresponding to the characteristic first-order phonon of the silicon from the substrate with a (100) crystal orientation [30], has been widely used as a reliable calibration of Raman measurements. As a comparison, when a Raman measurement was taken along the edge of the synthesized layers, there was no significant change, except a giant signal at this wavenumber being observed. The Raman spectroscopy analysis also confirms the presence of amorphous carbon, as indicated by the D band at 1350 cm^{-1} and the G band at 1580 cm^{-1}, characteristic of sp^2 hybridization.

Figure 1c exhibits the EDX mapping analysis of the ZnO sample before and after MoS_2 coating and annealing. Prior to MoS_2 deposition, the atomic percentage ratio of Zn to O was 42.5%/26.34% = 1.6, with additional signals from silicon (Si) originating from the substrate and from carbon (C) from contamination in the RF magnetron sputtering chamber. The observed Zn/O ratio indicates the presence of oxygen vacancies, which are common native point defects in ZnO. These vacancies contribute to the material's intrinsic n-type conductivity by acting as positively charged donors. Following MoS_2 coating and annealing, the EDX spectra reveal no significant change in the Zn signal, apart from the Mo and S signals overlapping at 2.3 keV. However, a notable increase in the C, O, and Si signals suggests additional contamination introduced during the annealing process.

An elemental analysis post-MoS_2 deposition and annealing identified zinc (21 at%), oxygen (38 at%), molybdenum (0.96 at%), and sulfur (4.2 at%). The relatively low Mo and S content is attributed to the simple and cost-effective spin-coating process, which results in a thin MoS_2 layer over the ZnO nanoparticles. While the synthesized ZnO nanoparticles exhibited intrinsic n-type conductivity with a high electron density [31,32], the Mo vacancies in the MoS_2 induced p-type behavior [33]. These findings confirm the formation of a p-n heterojunction in the ZnO-MoS_2 samples.

Subsequently, Au electrodes were deposited using the plasma sputtering technique onto the two sides of the synthesized ZnO–MoS_2 heterostructures to build prototypes. Figure 2a shows a schematic of a prototypic photodetector. The I-V properties were characterized, as shown in Figure 2b, using an HP34401 and a Keithley 6517A multimeter controlled via the LabVIEW 2024 Q3 program. The measurements were carried out in standard ambient conditions without and with light illumination. Stable hysteresis loops were observed when the heterostructure was operated at room temperature.

As shown in Figure 2b, the I-V curve exhibits the characteristic behavior of a simple p-n junction diode [34]. In the reverse bias region, a low reverse saturation current through the device indicates that the backward current is partially suppressed. In contrast, the forward current increases gradually at first and then rapidly with an increase in the forward

voltage. It is interesting to note that while neither ZnO nor MoS_2 is intrinsically ferroelectric, the synergistic effects within the heterostructure—arising from the piezoelectricity of ZnO and the vacancy defects in MoS_2—may facilitate polarization switching under an external electric field.

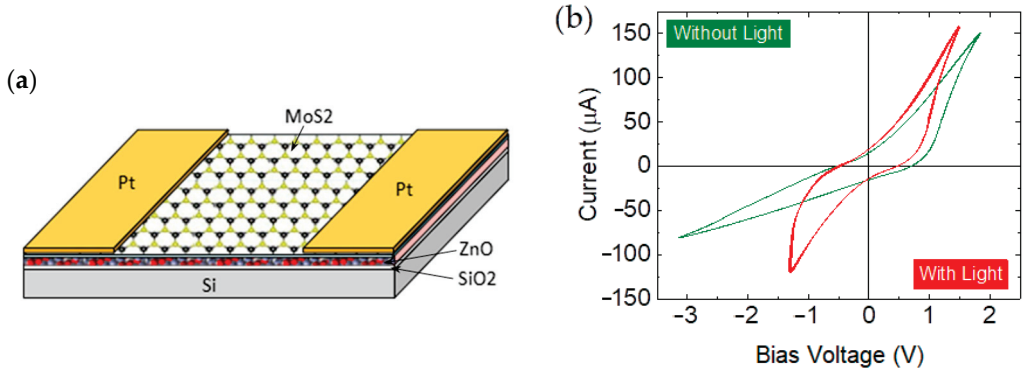

Figure 2. (**a**) Schematic of the ZnO-MoS_2 heterostructure-based broadband photodetector. (**b**) The room-temperature current–voltage (I-V) characteristics without and with light illumination, corresponding to a dark current and a photocurrent (illuminated by 450 nm light with an intensity of 50 mW/cm^2). Each hysteresis loop represents 10 repeated measurements.

In the absence of light illumination, the observed hysteresis suggests resistive switching due to the bilayer's interfacial properties and the intrinsic defects in the ZnO-MoS_2 bilayer. The non-zero open-circuit voltage (V_{oc}) is measured at −0.56 V and 0.68 V, respectively, when the dark current is zero. Similarly, the short-circuit current (I_{sc}) is −15 μA and 15 μA, respectively, at zero bias voltage. Under 50 mW/cm^2 blue light (λ = 450 nm) irradiation, a light-controlled hysteresis loop emerges, demonstrating an increase in the photocurrent with a rising bias voltage due to photoconductivity. Preliminary investigations of V_{oc} and I_{sc} were conducted in our previous work [6], which were influenced by several factors like temperature, different light illumination, the active layer's properties, the quality of the interconnections, etc. The operating temperature appears to have a significant impact on V_{oc}, while light illumination directly affects I_{sc}.

The changes in the hysteresis curve under light illumination are likely driven by photo-induced modifications in the electronic and charge transport properties of the ZnO-MoS_2 bilayer. Photons with energy exceeding the bandgap of ZnO and MoS_2 generate electron–hole pairs, leading to an increase in the carrier density and enhanced conductivity, which explains the higher current observed in the hysteresis curve. The increase in the current under the applied bias suggests that the photovoltaic effect contributes to the charge transport. Additionally, both ZnO and MoS_2 contain abundant defect states, as indicated by the EDX measurements, which can trap the charges during I-V cycling. Under illumination, photon energy liberates these trapped charges, altering the overall charge transport dynamics and reducing the hysteresis loop area. Furthermore, the built-in electric field generated by the photovoltaic effect can facilitate the carrier transport, further minimizing hysteresis and modifying the loop shape. These I-V characteristics confirm the ZnO-MoS_2 bilayer's sensitivity to light, making it a promising candidate for photodetectors or memory elements.

Figure 3a–e present the measured time properties of the prototype when tested under light of various wavelengths ranging from 365 nm to 10 μm, all at a consistent intensity of 1.2 mW/cm^2. The device was operated at room temperature under zero voltage bias, functioning as a self-powered photodetector. This capability minimizes the dependence on external power sources, enhancing its sustainability and making the device well suited to remote or inaccessible locations, aligning with the demands of IoT applications. However,

at the 10 μm wavelength, the photocurrent exhibits a smaller signal with a significant noise background.

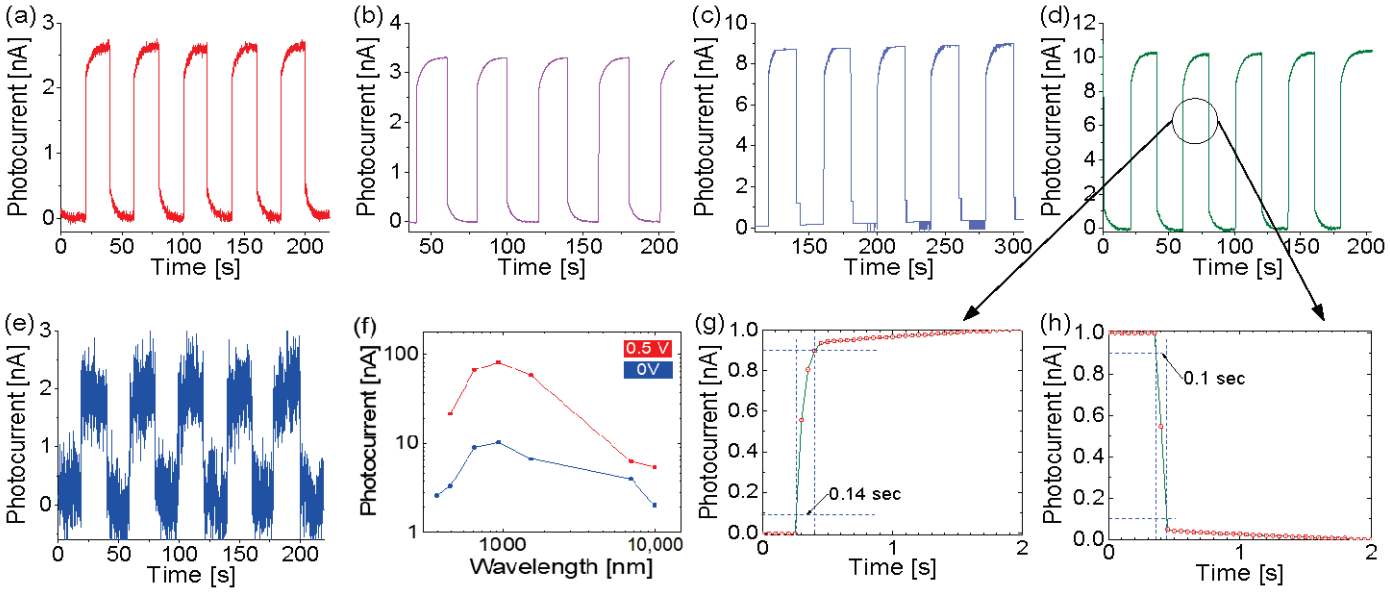

Figure 3. The measured photocurrent of the prototype when the device was operating at room temperature under 0 V bias, with on–off illumination light of different wavelengths at the same light intensity of 1.2 mW/cm^2. (**a**) λ_{UV} = 365 nm, (**b**) λ_{blue} = 450 nm, (**c**) λ_{red} = 650 nm, (**d**) λ_{NIR} = 940 nm, and (**e**) λ_{MIR} = 10,000 nm. (**f**) The measured photocurrent under 0 V and 0.5 V bias as a function of the illumination wavelength. (**g**) The response time and (**h**) recovery time corresponding to 940 nm radiation.

As shown in Figure 3f, the photodetector demonstrates a broadband wavelength response, with a photocurrent recorded under excitation wavelengths ranging from UV (365 nm) to MIR (10 μm), approximately 3.39 eV to 0.124 eV. The highest responsivity was observed at around 940 nm, reaching 0.17 mA/W at zero bias. In comparison, applying a 0.5 V bias increases the responsivity by a factor of eight, achieving 1.46 mA/W at 940 nm. These measurements suggest that the photodetector may have an even broader response extending into the THz range, though the experimental range validation was constrained by the available radiation sources. A higher bias voltage could further enhance its responsivity.

The photodetectors also have a fast photocurrent rise time (140 ms) and recovery time (100 ms), as shown in Figure 3g,h. The rise and recovery times follow the standard definition, i.e., the time intervals taken for a change from 0.1 to 0.9 in the normalized photocurrents, or vice versa. Also, the rise and recovery times were consistent under different wavelength illuminations, especially when the wavelength was further extended to 10 μm. This phenomenon indicates that the photocurrent should likely be generated from the same sensing mechanism, i.e., the possibility of thermal effects, such as a photothermoelectric effect, which could take a longer time, is ruled out [35]. The real response and recovery times might be shorter than those shown in Figure 3g,h due to the relatively large step size used in the measurements.

The relatively low measured responsivity arose from the poor crystallinity of the synthesized heterostructures. To enhance their crystallinity, high-temperature annealing was performed post-synthesis. Crystallinity significantly influences the minority carrier lifetime, which directly affects the device performance. Poor crystallinity introduces defects that shorten the minority carrier lifetime, reducing the responsivity. In contrast, an extended minority carrier lifetime increases the photocurrent but compromises the response speed.

This intrinsic trade-off between the photocurrent gain and response time necessitates careful optimization to achieve a well-balanced performance.

When operating in photoconductive mode with a non-zero voltage bias, similar time characteristics to those in Figure 3 were observed but with larger photocurrent magnitudes at these wavelengths. Despite this similarity, the two mechanisms differ slightly: photoconductive mode generates a photocurrent when the light excites free carriers, whereas photovoltaic mode with zero voltage bias produces a photovoltage by separating the light-generated carriers through a built-in electric field. As the bias voltage increases, the response in photoconductive mode may become faster due to the enhanced carrier collection facilitated by the applied bias.

An increase in the photocurrent under blue light illumination has been observed in various nanomaterials and can arise from multiple factors, including localized surface plasmon resonance with metal nanoparticles [36], a ferro-pyro-phototronic effect under heating and cooling variations [37], photochemical reactions in nanofluidic devices [38], and a piezophototronic effect when the ambient pressure on the junction is increased to 23 MPa [39]. In the present study, while photoconductivity plays an important role, the observed increase in the photocurrent under light is also influenced by trap-limited processes and photovoltaic effects.

3. Discussion

Strain can induce bandgap narrowing in heterostructures; however, since our synthesis employed a room-temperature coating process, the induced strain is minimal compared to that in techniques such as molecular beam epitaxy (MBE) or chemical vapor deposition (CVD). Previous studies [40–42] have reported a redshift of approximately 70 meV per the percent of applied strain for direct transitions, implying an unrealistically high ~20% strain would be required for 10 μm MIR detection. Given the small lattice mismatch (~2%) between the hexagonal primitive unit cells of MoS_2 and ZnO, along with the random orientation of the MoS_2 nanosheets, the strain effects are expected to be minimal. This conclusion is further supported by previous characterizations using X-ray diffraction (XRD), X-ray photoelectron spectroscopy (XPS), and high-resolution transmission electron microscopy (HRTEM) [24,25,43]. Therefore, we primarily attribute the observed change in the bandgap to the Mo vacancies.

As shown in Figure 4a, density functional theory (DFT) simulations confirm that the ZnO monolayer is a wide-bandgap semiconductor with a calculated bandgap of 3.2 eV, corresponding to a UV wavelength of 387 nm, while the MoS_2 monolayer exhibits a bandgap of 1.8 eV, corresponding to a red wavelength of 689 nm. The band structure of the bilayer ZnO-MoS_2 is presented in Figure 4b. The synthesized heterostructure exhibits a narrower bandgap of 1.4 eV, enabling the absorption to shift towards longer wavelengths of 886 nm in the NIR region. Furthermore, the transition to few-layer MoS_2 results in a shift towards an indirect bandgap of approximately 1.3 eV, corresponding to a wavelength of ~954 nm [44]. The incorporation of MoS_2 effectively narrows the bandgap of ZnO, broadening the absorption spectrum to span the UV-NIR range. For simplicity, we only consider the most stable stacking of the ZnO and MoS_2 monolayers [45,46]. As shown in Figure 5d,e, the ZnO/MoS_2 heterostructure adopts an energetically favorable stacking arrangement in which the Zn atoms are positioned directly above the Mo atoms, while O and S atoms reside at the hexagonal centers of the opposing layers.

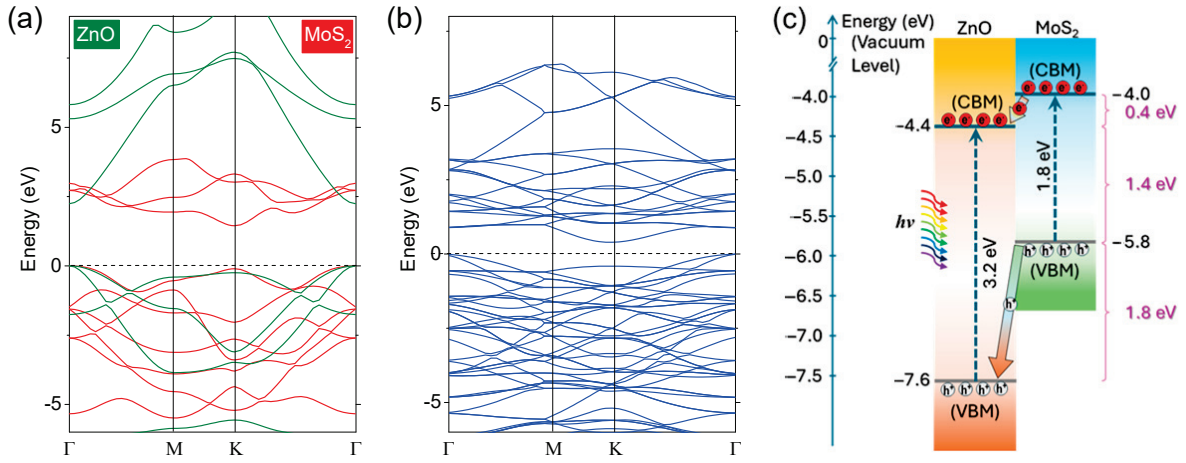

Figure 4. Simulated energy bandgaps of (**a**) ZnO and MoS_2 monolayers and (**b**) ZnO-MoS_2 heterostructure. The valence band maximum (VBM) is set to zero. (**c**) Schematic presentation of type II heterostructure formed of ZnO and MoS_2. CBM: conduction band minimum.

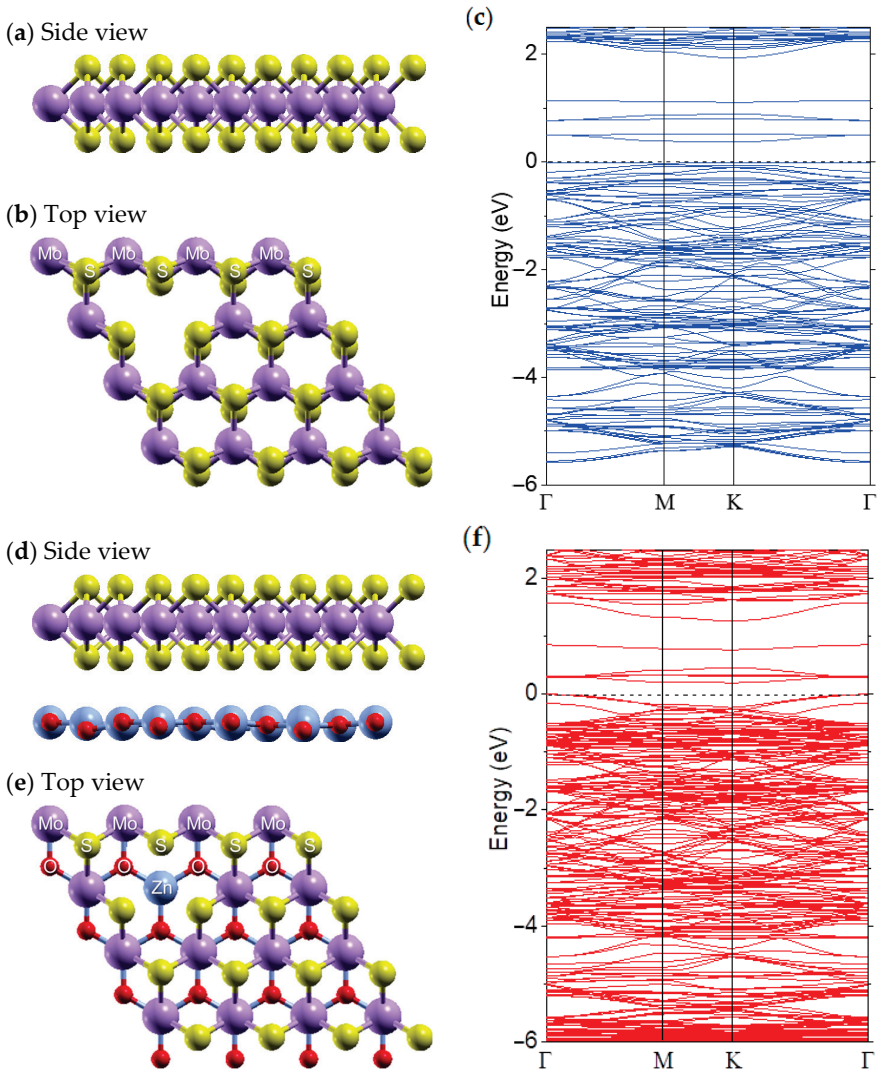

Figure 5. (**a**) Side view and (**b**) top view of the hexagonal-shaped wurtzite crystal structure of a ZnO monolayer with one Mo vacancy. (**c**) Band structure of MoS_2 with one Mo vacancy. (**d**) Side view and (**e**) top view of a ZnO-MoS_2 bilayer with one Mo vacancy. (**f**) Band structure of a ZnO-MoS_2 bilayer with one Mo vacancy. The valence band maximum is set to zero.

First-principle calculations further reveal that the heterostructure exhibits van der Waals interactions at the interface [47]. A type II band alignment is observed in ZnO-MoS_2 interfaces, facilitating effective charge separation driven by a built-in electric field, as illustrated in Figure 4c, where the bandgap data are based on the reported experimental values. The ZnO-MoS_2 heterostructure demonstrates strong optical absorption across the UV, visible, and infrared regions, ultrafast carrier dynamics, enhanced charge transfer, and efficient photogenerated charge separation, making it highly suitable for photovoltaic and photodetector applications.

Introducing vacancy defects enables the bandgap of the ZnO-MoS_2 heterostructure to be tailored to the sub-eV levels while maintaining the stability of the MoS_2 [48]. Figure 5a,b illustrate a side view and a top view of the most stable hexagonal crystal structure of monolayer MoS_2, comprising two sulfur atom layers sandwiching a molybdenum atom layer. The layers are bonded by strong covalent bonds. For simplicity, we only consider a single Mo vacancy, as depicted in Figure 5b. The corresponding band structure is shown in Figure 5c, revealing a bandgap of 0.43 eV, which corresponds to a wavelength of approximately ~2.9 μm.

DFT simulations indicate that Mo vacancies introduce shallow donor states near the conduction band (CB) and deep acceptor states near the valence band (VB), effectively narrowing the bandgap compared to that in pristine monolayer MoS_2 without vacancies. The localized electronic states within the MoS_2 bandgap arise from dangling bonds, altering the coordination environment around the vacancy site and enabling lower-energy (longer-wavelength) photon absorption. As a comparison, the calculated band structure of the ZnO-MoS_2 bilayer (Figure 5f) with one Mo vacancy further confirms that the Fermi energy lies within the valence band, indicating the p-type property of MoS_2 with Mo vacancies, and an even smaller bandgap of 0.20 eV is formed.

First-principle calculations by Yang et al. [48] show an interesting result—with an increase in the number of Mo vacancies, such as from single to double or triple vacancies, the bandgap narrows further, demonstrating that vacancy defect engineering is an effective approach to tuning the bandgap. At higher concentrations of Mo vacancies, the localized defect states overlap, forming impurity bands that can merge with the CB or the VB, resulting in significant bandgap narrowing. Mo vacancies can also lead to the formation of localized excitons with reduced binding energies, aligning with mid-infrared (MIR) photon energies.

Our experimental results align with the theoretical predictions, indicating that the Mo vacancies in MoS_2 are critical for band structure engineering to enable mid-infrared radiation absorption at wavelengths of around 10 μm. By introducing localized defect states and impurity bands within the bandgap, the Mo vacancies effectively reduce the bandgap, facilitating lower-energy electronic transitions corresponding to the MIR photon energies. This defect-induced bandgap modulation is corroborated by both experimental data and theoretical models. As a result, controlled Mo vacancy introduction is a promising strategy for tailoring the optical and electronic properties of MoS_2, broadening its potential for MIR-based technologies and advanced optoelectronic devices.

4. Materials and Methods

4.1. Photodetector Fabrication

Most ZnO and MoS_2 binary heterostructures reported for broadband photodetectors are synthesized by depositing ZnO nanowires over MoS_2 2D nanosheets. In this paper, to emphasize the optical absorption properties of MoS_2, we formed the heterostructure by coating ZnO with MoS_2 through a two-step process. First, ZnO was deposited using RF magnetron sputtering. A silicon wafer with a 300 nm SiO_2 insulating layer was used

as the substrate, which was pre-cleaned through ultrasonic treatment in deionized water, ethanol, and acetone for 20 min. The ZnO films were deposited onto Si (100) substrates in a plasma sputtering deposition chamber, utilizing a commercial sintered ZnO target (99.9%, 2 inches, MTI Company, Richmond, CA, USA). The substrate-to-target distance was maintained at 7–8 cm. Deposition occurred at room temperature with an RF power of 200 W. The chamber's base pressure was 10^{-5} Torr, and the working pressure, regulated by argon gas, was 8–10 mTorr.

Next, MoS_2 was applied using spin coating. A commercially available dispersion of atomically thin MoS_2 nanosheets (1 mg/mL in ethanol, XFNANO Materials Co., Ltd., Nanjing, China) was used. The thickness of the deposited layers was influenced by factors such as the solution's viscosity, concentration, rotation speed, and the number of spin-coating cycles. To ensure a uniform distribution and minimize agglomeration, the MoS_2 solution underwent ultrasonic cavitation for two hours prior to deposition. Each spin-coating step lasted 20 s at 3000 rpm. After each spin-coating cycle, the sample was placed in an oven at 80 °C for 5 min to dry before applying additional layers. Multiple layers were deposited to achieve a denser distribution of the MoS_2 nanostructures on the ZnO's surface. The ZnO-MoS_2 heterostructures were then annealed in the air at 800 °C for two hours to enhance the material integration and improve the physical and chemical properties.

Finally, the ZnO–MoS_2 heterostructure-based photodetectors were fabricated. Gold (Au) electrodes, 70–80 nm thick, were deposited on both sides of the active layer using plasma sputtering deposition. The fabricated prototype had an active layer exposure area of 10×0.5 mm^2. The device's structure was simple, and the fabrication process was rapid and cost-effective. Characterization and measurements of the photoconductor were conducted using a custom-built station [49].

4.2. The Computation Method

The first-principle calculations were carried out using the Quantum Espresso (QE) v.7.3 package [50], which is based on density functional theory (DFT) in a plane-wave basis set [51]. Density functional calculations utilizing generalized gradient approximation (GGA) of the Perdew–Burke–Ernzerhof (PBE) form to treat the exchange correlation contribution were performed to obtain the geometric structures [52]. For the monolayer calculations, the projected augmented wave (PAW) method was adopted to describe the pseudopotentials, and the valence configuration for the construction of the PAW potentials was Zn ($3d^{10}4s^2$), Mo ($4s^24p^64d^45s^2$), O ($2s^22p^4$), and S ($3s^23p^4$). For bilayers with vacancies, norm-conserving (NC) pseudopotentials were used. Additionally, the DFT-D3 van der Waals (vdW) correction proposed by Grimme was utilized to describe weak vdW interactions [53], which improved the accuracy of the structural and electronic property calculations, aligning the theoretical bandgap values with the experimental results. As confirmed by the DFT calculations, the interfacial coupling in the Zno-MoS_2 vdW heterostructures significantly impacts the device performance.

It is well known that DFT is notorious for underestimating bandgaps [54,55]. Hence, the Heyd–Scuseria–Ernzerhof (HSE06) hybrid density functional with a 25% Hartree–Fock exchange energy was used to obtain more accurate electronic structures [56]. For the monolayers, an energy cutoff of 800 eV, an energy convergence tolerance of 1.0×10^{-8} eV, convergence thresholds for the atomic force of 10^{-2} eV/Å, and a Monkhorst–Pack k-point grid of $13 \times 13 \times 1$ for a 1×1 unit of the ZnO and MoS_2 monolayers and 2×2 units of the ZnO-MoS_2 systems were found to be sufficient for the geometrical optimization and electronic structure calculations. For bilayers with vacancies, an energy cutoff of 500 eV, an energy convergence tolerance of 1.0×10^{-6} eV, and a $5 \times 5 \times 1$ k-point grid were used for 4×4 units of ZnO-MoS_2. A thickness of the vacuum space of 20 Å between neighboring

nanocomposites was adopted to avoid interactions. All of the structures were fully relaxed until the Hellmann–Feynman force on each atom was <0.01 eV/Å, leading to an interlayer spacing of 2.92 Å in the ZnO-MoS_2 bilayer.

5. Conclusions

The type II heterostructure of ZnO and MoS_2 reported in this study leverages the complementary properties of MoS_2's tunable bandgap and strong excitonic effects, along with ZnO's UV sensitivity and light-trapping capabilities. The synergistic interaction between these two materials results in the ferroelectric-like property of the heterostructure, as well as a p-n heterojunction. With ZnO's high electron mobility and high chemical stability and MoS_2's robust light–matter interaction over an ultrawide spectral range, the interface structure of the heterojunction further enhances the charge separation and reduces the recombination losses, thereby improving the overall device performance. Additionally, the formation of built-in electric fields at the heterojunction facilitates efficient charge transport, which is crucial for achieving high responsivity and fast response times.

The fabricated ZnO-MoS_2 photodetectors have demonstrated remarkable advancements, including enhanced light absorption over an ultrabroad spectral range of up to 10 μm, efficient charge transfer, and fast response times. Under photovoltaic mode, self-powered devices based on this heterostructure exhibit excellent sensitivity across the UV, visible, and MIR regions, highlighting their potential for diverse applications in optical communication, imaging systems, and environmental sensing, even though the photodetector operates in both photovoltaic mode without bias and photoconductive mode with a bias voltage. Self-powered operation is ideal for real-time Internet of Things (IoT) applications and wearable electronics, complemented by the flexibility provided by the heterostructure obtained.

Author Contributions: Study conception and design: P.X.F. and A.F.Z.; software, computation, and modeling: B.Z. and A.F.Z.; sample preparation: X.P., J.C. and P.X.F.; 3D printing and FTIR: C.M. and L.D.; characterization: P.X.F.; drafting: A.F.Z. All of the authors contributed to the data analysis and partook in critical discussion and modifications. All authors have read and agreed to the published version of the manuscript.

Funding: This work was financially supported by the NSF-CREST Center for Innovation, Research and Education in Environmental Nanotechnology (CIRE2N), grant HRD-1736093. A.F.Z. also acknowledges receipt of an IUP USRC research grant award.

Institutional Review Board Statement: Not applicable.

Informed Consent Statement: Not applicable.

Data Availability Statement: The data presented in this study are available upon request.

Acknowledgments: We thank the funding agents mentioned above for their financial support of this work.

Conflicts of Interest: The authors declare no conflicts of interest.

References

1. Si, W.; Zhou, W.; Liu, X.; Wang, K.; Liao, Y.; Yan, F.; Ji, X. Recent Advances in Broadband Photodetectors from Infrared to Terahertz. *Micromachines* **2022**, *13*, 427. [CrossRef] [PubMed]
2. Das, P.; Ganguly, S.; Rosenkranz, A.; Wang, B.; Yu, J.; Srinivasan, S.; Rajabzadeh, A.R. MXene/0D nanocomposite architectures: Design, properties and emerging applications. *Mater. Today Nano* **2023**, *24*, 100428. [CrossRef]
3. Dutta, A.; Sengupta, R.; Krishnan, A.; Islam, S.; Dhar, N. Broadband Detector for Optical Communication. In *Active and Passive Optical Components for Communications VII*; SPIE: Bellingham, WA, USA, 2007; Volume 6775, pp. 123–133.

4. Dutta, J.K.; Oduor, P.; Dutta, A.K.; Dhar, N.K. Analytical Model for Design-Optimization and Performances of Fabri-cated Broadband (VIS-SWIR) Photodetector for Image Sensor and Optical Communication Applications. In *Image Sensing Technologies: Materials, Devices, Systems, and Applications V*; SPIE: Bellingham, WA, USA, 2018; Volume 10656, pp. 127–135.
5. Khalid, A.; Naeem, M.; Atrooz, O.; Mozafari, M.R.; Anari, F.; Taghavi, E.; Rashid, U.; Aziz, B. State of the Art Synthesis of Ag-ZnO-Based Nanomaterials by Atmospheric Pressure Microplasma Techniques. *Surfaces* **2024**, *7*, 680–697. [CrossRef]
6. Zhou, A.F.; Flores, S.Y.; Pacheco, E.; Peng, X.; Zhang, S.G.; Feng, P.X. Ternary $TiO_2/MoS_2/ZnO$ heteronano-structure based multifunctional sensing devices. *Discov. Nano* **2024**, *19*, 157. [CrossRef] [PubMed]
7. Wang, X.; Zhang, H.; Yu, W. The study of electronic and optical properties of ZnO/MoS_2 and its vacancy hetero-structures by first principles. *Int. J. Quantum Chem.* **2024**, *124*, e27329. [CrossRef]
8. Ma, S.; Liu, N.; Li, Z.; Qin, C.; Jiao, Z. Defect-regulated charge carrier dynamics in two-dimensional ZnO/MoS_2 heterostructure. *Results Phys.* **2023**, *53*, 106948. [CrossRef]
9. Cao, F.; Liu, L.; Li, L. Short-wave infrared photodetector. *Mater. Today* **2023**, *62*, 327–349. [CrossRef]
10. Saenz, G.A.; Karapetrov, G.; Curtis, J.; Kaul, A.B. Ultra-high photoresponsivity in suspended metal-semicon-ductor-metal mesoscopic multilayer MoS_2 broadband detector from UV-to-IR with low Schottky barrier contacts. *Sci. Rep.* **2018**, *8*, 1276. [CrossRef] [PubMed]
11. Xie, Y.; Zhang, B.; Wang, S.; Wang, D.; Wang, A.; Wang, Z.; Yu, H.; Zhang, H.; Chen, Y.; Zhao, M.; et al. Ultrabroadband MoS_2 photodetector with spectral response from 445 to 2717 nm. *Adv. Mater.* **2017**, *29*, 1605972. [CrossRef]
12. Guo, J.; Li, S.; Ke, Y.; Lei, Z.; Liu, Y.; Mao, L.; Gong, T.; Cheng, T.; Huang, W.; Zhang, X. Broadband photodetector based on vertically stage-liked MoS_2/Si heterostructure with ultra-high sensitivity and fast response speed. *Scr. Mater.* **2020**, *176*, 1–6. [CrossRef]
13. Selamneni, V.; Ganeshan, S.K.; Sahatiya, P. All MoS 2 based 2D/0D localized unipolar heterojunctions as flexible broadband (UV-vis-NIR) photodetectors. *J. Mater. Chem. C* **2020**, *8*, 11593–11602. [CrossRef]
14. Gomathi, P.T.; Sahatiya, P.; Badhulika, S. Large-area, flexible broadband photodetector based on ZnS–MoS_2 hybrid on paper substrate. *Adv. Funct. Mater.* **2017**, *27*, 1701611. [CrossRef]
15. Shen, T.; Li, F.; Zhang, Z.; Xu, L.; Qi, J. High-performance broadband photodetector based on monolayer MoS_2 hybridized with environment-friendly CuInSe2 quantum dots. *ACS Appl. Mater. Interfaces* **2020**, *12*, 54927–54935. [CrossRef]
16. Tang, D.; Du, Z.; Xie, Y.; Zhao, F.; Yang, X.; Gu, C.; Shen, X. UV to NIR Broadband Flexible Photodetector Based on Solution-Processed MoS_2/PDPP3T Inorganic–Organic Hybrid Heterostructures. *Adv. Mater. Interfaces* **2024**, *11*, 2301065. [CrossRef]
17. Wadhwa, R.; Kaur, D.; Zhang, Y.; Alexender, A.; Kumar, D.; Kumar, P.; Namboothiry, M.A.; Qiao, Q.; Kumar, M. Fast response and high-performance UV-C to NIR broadband photodetector based on MoS_2/a-Ga_2O_3 heterostructures and impact of band-alignment and charge carrier dynamics. *Appl. Surf. Sci.* **2023**, *632*, 157597. [CrossRef]
18. Wang, X.; Shen, H.; Chen, Y.; Wu, G.; Wang, P.; Xia, H.; Lin, T.; Zhou, P.; Hu, W.; Meng, X.; et al. Multimechanism synergistic photodetectors with ultrabroad spectrum response from 375 nm to 10 μm. *Adv. Sci.* **2019**, *6*, 1901050. [CrossRef]
19. Sahatiya, P.; Badhulika, S. Discretely distributed 1D V2O5 nanowires over 2D MoS_2 nanoflakes for an enhanced broadband flexible photodetector covering the ultraviolet to near infrared region. *J. Mater. Chem. C* **2017**, *5*, 12728–12736. [CrossRef]
20. Kolli, C.S.R.; Selamneni, V.A.; Muñiz Martínez, B.; Fest Carreno, A.; Emanuel Sanchez, D.; Terrones, M.; Strupiechonski, E.; De Luna Bugallo, A.; Sahatiya, P. Broadband, ultra-high-responsive monolayer MoS_2/SnS_2 quantum-dot-based mixed-dimensional photodetector. *ACS Appl. Mater. Interfaces* **2022**, *14*, 15415–15425. [CrossRef] [PubMed]
21. Zheng, W.; Feng, W.; Zhang, X.; Chen, X.; Liu, G.; Qiu, Y.; Hasan, T.; Tan, P.; Hu, P.A. Anisotropic growth of nonlayered CdS on MoS_2 monolayer for functional vertical heterostructures. *Adv. Funct. Mater.* **2016**, *26*, 2648–2654. [CrossRef]
22. Gao, S.; Wang, Z.; Wang, H.; Meng, F.; Wang, P.; Chen, S.; Zeng, Y.; Zhao, J.; Hu, H.; Cao, R.; et al. Graphene/MoS_2/graphene vertical heterostructure-based broadband photodetector with high performance. *Adv. Mater. Interfaces* **2021**, *8*, 2001730. [CrossRef]
23. Ali, G.M. Performance analysis of planar Schottky photodiode based on nanostructured ZnO thin film grown by three different techniques. *J. Alloys Compd.* **2020**, *831*, 154859. [CrossRef]
24. Yang, B.; Kumar, A.; Feng, P.; Katiyar, R.S. Structural degradation and optical property of nanocrystalline ZnO films grown on Si (100). *Applied Physics Letters* **2008**, *92*, 233112. [CrossRef]
25. Peng, X.; Chen, J.; Wang, S.; Wang, L.; Duan, S.; Feng, P.; Chu, J. High-temperature operation of v-MoS_2 nanowalls/TiO_2 photodetectors with excellent performances. *Appl. Surf. Sci.* **2022**, *599*, 153904. [CrossRef]
26. Lee, C.; Yan, H.; Brus, L.E.; Heinz, T.F.; Hone, J.; Ryu, S. Anomalous lattice vibrations of single-and few-layer MoS_2. *ACS Nano* **2010**, *4*, 2695–2700. [CrossRef]
27. Mak, K.F.; Lee, C.; Hone, J.; Shan, J.; Heinz, T.F. Atomically Thin MoS_2: A New Direct-Gap Semiconductor. *Phys. Rev. Lett.* **2010**, *105*, 136805. [CrossRef]
28. Liu, H.Q.; Yao, C.B.; Liu, X.J.; Jiang, C.H. Heterointerface-enhanced ultrafast carrier dynamics and nonlinear optical response via constructing electronic structure-induced type-I ZnO-MoS_2 nn heterojunction. *Appl. Surf. Sci.* **2022**, *580*, 152222. [CrossRef]

29. Trajić, J.; Kostić, R.; Romčević, N.; Romčević, M.; Mitrić, M.; Lazović, V.; Balaž, P.; Stojanović, D. Raman Spectroscopy of ZnS Quantum Dots. *J. Alloys Compd.* **2015**, *637*, 401–406. [CrossRef]
30. Itoh, N. Verification of Si wafer first-order phonon peaks for reliable calibration of Raman microscopes. *J. Raman Spectrosc.* **2024**, *55*, 377–385. [CrossRef]
31. Yang, B.; Feng, P.; Kumar, A.; Katiyar, R.S.; Achermann, M. Structural and optical properties of N-doped ZnO nanorod arrays. *J. Phys. D Appl. Phys.* **2009**, *42*, 195402. [CrossRef]
32. Gurylev, V.; Perng, T.P. Defect Engineering of ZnO: Review on Oxygen and Zinc Vacancies. *J. Eur. Ceram. Soc.* **2021**, *41*, 4977–4996. [CrossRef]
33. Liu, C.; Ma, J.; Zhang, F.J.; Wang, Y.R.; Kong, C. Facile formation of Mo-vacancy defective MoS_2/CdS nanoparticles enhanced efficient hydrogen production. *Colloids Surf. A Physicochem. Eng. Asp.* **2022**, *643*, 128743. [CrossRef]
34. Srivastava, S.; Mohapatra, Y.N. MoS_2 | ZnO isotype heterostructure diode: Carrier transport and band alignment. *J. Appl. Phys.* **2021**, *129*, 205702. [CrossRef]
35. Zhou, J.; Zhang, N.; Liu, J.; Gao, Q.; Zhang, Y.; Gao, F.; Hu, P.; Feng, W. The Rise of 2D Materials-Based Photoelectrochemical Photodetectors: Progress and Prospect. *Adv. Opt. Mater.* **2024**, *12*, 2400706. [CrossRef]
36. Lee, S.H.; Bae, J.; Lee, S.W.; Jang, J.W. Improvement of Polypyrrole Nanowire Devices by Plasmonic Space Charge Generation: High Photocurrent and Wide Spectral Response by Ag Nanoparticle Decoration. *Nanoscale* **2015**, *7*, 17328–17337. [CrossRef]
37. Zhao, K.; Ouyang, B.; Yang, Y. Enhancing Photocurrent of Radially Polarized Ferroelectric $BaTiO_3$ Materials by Ferro-Pyro-Phototronic Effect. *iScience* **2018**, *3*, 208–216. [CrossRef] [PubMed]
38. Xiao, K.; Schmidt, O.G. Light-Driven Ion Transport in Nanofluidic Devices: Photochemical, Photoelectric, and Photothermal Effects. *CCS Chem.* **2022**, *4*, 54–65. [CrossRef]
39. Xue, F.; Chen, L.; Chen, J.; Liu, J.; Wang, L.; Chen, M.; Pang, Y.; Yang, X.; Gao, G.; Zhai, J.; et al. p-Type MoS_2 and n-Type ZnO Diode and Its Performance Enhancement by the Piezophototronic Effect. *Adv. Mater.* **2016**, *28*, 3391–3398. [CrossRef] [PubMed]
40. He, K.; Poole, C.; Mak, K.F.; Shan, J. Experimental Demonstration of Continuous Electronic Structure Tuning via Strain in Atomically Thin MoS_2. *Nano Lett.* **2013**, *13*, 2931–2936. [CrossRef] [PubMed]
41. Castellanos-Gomez, A.; Roldán, R.; Cappelluti, E.; Buscema, M.; Guinea, F.; Van Der Zant, H.S.; Steele, G.A. Local Strain Engineering in Atomically Thin MoS_2. *Nano Lett.* **2013**, *13*, 5361–5366. [CrossRef]
42. Manzeli, S.; Allain, A.; Ghadimi, A.; Kis, A. Piezoresistivity and Strain-Induced Band Gap Tuning in Atomically Thin MoS_2. *Nano Lett.* **2015**, *15*, 5330–5335. [CrossRef]
43. Peng, X.; Han, Y.; Zhang, Q.; Feng, P.; Jia, P.; Cui, H.; Wang, L.; Duan, S. Transactions on Electron Devices: Performance Improvement of MoS_2 Gas Sensor at Room Temperature. *IEEE Trans. Electron Devices* **2021**, *68*, 4644–4650. [CrossRef]
44. Tongay, S.; Zhou, J.; Ataca, C.; Lo, K.; Matthews, T.S.; Li, J.; Grossman, J.C.; Wu, J. Thermally driven crossover from indirect toward direct bandgap in 2D semiconductors: $MoSe_2$ versus MoS_2. *Nano Lett.* **2012**, *12*, 5576–5580. [CrossRef]
45. Wang, G.; Yuan, H.; Chang, J.; Wang, B.; Kuang, A.; Chen, H. ZnO/MoX_2 (X = S, Se) composites used for visible light photocatalysis. *RSC Adv.* **2018**, *8*, 10828–10835. [CrossRef]
46. Nayak, D.; Thangavel, R. Insight into enhanced photocatalytic properties of a type-II MoS_2/ZnO heterostructure and tuning its properties and interfacial charge transfer by strain. *New J. Chem.* **2023**, *47*, 3328–3340. [CrossRef]
47. Wang, S.; Ren, C.; Tian, H.; Yu, J.; Sun, M. MoS_2/ZnO van der Waals heterostructure as a high-efficiency water splitting photocatalyst: A first-principles study. *Phys. Chem. Chem. Phys.* **2018**, *20*, 13394–13399. [CrossRef]
48. Yang, K.; Liu, T.; Zhang, X.D. Bandgap engineering and near-infrared-II optical properties of monolayer MoS_2: A first-principle study. *Front. Chem.* **2021**, *9*, 700250. [CrossRef] [PubMed]
49. Feng, P.X.; Aldalbahi, A. A compact design of a characterization station for far UV photodetectors. *Rev. Sci. Instrum.* **2018**, *89*, 015001. [CrossRef] [PubMed]
50. Giannozzi, P.; Baroni, S.; Bonini, N.; Calandra, M.; Car, R.; Cavazzoni, C.; Ceresoli, D.; Chiarotti, G.L.; Cococcioni, M.; Dabo, I.; et al. QUANTUM ESPRESSO: A modular and open-source software project for quantum simulations of materials. *J. Phys. Condens. Matter* **2009**, *21*, 395502. [CrossRef]
51. Kresse, G.; Joubert, D. From ultrasoft pseudopotentials to the projector augmented-wave method. *Phys. Rev. B* **1999**, *59*, 1758–1775. [CrossRef]
52. Perdew, J.P.; Burke, K.; Ernzerhof, M. Generalized gradient approximation made simple. *Phys. Rev. Lett.* **1996**, *77*, 3865–3868. [CrossRef]
53. Grimme, S.; Antony, J.; Ehrlich, S.; Krieg, H. A consistent and accurate ab initio parametrization of density functional dispersion correction (DFT-D) for the 94 elements H-Pu. *J. Chem. Phys.* **2010**, *132*, 154104. [CrossRef] [PubMed]
54. Perdew, J.P.; Levy, M. Physical content of the exact Kohn-Sham orbital energies: Band gaps and derivative discontinuities. *Phys. Rev. Lett.* **1983**, *51*, 1884. [CrossRef]

55. Sham, L.J.; Schlüter, M. Density-functional theory of the energy gap. *Phys. Rev. Lett.* **1983**, *51*, 1888. [CrossRef]
56. Heyd, J.; Scuseria, G.E.; Ernzerhof, M. Erratum: Hybrid functionals based on a screened Coulomb potential. *J. Chem. Phys.* **2006**, *124*, 219906. [CrossRef]

molecules

MDPI

Article

Versatile Tunable Terahertz Absorption Device Based on Bulk Dirac Semimetals and Graphene

Jie Zhou [1,2], Xin Sun [3,*], Jun Xu [4,*], Shiyue Wu [4], Kaili Jin [4], Yongjian Tang [5], Zao Yi [5] and Yougen Yi [6]

1 School of Electronic Information and Electrical Engineering, Chengdu University, Chengdu 610100, China; zhoujie_cc@163.com
2 School of Materials Science and Engineering, Tsinghua University, Beijing 100084, China
3 College of Urban Construction, Zhejiang Shuren University, Hangzhou 310015, China
4 Institute of Guizhou Aerospace Measuring and Testing Technology, Guiyang 550009, China; wushiy@163.com (S.W.); jinkl845@163.com (K.J.)
5 Joint Laboratory for Extreme Conditions Matter Properties, Southwest University of Science and Technology, Mianyang 621010, China; tangyongjian2000@sina.com (Y.T.); yizaomy@swust.edu.cn (Z.Y.)
6 College of Physics, Central South University, Changsha 410083, China; yougenyi@csu.edu.cn
* Correspondence: 601261@zjsru.edu.cn (X.S.); xujun8617@163.com (J.X.); Tel./Fax: +86-0571-88297011 (X.S.); +86-0851-8699422 (J.X.)

Abstract: We employed the CST Microwave Studio software 2020 and the FDID algorithm for simulation. We have designed a terahertz broadband absorber based on Dirac semimetals and graphene, achieving continuous broadband absorption with a rate exceeding 80% over the range from 7.6776 to 9.172 THz. This broadband absorber features two independent tuning modes, utilizing graphene and Dirac semimetals, and exhibits strong electromagnetic adaptability. Furthermore, we conducted an in-depth analysis of the physical mechanisms underlying the high absorption in these absorbers using impedance matching theory and localized surface plasmon resonance (LSPR) theory. Variations in the dielectric constants of different dielectric layers and the relaxation time of graphene can also modulate the absorption rate. In summary, our proposed terahertz broadband absorber, employing two distinct tunable materials, enhances the device's flexibility and environmental adaptability, offering promising prospects for wideband absorption applications.

Keywords: absorber; metamaterial; Dirac semimetal; graphene; terahertz; wideband absorption

1. Introduction

Currently, there remains substantial room for advancement in the development and utilization of the terahertz frequency range (0.1–10 THz), often referred to as the "terahertz gap" [1,2]. Researchers have recognized the significance of this range and the vast potential it holds. Terahertz (THz) waves are poised to become the communication band for next-generation technologies, including 6G. They hold the potential to advance various fields such as defense, space exploration, biomedical applications, and economic development, offering new impetus for the progress of human civilization [3–5]. The availability of sophisticated electromagnetic sensors is a prerequisite for the effective exploitation of specific frequency ranges and the advancement of related technologies. However, the development and utilization of electromagnetic waves within the frequency range known as the "terahertz gap" (10^{11}–10^{13} Hz), characterized by its wide bandwidth, low energy, strong penetration, and high resolution, have long remained underexplored [6–8]. A critical factor for the advancement of electromagnetic wave technologies is the availability

of functional devices capable of responding to specific frequency bands. Among these, electromagnetic wave absorption is particularly significant, as it forms the foundation for effective utilization of such waves [9,10].

The terahertz gap lies at the intersection of electronics and photonics in the electromagnetic spectrum, making it challenging for natural materials to exhibit robust responses to terahertz waves. Consequently, the exploitation of this frequency range necessitates the development of materials with specialized electromagnetic properties.

Metamaterials, with their ability to be flexibly designed due to their periodic atomic structures, offer extraordinary electromagnetic characteristics not found in traditional materials [11–13]. The flexibility of metamaterials has led to the design of various electromagnetic absorbers, addressing the limitations of natural materials and potentially bridging the existing terahertz gap [14]. Since Landy et al. introduced the first metamaterial absorber in 2008, there has been considerable interest in the research and application of metamaterials in the electromagnetic field [15]. This has highlighted the immense potential of metamaterials in electromagnetic wave technologies. In recent years, graphene, noted for its exceptional optoelectronic properties, has garnered significant attention and is often referred to as a "game-changing material" [16–18]. Additionally, bulk Dirac semimetals, which represent a three-dimensional counterpart to graphene, have also attracted growing interest and are considered a "three-dimensional graphene" [19–22]. Hu et al. proposed a dynamic triple adjustable dual frequency metamaterial absorber that can be electrically, thermally, and magnetically controlled [23]. Qi et al. developed a dual-band terahertz broadband absorber using graphene [24].

Building upon the current research on terahertz absorbers based on graphene, Dirac semimetals, and other metamaterials, this study explores a dual-control broadband terahertz absorber combining the strengths of Dirac semimetals and graphene. This device achieves continuous broadband absorption with an efficiency exceeding 80% over the range from 7.6776 to 9.172 THz. Given that both Dirac semimetals and graphene can independently tune the Fermi level, the electromagnetic adaptability of this device is notably robust. We conducted a thorough investigation into the physical mechanisms underlying the high absorption using impedance matching theory and localized surface plasmon resonance (LSPR) theory. The impact of different dielectric layer refractive indices on device performance was also examined. Additionally, we explored the influence of the properties of the two metamaterials on the device. This absorber is expected to have significant applications in terahertz modulation and attenuation.

2. Modeling and Structural Parameters of the Micro-Nano Optical Devices

The proposed structure of our terahertz absorber is illustrated in Figure 1a, featuring a four-layer configuration. The structure of the top graphene layer is designed to be approximately complementary to that of the intermediate Dirac semimetal (DSM) layer when viewed from the projection plane. The uncovered portions of the graphene layer ensure that electromagnetic waves can penetrate to the DSM layer, thereby eliciting additional electromagnetic responses. The graphene pattern is derived from a difference set operation involving a square, a circle, an annulus, and four rectangles connected to the annulus, with detailed structural parameters provided in Table 1. The conductivity of gold is $4.561 \times 10^{+007}$ S/m, and the dielectric constant of aluminum oxide is 2.28.

The initial Fermi level of the graphene was set to 0.6 eV, with an initial relaxation time of 0.6 ps and a thickness of 1 nm. The initial Fermi level of the Dirac semimetal (DSM) was set to 90 meV. For the simulation, we employed CST software and utilized the FDID algorithm [25,26]. Periodic boundary conditions were applied in the X and Y

directions, while open boundary conditions were established in the Z direction, allowing electromagnetic waves to incident normally from the negative *z* axis onto the surface of the device [27,28].

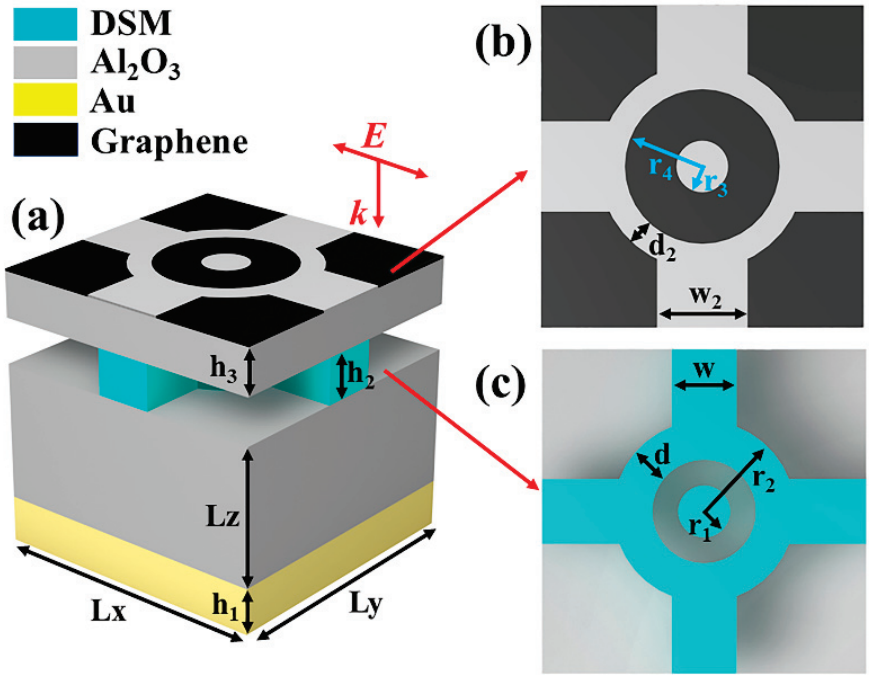

Figure 1. (**a**) Schematic diagram of the 3D structure of the designed wideband absorber. (**b**) Structural diagram of the graphene layer. (**c**) Structural diagram of DSM layer.

Table 1. Structural parameters of graphene layer.

Parameters	Lx	Ly	Lz	h_1	h_2	h_3	d	w	r_1	r_2	d_2	w_2	r_3	r_4
Unit (μm)	25	25	12	0.5	2	5	3	0.5	2	7	6	2.9	2	6

Then, we gave the manufacturing methods in bottom-up order. First, a 0.5 μm gold film was sputtered on the prepared substrate, and then a 12 μm thick alumina dielectric layer was grown by CVD. After that, a layer of Dirac semimetal film was sputtered again, with a thickness of 2 μm, and the desired microstructure was obtained through gluing, development, exposure, etching, and stripping processes. The same process can be followed separately to obtain an alumina dielectric layer and a graphene layer, which can then be covered on top of the Dirac semimetal film. The repeated lithography process finally obtains the array structure of the absorber [29,30].

In this paper, graphene conductivity can be described by the Kubo formula [31,32]:

$$\sigma_{\text{Graphene}} = \sigma_{\text{G\_intra}} + \sigma_{\text{G\_inter}} \tag{1}$$

In the above formula, $\sigma_{\text{G\_intra}}$ and $\sigma_{\text{G\_inter}}$ are as follows:

$$\sigma_{\text{G\_intra}} = \frac{ie^2 k_B T}{\pi\hbar^2(\omega + i\tau^{-1})}\left[\frac{E_F}{K_B T} + 2\ln(e^{-\frac{E_F}{k_B T}} + 1)\right] \tag{2}$$

$$\sigma_{\text{G\_inter}} = \frac{ie^2}{4\pi\hbar^2}\ln\left[\frac{2|E_F| - \hbar(\omega + i\tau^{-1})}{2|E_F| + \hbar(\omega + i\tau^{-1})}\right] \tag{3}$$

Here, $\hbar$ represents the reduced Planck constant, k_B is the Boltzmann constant, e denotes the charge of an electron, and E_F and τ refer to the Fermi level and relaxation time of the

graphene layer, respectively. ω represents the angular frequency of the incident wave, and T indicates the ambient temperature. Within the frequency range under investigation, the interband conductivity σ_{G_intra} of graphene can be considered negligible (since σ_{G_intra} approaches zero when $E_F >> kT$). Thus, at room temperature (298 K), the conductivity of graphene can be expressed in the Drude form [33]:

$$\sigma(\omega) = \frac{ie^2|E_F|}{\pi\hbar^2(\omega + i\tau^{-1})} \tag{4}$$

In the above formula,

$$\tau = \frac{E_F v}{e v_F^2} \tag{5}$$

In Equation (4), v denotes the carrier mobility of the top-layer graphene material, and $v_F = 10^6$ m/s is the Fermi velocity. Additionally, the dielectric constant of graphene can be expressed as follows [34]:

$$\varepsilon = 1 + \frac{i\sigma_{Graphene}}{\omega\varepsilon_0\Delta} \tag{6}$$

where ε_0 is the vacuum dielectric constant, and Δ represents the thickness of the graphene.

At the same time, the following expression can also be obtained by using the Kubo formula for Dirac semimetals [35]:

$$\sigma_{D\_intra} = \frac{ie^2}{\hbar}\frac{gk_F}{6\pi^2\Omega}\left[1 + \frac{\pi^2}{3}\left(\frac{T}{E_F}\right)^2\right] \tag{7}$$

$$\sigma_{D\_inter} = \frac{ie^2 g\omega}{3\pi^2\hbar v_F}\left[-\frac{\pi i}{2}\frac{G\left(\frac{\hbar\omega}{2}\right)}{4} + \int_0^\infty \left(\frac{G(\varepsilon) - G(\hbar\omega/2)}{\hbar^2\omega^2 - 4\varepsilon^2}\right)\varepsilon d\varepsilon\right] \tag{8}$$

Here, g = 40 is the damping formula, $\Omega = \hbar\omega/E_F$, and $\varepsilon_c = E_c/E_F$ (where $\varepsilon_c = 3$ represents the cutoff energy) are parameters related to the damping, $G(E) = \sinh(E/T)/[\cosh(E_F/T) + \cosh(E/T)]$ [36] is a relevant constant, and $k_F = E_F/(\hbar v_F)$ denotes the Fermi momentum. According to the Random Phase Approximation theory, the real and imaginary parts of the dynamic conductivity under condition $T << E_F$ can be expressed as follows [37]:

$$\text{Re } \sigma_{Dirac}(\Omega) = \frac{e^2}{\hbar}\frac{gk_F}{24\pi}\Omega G\left(\frac{\Omega}{2}\right) \tag{9}$$

$$\text{Im } \sigma_{Dirac}(\Omega) = \frac{e^2}{\hbar}\frac{gk_F}{24\pi^2}\left\{\frac{4}{\Omega}\left[1 + \frac{\pi^2}{3}\left(\frac{T}{E_F}\right)^2\right] + 8\Omega\int_0^{\varepsilon_c}\left[\frac{G(\varepsilon) - G\left(\frac{\Omega}{2}\right)}{\Omega^2 - 4\varepsilon^2}\right]\varepsilon d\varepsilon\right\} \tag{10}$$

Then, based on the two-band model, taking into account interband electron transport, the effective dielectric constant of the DSM can be expressed as follows [38,39]:

$$\varepsilon_{Dirac} = \varepsilon_b + \frac{i\sigma_{Dirac}}{\omega\varepsilon_0} = \varepsilon_b + i\frac{\text{Re}(\sigma_{Dirac}(\Omega)) + \text{Im}(\sigma_{Dirac}(\Omega))}{\omega\varepsilon_0} \tag{11}$$

where $\varepsilon_0 = 1$, and $\varepsilon_b = 1$.

3. Results and Discussion

Through the preceding analysis, we obtained the S parameters. Subsequently, we utilized these S parameters to calculate the absorption rate (A) and transmission rate (T). The absorption rate is expressed as $A = 1 - R - T$, where R represents the reflectance,

given by R = $|S_{11}|^2$, and the transmission rate is defined as T = $|S_{21}|^2$ [40,41]. Notably, the thickness of the underlying metallic reflective layer is configured to ensure that terahertz waves do not propagate through the absorber. Thus, the absorption rate can be simplified to A = 1 − R [36,42].

Figure 2a presents a comparative analysis of the absorption spectra for different absorber structures within the 6–10 THz frequency range under TE and TM mode electromagnetic wave incidence. The figure includes three absorber configurations: Absorber One, Absorber Two, and an absorber with only the graphene layer, after removing the intermediate Dirac semimetal (DSM) layer. All three absorber structures exhibited perfect rotational symmetry, ensuring that the absorption spectra corresponding to the two modes of incident electromagnetic waves would be identical [43]. When the absorber consisted solely of the graphene layer, it achieved continuous broadband absorption with an efficiency exceeding 80% over the range of 7.668–8.328 THz. This performance was evaluated using the following formula [44]:

$$B_w = 2 \times \frac{(f_{max} - f_{min})}{(f_{max} + f_{min})} \times 100\% \quad (12)$$

where f_{max} and f_{min} represent the highest and lowest frequencies of the corresponding absorption bands, respectively. The total absorption bandwidth of the device was calculated to be 0.66 THz, with a relative bandwidth (B_w) of 8.25%. However, the incorporation of graphene with a Dirac semimetal (DSM) significantly enhanced the broadband absorption characteristics of the absorber. For Absorber Two, the frequency range where the absorption efficiency exceeded 80% extended from 7.676 to 9.172 THz, with a total absorption bandwidth of 1.496 THz and a relative bandwidth of 17.76%, centered at 8.424 THz. This represents more than a two-fold improvement in broadband absorption performance compared to the graphene-only absorber. The superior broadband absorption is attributed to the synergistic effect of the top graphene layer and the intermediate DSM layer, with the DSM enhancing the response to electromagnetic waves [45,46]. As depicted in Figure 2b, within the 7.5–9.5 THz range, Absorber Two exhibited five prominent resonant absorption peaks, located at central frequencies of 7.928 THz (Mode I, absorption rate of 96.391%), 8.2 THz (Mode II, absorption rate of 99.05%), 8.516 THz (Mode III, absorption rate of 99.28%), 8.716 THz (Mode IV, absorption rate of 99.37%), and 9.016 THz (Mode V, absorption rate of 98.775%). The excellent broadband absorption characteristics of this absorber suggest its promising applications in terahertz wave modulation and attenuation [47].

We know that in the terahertz region, impedance matching theory has been used experimentally to achieve broadband absorption in other wavelength ranges, such as the microwave and visible to infrared regions. Therefore, we looked to better explain the absorption effect demonstrated by our above absorption devices. When the equivalent impedance of the absorber matches the impedance of the free space, the relative impedance Z = 1, the device will reach the critical coupling condition, thus showing strong electromagnetic absorption characteristics [48]. We calculated the relative impedance of the absorber in the 6–10 THz range according to Equation (13), with the results shown in Figure 3. The highlighted region in the blue dashed box corresponds to the 7.676–9.172 THz frequency range. It is evident that within the frequency range where the absorber achieved an absorption efficiency greater than 80%, the real part of the relative impedance remained close to 1, exhibiting only minor fluctuations. Similarly, the imaginary part remained near 0 with minimal variation. Throughout the strong absorption band, the relative impedance of the absorber was well matched with the impedance of free space, achieving near-perfect matching at the center frequencies of the five absorption peaks, where Im(Z_r) approaches 0 and Re(Z_r) approaches 1 [49]. This impedance matching elucidates the mechanism behind

the absorber's broadband absorption performance from the perspective of impedance matching theory [50,51]:

$$z_r = \pm\sqrt{\frac{(1+S_{11})^2 - S_{21}^2}{(1-S_{11})^2 - S_{21}^2}} = \frac{z}{\eta} \tag{13}$$

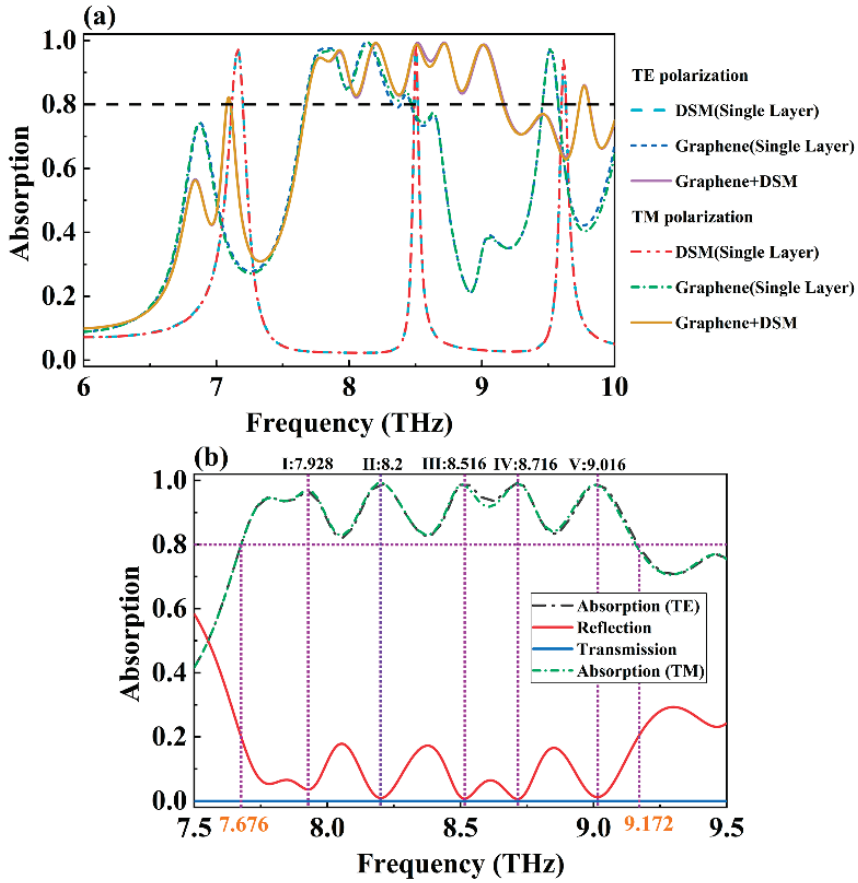

Figure 2. (**a**) Absorption spectra of different structures of absorbers under the incidence of TE and TM electromagnetic waves; (**b**) the absorption, reflection, and transmission spectra of the designed wideband absorber.

Here, η represents the impedance in free space, z represents the impedance of the absorber, and z_r represents the relative impedance of the absorber.

To further investigate the physical mechanisms behind broadband absorption, we computed the electric field distribution at the boundaries of the graphene layer, DSM layer, and the absorber unit structure at the center frequencies of the five prominent resonant absorption peaks [52,53]. As illustrated in the figures, under the influence of the external electric field, LSPR excites the boundaries of both the graphene layer and the DSM layer. This localization of the electric field in these specific regions leads to significant energy loss of the incident electromagnetic waves, resulting in strong absorption [54]. A detailed analysis reveals a transition in the electric field resonance modes, as shown in Figure 4a–e. Specifically, the field patterns in Figure 4a,b are similar, with concentration around the inner and outer boundaries of the central graphene ring, while the field at the outer graphene boundary is notably weaker. Conversely, the field distributions in Figure 4d,e are similar, with the fields at the IV and V central frequencies concentrated at the boundary of the outer graphene, while the field at the graphene ring is very weak. The field pattern corresponding to Mode III represents an intermediate state, with the primary field concentration shifting from the graphene ring to the outer graphene boundary. This indicates that the broadband

absorption achieved by the absorber results from the merging and expansion of adjacent resonance modes. Additionally, Figure 4f–j show that after the electromagnetic waves pass through the graphene layer and the upper dielectric plate to reach the DSM layer, different resonance modes are also excited. Figure 4k–o demonstrate that the electric field strength in the graphene layer is higher than in the DSM layer, indicating that graphene plays a predominant role in broadband absorption. The response modes of the DSM layer differ from those of the graphene layer, and its coupling with the graphene layer further enhances the absorber's effectiveness in absorbing electromagnetic waves [55]. This explains the significant improvement in broadband absorption characteristics when combining graphene with a DSM compared to using a single graphene layer, as shown in Figure 2a.

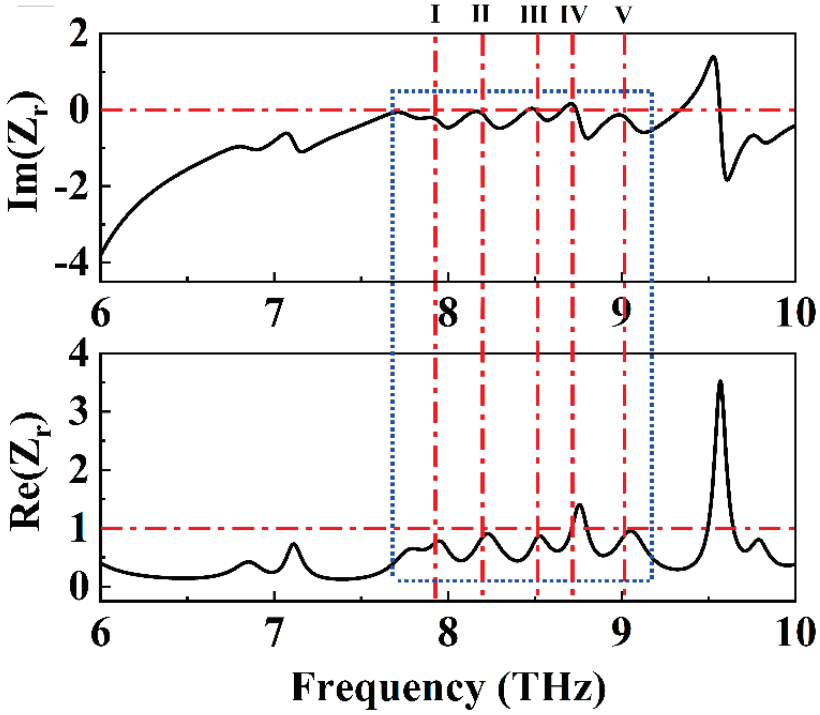

Figure 3. Virtual and real parts of the relative impedance of a wideband absorber in the range of 6–10 THz.

To explore the practical applicability of the absorber, we investigated its adaptability to different electromagnetic wave modes, as shown in Figure 5a. The absorber consistently exhibited excellent broadband absorption characteristics with high stability across a polarization angle range of 0–90°, demonstrating polarization insensitivity and suitability for complex electromagnetic environments [56–58]. Additionally, we examined the impact of variations in the dielectric constant of the absorber's dielectric layer on the absorption spectrum, with the results presented in Figure 5b. As the dielectric constant of alumina increased from 2.08 to 2.48, a noticeable shift in the absorption spectrum occurred. At a dielectric constant of 2.08, the broadband absorption performance of the absorber significantly weakened, primarily due to changes in the dielectric constant affecting the relative impedance of the entire absorber, leading to poor matching with free space over a wide frequency range [59,60]. However, within the dielectric constant range of 2.18 to 2.48, the absorber maintained good broadband absorption characteristics, with a redshift in the central frequency from 8.548 THz to 8.16 THz, while the absorption bandwidth remained relatively stable. This variation in the dielectric constant enables effective modulation of the absorption performance. The redshift in the central frequency results from the dielectric

constant's effect on the relative impedance of the absorber, allowing it to achieve better impedance matching with free space at different frequencies.

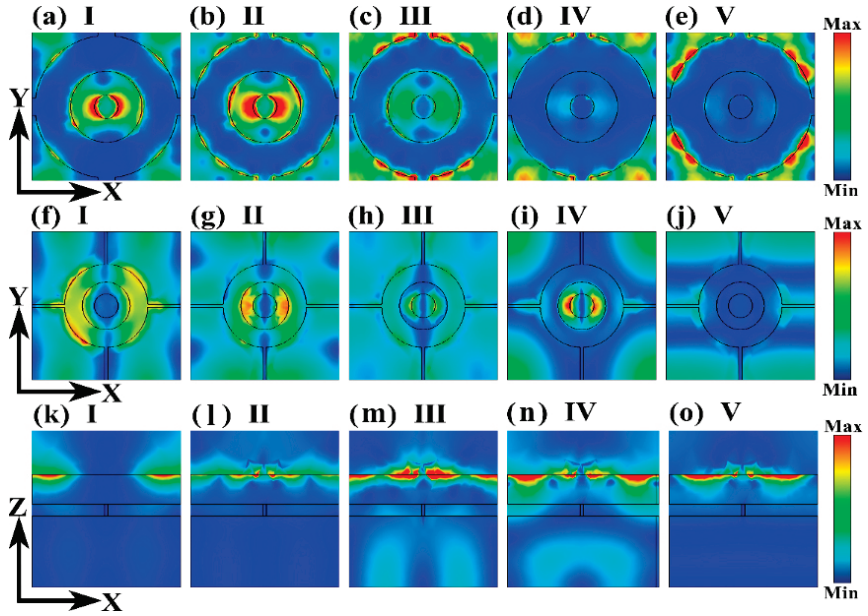

Figure 4. (**a**–**e**) show the electric field distribution on the XY plane of the graphene layer in the broadband absorber at the central frequencies of the five resonant absorption peaks. (**f**–**j**) illustrate the electric field distribution on the XY plane of the DSM layer at these same central frequencies. (**k**–**o**) depict the electric field distribution on the XZ plane at the interfaces of the absorber unit for the central frequencies of the five resonant absorption peaks.

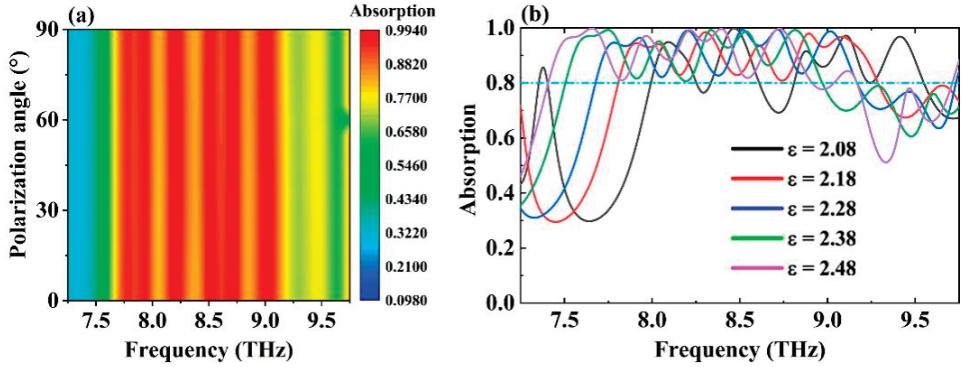

Figure 5. (**a**) The absorption spectrum of the wideband absorber in the range of 0–90° electric field polarization angle. (**b**) Absorption spectra of wideband absorbers under different dielectric constants of dielectric layers.

Given the dynamically tunable Fermi levels of both graphene and DSM, we employed a controlled variable method to separately investigate the relationship between the Fermi levels of these materials and the absorption spectrum of the absorber, exploring the graphene–Dirac semimetal dual-control adjustment mode [61,62]. When the Fermi level of the DSM was fixed at 90 meV, Figure 6a illustrates that as the Fermi level of graphene varied continuously within the range of 0.5–0.9 eV, the absorber's absorption bandwidth exhibited a trend of initial increase followed by a decrease. Within the Fermi level range of 0.58–0.64 eV, the absorber displayed optimal broadband absorption characteristics with notable tunability of the absorption frequency. Specifically, at a graphene Fermi level of 0.58 eV, the absorber achieved a bandwidth of 1.364 THz with an absorption rate exceeding 80%, centered at 8.202 THz. As the graphene Fermi level increased to 0.64 eV, the absorption bandwidth expanded to 1.7 THz, with a blueshift of the central frequency to 8.694 THz,

yielding a tunable range of 0.492 THz for the central frequency. The cause of this blueshift can be explained by the following equation:

$$\lambda_{re} = a + bn_{sp} \quad (14)$$

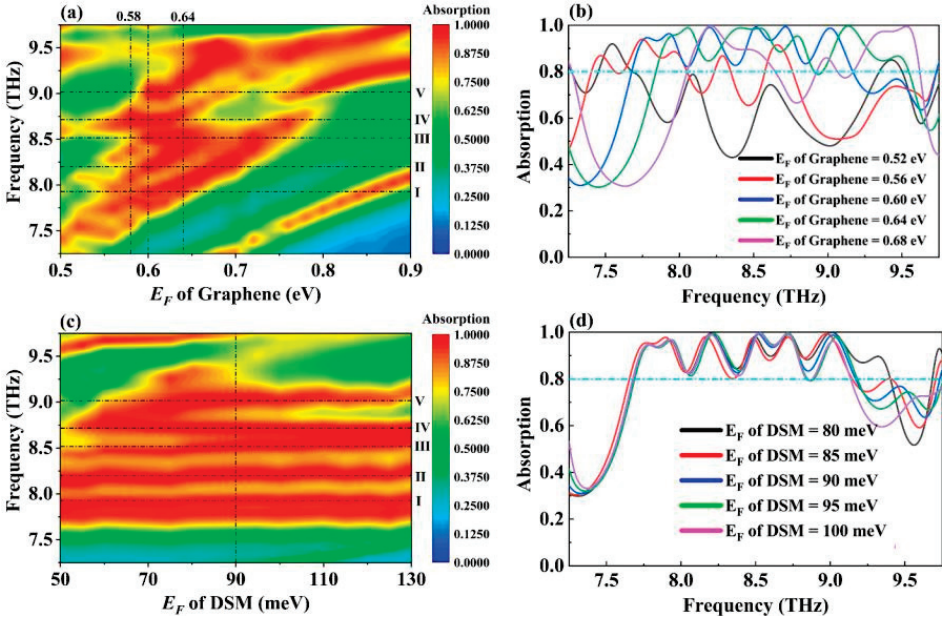

Figure 6. (**a**) Absorption spectra of wideband absorbers with Fermi levels of graphene in the range of 0.5–0.9 eV. (**b**) Changes in the absorption spectrum of the wideband absorber when the Fermi level of graphene varies in the range of 0.52–0.68 eV. (**c**) Absorption spectra of wideband absorbers at the Fermi level of DSM in the range of 50–130 meV. (**d**) Changes in the absorption spectra of wideband absorbers when the Fermi level of DSM varies in the range of 80–100 meV.

In the equation, λ_{sp} represents the resonant wavelength, a and b are constants related to the geometric structure of the model and the surrounding dielectric constants, and n_{sp} denotes the effective refractive index of graphene. There is a negative correlation between the Fermi level of graphene and its effective refractive index. As the Fermi level increases, the effective refractive index decreases, leading to a blueshift in the resonant wavelength [63,64]. As depicted in Figure 6b, the average absorption rate of the absorber in the 7.25–9.75 THz range exhibited an initial increase followed by a decrease as the Fermi level of graphene rose from 0.52 eV to 0.68 eV. According to Equations (2) and (3), the conductivity of graphene increases with its Fermi level. This suggests that the surface plasmon resonance of the graphene layer first approaches saturation and then becomes oversaturated, which explains the observed trend in the absorption bandwidth [65,66].

Figure 6c,d illustrate the impact of varying the Fermi level of the DSM on the performance of the absorber when the Fermi level of graphene has been fixed at 0.6 eV [67]. Similarly to the variation in graphene's Fermi level, an increase in the DSM's Fermi level from 50 meV to 130 meV initially enlarged and then reduced the absorber's absorption bandwidth, with a gradual splitting of Mode V. As shown in Figure 2, Mode V results from the combined effects of graphene and the Dirac semimetal, exhibiting the strongest coupling among all the resonant peaks. When the Fermi level of the DSM increased, the corresponding central frequency experienced the most significant blueshift. Overall, each of the five strong absorption peaks underwent a slight blueshift with increasing DSM Fermi levels, presenting an additional avenue for tuning the absorber's performance. The absorber's dual-control adjustment mode offers flexibility for practical applications, allowing for selection of the appropriate tuning method based on specific requirements.

Moreover, as indicated by Equation (5), the incorporation of organic molecules on the surface of graphene in practical applications can effectively modulate its carrier mobility, thereby enabling control over the relaxation time without altering other parameters [68,69]. Figure 7 depicts the changes in the absorption spectrum of the absorber as the relaxation time of graphene increased from 0.52 ps to 0.68 ps. It is evident that while the absorption bandwidth and central frequency of the absorber remained relatively unchanged, there was a noticeable decline in absorption rate. This decrease is attributed to the fact that as the relaxation time increases, the carriers in graphene approach saturation, leading to reflection of the incident electromagnetic waves and thereby reducing effective absorption. This approach can be utilized to adjust the absorber's absorption rate based on practical requirements.

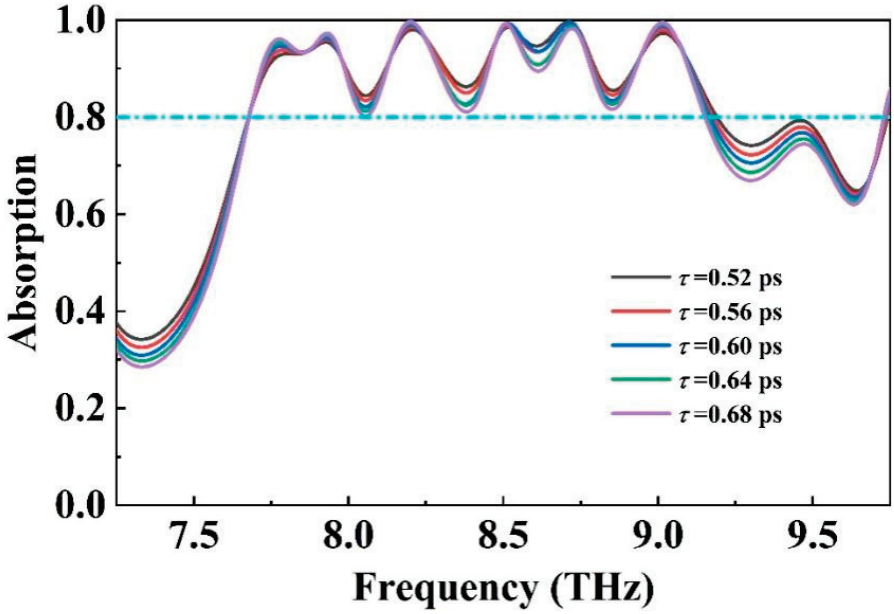

Figure 7. The relaxation time of graphene is increased from 0.52 ps to 0.68 ps in the absorption spectrum.

4. Conclusions

In this study, the proposed broadband absorber achieved continuous broadband absorption with an absorption rate exceeding 80% within the 7.676–9.172 THz frequency range, exhibiting an absorption bandwidth of 1.496 THz and a central absorption frequency of 8.424 THz. The absorber features five prominent resonant absorption peaks within its broadband absorption range. Analysis of the absorber's relative impedance reveals a good overall match with free space across the 7.676–9.172 THz band. The observed broadband strong absorption is attributed to the excitation of surface plasmons in both the graphene and DSM layers, with the coupling between these two metamaterials enhancing the fusion of adjacent resonant modes. Additionally, the absorber demonstrates excellent polarization insensitivity, maintaining robust broadband absorption performance under various incident electromagnetic wave modes. By varying the dielectric constant of the absorber's dielectric layer, it is possible to tune the central frequency within the range of 8.51–8.548 THz while maintaining nearly unchanged absorption bandwidth and good performance, which is practically achievable. Furthermore, the dual-control tuning mode, enabled by adjusting the Fermi levels of the Dirac semimetal and graphene, allows for precise control over the absorption frequency. In practical applications, the choice of tuning method can be tailored to specific needs. Finally, while the relaxation time of graphene has a minimal impact on the absorption bandwidth and central frequency, it

allows for adjustment of the absorption rate. In summary, the terahertz broadband absorber presented in this study leverages two distinct tunable materials to enhance flexibility and environmental adaptability. Its dual-control tuning mode suggests significant potential for applications in terahertz modulation and attenuation.

Author Contributions: Conceptualization, J.Z., X.S., S.W., K.J., J.X., Z.Y. and Y.Y.; data curation, J.Z., S.W., K.J., Y.T. and J.X.; formal analysis, J.Z., S.W., K.J., Z.Y. and J.X.; methodology, J.Z., S.W., K.J., Y.T., Y.Y. and J.X.; resources, J.Z., S.W., K.J. and J.X.; software, J.Z., S.W., K.J., Y.T., Y.Y. and J.X.; data curation, J.Z., S.W., K.J., Y.T., Y.Y. and J.X.; writing—original draft preparation, J.Z., S.W. and K.J.; writing—review and editing, J.Z., X.S., S.W., K.J. and J.X. All authors have read and agreed to the published version of the manuscript.

Funding: The authors are grateful to the support by National Natural Science Foundation of China (No. 51606158, 11604311, 12074151); funding from the Fourth Basic Scientific Research Plan of Science and Technology Industry Bureau (JCKY2023204C035); funding from the Chengdu University funded project (X2060); and funding from the Science Foundation of Zhejiang University of Technology (GYY-ZH-2023084).

Institutional Review Board Statement: Not applicable.

Informed Consent Statement: Not applicable.

Data Availability Statement: Publicly available datasets were analyzed in this study. These data can be found here: [https://www.lumerical.com/] (accessed on 1 January 2020).

Conflicts of Interest: The authors declare no conflicts of interest.

References

1. Rane, S.; Prabhu, S.; Chowdhury, D.R. Physics and applications of terahertz metagratings. *Opto-Electron. Sci.* **2024**, *3*, 230049. [CrossRef]
2. Li, J.; Lu, X.G.; Li, H.; Song, C.; Tan, Q.; He, Y.; Liu, J.; Luo, L.; Tang, T.; Liu, T.; et al. Racemic dielectric metasurfaces for arbitrary terahertz polarization rotation and wavefront manipulation. *Opto-Electron. Adv.* **2024**, *7*, 240075. [CrossRef]
3. Liu, M.L.; Li, B.X.; Zeng, L.L.; Wei, Y.; Wen, R.Q.; Zhang, X.J.; Deng, C.S. Dynamic tunable narrow-band perfect absorber for fiber -optic communication band based on liquid crystal. *J. Phys. D Appl. Phys.* **2023**, *56*, 505102. [CrossRef]
4. Xiang, T.; Sun, Z.; Wang, L.L.; Lin, Q.; Liu, G.D. Polarization independent perfect absorption of borophene metamaterials operating in the communication band. *Phys. Scr.* **2024**, *99*, 085519. [CrossRef]
5. Tian, Y.X.; Dong, B.Y.; Li, Y.X.; Xiong, B.; Zhang, J.; Sun, C.; Hao, Z.; Wang, J.; Wang, L.; Han, Y.; et al. Photonics-assisted THz wireless communication enabled by wide-bandwidth packaged back-illuminated modified uni-traveling-carrier photodiode. *Opto-Electron. Sci.* **2024**, *3*, 230051. [CrossRef]
6. Chernomyrdin, N.V.; Musina, G.R.; Nikitin, P.V.; Dolganova, I.N.; Kucheryavenko, A.S.; Alekseeva, A.I.; Wang, Y.; Xu, D.; Shi, Q.; Tuchin, V.V.; et al. Terahertz technology in intraoperative neurodiagnostics: A review. *Opto-Electron. Adv.* **2023**, *6*, 220071. [CrossRef]
7. Li, Z.T.; Cheng, S.B.; Zhang, H.F.; Yang, W.X.; Yi, Z.; Yi, Y.G.; Wang, J.Q.; Ahmad, S.; Raza, R. Ultrathin broadband terahertz metamaterial based on single-layer nested patterned graphene. *Phys. Lett. A* **2025**, *534*, 130262. [CrossRef]
8. Fan, J.X.; Li, Z.L.; Xue, Z.Q.; Xing, H.Y.; Lu, D.; Xu, G.; Gu, J.; Han, J.; Cong, L. Hybrid bound states in the continuum in te-rahertz metasurfaces. *Opto-Electron. Sci.* **2023**, *2*, 230006. [CrossRef]
9. Yang, C.; Luo, M.H.; Ju, X.W.; Hu, J.Y. Ultra-narrow dual-band perfect absorber based on double-slotted silicon nanodisk arrays. *J. Phys. D Appl. Phys.* **2024**, *57*, 345104. [CrossRef]
10. Gao, H.; Fan, X.H.; Wang, Y.X.; Liu, Y.C.; Wang, X.G.; Xu, K.; Deng, L.; Zeng, C.; Li, T.; Xia, J.; et al. Multi-foci metalens for spectra and polarization ellipticity recognition and reconstruction. *Opto-Electron. Sci.* **2023**, *2*, 220026. [CrossRef]
11. Li, Y.M.; Tan, C.X.; Hu, J.Y.; Bai, W.D.; Zhang, R.L.; Lin, Q.; Zhang, Y.; Wang, L.L. Ultra-narrow band perfect absorbance induced by magnetic lattice resonances in dielectric dimer metamaterials. *Results Phys.* **2022**, *39*, 105730. [CrossRef]
12. He, C.; Zhao, D.; Fan, F.; Zhou, H.; Li, X.; Li, Y.; Li, J.; Dong, F.; Miao, Y.-X.; Wang, Y.; et al. Pluggable multitask diffractive neural networks based on cascaded metasurfaces. *Opto-Electron. Adv.* **2024**, *7*, 230005. [CrossRef]
13. Ling, Z.X.; Zeng, Y.; Liu, G.D.; Wang, L.L.; Lin, Q. Unified model for plasmon-induced transparency with direct and indirect coupling in borophene-integrated metamaterials. *Opt. Express* **2022**, *30*, 21966. [CrossRef] [PubMed]

14. Li, X.; Li, Z.T.; Wang, L.L.; Lin, Q. Unidirectional reflectionless propagation in borophene plasmonic metamaterials. *J. Phys. D Appl. Phys.* **2023**, *57*, 015103. [CrossRef]
15. Landy, N.I.; Sajuyigbe, S.; Mock, J.J.; Smith, D.R.; Padilla, W.J. Perfect Metamaterial Absorber. *Phys. Rev. Lett.* **2008**, *100*, 207402. [CrossRef]
16. Geim, A.K. Graphene: Status and prospects. *Science* **2009**, *324*, 1530. [CrossRef]
17. Zeng, Y.; Ling, Z.X.; Liu, G.D.; Wang, L.L.; Lin, Q. Tunable plasmonically induced transparency with giant group delay in gain-assisted graphene metamaterials. *Opt. Express* **2022**, *30*, 455954. [CrossRef]
18. Ma, R.; Zhang, L.G.; Zeng, Y.; Liu, G.D.; Wang, L.L.; Lin, Q. Extreme enhancement of optical force via the acoustic graphene plasmon mode. *Opt. Express* **2023**, *31*, 482723. [CrossRef]
19. Kotov, O.V.; Lozovik, Y.E. Dielectric response and novel electromagnetic modes in three-dimensional Dirac semimetal films. *Phys. Rev. B* **2016**, *93*, 235417. [CrossRef]
20. Chen, Z.Y.; Cheng, S.B.; Zhang, H.F.; Yi, Z.; Tang, B.; Chen, J.; Zhang, J.G.; Tang, C.J. Ultra wideband absorption absorber based on Dirac semimetallic and graphene metamaterials. *Phys. Lett. A* **2024**, *517*, 129675. [CrossRef]
21. Cheng, S.B.; Li, W.X.; Zhang, H.F.; Akhtar, M.N.; Yi, Z.; Zeng, Q.D.; Ma, C.; Sun, T.Y.; Wu, P.H.; Ahmad, S. High sensitivity five band tunable metamaterial absorption device based on block like Dirac semimetals. *Opt. Commun.* **2024**, *569*, 130816. [CrossRef]
22. Zeng, Z.L.; Liu, H.F.; Zhang, H.F.; Cheng, S.B.; Yi, Y.G.; Yi, Z.; Wang, J.Q.; Zhang, J.G. Tunable ultra-sensitive four-band terahertz sensors based on Dirac semimetals. *Photonics Nanostruct. Fundam. Appl.* **2025**, *63*, 101347. [CrossRef]
23. Hu, B.; Huang, M.; Cai, C.; Yang, L. A Triple-Tunable Dual-Band Metamaterial Absorber Based on Dirac Semimetal and InSb. *Photonics* **2024**, *11*, 1039. [CrossRef]
24. Qi, L.; Liu, C.; Shah, S.M.A. A broad dual-band switchable graphene-based terahertz metamaterial absorber. *Carbon* **2019**, *153*, 179–188. [CrossRef]
25. Li, B.X.; Zeng, L.L.; Wen, R.Q.; Zhang, X.J. Dynamic Regulation of Multiple Fano Resonances Based on Liquid Crystal. *IEEE Photonics J.* **2023**, *15*, 2200506. [CrossRef]
26. Hu, J.Y.; Tan, C.X.; Bai, W.D.; Li, Y.M.; Lin, Q.; Wang, L.L. Dielectric nanocavity-coupled surface lattice resonances for high-efficiency plasmonic sensing. *J. Phys. D Appl. Phys.* **2022**, *55*, 075105. [CrossRef]
27. Zhang, H.; Feng, L.; Wang, F.Y.; Liu, M.Z.; Zhang, Y.Y.; Zhu, J.; Lu, Y.; Xu, T. Janus aramid nanofiber aerogel incorporating plasmonic nanoparticles for high-efficiency interfacial solar steam generation. *Opto-Electron. Adv.* **2023**, *6*, 220061. [CrossRef]
28. Tan, Z.Q.; Lin, Q.; Du, W.J.; Wang, L.L.; Liu, G.D. Simultaneously enhance electric and magnetic Purcell factor by strong coupling between toroidal dipole quasi-BIC and electric dipole. *J. Appl. Phys.* **2025**, *137*, 033103. [CrossRef]
29. Sun, J.; Huang, X.; Liu, Y.; Zhang, K.; Yan, Y.; Liu, Y.; Yan, X. Enhanced microwave absorption performance originated from interface and unrivaled impedance matching of SiO_2/carbon fiber. *Appl. Surf. Sci.* **2023**, *623*, 157029. [CrossRef]
30. Sang, T.; Qi, H.; Wang, X.; Yin, X.; Li, G.; Niu, X.; Ma, B.; Jiao, H. Ultrabroadband Absorption Enhancement via Hybridization of Localized and Propagating Surface Plasmons. *Nanomaterials* **2020**, *10*, 1625. [CrossRef]
31. Wang, H.Y.; Ma, R.; Liu, G.D.; Wang, L.L.; Lin, Q. Optical force conversion and conveyor belt effect with coupled graphene plasmon waveguide modes. *Opt. Express* **2023**, *31*, 32422. [CrossRef] [PubMed]
32. Li, B.X.; Liu, M.L.; Wen, R.Q.; Wei, Y.; Zeng, L.L.; Deng, C.S. Dynamic control of Fano-like interference in the graphene periodic structure. *J. Phys. D Appl. Phys.* **2023**, *56*, 115104. [CrossRef]
33. Jo, Y.; Park, H.; Yoon, H.; Kim, I. Advanced biological imaging techniques based on metasurfaces. *Opto-Electron. Adv.* **2024**, *7*, 240122. [CrossRef]
34. Li, Z.T.; Li, X.; Liu, G.D.; Wang, L.L.; Lin, Q. Analytical investigation of unidirectional reflectionless phenomenon near the exceptional points in graphene plasmonic system. *Opt. Express* **2023**, *31*, 30458. [CrossRef]
35. Ye, Y.; Pan, J.; Chen, W.; Zhang, H.; Wang, R. Tunable Nonlinear Optical Bistability Based on the Fabry–Perot Cavity Composed of Dirac Semimetal and Two Symmetric Photonic Crystals. *Coatings* **2024**, *14*, 705. [CrossRef]
36. He, M.Y.; Wang, Q.Q.; Zhang, H.; Xiong, J.; Liu, X.P.; Wang, J.Q. Analog electromagnetic induced transparency of T-type Si-based metamaterial and its applications. *Phys. Scr.* **2024**, *99*, 035506. [CrossRef]
37. Sukprasert, N.; Rakrong, P.; Saipaopan, C.; Choopan, W.; Liewrian, W. Asymmetric Tilt-Induced Quantum Beating of Conductance Oscillation in Magnetically Modulated Dirac Matter Systems. *Nanomaterials* **2024**, *14*, 811. [CrossRef]
38. Wu, X.; Guo, Y.; Long, X.; Wang, Q. Nonlinear Optical Bistability Based on Surface Plasmons with Nonlinear Dirac Semimetal Substrate. *Coatings* **2024**, *14*, 394. [CrossRef]
39. Ren, M.; Ji, C.; Tang, X.; Tian, H.; Jiang, L.; Dai, X.; Wu, X.; Xiang, Y. Sensitivity-Tunable Terahertz Liquid/Gas Biosensor Based on Surface Plasmon Resonance with Dirac Semimetal. *Sensors* **2023**, *23*, 5520. [CrossRef]
40. Luo, M.H.; Hu, J.Y.; Li, Y.M.; Bai, W.D.; Zhang, R.L.; Lin, Q.; Wang, L.L. Anapole-assisted ultra-narrow-band lattice resonance in slotted silicon nanodisk arrays. *J. Phys. D Appl. Phys.* **2023**, *56*, 375102. [CrossRef]
41. Wang, X.Y.; Lin, Q.; Wang, L.L.; Liu, G.D. Dynamic control of polarization conversion based on borophene nanostructures in optical communication bands. *Phys. Scr.* **2024**, *99*, 085531. [CrossRef]

42. Yang, J.P.; Tang, A.; Lian, B.W.; Xiong, Z.J.; Ma, Z.B.; Gu, N.T. Optimal multi-spectrum polarization detection with full-Stokes in a single channel by using standard retarders. *Measurement* **2025**, *242*, 116052. [CrossRef]
43. Li, X.T.; Cai, X.D.; Liu, C.; Kim, Y.; Badloe, T.; Liu, H.; Rho, J.; Xiao, S. Cascaded metasurfaces enabling adaptive aberration corrections for focus scanning. *Opto-Electron. Adv.* **2024**, *7*, 240085. [CrossRef]
44. Li, W.X.; Cheng, S.B.; Yi, Z.; Zhang, H.F.; Song, Q.J.; Hao, Z.Q.; Sun, T.Y.; Wu, P.H.; Zeng, Q.D.; Raza, R. Advanced optical reinforcement materials based on three-dimensional four-way weaving structure and metasurface technology. *Appl. Phys. Lett.* **2025**, *126*, 033503. [CrossRef]
45. Zeng, L.L.; Li, B.X.; Wen, R.Q.; Zhang, X.J. Plasmonic Sensor Based on Multi Fano Resonance in Inverse T Shape Structure for Detection of CO2 Concentration. *IEEE Photonics J.* **2023**, *15*, 2201805. [CrossRef]
46. Gu, X.; Liu, X.; Yan, X.F.; Du, W.J.; Lin, Q.; Wang, L.L.; Liu, G.D. Polaritonic coherent perfect absorption based on self-hybridization of a quasi-bound state in the continuum and exciton. *Opt. Express* **2023**, *31*, 4691–4700. [CrossRef]
47. Huang, Z.; Liu, G.D.; Wang, L. Active modulation of quasi-bound state in the continuum based on bulk Dirac semimetals metamaterial. *Appl. Phys. Express* **2022**, *15*, 032006. [CrossRef]
48. Wang, Q.S.; Fang, Y.; Meng, Y.; Hao, H.; Li, X.; Pu, M.; Ma, X.; Luo, X. Vortex-field enhancement through high-threshold geometric metasurface. *Opto-Electron. Adv.* **2024**, *7*, 240112. [CrossRef]
49. Zhang, Y.X.; Lin, Q.; Yan, X.Q.; Wang, L.L.; Liu, G.D. Flat-band Friedrich-Wintgen bound states in the continuum based on borophene metamaterials. *Opt. Express* **2024**, *32*, 10669–10678. [CrossRef]
50. Li, W.; Cheng, S.; Zhang, H.; Yi, Z.; Tang, B.; Ma, C.; Wu, P.; Zeng, Q.; Raza, R. Multi-functional metasurface: Ultra-wideband/multi-band absorption switching by adjusting guided mode resonance and local surface plasmon resonance effects. *Commun. Theor. Phys.* **2024**, *76*, 065701. [CrossRef]
51. Hu, J.Y.; Bai, W.D.; Tan, C.X.; Li, Y.M.; Lin, Q.; Wang, L.L. Highly electric field enhancement induced by anapole modes coupling in the hybrid dielectric-metal nanoantenna. *Opt. Commun.* **2022**, *511*, 127987. [CrossRef]
52. Jing, Z.; Li, S.L.; Ouyang, S.Y.; Lu, J.J.; Wang, Y.K.; Huang, L.J.; Li, L.; Sang, T. Observation of the generalized Kerker effect mediated by quasi-bound states in the continuum. *Nano Lett.* **2025**, *25*, 522–528. [CrossRef] [PubMed]
53. Li, W.; Yi, Y.; Yang, H.; Cheng, S.; Yang, W.X.; Zhang, H.; Yi, Z.; Yi, Y.; Li, H. Active Tunable Terahertz Band-width Absorber Based on single layer Graphene. *Commun. Theor. Phys.* **2023**, *75*, 045503. [CrossRef]
54. Yan, X.F.; Lin, Q.; Wang, L.L.; Liu, G.D. Tunable strong plasmon–exciton coupling based modulator employing borophene and deep subwavelength perovskite grating. *J. Phys. D Appl. Phys.* **2023**, *56*, 435106. [CrossRef]
55. Mao, Y.; Zhang, H.; Xiong, J.; Liu, X.P.; Wang, Q.Q.; Wang, J.Q. Controlling of spontaneous emission of quantum dots based on hyperbolic metamaterials. *J. Phys. D Appl. Phys.* **2024**, *57*, 255111. [CrossRef]
56. Wang, J.Q.; Sun, J.Y.; Sun, S.; Zhang, H.; Wang, Q.Q.; Yang, J.Y.; Mei, Y.W. Numerical simulation of electromagnetically induced transparency in composite metamaterial. *Phys. Scr.* **2025**, *100*, 025512. [CrossRef]
57. Tang, C.J.; Nie, Q.M.; Cai, P.G.; Liu, F.X.; Gu, P.; Yan, Z.D.; Huang, Z.; Zhu, M.W. Ultra-broadband near-infrared absorption enhancement of monolayer graphene by multiple-resonator approach. *Diam. Relat. Mater.* **2024**, *141*, 110607. [CrossRef]
58. Yan, X.; Lin, Q.; Wang, L.; Liu, G.D. Active absorption modulation by employing strong coupling between magnetic plasmons and borophene surface plasmons in the telecommunication band. *J. Appl. Phys.* **2022**, *132*, 063101. [CrossRef]
59. Sang, T.; Mi, Q.; Yang, C.Y.; Zhang, X.H.; Wang, Y.K.; Ren, Y.Z.; Xu, T. Achieving asymmetry parameter-insensitive resonant modes through relative shift-induced quasi-bound states in the continuum. *Nanophotonics* **2024**, *13*, 369–1377. [CrossRef]
60. Yang, C.; Lin, Q.; Du, W.J.; Wang, L.L.; Liu, G.D. Bi-tunable absorber based on borophene and VO2 in the optical telecommunication band. *J. Opt. Soc. Am. B* **2022**, *39*, 2969–2974. [CrossRef]
61. Xiong, H.; Yang, Q.; Huang, Y.Z.; Deng, J.H. High-Efficiency Microwave Wireless Power Transmission via Reflective Phase Gradient Metasurfaces and Surface Wave Aggregation. *ACS Appl. Mater. Interfaces* **2024**, *16*, 60189–60196. [CrossRef] [PubMed]
62. Sun, Y.B.; Yang, L.L.; Wang, J.X.; Cheng, Y.Z.; Luo, H.; Chen, F.; Li, X.C. Microstrip antenna loaded with focusing metasurface for high-gain dual-polarization and bidirectional radiation. *J. Appl. Phys.* **2025**, *137*, 013104. [CrossRef]
63. Lu, J.L.; Zhang, X.Q.; Yan, X.; Liu, D.D.; Wang, L.X.; Wang, Y.S.; Huang, X.X.; Wen, G.W. Sodium citrate-induced generation of multi-interfacial embroidered spherical SnO2 for augmented electromagnetic wave absorption. *J. Mater. Chem. C* **2023**, *11*, 4855–4866. [CrossRef]
64. Ding, C.Y.; Fu, H.; Wu, T.; Li, Y.J.; Wu, S.S.; Ren, X.Z.; Gao, Z.L.; Guo, K.; Xia, L.; Wen, G.W.; et al. Wave-transparent LAS enabling superior bandwidth electromagnetic wave absorption of a 2D pitaya carbon slice. *J. Mater. Chem. A* **2022**, *10*, 17603–17613. [CrossRef]
65. Zhu, J.; Wu, Z.B.; Fu, D.L.; Lu, G.J.; Hu, H.J. Novel optical switch and four-to-one data selector utilizing an MIM waveguide structure based on surface plasmon polaritons. *Measurement* **2025**, *241*, 115681. [CrossRef]
66. Xiao, Y.F.; Ma, C.; Sun, T.Y.; Song, Q.J.; Bian, L.; Yi, Z.; Hao, Z.Q.; Tang, C.J.; Wu, P.H.; Zeng, Q.D. Investigation of a high-performance solar absorber and thermal emitter based on Ti and InAs. *J. Mater. Chem. A* **2024**, *12*, 29145. [CrossRef]

67. Cao, A.; Chen, N.; Zhu, W.; Chen, Z. Graphene-Based Dual-Band Metasurface Absorber with High Frequency Ratio. *Nanomaterials* **2024**, *14*, 1522. [CrossRef]
68. Zhu, J.; Xiong, J.Y. Logic operation and all-optical switch characteristics of graphene surface plasmons. *Opt. Express* **2023**, *31*, 36677. [CrossRef]
69. Yang, C.; Guo, C.M.; Xu, J.; Zhang, H.F. Device Design for Multitask Graphene Electromagnetic Detection Based on Second Harmonic Generation. *IEEE Trans. Microw. Theory Tech.* **2024**, *72*, 4174–4182. [CrossRef]

molecules

MDPI

Article

Two-Dimensional Carbon Film-Supported ZnS Nanocomposites Obtained from Thermal Decomposition of Organic Zinc Salts and Sulfidation Reactions for Lithium Storage

Denghu Wei [1,*], Ting Wang [1], Ranran Jiao [2], Lixue Qu [1] and Suyuan Zeng [2,*]

[1] School of Materials Science and Engineering, Liaocheng University, Liaocheng 252059, China; wangtinglcu@163.com (T.W.); 19861210661@163.com (L.Q.)
[2] School of Chemistry and Chemical Engineering, Liaocheng University, Liaocheng 252059, China; jrr1175@mail.ustc.edu.cn
* Correspondence: dhweilcu@163.com (D.W.); drsyzeng@163.com (S.Z.)

Abstract: This article reports a general method for carbon-composited ZnS nanoparticles. By mixing thiourea with an appropriate amount of citric acid zinc, glycine zinc, lactate zinc, and gluconate zinc, respectively, and then heating at 700 °C under a nitrogen atmosphere for 4 h, four types of target product ZnS/C were obtained. Thiourea and organic zinc salts serve as reactants, providing zinc, sulfur, and carbon sources. During the thermal decomposition process, sulfidation and carbonization can be completed simultaneously. As an anode material for lithium-ion batteries, all four products exhibit excellent lithium storage performance. The two-dimensional carbon film can, on the one hand, enhance the conductivity of the material, and on the other hand, act as a carrier for ZnS particles, effectively cushioning the volume deformation of ZnS during the lithiation process.

Keywords: ZnS/C; carbon film; one-step reaction; lithium storage; general method

1. Introduction

Compared with metal oxides, metal sulfides generally have better conductivity, and the band gap energy of M-S bonds is smaller, which is more easily broken in electrochemical reactions. Therefore, metal sulfides as anode materials for lithium-ion batteries have better electrochemical reactivity [1–8]. Among them, zinc sulfide (ZnS) has attracted widespread attention from researchers (not only in the field of lithium-ion batteries [9–16], but also in the fields of sodium-ion [17–20], potassium-ion [21], lithium-sulfur batteries [22–24], and supercapacitors [25,26]) due to its abundant reserves, environmental friendliness, and high capacity. ZnS stores lithium based on conversion and alloying reaction mechanisms, which can cause significant volume expansion and contraction during the cycling process. The stress generated by this change can lead to the pulverization and collapse of the electrode structure, resulting in rapid capacity decay. Nanosizing and carbon composites are effective methods to alleviate this problem [9–13]. When the size of the electrode material is reduced to the nanoscale, the specific surface area increases, the contact area between the electrode and the electrolyte increases, and the diffusion distance of lithium ions in the electrode material is significantly reduced. Moreover, nanosizing can reduce the stress generated during the intercalation and deintercalation process of lithium ions, thereby improving the lithium storage performance of the material. In addition, the composite of zinc sulfide and carbon can improve the conductivity of the electrode material and alleviate the volume expansion and contraction during the cycling process (because amorphous carbon has a certain flexibility), thereby improving the material's cycle stability.

Based on the above analysis, we selected thiourea (primarily providing a sulfur source, and also possibly providing a portion of the carbon source) and lactate zinc (zinc source, carbon source) as reactants and carried out thermal decomposition and sulfidation (synchronously completed) under a nitrogen atmosphere to prepare carbon composite ZnS nanostructures. This composite acts as an anode material for lithium-ion batteries and shows high capacity and cycle stability. We have expanded this method to prepare three other types of carbon composite ZnS nanomaterials, and all have been tested for lithium storage performance, with good results.

2. Results and Discussion

Figure 1 is a schematic diagram of the synthesis of ZnS/C. Organic zinc salts served as zinc and carbon sources; thiourea mainly served as a sulfur source and may also have provided some carbon source; sodium chloride acted as a heat transfer medium, a load body for the reactants, and a template for pore formation. During the heat treatment under a nitrogen atmosphere, carbonization and sulfidation could be completed synchronously, resulting in the target product. After pyrolysis, the black product was washed with diluted hydrochloric acid to remove impurities such as sodium chloride, resulting in various ZnS/C products. Figure 2 is the XRD pattern of ZnS/C. It can be seen from the figure that all the characteristic peaks correspond to the diffraction peaks of hexagonal ZnS crystals (PDF# 79-2204). The diffraction peak of carbon is not obvious, indicating that the carbon produced is amorphous. Figure 3 and Figures S1–S4 are the SEM morphologies of the products. It can be clearly seen from the figure that in the ZnS/C-3 sample, ZnS and carbon are the best composite, that is, ZnS nanoparticles (about 100 nanometers) are coated in the carbon film. The image formed by the transmission electron microscope also confirms this situation, as shown in Figure 4a–c. In the other three types of ZnS/C samples, some ZnS particles are hidden in the carbon skeleton, and some particles are attached to the surface of the carbon layer. The overall composite effect is not as good as that of ZnS/C-3. The subsequent lithium storage performance test also confirmed this, that is, the performance of ZnS/C-3 is superior.

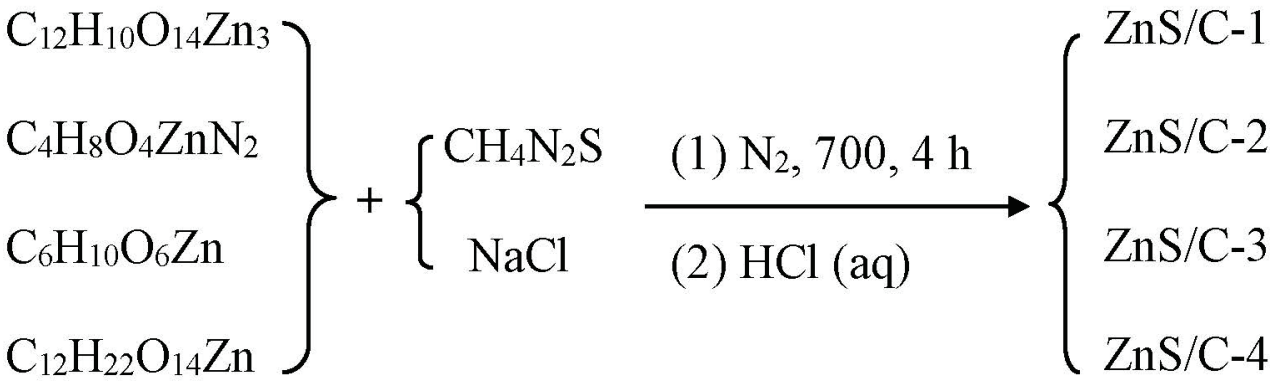

Figure 1. Synthetic route to prepare Zn/C samples.

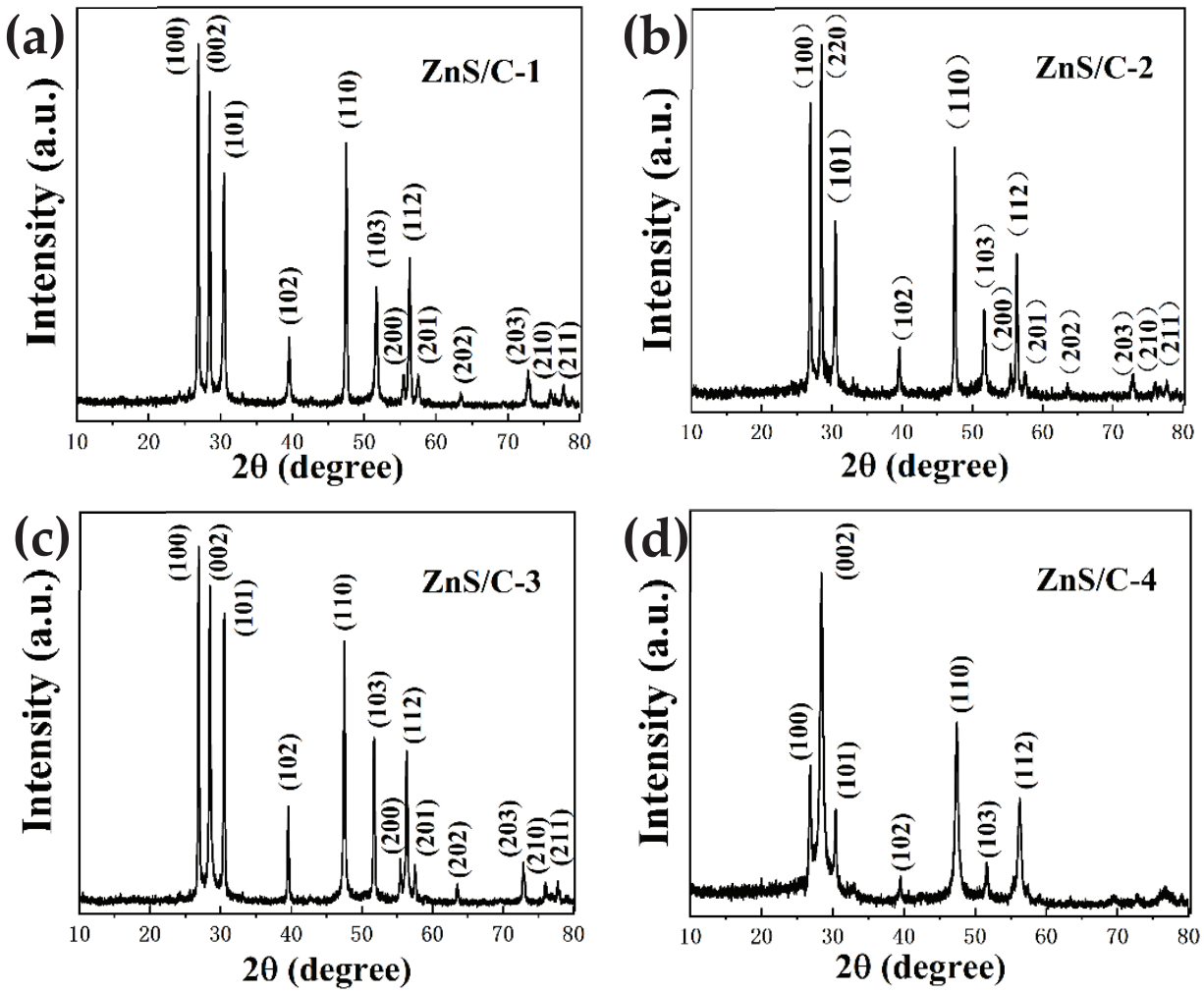

Figure 2. XRD of the samples: (**a**) ZnS/C-1; (**b**) ZnS/C-2; (**c**) ZnS/C-3; and (**d**) ZnS/C-4.

Figure 4d–d3 show the elemental distribution mapping of ZnS/C-3. The results show that the distribution of various elements in the sample is relatively uniform. Figure 4e and Figure S5 are HRTEM images, from which more crystallographic information about the ZnS/C-3 sample can be obtained. The measured interplanar spacings in the figure are 0.333 nm and 0.294 nm, corresponding to the (100) and (101) planes of hexagonal ZnS crystals, respectively. The electron diffraction results (Figure 4f) further confirm the crystal structure of ZnS/C-3. Figure 5 shows the EDS spectra and elemental distribution of the four types of ZnS/C samples. The results show that various elements are well distributed in their respective samples, appearing in their respective EDS spectra. To identify the carbon content in the ZnS/C products, we performed thermogravimetric analysis tests on the four samples (Figure 6). Under an air atmosphere, the product would undergo the following reaction:

$$ZnS/C + O_2 = ZnO + SO_2 + CO_x \quad (1)$$

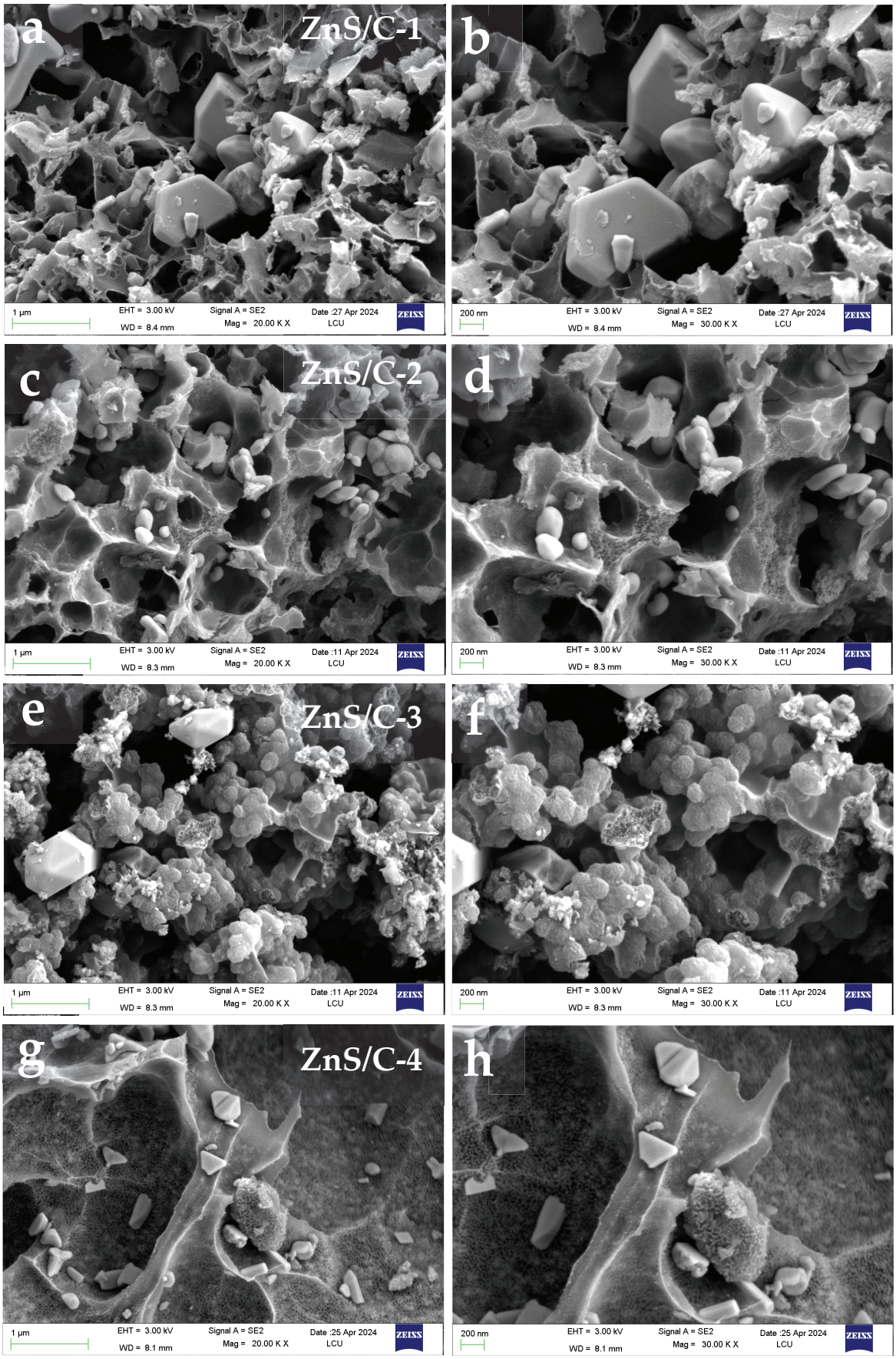

Figure 3. SEM images of the samples: (**a**,**b**) ZnS/C-1; (**c**,**d**) ZnS/C-2; (**e**,**f**) ZnS/C-3; and (**g**,**h**) ZnS/C-4.

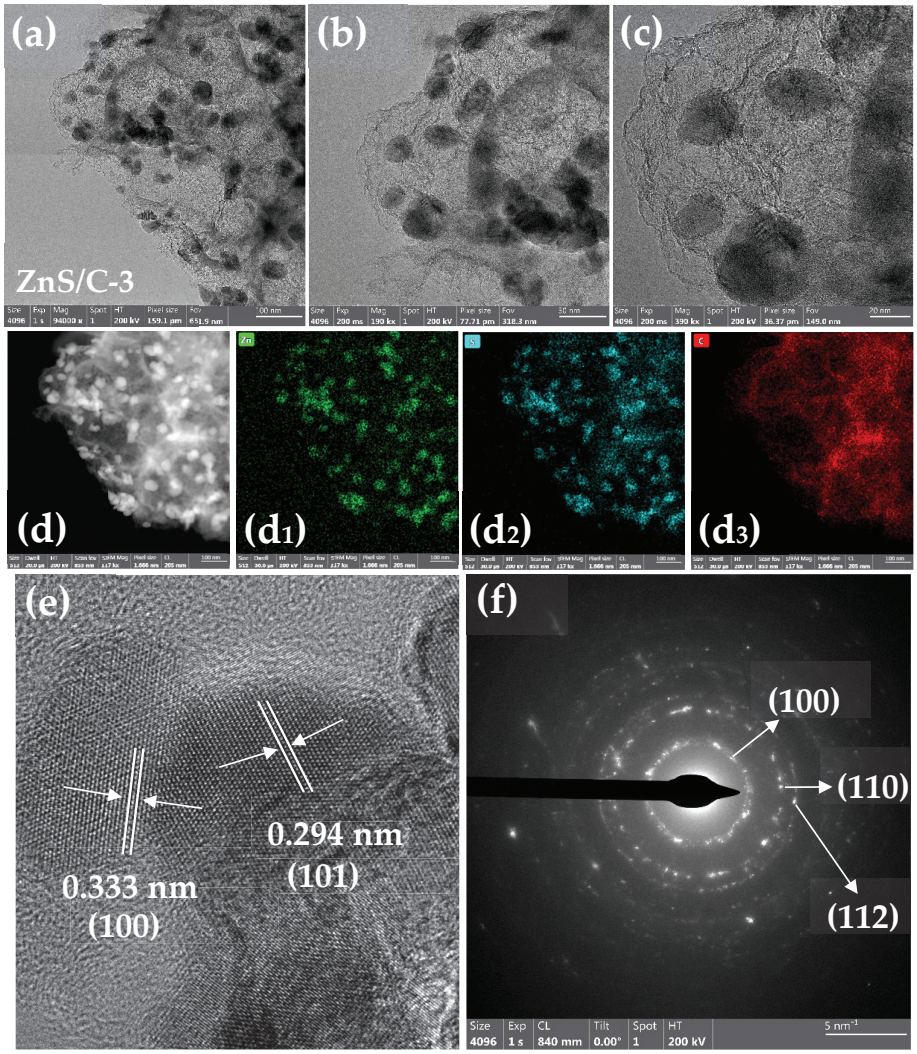

Figure 4. TEM images (**a**–**c**), EDS mapping (**d**–**d3**), HRTEM image (**e**), and electron diffraction (**f**) of the ZnS/C-3 sample.

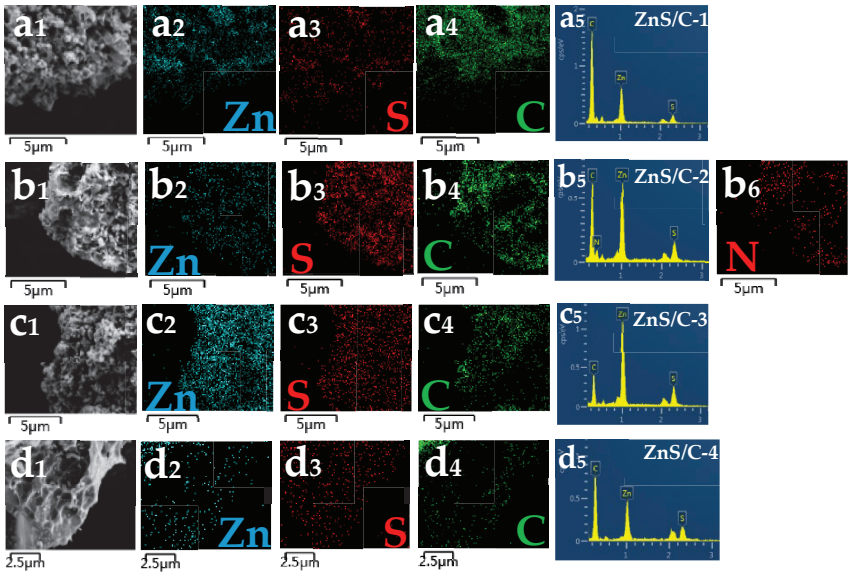

Figure 5. EDS spectra and mapping of the samples: (**a**$_1$–**a**$_5$) ZnS/C-1; (**b**$_1$–**b**$_6$) ZnS/C-2; (**c**$_1$–**c**$_5$) ZnS/C-3; and (**d**$_1$–**d**$_5$) ZnS/C-4.

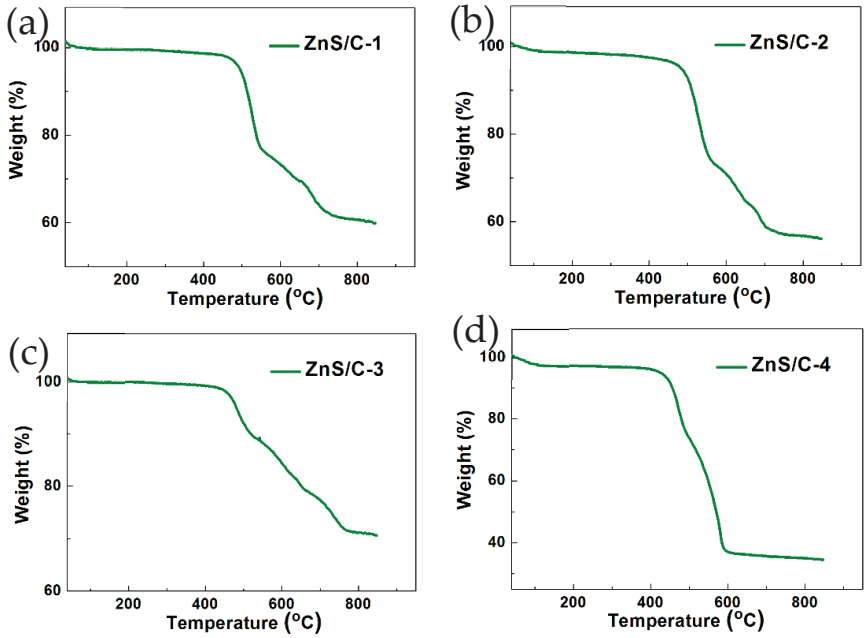

Figure 6. TG curves of the ZnS/C materials under air atmosphere: (**a**) ZnS/C-1; (**b**) ZnS/C-2; (**c**) ZnS/C-3; and (**d**) ZnS/C-4.

According to the reaction formula (1), the carbon content in each sample can be calculated, which is 27% (ZnS/C-1), 31.7% (ZnS/C-2), 13.8% (ZnS/C-3), and 55.6% (ZnS/C-4), respectively. The carbon content in sample No.4 (ZnS/C-4) is the highest because its reactant is gluconate zinc, and the molar ratio of carbon to zinc in the gluconate zinc is the largest, which is 12.

Figure 7a shows the first three CV curves of ZnS/C-3, with a voltage range of 0.01 to 3 V and a scan rate of 0.2 mV s^{-1}. During the first scan, a reduction peak is located near 0.4 V, corresponding to the conversion reaction of ZnS, generating Li_2S and elemental zinc [9–11]. The peak near 0.01 V corresponds to the alloying reaction of lithium with zinc, as well as the formation of the solid-state electrolyte interphase (SEI) film. In the initial anodic scan, the weak peaks between 0.2 and 0.7 V represent the delithiation process of the lithium-zinc alloy [10–12]. Several peaks between 1.2 and 3 volts are attributed to the transformation of zinc to zinc sulfide [11–14]. In the subsequent two CV curves, the position of the reduction peak shifts to the right due to the activation of the electrode after the first cycle. Figure 7b shows the first three charge–discharge curves of ZnS/C-3, with a current density of 0.2 A g^{-1} and a voltage range consistent with the CV test. The initial discharge capacity is 800 mAh g^{-1}, and the charge capacity is 546 mAh g^{-1}, with a corresponding initial Coulomb efficiency (CE) of 68%. The loss of capacity in the first cycle is mainly due to the formation of the SEI film, causing irreversible lithium ion extraction [1–9]. From the fourth cycle, the CE remains above 95%, indicating that after three activation cycles, the ZnS/C-3 electrode exhibits good reversibility. Figure 7c–e show the cycling performance test results of ZnS/C-3 at current densities of 0.2 A, 0.5 A, and 1 A g^{-1}, respectively. The results show that under the three different current densities, the capacity of the ZnS/C-3 electrode will go through a process of initial decline followed by a gradual increase. The initial capacity decay during cycling may be due to the insufficient contact between the particles inside ZnS and the electrolyte, which cannot fully demonstrate their lithium storage capacity. As the charge and discharge cycles continue, the battery capacity gradually increases, indicating that the internal particles of the electrode material are gradually activated and gradually exhibit lithium storage performance. Of course, the specific reasons for the capacity increase

during the cycle need further research to confirm. After cycling for 1000 cycles at a current density of 0.5 A g^{-1}, the ZnS/C-3 electrode can still maintain a discharge capacity of 749 mAh g^{-1}. The good lithium storage performance of ZnS/C-3 under different current densities is mainly due to the following: the ZnS particles are almost fully encapsulated in the carbon film during the formation process (Figure 3e,f and Figure 4), which can effectively prevent particle aggregation during the charge and discharge process; the carbon film with certain flexibility can buffer volume deformation; and although the ZnS particles will still have problems such as pulverization and aggregation during the cycle, the changed particles can still be attached to the carbon film, avoiding loss from the electrode. Compared with the literature reports, the ZnS/C-3 material shows certain improvements in terms of cycle numbers or capacity retention rate, as shown in Table S1. Moreover, the synthesis method is simple: by selecting an organic zinc salt that is homologous with carbon and reacting it with thiourea, the carbonization process and the formation of the zinc sulfide phase can be simultaneously achieved. This method is universal, and when other types of organic zinc sources are used, carbon composite zinc sulfide materials can still be obtained (ZnS/C-1, ZnS/C-2, and ZnS/C-4), and the lithium storage performance of the resulting materials is also quite excellent (Please refer to the section below).

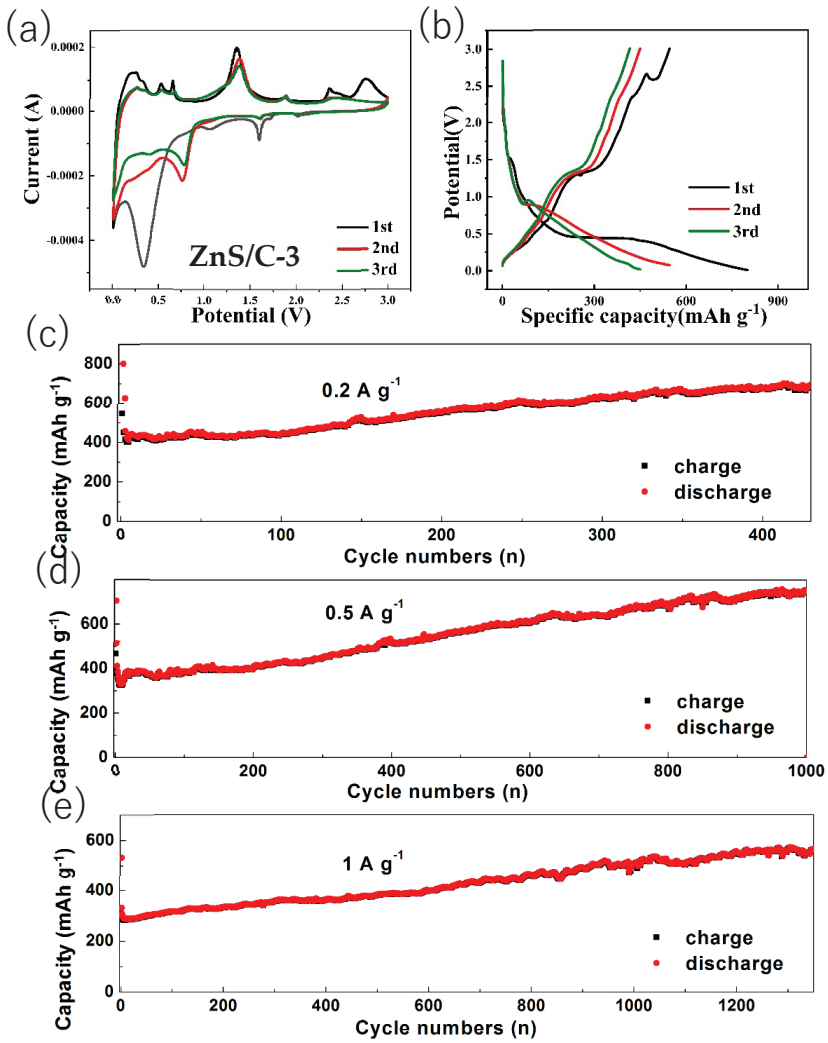

Figure 7. CV curves (**a**), charge–discharge profiles (**b**), and cycle performance (**c**–**e**) of the ZnS/C-3.

To further understand the excellent lithium storage performance of ZnS/C-3, we conducted additional characterizations on this product, such as Raman spectroscopy

(Figure 8a), specific surface area testing (Figure 8b), and X-ray photoelectron spectroscopy (XPS) analysis (Figure 8c–e). Raman spectroscopy is a very powerful tool to verify the presence of carbon in the composite and the degree of graphitization. As shown in Figure 8a, the I_G/I_D ratio based on the area under the D- and G-band was 1.83, implying that a portion of the carbon component in the ZnS/C-3 sample had been graphitized, which helped to enhance the electronic conductivity of the sample when used as an anode material for lithium storage [9]. Figure 8b shows the nitrogen adsorption–desorption isotherms and the BJH pore size distribution curve (the inset) of the ZnS/C-3 sample. The measured data indicate that the specific surface area of the sample is 54.541 m^2/g ($a_{s,\ BET}$), and the average diameter of pores is 10.85 nm (based on the BJH model analysis). This pore structure is beneficial for the electrode material to be fully wetted by the electrolyte, and it may also increase some active sites, thereby enhancing the lithium storage performance of the material [9,11]. Figure 8c shows the XPS spectrum of Zn 2p, with two peaks located at 1021.95 eV and 1044.95 eV, corresponding to Zn $2p_{3/2}$ and Zn $2p_{1/2}$, respectively, thereby confirming the presence of Zn ions (Zn^{2+}) [9]. It is worth noting that the binding energy values of these peaks are slightly higher than those of Zn ions in pure ZnS, indicating a strong interaction between ZnS particles and the carbon film (C-Zn-S-C), which facilitates electron transfer between ZnS particles and the carbon film [12,19]. Figure 8d shows two peaks at 161.6 eV and 162.8 eV, confirming the presence of sulfur ions (S^{2-}). Figure 8e presents the XPS spectrum of C 1s, further revealing the existence of C-S bonds (at 285.8 eV), which is consistent with Figure 8c.

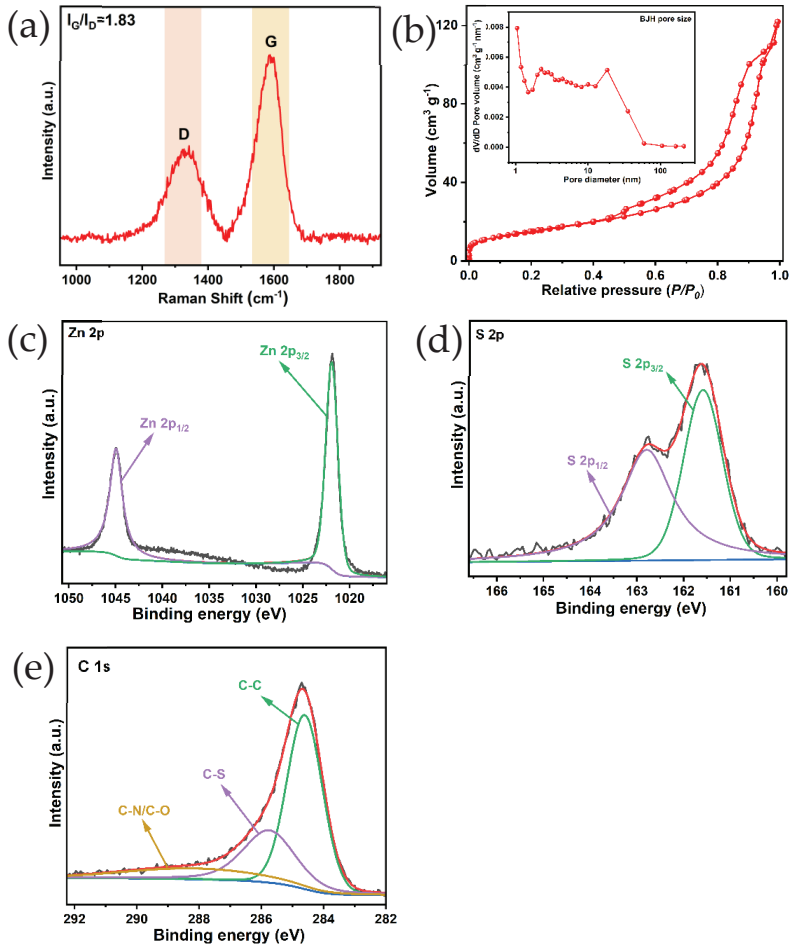

Figure 8. Raman spectrum (**a**), N_2 adsorption–desorption and pore size distribution diagrams (**b**) of ZnS/C-3. XPS spectra of Zn 2p (**c**), S 2p (**d**), and C 1s (**e**) of the ZnS/C-3 sample.

To understand the mechanism of charge storage in the ZnS/C-3 electrode, the electrochemical kinetic behavior was investigated via CV curves with different scan rates. Figure 9a shows the CV curves at different scan rates. It can be observed that the shapes of the CV curves are basically similar at different scan rates, and the peak current is directly proportional to the scan rate. With the increase in scan rate, the peak positions of the CV curves shift, indicating that the electrode material undergoes a certain degree of polarization [9,11,12]. Figure 9b shows the fitted curves of log(i) versus log(v). Calculations reveal that for the ZnS/C-3 electrode, the b values corresponding to the oxidation peak and reduction peak are 0.86 and 0.74, respectively (both values lie between 0.5 and (1)). This suggests that the electrochemical reactions of the electrode involve both diffusion-controlled behavior and capacitive behavior [9,11,12]. As the scan rate increases, the contribution of capacitance increases (Figure 9c,d), which is beneficial for the cycling stability of the electrode material [9,11,12]. This also explains the excellent lithium storage performance of ZnS/C-3 (Figure 7c–e).

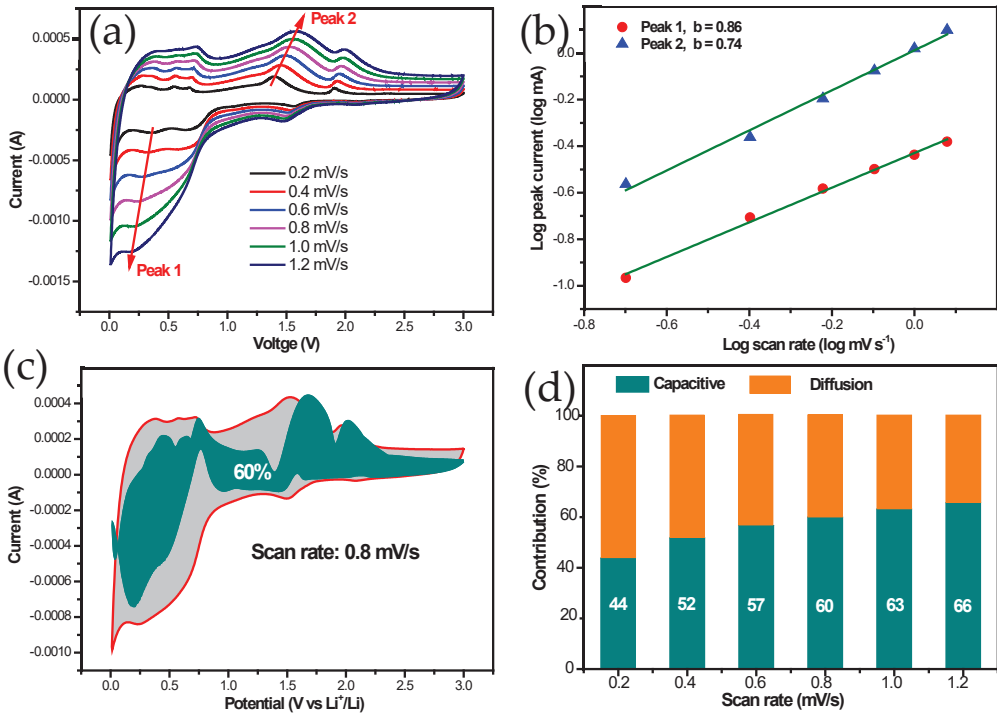

Figure 9. (**a**) CV curves at various scanning rates, (**b**) Linear relation between log (peak current) and log (scan rate), (**c**) surface capacitance contributions (dark cyan) at 0.8 mV s^{-1} and (**d**) the percentage of surface capacitance contributions at various scanning rates of the ZnS/C-3.

Although the composite situation of ZnS and carbon in the other three ZnS/C materials is not as ideal as ZnS/C-3, we also conducted lithium storage performance tests on them to verify the effectiveness of the presence of the carbon framework, and the results are shown in Figure 10. In the cycle tests, the capacity also went through a process of initial decline followed by a gradual increase (corresponding to the capacity retention rate shown in Figure 11), which is consistent with that of the ZnS/C-3. At a current density of 0.5 A g^{-1}, after cycling for hundreds or even a thousand times, the capacity could basically be maintained above 500 mAh g^{-1}. Due to the formation of the SEI film and the irreversible intercalation of lithium ions, the initial CE of the three materials was relatively low. After a few cycles, it quickly increased to above 90%. In the subsequent cycling process, the CE remained close to 100% (Figure 11), indicating that all three materials exhibited good electrochemical reversibility. This also confirms the effectiveness of this general synthesis

method for ZnS/C composites (used as anode materials for lithium storage) from different organic zinc salts.

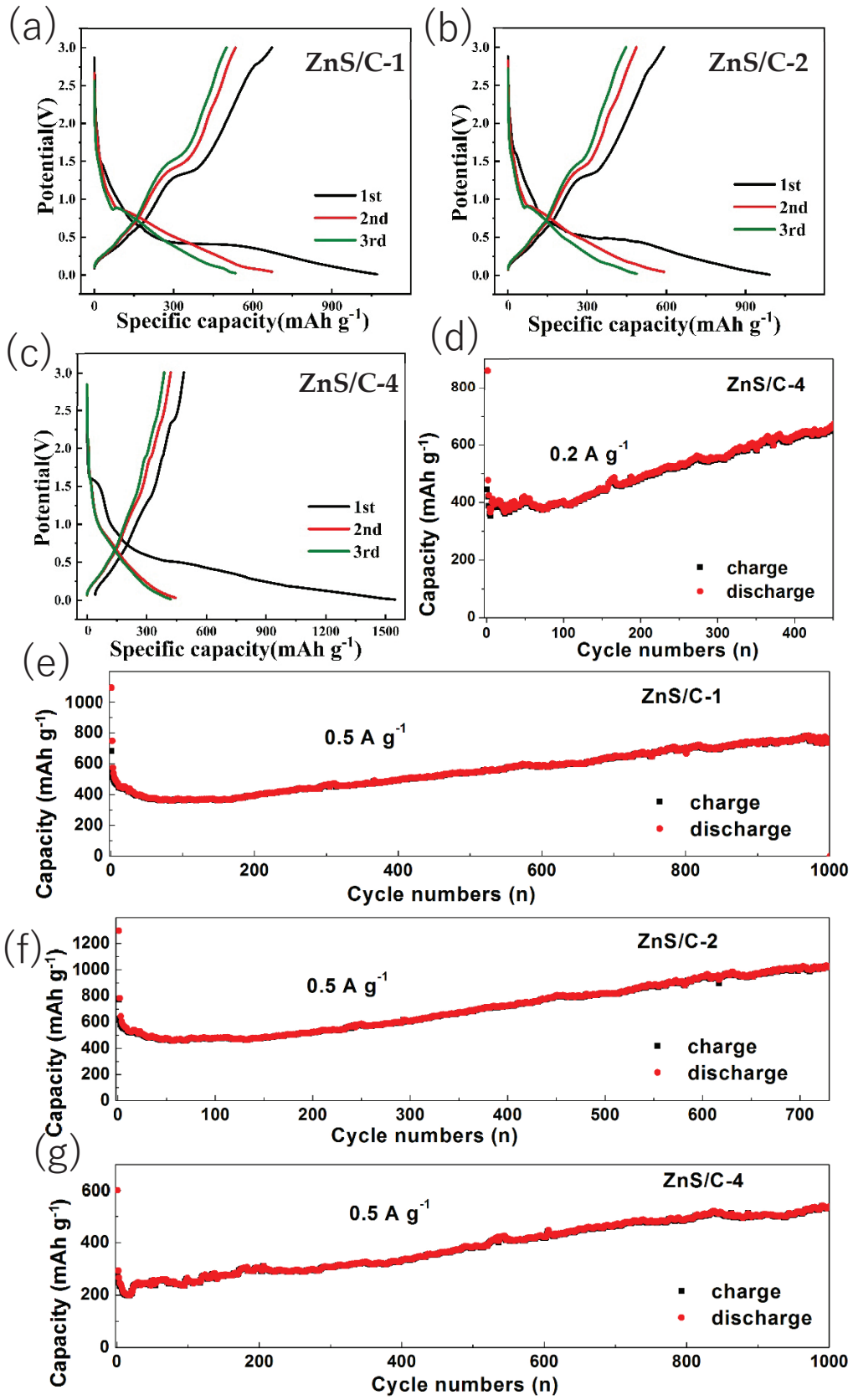

Figure 10. Charge–discharge profiles and cycle performances of the ZnS/C anode materials: (**a**,**e**) ZnS/C-1; (**b**,**f**) ZnS/C-2; (**c**,**d**,**g**) ZnS/C-4.

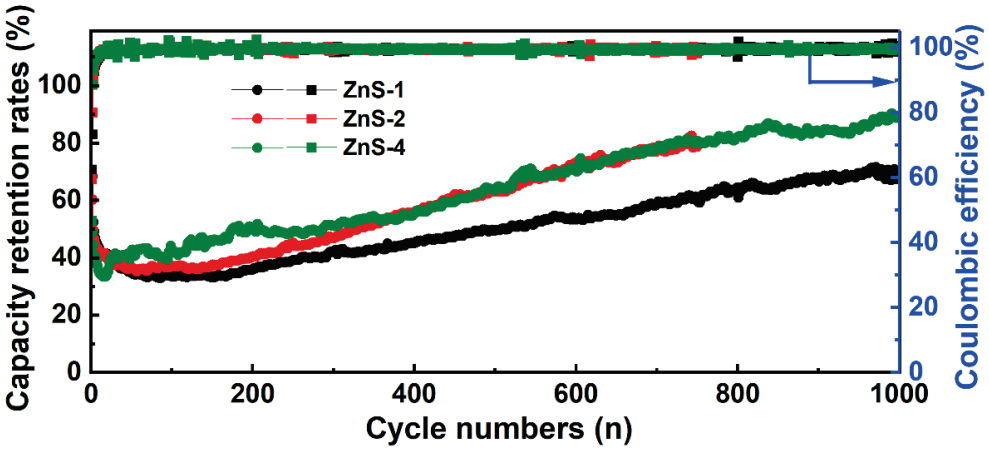

Figure 11. Capacity retention rates and Coulomb efficiency over multiple cycles for the other three composites (ZnS/C-1, ZnS/C-2, and ZnS/C-4).

3. Experimental Section

Synthesis of ZnS/C-1: In a ball milling jar (50 mL), 2 g of citric acid zinc (Macklin Reagents, Shanghai, China). All the reagents mentioned below are from this manufacturer), 0.955 g of thiourea, 3 g of sodium chloride, and 10 mL of ethanol were added, ball milled for 8 h (200 revolutions per minute), dried, and then transferred to a corundum boat. Then, the white powder was heated at 700 °C under a nitrogen atmosphere for 4 h (with a heating rate of 5 degrees per minute) and naturally cooled down to room temperature to obtain a black powder. The product was dispersed in 50 mL of diluted hydrochloric acid (0.1 mol L^{-1}), stirred for two hours, vacuum filtered, washed with water and ethanol several times, and dried.

Synthesis of ZnS/C-2: The preparation method was the same as that of the ZnS/C-1, with the materials added being 2.135 g of glycine zinc, 0.914 g of thiourea, 3 g of sodium chloride, and 10 mL of ethanol.

Preparation of ZnS/C-3: Here, 2.435 g of lactate zinc, 0.914 g of thiourea, 3.4 g of sodium chloride, and 10 mL of ethanol were mixed, ball milled, and dried. Then, the white powder was pressed into several circular columns with a diameter of 15 mm (4–6 MPa for 20 s) and then heated to 700 °C for 4 h with the heating rate of 5 °C min^{-1} under N_2 atmosphere. The subsequent treatment process was the same as that of ZnS/C-1.

Preparation of ZnS/C-4: Then, 2.5 g of gluconate zinc, 0.5 g of thiourea, and 3 g of sodium chloride were mixed, ball milled, and dried. The subsequent treatment process was the same as that of ZnS/C-3. The amount of hydrochloric acid used was changed to 25 mL.

3.1. Characterization

The phase analysis of the product was completed by X-ray diffraction (XRD) (D8 ADVANCE diffractometer, Bruker Co., Berlin, Germany). The morphology was observed by scanning electron microscopy (SEM) (Merlin Compact, Carl Zeiss AG, Oberkochen, Germany) and transmission electron microscopy (TEM) (Thermo Fischer, Talos F200x, Waltham, MA, USA). Electron diffraction, lattice, energy-dispersive spectroscopy, and element distribution were completed using a scanning electron microscope and a high-resolution transmission electron microscope (HRTEM) (Thermo Fischer, Talos F200x, Waltham, MA, USA) with an energy spectrometer attachment. The carbon content was determined by thermogravimetric analysis. Raman spectroscopy, specific surface area testing, and X-ray photoelectron spectroscopy (XPS) analysis were also performed.

3.2. Lithium Storage Performance Test

According to the ratio of 75:10:15, the prepared samples (ZnS/C), acetylene black, and PVDF (PVDF dissolved in NMP, prepared into a 3% mass concentration PVDF solution) were weighed, that is, 0.15 g of the prepared sample, 0.02 g of acetylene black, and 1 g of PVDF solution. The weighed materials were added to a mortar and ground for 40 min. If the paste was found to be sticky, an appropriate amount of NMP solvent could be added, and the materials could be ground for another 10 min. The obtained paste was applied to a copper foil. A 75-micron-thickness caliper was used. Then, the copper foil was transferred to a vacuum drying box, heated at 60 degrees for 8 h, and naturally cooled, and the copper foil was taken out and cut into a circle with a diameter of 12 mm. The load of the active material was about 0.7~1.0 mg cm^{-2}. The circle was placed in a glove box, with a metal lithium sheet as the counter electrode, Celgard 2400 film as the separator, and 1 mol L^{-1} $LiPF_6$ [in the mixture of EC:DEC (1:1 Vol% with 5% FEC)] as the electrolyte, to assemble a button battery. The assembled battery was left to stand overnight to ensure that the electrolyte could fully soak the electrode material and separator. Cyclic voltammetry (CV) was performed at a scan rate of 0.2 mV s^{-1} from 0.001 V to 3.0 V using a coin cell. Charge–discharge tests were performed between 0.01 and 3.0 V using a LANDCT2001A battery tester.

4. Conclusions

We used commercial thiourea and zinc lactate as raw materials and obtained a ZnS/C composite by heating at a nitrogen atmosphere for 4 h. At high temperature, the thermal decomposition process and the sulfidation process can be completed simultaneously, with ZnS nanoparticles being well encapsulated within the carbon framework. As an anode material for lithium-ion batteries, ZnS/C exhibits good reversible capacity and cycling stability. We expanded this synthesis method to obtain three other types of ZnS/C materials and tested their lithium storage performance, achieving satisfactory results. Furthermore, these four types of ZnS/C materials may also find applications in other electrochemical fields.

Supplementary Materials: The following supporting information can be downloaded at: https://www.mdpi.com/article/10.3390/molecules30040893/s1, Figure S1. SEM images of ZnS/C-1. Figure S2. SEM images of ZnS/C-2. Figure S3. SEM images of ZnS/C-3. Figure S4. SEM images of ZnS/C-4. Figure S5. HRTEM image of ZnS/C-3. Table S1. comparison between the ZnS/C-3 and reported ZnS/C-based materials.

Author Contributions: D.W.: (conceptualization; funding acquisition; project administration; resources; supervision; writing—original draft); T.W.: (data curation; investigation; methodology); R.J.: (methodology; validation; visualization); L.Q.: (investigation; methodology; software); S.Z.: (investigation; resources; writing—original draft). All authors have read and agreed to the published version of the manuscript.

Funding: This work was supported by the Natural Science Foundation of Shandong Province (ZR2017QB017).

Institutional Review Board Statement: Not applicable.

Informed Consent Statement: Not applicable.

Data Availability Statement: The original contributions presented in this study are included in the article/Supplementary Materials. Further inquiries can be directed to the corresponding author(s).

Conflicts of Interest: The authors declare that they have no known competing financial interests or personal relationships that could have appeared to influence the work reported in this paper. This manuscript is original and is not being considered for publication elsewhere. We hope this paper is suitable for *Molecules*. Thank you very much for your attention and consideration.

References

1. Zhang, X.J.; Xie, J.; Lu, Z.J.; Liu, X.H.; Tang, Y.K.; Wang, Y.; Hu, J.D.; Cao, Y.L. Engineering sulfur defective Bi_2S_3@C with remarkably enhanced electrochemical kinetics of lithium-ion batteries. *J. Colloid Interface Sci.* **2024**, *667*, 385–392. [CrossRef] [PubMed]
2. Jang, J.H.; Lee, M.; Park, S.; Oh, J.M.; Park, J.K.; Paek, S.M. Long-term cycling stability of a SnS_2-based covalent organic nanosheet anode for lithium-ion batteries. *J. Mater. Chem. A* **2023**, *11*, 13320–13330. [CrossRef]
3. Min, W.L.; Chen, X.H.; Huang, S.H.; Liao, Y.L.; Liang, Z.Y.; Lei, Y.; Xu, J.T. High performance lithium ion battery cathode based reduced holey graphene oxides from spent lithium ion batteries. *Carbon* **2023**, *210*, 118038. [CrossRef]
4. Liao, S.Y.; Chen, J.; Cui, S.F.; Shang, J.Q.; Li, Y.Z.; Cheng, W.X.; Liu, Y.D.; Cui, T.T.; Shu, X.G.; Min, Y.G. CoS_2 enhanced SnO_2@rGO heterostructure quantum dots for advanced lithium-ion battery anode. *J. Power Sources* **2023**, *553*, 232265. [CrossRef]
5. Marriam, I.; Tebyetekerwa, M.; Chen, H.; Chathuranga, H.; Motta, N.; Motta, J.A.; He, Z.J.; Zheng, J.C.; Zheng, A.J.; Yan, C. Few-layer MoS_2 nanosheets with and without silicon nanoparticles as anodes for lithium-ion batteries. *J. Mater. Chem. A* **2023**, *11*, 2670. [CrossRef]
6. Xie, M.; Lv, Z.R.; Zhao, W.; Fang, Y.Q.; Huang, J.; Huang, F.Q. Intercalated hydrates stabilize bulky MoS_2 anode for Lithium-ion battery. *Chem. Eng. J.* **2023**, *470*, 144282. [CrossRef]
7. Li, X.F.; Wang, R.; Wu, Q.; Yu, Y.H.; Gao, T.L.; Yao, T.; Wang, X.J.; Han, J.C.; Song, B. Synergistically designed dual interfaces to enhance the electrochemical performance of MoO_2/MoS_2 in Na- and Li-ion batteries. *Small* **2023**, *19*, 2206940. [CrossRef]
8. Li, Z.W.; Yuan, F.; Han, M.S.; Yu, J. Atomic-scale laminated structure of O-doped WS_2 and carbon layers with highly enhanced ion transfer for fast-charging lithium-ion batteries. *Small* **2022**, *18*, 2202495. [CrossRef]
9. Zhai, L.F.; Yu, J.M.; Yang, T.; Li, H.H.; Li, H.; Pan, Z.C.; Xiong, W.W. Rational design of p-ZnS@CN with 3D interconnected hierarchical pore structure through pyrolysis of an organic hybrid zinc thiocyanide for electrochemical lithium storage. *Chem. Eng. J.* **2023**, *477*, 147114. [CrossRef]
10. Yu, Q.X.; Li, H.X.; Wen, Y.L.; Xu, C.X.; Qin, S.F.; Kuang, Y.F.; Zhou, H.H.; Huang, Z.Y. The in situ formation of ZnS nanodots embedded in honeycomb-like N-S co-doped carbon nanosheets derived from waste biomass for use in lithium-ion batteries. *New Carbon Mater.* **2023**, *38*, 543–552. [CrossRef]
11. Wang, P.; Yuan, A.; Wang, Z.; Shen, X.; Chen, H.; Zhou, H. Self-templated formation of hierarchically yolk-shell-structured ZnS/NC dodecahedra with superior lithium storage properties. *Nanoscale* **2021**, *13*, 1988–1996. [CrossRef] [PubMed]
12. Hou, T.Y.; Liu, B.R.; Sun, X.H.; Fan, A.R.; Xu, Z.K.; Cai, S.; Zheng, C.M.; Yu, G.H.; Tricoli, A. Covalent Coupling-Stabilized Transition-Metal Sulfide/Carbon Nanotube Composites for Lithium/Sodium-Ion Batteries. *ACS Nano* **2021**, *15*, 6735–6746. [CrossRef] [PubMed]
13. Feng, S.H.; Wang, Z.X.; Guo, H.J.; Li, X.H.; Yan, G.C.; Wang, J.X. First-Principle Study of a ZnS/Graphene Heterostructure as a Promising Anode Material for Lithium-Ion Batteries. *Energy Fuels* **2022**, *36*, 677–683. [CrossRef]
14. Huang, B.Y.; Zhang, Y.L.; Zhong, H.; Wu, Y.B.; Lin, X.M.; Xu, W.Q.; Ma, G.Z. Strategy for the Preparation of ZnS/ZnO Composites Derived from Metal-Organic Frameworks toward Lithium Storage. *Inorg. Chem.* **2024**, *63*, 12281–12289. [CrossRef]
15. Guo, C.; Wang, Q.H.; He, J.P.; Wu, C.P.; Xie, K.X.; Liu, Y.; Zhang, W.C.; Cheng, H.Y.; Hu, H.; Wang, C. Rational Design of Unique ZnO/ZnS@N-C Heterostructures for High-Performance Lithium-Ion Batteries. *J. Phys. Chem. Lett.* **2020**, *11*, 905–912. [CrossRef]
16. Hu, P.; Jia, Z.Y.; Wang, Y.; Zhou, Q.Q.; Liu, N.; Li, F.; Wang, J.S. Interface Engineering of Hierarchical MoS2/ZnS/C Heterostructures as Anode Materials for Highly Improved Lithium Storage Capability. *ACS Appl. Energy Mater.* **2020**, *3*, 7856–7864. [CrossRef]
17. Jin, Y.; Seong, H.; Moon, J.H.; Lee, S.Y.; Kim, S.K.; Yang, M.; Lee, J.B.; Cho, S.Y.; Choi, J. Study on colloidal synthesis of ZnS nanospheres embedded in reduced graphene oxide materials for sodium-ion batteries and energy storage mechanism. *J. Alloys Compd.* **2023**, *943*, 169076. [CrossRef]
18. Li, H.Y.; Luo, J.; Han, D.Y.; Liu, A.; Zhou, M.; Huang, J.L.; Zhu, Y.C.; Hou, Z.H.; Yin, H. Layer-by-layer hetero-carbon modifying ZnS nanocubes anode with improved long-term life for sodium-ion batteries. *Ceram. Int.* **2023**, *49 Pt B*, 18421–18431. [CrossRef]
19. Zhao, L.; Yin, J.; Lin, J.X.; Chen, C.L.; Chen, L.H.; Qiu, X.Q.; Alsharee, H.N.; Zhang, W.L. Highly Stable ZnS Anodes for Sodium-Ion Batteries Enabled by Structure and Electrolyte Engineering. *ACS Nano* **2024**, *18*, 3763–3774. [CrossRef]
20. Wei, X.B.; Yuan, H.C.; Wang, H.J.; Jiang, R.Q.; Lan, J.L.; Yu, Y.H.; Yang, X.P. The metal-organic framework mediated synthesis of bell string-like hollow ZnS-C nanofibers to enhance sodium storage performance. *Mater. Chem. Front.* **2021**, *5*, 4712–4724. [CrossRef]

21. Choi, S.G.; Kim, Y.H.; Lee, G.W.; Choi, H.S.; Kim, K.B. MOF-derived carbon/ZnS nanoparticle composite interwoven with structural and conductive CNT scaffolds for ultradurable K-ion storage. *Chem. Eng. J.* **2023**, 141663. [CrossRef]
22. Zhu, Y.J.; Yu, L.H.; Xi, J.Y. Hierarchically structured catalytic and adsorptive ZnS-modified carbon microtubule interlayers for lithium-sulfur batteries. *J. Energy Storage* **2024**, *84 Pt B*, 110938. [CrossRef]
23. Jin, L.N.; Chen, J.Y.; Fu, Z.H.; Qian, X.Y.; Cheng, J.; Hao, Q.Y.; Zhang, K. ZIF-8/ZIF-67 derived ZnS@Co-N-C hollow core-shell composite and its application in lithium-sulfur battery. *Sustain. Mater. Technol.* **2023**, *35*, e00571. [CrossRef]
24. Liu, R.; Tao, W.; Du, Y.X.; Wu, C.X.; Ye, H.; Fan, M.; Chen, S.G.; Chen, G.H.; Mao, J.J.; Xin, S.; et al. ZnS-Nanoparticle-Coated Carbon Cloth as an Efficient Interlayer for High-Performance Li-S Batteries. *ACS Appl. Energy Mater.* **2022**, *5*, 12408–12414. [CrossRef]
25. Ansari, S.; Kumar, S.; Nayak, D.; Mandal, G.; Bauri, J.; Choudhary, R.B. Zinc sulfide (ZnS) incorporated polypyrrole (PPy) matrix for highperformance supercapacitor. *Mater. Today Proc.* 2024, *in press*. [CrossRef]
26. Salah, N.; Shehab, M.; Nady, J.E.; Ebrahim, S.; El-Maghraby, E.M.; Sakr, A.H. Polyaniline/ZnS quantum dots nanocomposite as supercapacitor electrode. *Electrochim. Acta* **2023**, *449*, 142174. [CrossRef]

molecules

MDPI

Article

High-Quality Epitaxial Cobalt-Doped GaN Nanowires on Carbon Paper for Stable Lithium-Ion Storage

Peng Wu [1], Xiaoguang Wang [1], Danchen Wang [1], Yifan Wang [1], Qiuju Zheng [2], Tailin Wang [2], Changlong Sun [3], Dan Liu [4], Fuzhou Chen [3,*] and Sake Wang [5,*]

[1] College of Sino-German Science and Technology, Qingdao University of Science and Technology, Qingdao 266061, China; peng2004wu@163.com (P.W.); xgwang689@163.com (X.W.); wangdanchen1232024@163.com (D.W.); 13153710919@163.com (Y.W.)
[2] School of Materials Science and Engineering, Qilu University of Technology, Jinan 250353, China; qlzhengqj@163.com (Q.Z.); tawangtailin@163.com (T.W.)
[3] Key Laboratory of Chemical Engineering in South Xinjiang, College of Chemistry and Chemical Engineering, Tarim University, Alar 843300, China; happysunchanglong@126.com
[4] School of Materials Science and Engineering, Dongguan University of Technology, No. 1, Daxue Rd, Songshan Lake, Dongguan 523403, China; liudan@dgut.edu.cn
[5] College of Science, Jinling Institute of Technology, Nanjing 211169, China
* Correspondence: cfz866@163.com (F.C.); isaacwang@jit.edu.cn (S.W.)

Abstract: Due to its distinctive structure and unique physicochemical properties, gallium nitride (GaN) has been considered a prospective candidate for lithium storage materials. However, its inferior conductivity and unsatisfactory cycle performance hinder the further application of GaN as a next-generation anode material for lithium-ion batteries (LIBs). To address this, cobalt (Co)-doped GaN (Co-GaN) nanowires have been designed and synthesized by utilizing the chemical vapor deposition (CVD) strategy. The structural characterizations indicate that the doped Co elements in the GaN nanowires exist as Co^{2+} rather than metallic Co. The Co^{2+} prominently promotes electrical conductivity and ion transfer efficiency in GaN. The cycling capacity of Co-GaN reached up to 495.1 mA h g^{-1} after 100 cycles. After 500 cycles at 10 A g^{-1}, excellent cycling capacity remained at 276.6 mA h g^{-1}. The intimate contact between Co-GaN nanowires and carbon paper enhances the conductivity of the composite. Density functional theory (DFT) calculations further illustrated that Co substitution changed the electron configuration in the GaN, which led to enhancement of the electron transfer efficiency and a reduction in the ion diffusion barrier on the Co-GaN electrode. This doping design boosts the lithium-ion storage performance of GaN as an advanced material in lithium-ion battery anodes and in other electrochemical applications.

Keywords: GaN; doped; CVD method; lithium-ion batteries; DFT

1. Introduction

Lithium-ion batteries (LIBs) are considered one of the most promising energy storage devices [1–3]. However, commercial anodes based on graphite materials fail to satisfy practical utilization requirements due to their limited capacity and rate performance [4]. Metal nitrides (MNs) have emerged as potential alternatives [5–8], but their slow charge transport and poor cycling stability hinder their widespread adoption as anode materials [9]. As a result, research on new anode materials with enhanced structure stability and ion transport kinetics is crucial for achieving high-rate performance and cycling stability in LIBs [10,11]. Gallium nitride (GaN) is a strong candidate material for LIBs owing to its excellent structure stability and lithium storage mechanism [12,13]. Nevertheless, the rate performance of GaN is often restricted by inadequate ion transfer kinetics. Moreover, the low anode capacity of unsubstituted GaN (189 mA h g^{-1}) remains a significant challenge for broader applications [14].

Recent research on improving the conductivity and ion transfer in GaN-based materials has mainly focused on morphological and structural modifications. Common strategies, such as nanostructuring and surface graphitization, have reinforced the lithium storage performance and the kinetics of GaN-based composite anodes. However, the lithium storage properties of pure GaN are hindered by its intrinsically low charge transfer efficiency, and improvements to GaN at this point are still challenging [15]. One potential approach to alleviate this shortcoming is to regulate the mobility of electrons enhancing lithium-ion storage kinetics in GaN-based materials for advanced LIBs [16].

The electron configurations of atoms in GaN control the diffusion efficiency during electrochemical reactions and determine the rate performance of GaN anode materials [17]. Electron density engineering has been proposed as an effective strategy to improve ion diffusion efficiency [18]. Consequently, designing the electronic structure of GaN anodes is crucial. In particular, many studies have proven that metal cationic substitution is an efficient strategy for regulating electron mobility and charge transfer efficiency in anode materials [19]. For example, Fe-doped GeO_2 introduces active sites for lithium storage and enhances conductivity, resulting in ultra-long cycling stability [20]. The Fe-doped ZnS materials demonstrated an impressive capacity retention of 651 mA h g^{-1} with 94% of the capacity reserved [21]. Among the various cation substitution candidates, cobalt (Co) stands out because it is easy to access, inexpensive, and demonstrates superior electrical properties. Co cation substitution has been shown to enrich active sites for lithium insertion and optimize the adsorption energy of lithium ions [22,23]. Moreover, Co cation substitution activates the lithium storage processes by creating an increased number of active sites [24,25]. Considering the electron configuration of the Co element, Co cation substitution is an efficient way to enhance ion diffusion in GaN-based anodes. However, studies on the reorganization of the electronic structure of GaN through Co cation substitution for optimized electrochemical performance remain limited.

In this work, Co-substituted GaN (Co-GaN) nanowires on carbon paper were designed and synthesized via a facile chemical vapor deposition (CVD) strategy. Electrochemical measurements and DFT calculations confirmed improvement of the lithium-ion storage performance in the Co-substituted GaN. The orbital hybridization between the Co and N elements revealed a significant decrease in the bandgap and increased electron delocalization. Consequently, Co substitution enhanced electron conductivity and ion transfer in GaN, thus achieving high-rate performance with stable cycling capacity. The lithium storage capacity of the Co-GaN electrode reached 813.2 mA h g^{-1} after 200 cycles at a current density of 0.1 A g^{-1}. This electron density reorganization engineering through Co cation substitution offers profound insights into designing high-performance lithium storage anode materials and in other realms.

2. Results and Discussion

2.1. Morphology Characterization

Co-GaN nanowires were synthesized using the CVD method. The scanning electron microscopy (SEM) image in Figure 1a illustrates the nanowire morphology of Co-GaN. The high-resolution SEM image (Figure 1b) reveals that the surface of Co-GaN remained smooth and showed no significant changes after cobalt substitution. The energy-dispersive X-ray (EDX) analysis (Figure 1c) confirmed the presence of Co, Ga, and N elements in the nanowires, with atomic percentages of approximately 5.3%, 40.5%, and 54.2%, respectively. Elemental mapping (Figure 1g–j) directly showed the uniform distribution of Co, Ga, and N, indicating successful Co doping in the nanowires. The transmission electron microscope (TEM) image (Figure 1d) shows the fine structure of Co-GaN nanowires with a diameter of around 50 nm. The high-resolution TEM (HRTEM) image in Figure 1e depicts the fine crystallization structure of Co-GaN with an interplanar spacing of 2.76 Å. Selected area electron diffraction (SAED) (Figure 1f) confirmed that the Co-GaN nanowires grew along the (100) direction. The fine crystal structure of Co-GaN, which is crucial for achieving high-rate performance in lithium anodes, was further confirmed by means of HRTEM

imaging [26]. Furthermore, interface integration between the Co-GaN nanowires and the carbon paper, which can greatly reduce the lithium-ion transport distance and ensure efficient electron conductivity, was confirmed. These designed structural characteristics and synergistic effects contribute to the enhanced electrochemical performance.

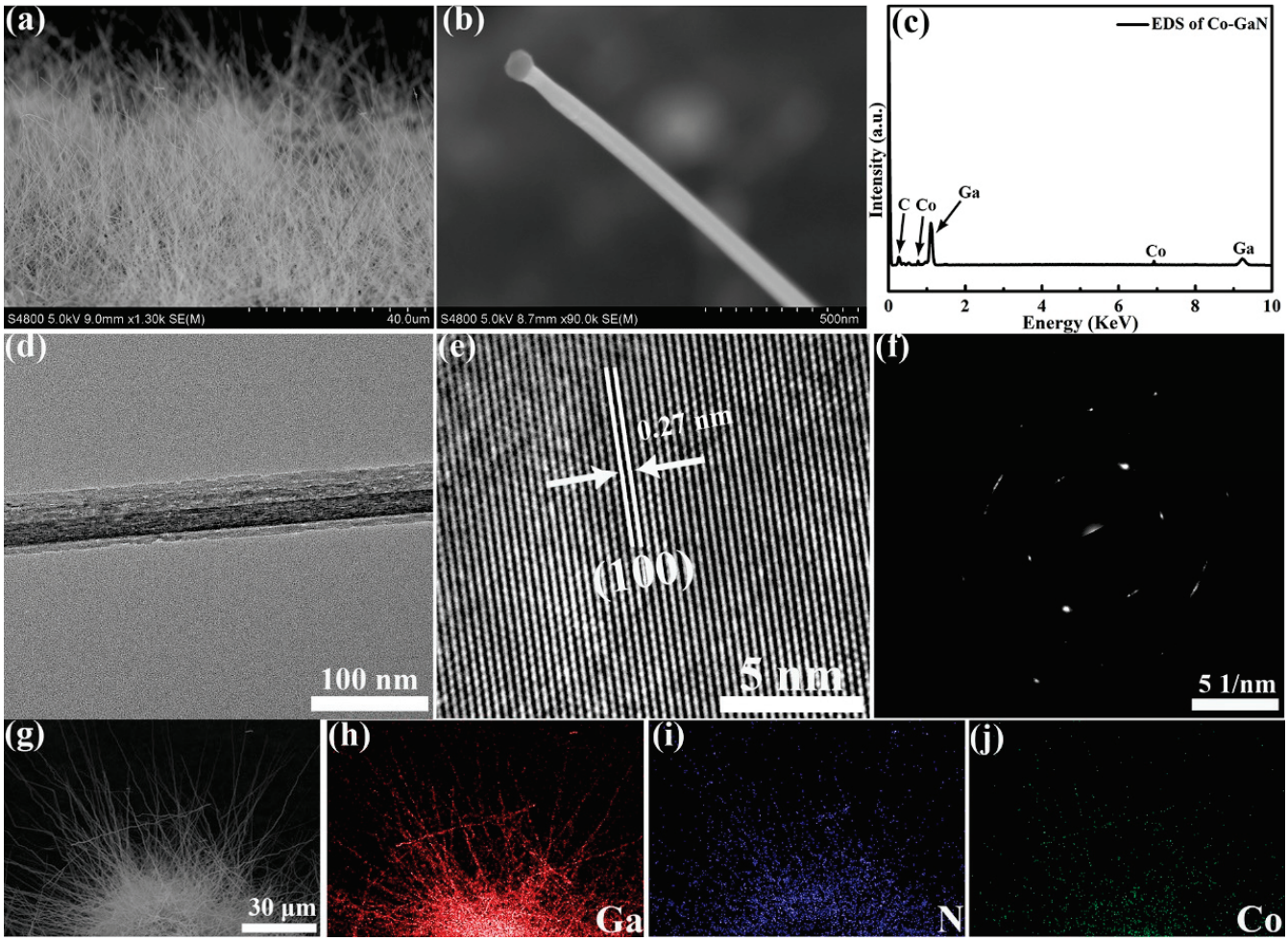

Figure 1. (**a**,**b**) SEM images at different magnifications. (**c**) Energy-dispersive X-ray (EDX) elemental test. (**d**) TEM image. (**e**) High-resolution TEM images. (**f**) SAED images. (**g**–**j**) EDS mapping analysis of Co-GaN.

2.2. Structure Characterization

The crystallographic structure of both pristine GaN and Co-GaN was further characterized using X-ray diffraction (XRD). As depicted in Figure 2a, all peaks for both pristine GaN and Co-GaN nanowires were indexed to a hexagonal crystal system [C 6v4 P63mc, JCPDS: No. 50-0792]. The peak intensity result shows that Co doping has limited effect on Co-GaN crystallinity. Figure 2b shows that the primary peaks of (100), (002), and (101) in Co-GaN shifted to higher angles compared to the GaN pattern. This shift is attributed to the substitution of smaller Ga ions with Co ions according to the Bragg equation ($2d \sin \theta = k\lambda$). Additionally, the full width at half-maximum (FWHM) of the Co-GaN nanowire peaks increased compared to that for the GaN pattern, illustrating the presence of the Co dopant, which changed the crystal structure of GaN (Figure 2c). No impurity peaks were found in the Co-GaN patterns, allowing us to infer that there was no pollution in the Co-doped sample. In the Raman spectra (Figure 2d), two peaks were found at 534 cm^{-1} and 569 cm^{-1}. The 534 cm^{-1} peak corresponds to the A_1 mode of GaN, while the 569 cm^{-1} peak indicates the E_2 mode of GaN [27]. In the Co-GaN sample, a broad peak located at 664.7 cm^{-1} was

observed, which was caused by the defect states introduced by Co doping [28]. The similarity in Raman spectra between the GaN and Co-doped GaN nanowires confirms that the origin microstructure of GaN was well-preserved after Co doping. This well-maintained structure facilitates efficient electron transport, which is essential for elevating the rate performance of the active Co-GaN nanowires.

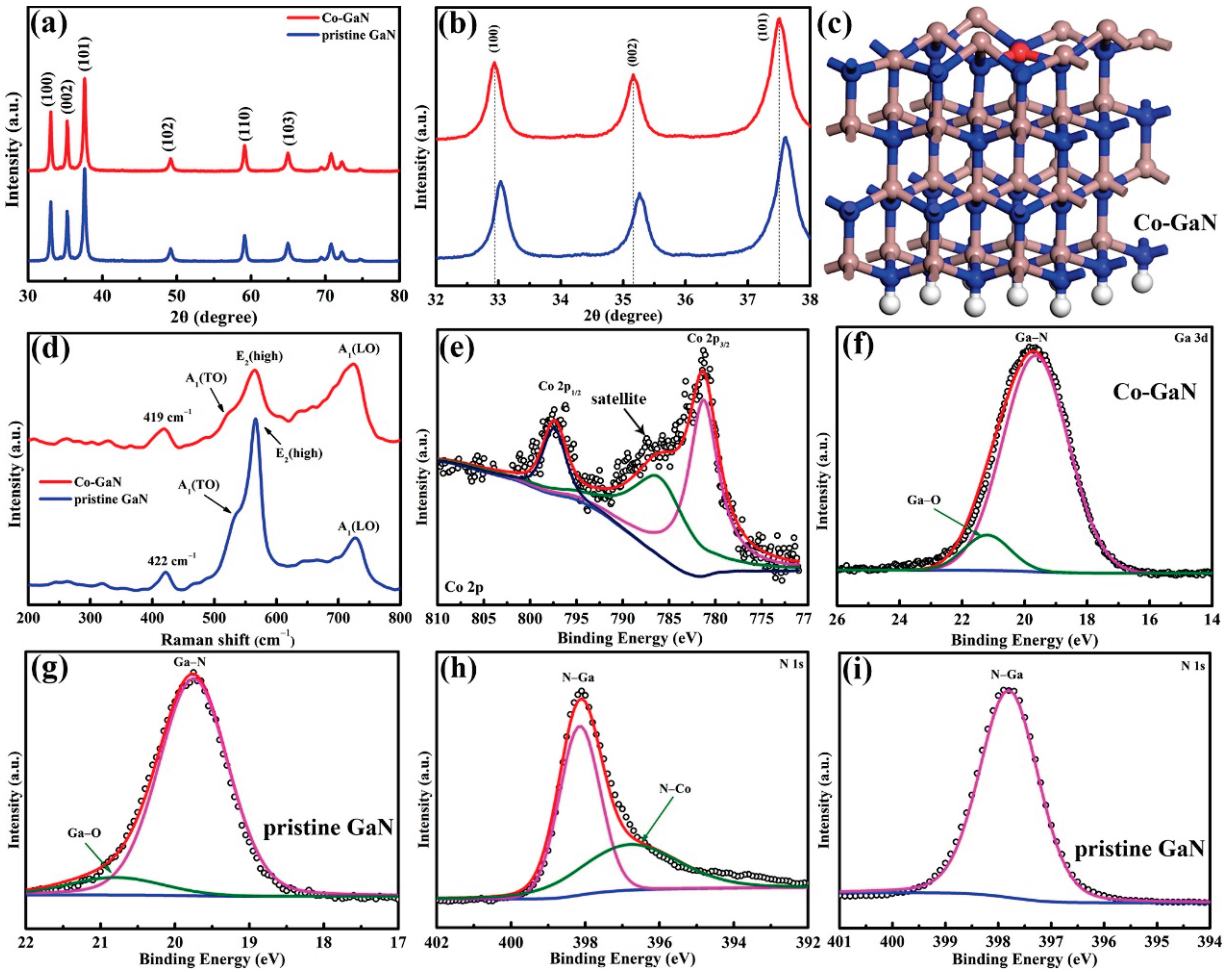

Figure 2. (**a**) XRD patterns, (**b**) amplified XRD patterns from 32° to 38°, and (**c**) the corresponding schematic structure model of Co-GaN (White ball for hydrogen atom, pink ball for gallium atom, blue ball for nitrogen atom and red ball for cobalt atom). (**d**) Raman spectra, (**e**) Co 2p, (**f**,**g**) Ga 3d, and (**h**,**i**) N 1s XPS spectra of GaN and Co-GaN, respectively.

X-ray photoelectron spectroscopy (XPS) was implemented to examine the chemical bonding of Co, Ga, and N in the Co-GaN nanowires and to reveal the change in the chemical environment after the Co doping. The XPS spectra of the Co 2p are shown in Figure 2e. These spectra are deconvoluted into two primary peaks. The peaks at 781.3 eV and 797.5 eV correspond to the Co $2p_{3/2}$ and Co $2p_{1/2}$ levels, respectively. The Co $2p_{3/2}$ spectrum possesses a satellite peak at 785.4 eV [29], and the observed energy separation (ΔE) reveals the exchange interaction energy. The spin-orbit splitting of 16.2 eV for the Co 2p doublet indicates a blended valence state of Co of approximately 2+ and 3+. The existence of Co^{2+} and Co^{3+} indicates that Co donated electrons to GaN and changed the electron distribution in GaN. Based on the Co 2p spectra, the Co concentration in the Co-GaN nanowires was calculated to be 4.6% (atomic percent). These results confirm that the Co element was successfully doped into the GaN nanowires. Figure 2f shows the high-resolution core-level spectra of Ga 3d for both GaN and Co-GaN nanowires. The Ga XPS spectra were deconvoluted into a peak located at 19.5 eV, indicating the Ga-N bond, and a

peak located at 21.2 eV, indicating the Ga-O bond. The presence of Ga-O bonds is due to the slight oxidation during the nitridation process of Co-GaN nanowire formation. Notably, Co doping reduced the percentage of Ga-O bonds, as reflected by the diminished Ga-O peak intensity in Figure 2g. This reduction is likely due to Co's lower electronegativity increasing the electron density around Ga atoms. The negative shift in the Ga 3d binding energy confirms enhanced coupling between Co and GaN due to Co doping. The N 1s spectra of pristine GaN (Figure 2h) and Co-GaN nanowires (Figure 2i) reveal N-Ga bonds at 397.9 eV [30]. Additionally, in the Co-GaN nanowires, the characteristic binding energy for N-Co bonds at 396.4 eV was observed, further confirming the incorporation of Co into the nanowires. The Co 2p and N 1s spectra together provide strong evidence for successful Co doping in the Co-GaN nanowires.

2.3. Electrochemical Analysis

Figure 3a shows the cyclic voltammetry (CV) test result for the Co-doped GaN. In the first cycle, the broad peaks observed at 0.5 and 1.1 V denote the formation of the solid electrolyte interphase (SEI) layer [31]. In the subsequent cycles, a peak located at 0.85 V corresponds to the interaction between Li and N [32]. The following CV curves overlaid with the former one indicate excellent stability in the cycling processes, with the similarity in peak positions suggesting that Co doping does not change the lithium storage mechanism. The cycling capacity and stability of Co-GaN are shown in Figure 3b. The irreversible capacity was 747.2 mA h g^{-1} in the first discharge cycle. The irreversible capacity reduction in the first discharge and charge process may have been induced by the consumption of lithium ions forming SEI layers [33]. In subsequent cycles, the overlapping galvanostatic charge and discharge (GCD) profiles suggest stable structure retention and the steady lithium storage mechanism of the Co-GaN sample [34]. The cycling capacity remained at 495.1 mA h g^{-1}, with the Coulombic efficiency maintained at ~100% after 100 cycles (Figure 3c). The reasons for this elevated lithium-ion storage performance are the improved ion diffusion kinetics and the lowered ion diffusion barrier after Co doping. As shown in Figure 3d, the Co-GaN electrode achieved rate capacities of 452.9, 431.1, 426.5, 403.4, 337.3, and 276.6 mA h g^{-1} at current densities of 0.1, 0.2, 0.5, 1.0, 2.0, and 5.0 A g^{-1}, respectively. Even at the high current density of 10.0 A g^{-1}, the electrode demonstrated a specific capacity of 181.5 mA h g^{-1}, significantly better than the capacity of the GaN sample. After the current density changed back to 0.1 A g^{-1}, the specific capacity returned to 455.8 mA h g^{-1}, reflecting excellent reversibility in lithium storage. The excellent rate performance presented by the Co-GaN sample is due to the improved ion diffusion and enhanced electron conductivity [35]. The ultralong cycling performance of Co-GaN was also tested at the high rate of 10.0 A g^{-1} (Figure 3e). After 500 cycles, the cycling capacity remained at 167.7 mA h g^{-1}, indicating that Co doping significantly improved the lithium-ion activity in the Co-GaN nanowires. Figure 3f provides a direct model of the lithium diffusion channel in the Co-doped GaN sample; this model illustrates the decreased lithium diffusion length and the utility of the Co dopant [36]. The increased cycling and rate performance demonstrate the excellent electrochemical properties of Co-GaN.

The CV curves for Co-GaN under various scan rates are depicted in Figure 4a. The CV curves at various scan rates have similar shapes, indicating the stable lithium storage mechanism and small polarization during the lithium storage reaction under high current densities [37]. The lithium storage behavior and the pseudocapacitive contribution of Co-GaN can be calculated according to Equation (1),

$$i = av^b \quad (1)$$

where i is the current, and v is the scan rate. Constants a and b denote the lithium storage behavior, which can be calculated from the data under different scan rates [38]. The calculated b value (Figure 4b) shows the lithium storage behavior containing both diffusion contributions and capacitive contributions. These two contributions can be calculated from

the capacitive effect (k_1v) [39]. In the Co-GaN nanowire electrode (Figure 4c), over 40% of the total capacity results from the capacitive process (the purple region).

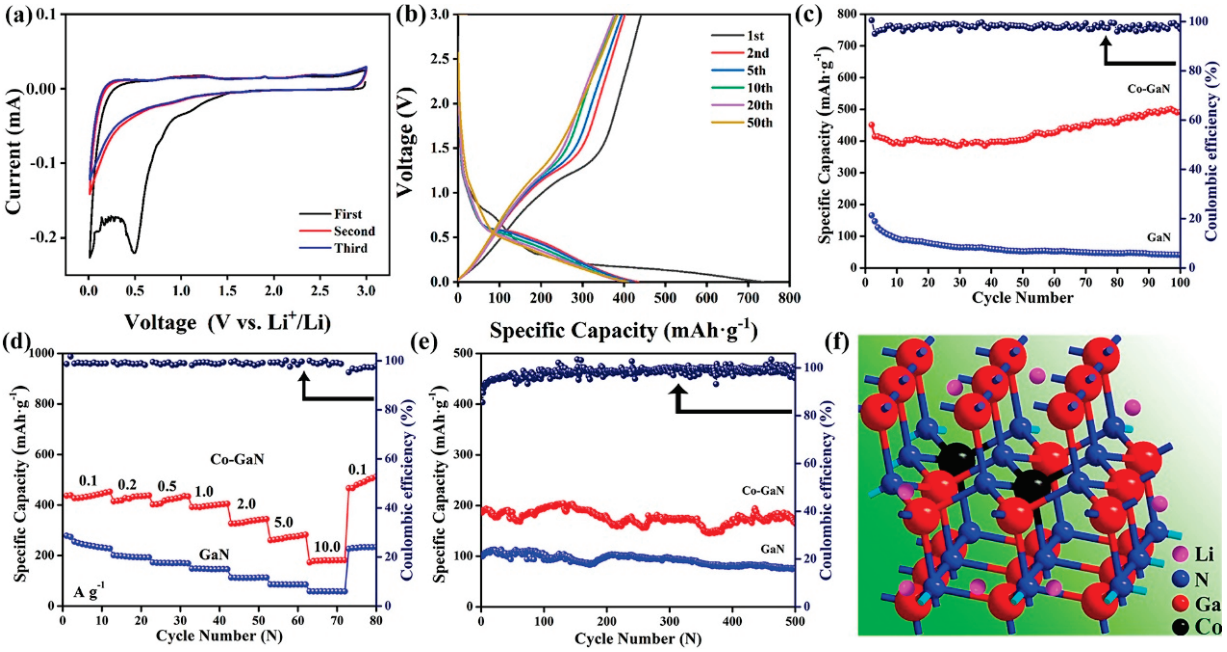

Figure 3. Electrochemical test results of the Co-GaN nanowires: (**a**) CV tests at a scan rate of 0.1 mV s^{-1}. (**b**) Galvanostatic charge and discharge (GCD) tests. (**c**) Cycling performance test. (**d**) Rate performance test of GaN and Co-GaN nanowire electrodes. (**e**) The long cycling at a high current density of 10.0 A g^{-1}. (**f**) Schematic illustration of lithium transfer channel.

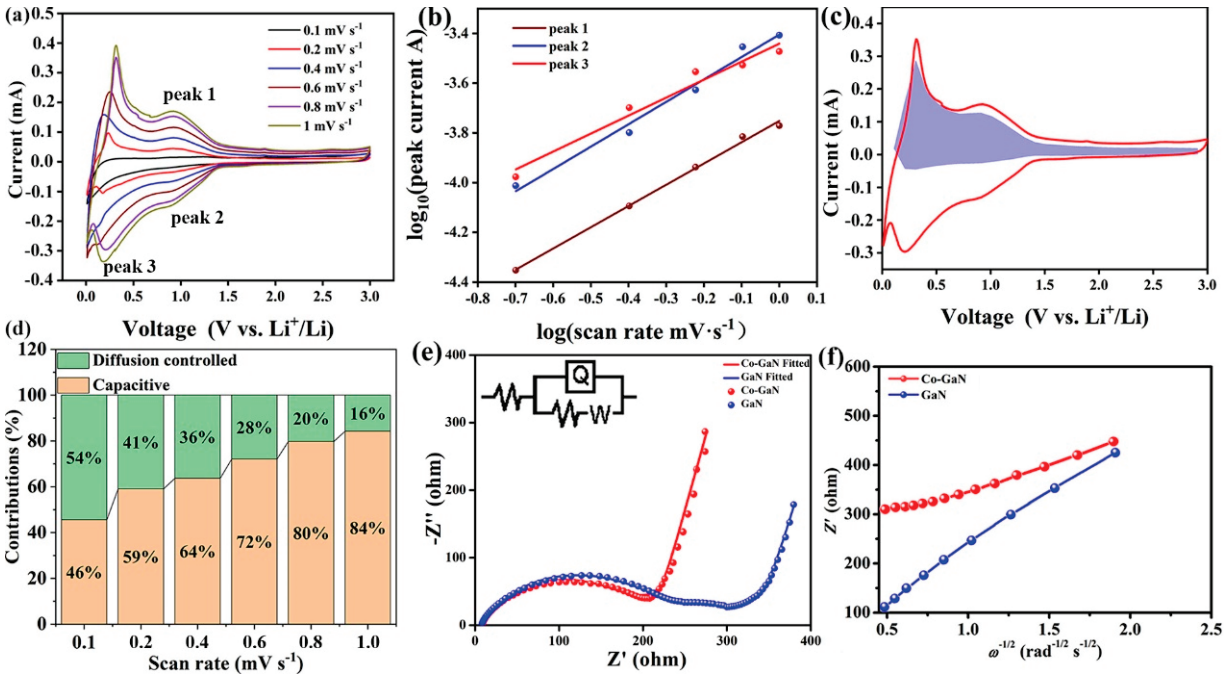

Figure 4. (**a**) CV tests of Co-GaN at various scan rates. (**b**) Determination of the calculated *b* value. (**c**) Pseudocapacitive contribution at 1.0 mV s^{-1}. (**d**) Pseudocapacitive contribution illustration at the scan rate of 1.0 mV s^{-1}. (**e**) Electrochemical impedance spectra (EIS) with the fitted Nyquist plots and the equivalent circuit of the GaN and Co-GaN electrodes. (**f**) The calculation of relationships between Z′ and $\omega^{-1/2}$.

The two different capacitive contributions can be calculated from the various CV plots under various scan rates. The calculated contributions of Co-GaN at different scan rates are shown in Figure 4d. The pseudocapacitive contribution in Co-GaN increases with an increasing scan rate, which is consistent with previous test results [40]. To further assess the elevating effect of Co cation substitution on ion diffusion, Nyquist plots were analyzed (Figure 4e). The semicircles at high-to-medium frequencies denote the charge-transfer resistance (Rct), while the inclined lines at low frequencies correspond to the mass-transfer resistance [41]. After the data were fitted to an equivalent circuit (inset of Figure 4e), the Rct of the Co-GaN electrode (204.6 Ω) was significantly lower than that of GaN (297.5 Ω), indicating improved conductivity and enhanced ion diffusion efficiency after Co doping [42]. In the low-frequency region, the slope of Co-GaN was steeper than that of the pristine GaN sample, confirming improved lithium-ion mobility and a more favorable pore structure or diffusion pathway in the Co-GaN electrode [43]. According to Equation (2),

$$D_{\mathrm{Li+}} = R^2T^2/2A^2n^4F^4C^2\sigma^2, \quad (2)$$

where T, F, and R are constants that stand for the absolute temperature, Faraday's constant, and the gas constant. A is the area of the electrode, and C is the lithium-ion molar concentration. The Warburg factor (σ) can be calculated using Equation (3):

$$Z_{real} = R_e + R_{ct} + \sigma\omega^{-1/2} \quad (3)$$

In Figure 4f, the calculated σ values for Co-GaN and GaN are 121.6 and 87.3; the σ value for Co-GaN is much higher than that for GaN (87.3). The lithium-ion diffusion coefficient ($D_{\mathrm{Li+}}$) for Co-GaN is 4.9×10^{-12} cm^2 s^{-1} according to the calculation, which is much higher than that for GaN (6.2×10^{-13} cm^2 s^{-1}). The enhanced diffusion coefficient indicates elevated ion diffusion efficiency and enhanced charge transfer kinetics in Co-GaN brought about by the Co doping. Moreover, one can infer from the electrochemical results that there was no conversion or alloy lithium storage mechanism in the Co-doped GaN, further illustrating the derivation of the stable lithium-ion storage performance. These results also indicate that Co doping had a minimal impact on the fundamental lithium-ion storage mechanism, highlighting the enhanced conductivity and improved ion diffusion kinetics achieved through Co doping.

2.4. First-Principles Analysis

To determine the chemical origin of the enhanced lithium storage performance in Co-GaN, DFT analysis was utilized to study the effects of Co doping on the electronic configuration of Co-GaN. The calculated band structures based on the models of GaN and Co-GaN are illustrated in Figure 5a,b. In Figure 5a, discrete energy levels can be observed in the pristine GaN band structure, resulting in semiconductor behavior in GaN [13]. For Co-GaN, the band structure indicates a continuous energy band near the Fermi level (Figure 5b) compared with the GaN band structure. Therefore, Co doping results in stronger conductivity brought about by the additional orbits around the Fermi level. These DFT results indicate that Co doping effectively modulated the electron density in the GaN. Therefore, the change in the band structure accelerated the electrochemical kinetics for lithium-ion storage. Furthermore, a charge density analysis was conducted to provide a better understanding of the charge transfer produced by Co doping (Figure 5c,d). The results showed that charge density accumulates at the Co atom side after Co doping. After the Co doping, the bond length between Co and N was shortened due to the strong covalent link. Due to the stronger electronegativity of Co, the electrons accumulate near the Co atom while the Ga atoms possess the electron depletion region. These results definitively demonstrate the uneven distribution of charge density in Co-GaN (Figure 5d). Therefore, based on the DFT calculation, the enhanced electrochemical properties and improved lithium storage performance are derived from the significant charge transfer induced by

Co doping. This pronounced charge transfer facilitates more efficient lithium-ion storage, contributing to the superior electrochemical performance of Co-GaN.

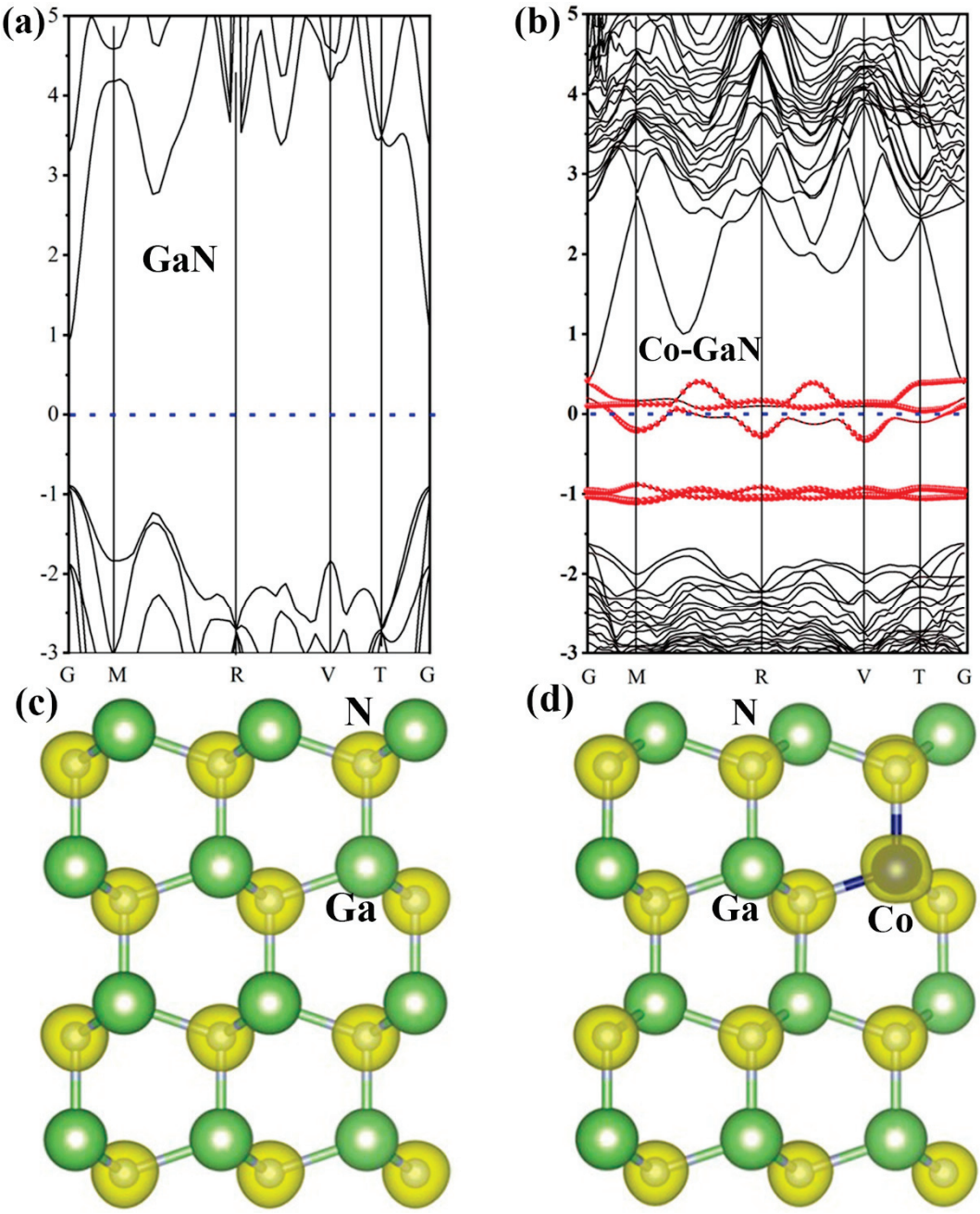

Figure 5. Band structure of (**a**) GaN and (**b**) Co-GaN. (**c**,**d**) Differences in charge density of GaN and Co-GaN.

3. Materials and Methods

3.1. Synthesis of Co-GaN Loaded on Carbon Paper

Co-GaN nanowires on carbon paper were synthesized using a designed chemical vapor deposition (CVD) method. In this process, 0.5 g of Ga_2O_3 and 0.32 g of $CoCl_2$ were placed in an alumina boat and then set at the center of a tube furnace. A carbon paper substrate was positioned approximately 2 inches from the alumina boat. The tube was initially purged with nitrogen (N_2) to remove any residual air before initiating the growth process. After evacuation, the tube was heated to 1100 °C at a rate of approximately 8 °C/min using a local heater while maintaining a constant N_2 flow acting as a protective

gas. Once the furnace reached the set temperature, ammonia (NH_3) was introduced at a flow rate of 100 sccm to trigger the reaction. After the growth was completed, the furnace was cooled under continuous N_2 flow.

3.2. Electrochemical Measurements

The lithium storage performance was evaluated using CR2016-type coin cells. The assembly was conducted in an argon-filled glove box. Carbon paper coated with Co-GaN nanowires (12 mm in diameter) was used as the anode, with an average loading density of approximately 1.9 mg cm^{-2}. A lithium metal cathode, along with pristine GaN and Co-GaN electrodes, was electronically separated by glass microfiber filters (Whatman GF/D), which were saturated with an electrolyte solution of 1 M $LiPF_6$ in a 1:1:1 volumetric mixture of ethylene carbonate, dimethyl carbonate, and diethyl carbonate.

The electrochemical performance was measured using an EWARE battery testing system and a CHI660D electrochemical workstation (Shanghai CH Instruments Co., Shanghai, China). Electrochemical impedance spectroscopy (EIS) was performed with a frequency range of 0.01 Hz to 1 MHz and at a 5 mV amplitude signal.

3.3. Measurement and Characterization

The structure and morphology of pristine GaN and Co-GaN nanowires were characterized using scanning electron microscopy (SEM, SigmaHD, Cambridge, UK). Powder X-ray diffraction (XRD) tests were conducted on a Rigaku D/MAXRB diffractometer, over a 2θ range from 20° to 80°, utilizing Cu Kα radiation (λ = 0.15 nm) (BRUKER D8 ADVANCE, Karlsruhe, Germany). Transmission electron microscopy (TEM) and high-resolution TEM (HRTEM) images were obtained with a JEOL JEM-F200 microscope operated at an acceleration voltage of 200 kV. Raman spectra were recorded using 532 nm laser excitation on a DXR2 micro-Raman spectrometer (Thermo Fisher, Carlsbad, CA, USA) equipped with an Olympus BX 41 optical microscope. X-ray photoelectron spectroscopy (XPS, Kratos Analytical Ltd., Manchester, UK) was conducted to verify the surface's chemical composition and electron configuration.

3.4. Density Functional Theory Calculation

We performed first-principles calculations based on density functional theory (DFT) using the Vienna Ab-initio Simulation Package (VASP). The generalized gradient approximation (GGA) with the Perdew–Burke–Ernzerhof (PBE) functional was employed for the exchange-correlation potential. A plane-wave energy cutoff of 500 eV was applied. Structural relaxations were carried out until the forces were below 0.01 eV/Å, and the energy convergence criterion was set to 10^{-6} eV per atom. To simulate Co doping, a Ga atom was substituted with a Co atom, resulting in a Ga23Co1N24 bulk structure. For comparison, a GaN bulk supercell containing 48 atoms was also constructed, with an expansion coefficient of $2 \times 3 \times 2$. The Brillouin zone was sampled using a $3 \times 2 \times 3$ Monkhorst–Pack k-point mesh. The valence electrons included the 2s and 2p orbitals of N, the 4s and 4p orbitals of Ga, and the 4s and 3d orbitals of Co.

4. Conclusions

In summary, Co-GaN nanowires were designed and synthesized via the facile CVD method. An XPS analysis confirmed that Co doping effectively modulated the electronic properties of the GaN nanowires. Compared to pure GaN, the optimized Co-GaN nanowires exhibited significantly higher cycling capacity, enhanced rate performance, and superior cycling stability. More importantly, a DFT analysis revealed the emergence of hybridized electronic states after Co doping, which improved both the conductivity and lithium-ion diffusion. An electrochemical analysis further validated the exceptional lithium storage performance of the Co-GaN nanowires. This design strategy provides a practical approach for activating GaN by regulating its electronic structure and provides a profound understanding about the influence of transition metal doping at the atomic level.

Author Contributions: P.W.: methodology, formal analysis, data curation, and writing—original draft. X.W.: methodology. D.W.: methodology. Y.W.: methodology. Q.Z.: methodology, funding acquisition, and writing—review and editing. T.W.: review and editing. C.S.: review and editing. D.L.: review and editing. F.C.: methodology and formal analysis. S.W.: conceptualization, formal analysis, and writing—review and editing. All authors have read and agreed to the published version of the manuscript.

Funding: This work was supported by the National Natural Science Foundation of China (52372006), the Natural Science Foundation of Shandong Province (ZR2023QE059), the Anhui Provincial Natural Science Foundation (2308085QE142), the Taishan Youth Scholar Project of Shandong Province (Grant No. 202211209), the Natural Science Foundation of Jiangsu Province (No. BK20211002), the Qinglan Project of Jiangsu Province, China, the Guangdong Provincial Natural Science Foundation Management Committee, the Regional Cultivation Project (2021B1515140055), and the Graduate Education Innovation program of Dongguan University of Technology (2023XJJG03).

Institutional Review Board Statement: Not applicable.

Informed Consent Statement: Not applicable.

Data Availability Statement: The data that support the findings of this study are available from the corresponding author upon reasonable request.

Conflicts of Interest: The authors declare no conflicts of interest.

References

1. Kiran, L.; Aydinol, M.K.; Ahmad, A.; Shah, S.S.; Bahtiyar, D.; Shahzad, M.I.; Eldin, S.M.; Bahajjaj, A.A.A. Flowers Like a-MoO_3/CNTs/PANI Nanocomposites as Anode Materials for High-Performance Lithium Storage. *Molecules* **2023**, *28*, 3319. [CrossRef] [PubMed]
2. Zhao, L.; Ning, Y.; Dong, Q.; Ullah, Z.; Zhu, P.; Zheng, S.; Xia, G.; Zhu, S.; Li, Q.; Liu, L. Longer cycle life and higher discharge voltage of a small molecular indanthrone resulting from the extended conjugated framework. *J. Power Sources* **2023**, *556*, 232518. [CrossRef]
3. Mostafa, M.M.M.; Alshehri, A.A.; Salama, R.S. High performance of supercapacitor based on alumina nanoparticles derived from Coca-Cola cans. *J. Energy Storage* **2023**, *64*, 107168. [CrossRef]
4. Zhang, W.; Sun, M.; Yin, J.; Wang, W.; Huang, G.; Qiu, X.; Schwingenschlögl, U.; Alshareef, H.N. Rational design of carbon anodes by catalytic pyrolysis of graphitic carbon nitride for efficient storage of Na and K mobile ions. *Nano Energy* **2021**, *87*, 106184. [CrossRef]
5. Zhu, Y.; Zhang, Y.; Das, P.; Wu, Z.-S. Recent Advances in Interface Engineering and Architecture Design of Air-Stable and Water-Resistant Lithium Metal Anodes. *Energy Fuels* **2021**, *35*, 12902–12920. [CrossRef]
6. Sun, C.; Tang, X.; Yin, Z.; Liu, D.; Wang, Y.; Yang, G.; Ignaszak, A.; Zhang, J. Self-supported GaN nanowires with cation-defects, lattice distortion, and abundant active sites for high-rate lithium-ion storage. *Nano Energy* **2020**, *68*, 104376. [CrossRef]
7. Sun, M.; Yan, Y.; Schwingenschlögl, U. Beryllene: A Promising Anode Material for Na- and K-Ion Batteries with Ultrafast Charge/Discharge and High Specific Capacity. *J. Phys. Chem. Lett.* **2020**, *11*, 9051. [CrossRef]
8. Sun, M.; Schwingenschlögl, U. Structure Prototype Outperforming MXenes in Stability and Performance in Metal-Ion Batteries: A High Throughput Study. *Adv. Energy Mater.* **2021**, *11*, 2003633. [CrossRef]
9. Zhang, J.; Wang, T.; Pohl, D.; Rellinghaus, B.; Dong, R.; Liu, S.; Zhuang, X.; Feng, X. Interface Engineering of MoS_2/Ni_3S_2 Heterostructures for Highly Enhanced Electrochemical Overall-Water-Splitting Activity. *Angew. Chem. Int. Ed.* **2016**, *55*, 6702–6707. [CrossRef]
10. Li, X.; Zhang, W.; Cai, J.; Yan, H.; Cui, M.; Wu, G.; Li, M. Hierarchical nanosheets constructed by integration of bimetallic sulfides into N-Doped carbon: Enhanced diffusion kinetics and cycling stability for sodium storage. *Nano Energy* **2019**, *62*, 239–249. [CrossRef]
11. Yang, Z.; Zhu, P.; Ullah, Z.; Zheng, S.; Yu, S.; Zhu, S.; Liu, L.; Li, Q. Synchronous Light Harvesting and Energy Storing Organic Cathode Material 1,4-Dihydroxyanthraquinone for Lithium-Ion Batteries. *Chem. Eng. J.* **2023**, *468*, 143787. [CrossRef]
12. Wang, S.; Hung, N.T.; Tian, H.; Islam, M.S.; Saito, R. Switching behavior of a heterostructure based on periodically doped graphene nanoribbon. *Phys. Rev. Appl.* **2021**, *16*, 024030. [CrossRef]
13. He, W.; Zhang, S.; Luo, Y.; Wang, S. Exploring Monolayer GaN Doped with Transition Metals: Insights from First-Principles Studies. *J. Supercond. Nov. Magn.* **2024**, *37*, 157. [CrossRef]
14. Kong, L.L.; Wang, L.; Sun, D.Y.; Meng, S.; Xu, D.D.; He, Z.X.; Dong, X.Y.; Li, Y.F.; Jin, Y.C. Aggregation-Morphology-Dependent Electrochemical Performance of Co_3O_4 Anode Materials for Lithium-Ion Batteries. *Molecules* **2019**, *24*, 3149. [CrossRef] [PubMed]
15. Liu, Y.L.; Yang, R.F.; Li, X.X.; Yang, W.S.; Lin, Y.W.; Zhang, G.Q.; Wang, L.J. Nb_2O_5 Coating to Improve the Cyclic Stability and Voltage Decay of Li-Rich Cathode Material for Lithium-Ion Battery. *Molecules* **2023**, *28*, 3890. [CrossRef]

16. Sun, C.; Xu, X.; Cui, C.; Chen, F.; Wang, Y.; Chen, S.; Shao, M.; Wang, J. High-Quality Epitaxial N Doped Graphene on SiC with Tunable Interfacial Interactions via Electron/Ion Bridges for Stable Lithium-Ion Storage. *Nano-Micro Lett.* **2023**, *15*, 202. [CrossRef]
17. Li, L.; Xie, F.; Wu, H.; Zhu, Y.; Zhang, P.; Li, Y.; Li, H.; Zhao, L.; Zhu, G. N-Doped Porous Carbon-Nanofiber-Supported Fe_3C/Fe_2O_3 Nanoparticles as Anode for High-Performance Supercapacitors. *Molecules* **2023**, *28*, 5751. [CrossRef]
18. Ma, L.; Zhou, X.; Sun, J.; Zhang, P.; Hou, B.; Zhang, S.; Shang, N.; Song, J.; Ye, H.; Shao, H.; et al. Synergy mechanism of defect engineering in $MoS_2/FeS_2/C$ heterostructure for high-performance sodium-ion battery. *J. Energy Chem.* **2023**, *82*, 268–276. [CrossRef]
19. Sun, C.; Wang, Y.; Liu, D.; Fang, B.; Yan, W.; Zhang, J. Tailoring interfacial interaction in GaN@NG heterojunction via electron/ion bridges for enhanced lithium-ion storage performance. *Chem. Eng. J.* **2022**, *453*, 139603. [CrossRef]
20. Wu, J.; Luo, N.; Huang, S.; Yang, W.; Wei, M. Reversible conversion reaction of GeO_2 boosts lithium-ion storage via Fe doping. *J. Mater. Chem. A* **2019**, *7*, 4574. [CrossRef]
21. Zhou, J.; Jiang, F.; Li, S.; Zhao, W.; Sun, W.; Ji, X.; Yang, Y. Natural marmatite with low discharge platform and excellent cyclicity as potential anode material for lithium-ion batteries. *Electrochim. Acta* **2019**, *321*, 134676. [CrossRef]
22. Li, J.; Lan, H.; Zhang, W.; An, X.; Liu, H.; Qu, J. Characterization on the formation mechanism of $Fe^0/Fe_3C/C$ nanostructure and its effect on PMS activation performance towards BPA degradation. *Chem. Eng. J.* **2022**, *435*, 134709. [CrossRef]
23. Xu, J.-S.; Zhu, Y.-J. Monodisperse Fe_3O_4 and γ-Fe_2O_3 Magnetic Mesoporous Microspheres as Anode Materials for Lithium-Ion Batteries. *ACS Appl. Mater. Interfaces* **2012**, *4*, 4752–4757. [CrossRef] [PubMed]
24. Al-Thabaiti, S.A.; Mostafa, M.M.M.; Ahmed, A.I.; Salama, R.S. Synthesis of copper/chromium metal organic frameworks-Derivatives as an advanced electrode material for high-performance supercapacitors. *Ceram. Int.* **2023**, *49*, 5119–5129. [CrossRef]
25. He, H.; Gan, Q.; Wang, H.; Xu, G.-L.; Zhang, X.; Huang, D.; Fu, F.; Tang, Y.; Amine, K.; Shao, M. Structure-dependent performance of TiO_2/C as anode material for Na-ion batteries. *Nano Energy* **2018**, *44*, 217–227. [CrossRef]
26. Xia, T.; Zhang, W.; Li, W.J.; Oyler, N.A.; Liu, G.; Chen, X.B. Hydrogenated Surface Disorder Enhances Lithium ion Battery Performance. *Nano Energy* **2013**, *2*, 826–835. [CrossRef]
27. Wang, L.; Yang, H.; Shu, T.; Xin, Y.; Chen, X.; Li, Y.; Li, H.; Hu, X. Nanoengineering S-Doped TiO_2 Embedded Carbon Nanosheets for Pseudocapacitance-Enhanced Li-Ion Capacitors. *ACS Appl. Energy Mater.* **2018**, *1*, 1708–1715. [CrossRef]
28. Shi, S.; Li, Z.; Sun, Y.; Wang, B.; Liu, Q.; Hou, Y.; Huang, S.; Huang, J.; Zhao, Y. A covalent heterostructure of monodisperse Ni_2P immobilized on N, P-co-doped carbon nanosheets for high performance sodium/lithium storage. *Nano Energy* **2018**, *48*, 510–517. [CrossRef]
29. Wu, X.; Zhang, T.; Wei, J.; Feng, P.; Yan, X.; Tang, Y. Facile synthesis of Co and Ce dual-doped Ni_3S_2 nanosheets on Ni foam for enhanced oxygen evolution reaction. *Nano Res.* **2020**, *13*, 2130–2135. [CrossRef]
30. Wang, R.C.; Luo, C.; Wang, T.S.; Zhou, G.M.; Deng, Y.Q.; He, Y.B.; Zhang, Q.F.; Kang, F.Y.; Lv, W.; Yang, Q.H. Bidirectional Catalysts for Liquid-Solid Redox Conversion in Lithium-Sulfur Batteries. *Adv. Mater.* **2020**, *32*, 2000315. [CrossRef]
31. Wang, D.; Song, Y.; Guo, T.; Liu, R.; Wu, Z. Construction of $FeS_2@MoS_2$ heterostructures for enhanced hydrogen evolution. *Sustain. Energy Fuels* **2022**, *6*, 2243–2248. [CrossRef]
32. Yang, J.; Wang, K.; Zhu, J.; Zhang, C.; Liu, T. Self-Templated Growth of Vertically Aligned 2H-1T MoS_2 for Efficient Electrocatalytic Hydrogen Evolution. *ACS Appl. Mater. Interfaces* **2016**, *8*, 31702–31708. [CrossRef] [PubMed]
33. Pian, C.; Peng, W.; Ren, H.; Ma, C.; Su, Y.; Ti, R.; Chen, X.; Zhu, L.; Liu, J.; Sun, X.; et al. Robust α-$Fe_2O_3@TiO_2$ Core–Shell Structures with Tunable Buffer Chambers for High-Performance Lithium Storage. *Front. Chem.* **2022**, *10*, 866369. [CrossRef] [PubMed]
34. Puente Santiago, A.R.; He, T.; Eraso, O.; Ahsan, M.A.; Nair, A.N.; Chava, V.S.N.; Zheng, T.; Pilla, S.; Fernandez-Delgado, O.; Du, A.; et al. Tailoring the Interfacial Interactions of van der Waals 1T-MoS_2/C_{60} Heterostructures for High-Performance Hydrogen Evolution Reaction Electrocatalysis. *J. Am. Chem. Soc.* **2020**, *142*, 17923–17927. [CrossRef] [PubMed]
35. Bai, J.; Zhao, B.; Zhou, J.; Si, J.; Fang, Z.; Li, K.; Ma, H.; Dai, J.; Zhu, X.; Sun, Y. Glucose-Induced Synthesis of 1T-MoS_2/C Hybrid for High-Rate Lithium-Ion Batteries. *Small* **2019**, *15*, 1805420. [CrossRef]
36. Huang, Y.; Xu, Z.; Mai, J.; Lau, T.-K.; Lu, X.; Hsu, Y.-J.; Chen, Y.; Lee, A.C.; Hou, Y.; Meng, Y.S.; et al. Revisiting the Origin of Cycling Enhanced Capacity of Fe_3O_4 Based Nanostructured Electrode for Lithium ion Batteries. *Nano Energy* **2017**, *41*, 426–433. [CrossRef]
37. Wang, Z.; Wang, Y.; Chen, Y.; Yousaf, M.; Wu, H.; Cao, A.; Han, R.P.S. Reticulate Dual-Nanowire Aerogel for Multifunctional Applications: A High-Performance Strain Sensor and a High Areal Capacity Rechargeable Anode. *Adv. Funct. Mater.* **2019**, *29*, 1807467. [CrossRef]
38. Li, W.; Li, X.; Yu, J.; Liao, J.; Zhao, B.; Huang, L.; Ali, A.; Zhang, H.; Wang, J.H.; Guo, Z.; et al. A self-healing layered GeP anode for high-performance Li-ion batteries enabled by low formation energy. *Nano Energy* **2019**, *61*, 594–603. [CrossRef]
39. Fan, Q.; Noh, H.-J.; Wei, Z.; Zhang, J.; Lian, X.; Ma, J.; Jung, S.-M.; Jeon, I.-Y.; Xu, J.; Baek, J.-B. Edge-thionic acid-functionalized graphene nanoplatelets as anode materials for high-rate lithium ion batteries. *Nano Energy* **2019**, *62*, 419–425. [CrossRef]
40. Pu, X.; Zhao, D.; Fu, C.; Chen, Z.; Cao, S.; Wang, C.; Cao, Y. Understanding and Calibration of Charge Storage Mechanism in Cyclic Voltammetry Curves. *Angew. Chem. Int. Ed.* **2021**, *60*, 21310–21318. [CrossRef]
41. Chen, F.; Shi, D.; Yang, M.; Jiang, H.; Shao, Y.; Wang, S.; Zhang, B.; Shen, J.; Wu, Y.; Hao, X. Novel Designed MnS-MoS_2 Heterostructure for Fast and Stable Li/Na Storage:Insights into the Advanced Mechanism Attributed to Phase Engineering. *Adv. Funct. Mater.* **2021**, *31*, 2007132. [CrossRef]

42. Zhou, Y.; Yan, D.; Xu, H.; Feng, J.; Jiang, X.; Yue, J.; Yang, J.; Qian, Y. Hollow nanospheres of mesoporous Co_9S_8 as a high-capacity and long-life anode for advanced lithium ion batteries. *Nano Energy* **2015**, *12*, 528–537. [CrossRef]
43. Xing, L.; Li, X.; Wu, Z.; Yu, X.; Liu, J.; Wang, L.; Cai, C.; You, W.; Chen, G.; Ding, J.; et al. 3D hierarchical local heterojunction of MoS_2/FeS_2 for enhanced microwave absorption. *Chem. Eng. J.* **2020**, *379*, 122241. [CrossRef]

molecules

MDPI

Article

Harvesting Friction Energy on Zinc Oxide and Zinc Oxide/Europium Oxide Sol-Gel Catalysts for Tribocatalytic Paracetamol Degradation

Dobrina Ivanova [1], Hristo Kolev [2], Ralitsa Mladenova [2], Bozhidar I. Stefanov [3] and Nina Kaneva [1,*]

[1] Laboratory of Nanoparticle Science and Technology, Department of General and Inorganic Chemistry, Faculty of Chemistry and Pharmacy, University of Sofia, 1 James Bourchier Blvd., 1164 Sofia, Bulgaria; dobrina.k.ivanova@gmail.com
[2] Institute of Catalysis, Bulgarian Academy of Sciences, "Acad. G. Bonchev" Str., Bldg. 11, 1113 Sofia, Bulgaria; hgkolev@ic.bas.bg (H.K.); ralitsa@ic.bas.bg (R.M.)
[3] Department of Chemistry, Technical University of Sofia, 8 Kliment Ohridsky Blvd., 1756 Sofia, Bulgaria; b.stefanov@tu-sofia.bg
* Correspondence: nina_k@abv.bg

Abstract: In the natural environment, mechanical energy is widely available as a sustainable and green energy source. In this paper, we successfully convert mechanical energy on ZnO and ZnO/Eu_2O_3 tribocatalysts via a friction route. Electrons were transferred across the contact interface when the catalyst particles and the polytetrafluoroethylene (PTFE)-sealed magnetic bar rubbed against each other under magnetic stirring. At the same time, holes were left on the catalyst while the PTFE absorbed the electrons. Similar to photocatalysis, organic pollutants can be effectively oxidized by the holes in the valence band of sol-gel catalysts due to their strong oxidative ability. The tribocatalytic tests demonstrated that ZnO and ZnO/Eu_2O_3 could eliminate organic analgesics (paracetamol) under magnetic stirring in the dark. By controlling the quantity of rare earth elements (1, 2, and 3 mol%), stirring speed, and the number of magnetic rods, we could further enhance the tribocatalytic performance. In addition to developing a green tribocatalysis approach for the oxidative purification of organic pollutants, this work offers a potential route for converting environmental mechanical energy into chemical energy, which could be used in sustainable energy and environmental remediation.

Keywords: tribocatalysis; sol-gel ZnO; ZnO/Eu_2O_3; paracetamol

1. Introduction

The increasing demand for clean and sustainable water resources, combined with the persistent contamination of aquatic systems by pharmaceutical residues, has driven the development of various advanced oxidation processes (AOPs) for the degradation of organic pollutants [1,2]. Techniques that utilize physical activation sources—such as light, ultrasound, electric, and magnetic fields—have attracted considerable interest for their efficiency in degrading recalcitrant compounds [3–7]. In particular, the contamination caused by pharmaceuticals such as antibiotics is of growing concern due to their persistence and potential to promote antibiotic resistance. While conventional AOPs, such as photocatalysis and electrochemical oxidation, are effective, they often rely on external energy sources such as light or electricity, limiting their practicality in ambient or off-grid conditions [8–14].

Recently, mechanical energy-driven processes, including tribocatalysis have emerged as sustainable and light-independent alternatives. Tribocatalysis is a mechanochemical

process that utilizes friction-induced charge generation to produce reactive oxygen species capable of oxidizing organic pollutants [15–17]. Its mechanism shares conceptual similarities with piezocatalysis and mechanochemistry, where mechanical forces are harnessed to drive redox reactions [18,19].

Zinc oxide (ZnO), a wide-bandgap semiconductor with intrinsic piezoelectric properties, is widely studied for such applications due to its low cost, chemical stability, and environmental friendliness [20]. Therefore, we believe that the triboelectric properties of ZnO could be used to oxidize pollutants, achieving the frictional conversion of mechanical energy to chemical energy [21–24]. Thus, the use of nanomaterials' frictional effects to degrade pollutants has emerged as a novel concept. ZnO, an excellent semiconductor material with great chemical stability and environmental friendliness, can significantly affect catalytic activity due to its various morphologies [21,25]. In fact, more active sites are found in nanomaterials with a higher specific surface area, and these sites are crucial for accelerating the breakdown of organic compounds. The tribocatalytic efficiency of zinc oxide can be significantly enhanced through doping with rare-earth elements, which can improve charge carrier separation, tailor surface states, and modulate the band structure. Europium (Eu), capable of existing in multiple oxidation states (Eu^{3+} and Eu^{2+}), is a promising dopant that can influence the surface chemistry and electronic properties of ZnO-based materials [26]. While Eu-doped ZnO has shown promising activity in photocatalytic and luminescent applications, its behavior under tribocatalytic conditions remains largely unexplored. Furthermore, there is a lack of systematic studies on how tribocatalysis affects the surface chemistry of doped ZnO systems, including changes in oxidation state, surface composition, and defect generation.

In this study, we investigate the tribocatalytic degradation of paracetamol using pure and Eu^{3+}-modified ZnO nanomaterials (0, 1, 2, and 3 mol%) synthesized by a sol-gel method. The materials are evaluated under dark stirring conditions to simulate ambient mechanical activation. The impact of Eu doping on the catalytic activity is correlated with changes in surface chemistry and structural properties. A comprehensive suite of characterization techniques—X-ray photoelectron spectroscopy (XPS), electron paramagnetic resonance (EPR), scanning and transmission electron microscopy (SEM and TEM), X-ray diffraction (XRD), energy-dispersive X-ray spectroscopy (EDS), and UV–vis spectroscopy—is employed to elucidate the relationship between material structure and tribocatalytic performance. This work offers new insights into the role of rare-earth elements in enhancing tribocatalysis and demonstrates the potential of Eu-doped ZnO as an effective catalyst for the degradation of pharmaceutical pollutants in water.

2. Results and Discussion

2.1. Structure Analysis

The morphology of pristine and Eu_2O_3-modified ZnO particles is investigated using scanning electron microscopy (SEM), as shown in Figure 1. Identifying the structural morphological changes between pure ZnO and ZnO modified with europium is straightforward. A generally homogeneous dispersion of particles with varying sizes and shapes is visible in the ZnO/Eu_2O_3 SEM images. The europium ions strongly promote crystal nucleation. One possible explanation for this trend is the difference in ionic radii between europium and zinc [27]. The results of Chao et al. [28] are similar to the SEM results obtained.

Energy-dispersive X-ray spectroscopy (EDS) analysis is carried out on the ZnO/Eu_2O_3 samples to verify the presence of Eu on the surface of the ZnO. Figure 1 displays representative spectra. The atomic percentages of elements in the four types of tribocatalysts are established: ZnO (Zn 12.18 at%, O 87.82 at%), ZnO/1 mol%, Eu_2O_3 (Zn 21.07 at%, O 77.22 at%, Eu 1.71 at%), ZnO/2 mol%, Eu_2O_3 (Zn 25.40 at%, O 70.90 at%, Eu 3.70 at%),

and ZnO/3 mol%, Eu_2O_3 (Zn 22.26 at%, O 73.90 at%, Eu 4.48 at%). Eu content rises marginally for particles treated with the highest concentration. The four catalysts were prepared on a carbon patch and coated with gold during their characterization. For this reason, carbon and gold peaks are observed in the EDS spectra. No other elemental peaks were found; the purity of the ZnO and ZnO/Eu_2O_3 tribocatalysts was confirmed.

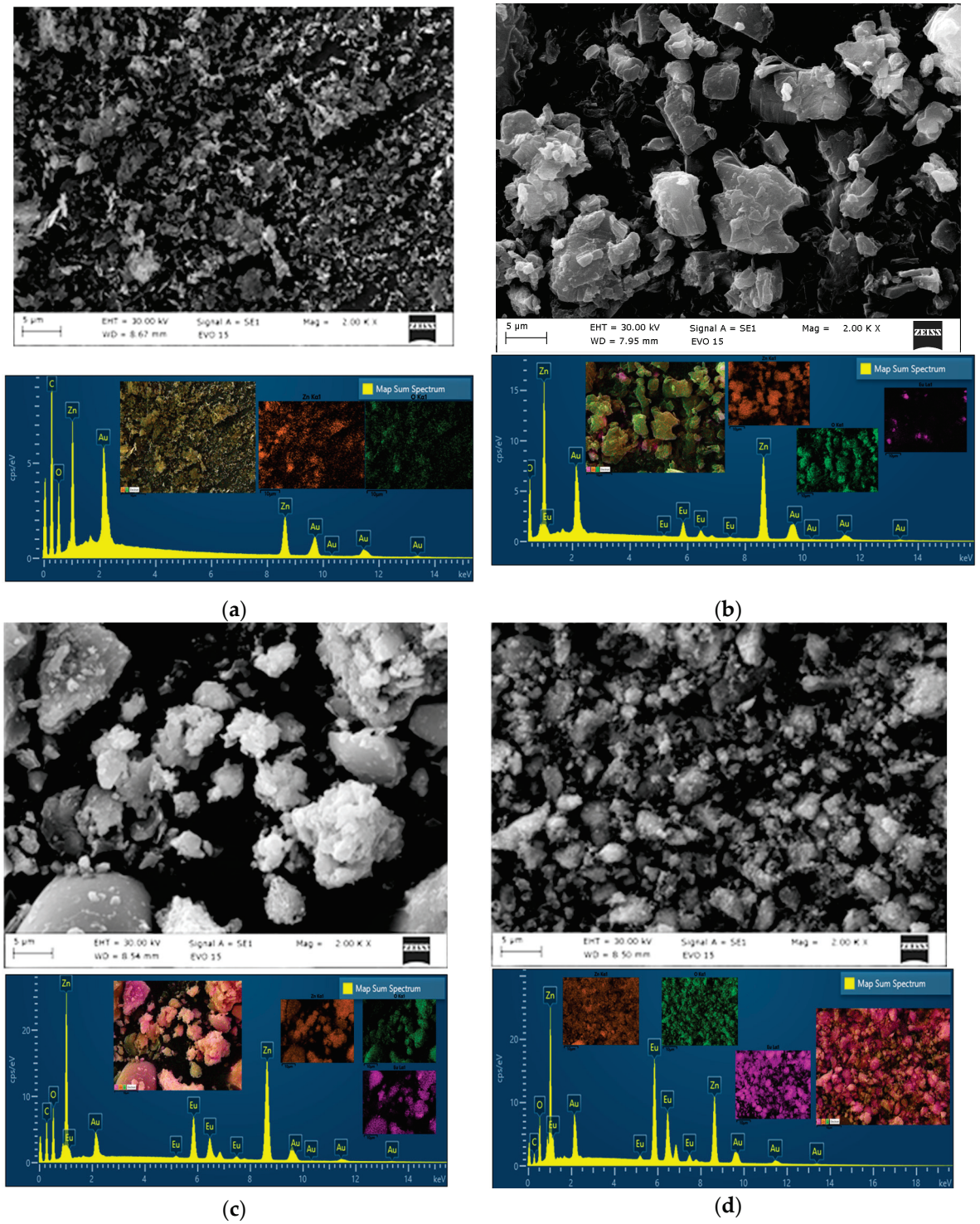

Figure 1. SEM micrographs and EDS spectra of ZnO (**a**), ZnO/1 mol% Eu_2O_3 (**b**), ZnO/2 mol% Eu_2O_3 (**c**), and ZnO/3 mol% Eu_2O_3 (**d**). The insets show composition maps of Zn, O, and Eu.

Figure 2 displays TEM images of the two distinct phases (ZnO and Eu_2O_3). The ZnO particles, exhibiting a hexagonal wurtzite structure, are depicted in Figure 2a. The modified

ZnO/Eu_2O_3 is presented in Figure 2b. The high-resolution TEM (HRTEM) of the two-phase interface, located in the chosen region of Figure 2b, is shown in Figure 2. The (400) plane of Eu_2O_3 single crystals, PDF 76-0154 (cubic structure), corresponds to the continuous (400) atomic plane.

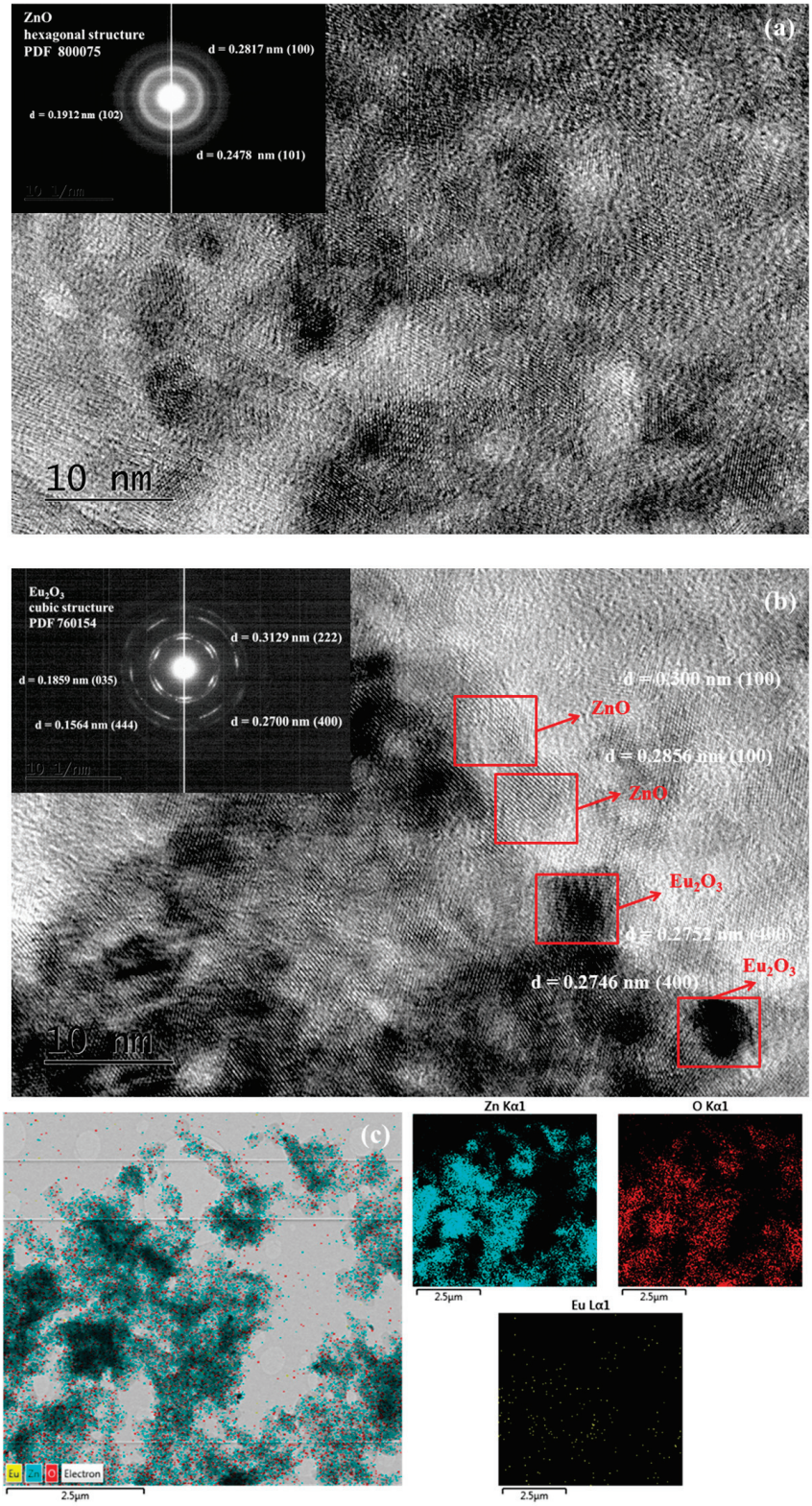

Figure 2. HRTEM image of ZnO and ZnO/Eu_2O_3 tribocatalysts. The inset in (**a**,**b**) is the corresponding SAED pattern. (**c**) The composition map of elements using STEM-XEDS analysis.

The hexagonal wurtzite structure of ZnO is confirmed by selected area electron diffraction patterns (SAED, insets in Figure 2a,b) derived from TEM images, which align with the XRD data. The insets reveal no change in the interplanar distances of the crystal lattice of both pure and modified ZnO catalysts (d100–0.2817 nm, d101–0.2478 nm, and d102–0.1807 nm). The composition map generated by STEM-XEDS analysis was utilized to examine the distribution of elements in the sol-gel sample. The findings from the mapping study indicate that the Zn, O, and Eu elements coexist and are uniformly distributed (Figure 2c). These results also demonstrate that the Eu doping in the ZnO nanoparticles was uniform.

The XRD patterns of the prepared ZnO and ZnO/Eu_2O_3 samples are shown in Figure 3. Diffraction from the (100), (002), and (101) planes of the hexagonal wurtzite structure of ZnO resulted in three prominent peaks. The indices (102), (110), (103), (200), (112), (201), and (202) also appear in the samples as additional diffraction peaks. This analysis indicates that the wurtzite structure, which possesses a polycrystalline nature, is present in ZnO produced with varying europium concentrations. For pure ZnO nanoparticles, the observed diffraction peaks were very similar to the data reported by Wang, R. H., et al. [29] and Aydin et al. [30]. The XRD patterns demonstrated that the (101) plane was the preferred growth orientation. Although only two diffraction peaks, (222) and (400) (cubic Eu_2O_3 phase JCPDS Card No. 34-0392 and 76-0704), were detected, other europium oxide peaks were not observed. No peaks from other impurities were found, suggesting that Eu_2O_3 NPs are present on the ZnO surface but were not integrated into the ZnO lattice [31]. As shown in Figure 3, the intensities of the diffracted peaks decreased as the Eu concentration increased to 3 mol%, indicating a reduction in the sample's crystallization. This decrease in crystallinity is likely due to the significant ionic size difference between Zn^{2+} and Eu^{3+} [32,33]. Furthermore, Table 1 presents all of the calculated structural parameters for pure and modified tribocatalysts.

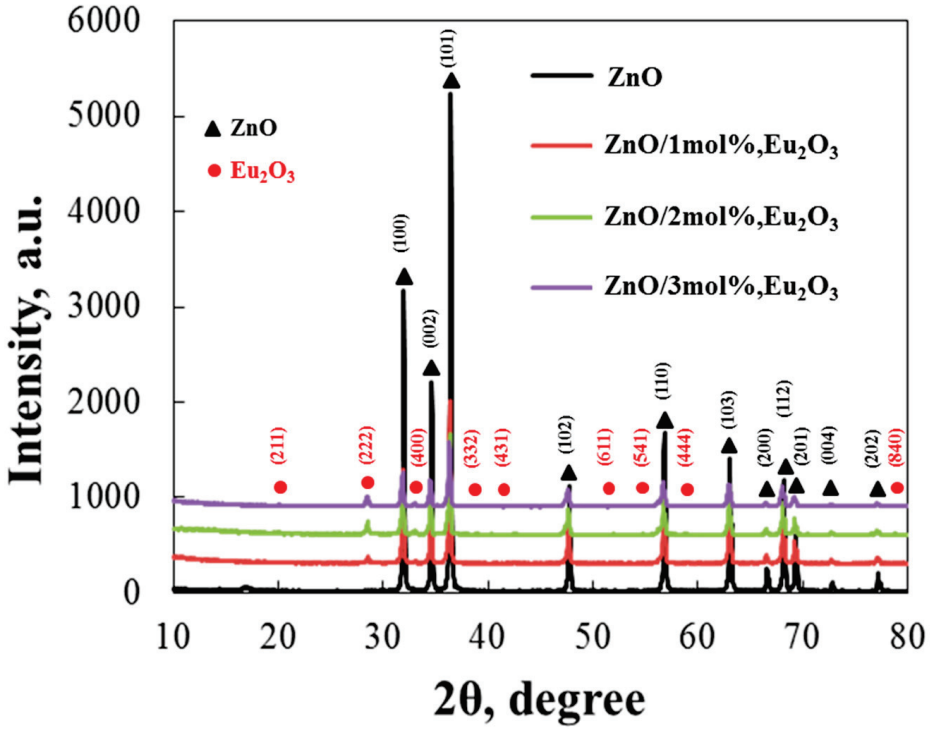

Figure 3. XRD patterns of ZnO/Eu_2O_3 samples prepared by the sol-gel method at europium concentrations of 0, 1, 2 and 3 mol%.

Table 1. The structural parameters calculated from XRD patterns of the ZnO and ZnO/Eu_2O_3 samples.

Tribocatalysts	ZnO Phase		Eu_2O_3 Phase	
Crystal. Size Parameters	Vol. Mi- % Crostrain	Crystal. Size Parameters	Vol. At. % %	Mi- Crostrain
ZnO: 42.4 a, b: 3.2407 c: 5.2017	100 1.8 × 10^{-3}	—	—	—
ZnO/1 mol% Eu_2O_3 39.0 a, b: 3.2484 c: 5.2043		33.4 a, b, c: 10.8485		
ZnO/2 mol% Eu_2O_3 36.0 a, b: 3.2475 c: 5.2032	97.8 3.3 × 10^{-4} 94.8 2.1 × 10^{-4} 93.7 9.2 × 10^{-4}	34.1 a, b, c: 10.8592	2.2 0.68 5.2 1.65 6.3 2.01	1.5 × 10^{-3} 9.9 × 10^{-4} 2.5 × 10^{-1}
ZnO/3 mol% Eu_2O_3 30.2 a, b: 3.2485 c: 5.2039		26.8 a, b, c: 10.8587		

The addition of europium ions had no discernible effect on the crystal size, as shown in the XRD results. Nevertheless, the intensity of the ZnO peaks dropped when the particles were modified. The average crystallite size shrank as the concentration of europium increased, suggesting that the crystalline lattice remained relatively stable. The structural parameters of the pure and 1, 2, and 3 mol% europium-modified sol-gel samples are presented in Table 1. The pure ZnO's unit cell parameters were found to be extremely similar to those of the europium-modified samples. Tensile strain was represented by positive values in the computations. According to the estimations in Table 1, the modified particles exhibited a higher magnitude tensile strain than the pure samples, and the strain in the sol-gel-derived samples was tensile.

Electron spectroscopy for chemical analysis (ESCA), more commonly known as X-ray photoelectron spectroscopy (XPS), was employed to investigate the surface atomic composition and oxidation states of elements in the ZnO/xEu (x = 0, 1, 2, and 3 mol%) samples before and after tribocatalytic testing. Our analysis focuses on the Eu $3d_{5/2}$ core level, due to europium's role in modifying the ZnO surface, and the O 1s core level, where changes were observed with increasing europium content. The Zn 2p core level exhibited no significant variations and is therefore not discussed in detail; its binding energy remains consistent with that reported for pure ZnO, as shown in Ivanova et al. [34]. Survey and high-resolution X-ray photoelectron spectra of Eu 3d and O 1s core levels for ZnO/xEu samples (x = 0, 1, 2, and 3 mol%) before and after tribocatalytic testing are shown in Figure 3. The survey spectra measured using AlKα radiation identify core level peaks corresponding to zinc (Zn2p, Zn3p, Zn3s and Auger peak ZnLMM), oxygen (O 1s, O2s), and europium (Eu3d, Eu4d), which constitute the studied surfaces. Additionally, adventitious carbon (C 1s core level) as a contamination from the vacuum system is also detected. Further insights can be obtained from the high-resolution XP spectra.

Figure 4 presents high-resolution XPS spectra of (b) Eu $3d_5/_2$ and (c) the curve-fitted O 1s region for the samples before tribocatalytic testing, with increasing europium concentration from bottom to top. The Eu $3d_5/_2$ spectra show an intensity increase and the emergence of a peak-like structure centered around 1135 eV, indicating the presence of Eu^{3+} ions in the 1Eu, 2Eu, and 3Eu samples [34]. Additionally, a feature near 1127 eV is attributable to Eu^{2+} species [35], suggesting the coexistence of Eu^{2+} on the sample surfaces. The presence of Eu^{2+} is further confirmed by EPR analysis. Figure 4c shows the curve-fitting of the O 1s core level spectra into three components. The most intense peak (green) is assigned to lattice oxygen in Zn–O bonds (~530.7 eV) [34]. The second peak (blue),

located at ~531.5 eV, corresponds to non-lattice oxygen species such as oxygen vacancies and low coordination sites. The third component (magenta), found between 532.5–533.0 eV, is attributed to oxygen from adsorbed water.

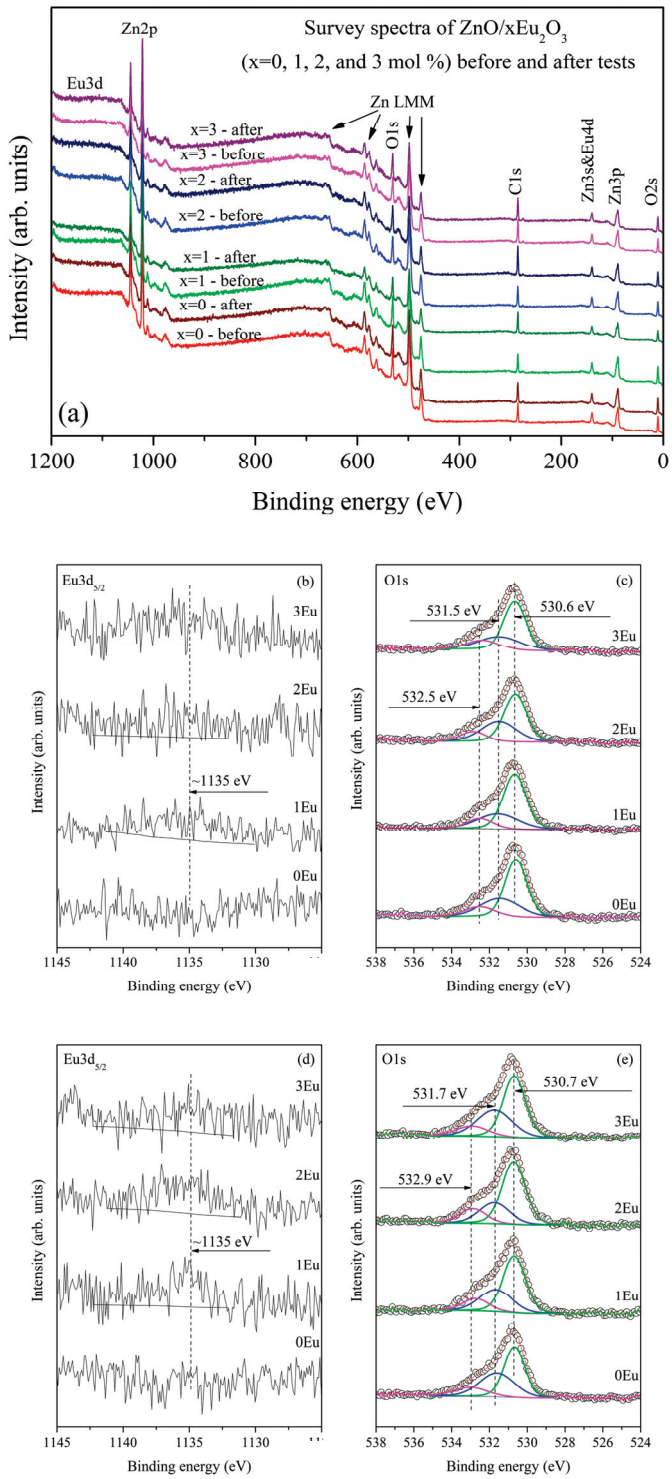

Figure 4. (**a**) Survey and high-resolution X-ray photoelectron spectra of (**b**) Eu 3d and (**c**) O 1s core levels for ZnO/xEu samples (x = 0, 1, 2, and 3 mol%) before and after tribocatalytic testing (**d**) Eu 3d and (**e**) O 1s core levels for ZnO/xEu samples (x = 0, 1, 2, and 3 mol%).

Table 2 summarizes the surface atomic concentrations (at.%), binding energies (BE, eV), and associated oxidation states or bonding environments for the ZnO/xEu samples prior to tribocatalytic testing. Despite the relatively poor signal-to-noise ratio in the Eu $3d_5/_2$ spec-

tra, the surface europium concentration shows a clear increasing trend with nominal doping level. Meanwhile, the concentrations of non-lattice oxygen and adsorbed water remain relatively unchanged within error margins, indicating minimal surface modification at low europium levels. Figure 4d,e presents the Eu $3d_5/_2$ and O 1s spectra of the samples after tribocatalytic testing, again shown with increasing europium content from bottom to top. The Eu $3d_5/_2$ spectra retain a prominent peak at ~1135 eV, confirming the presence of Eu^{3+} ions post-reaction. However, no distinct feature is observed near 1127 eV, suggesting the absence of Eu^{2+} species after testing. This observation is consistent with EPR results, which also failed to detect Eu^{2+} after the tribocatalytic process. In Figure 4e, the same color scheme is used for O 1s peak fitting: green for Zn–O lattice bonds (~530.7 eV), blue for non-lattice oxygen (~531.7 eV), and magenta for adsorbed water (~532.9 eV).

Table 2. Surface atomic concentrations (at.%), binding energies (eV), and corresponding oxidation states/bond types of elements in xEu/ZnO samples (x = 0, 1, 2, and 3 mol%) prior to tribocatalytic testing.

Before O 1s Tribocatalysts		Zn2p		Eu$3d_{5/2}$		
BE, eV		Conc., at%	BE, eV	Conc., at%	BE, eV	Conc., at%
ZnO	530.6	27.67	1021.7			
	531.6	15.78		49.80	—	0.00
	532.5	6.76				
ZnO/1 mol% Eu_2O_3	530.7	29.40	1021.7			
	531.6	14.27				
	532.5	6.21				
ZnO/2 mol% Eu_2O_3	530.7	28.88	1021.7	50.16	~1135.0	0.17
	531.7	14.75		50.35	~1135.9	0.23
	532.7	5.79		42.73	~1136.0	0.32
ZnO/3 mol% Eu_2O_3	530.7	28.32	1021.7			
	531.5	15.30				
	532.4	8.32				

Table 3 presents the surface atomic concentrations and corresponding chemical states for the post-reaction samples. Interestingly, the trend of increasing europium concentration observed before testing is no longer present. For instance, the 3 mol% Eu sample shows the lowest measured surface concentration (0.16 at%), indicating a possible redistribution or loss of europium during tribocatalysis. A new correlation is observed between europium content and non-lattice oxygen: samples with lower surface europium exhibit higher concentrations of non-lattice oxygen.

Comparison of the XPS data before and after tribocatalytic testing indicates that Eu^{3+} is the dominant surface species in both cases, while Eu^{2+} is present only prior to testing. Furthermore, a correlation between surface europium and non-lattice oxygen is evident after tribocatalysis—lower europium concentrations are associated with increased non-lattice oxygen levels. This trend was not observed in the pre-reaction samples, where the europium content increased without significantly affecting non-lattice oxygen. These findings suggest that non-lattice oxygen species, including oxygen vacancies and low coordination sites, may play an active role in the tribocatalytic process.

EPR spectroscopy was used to investigate the influence of increasing Eu_2O_3 content on the electronic properties of ZnO, as well as on the local site symmetry around doped paramagnetic ions (rare earth ions). Figure 5a shows the X-band EPR spectra of ZnO doped with increasing amounts of Eu_2O_3 quantity (1, 2, and 3 mol%), recorded at room temperature. The Eu^{2+} ion, with an electron configuration of 4f7 and a ground state of 8S = 7/2, is an EPR active species. Naturally occurring europium consists of two isotopes: 151Eu (48% abundance) and 153Eu (52% abundance), with a nuclear spin I = 5/2. This led

to the splitting of the absorption line into 2I + 1 hyperfine components due to an electron-nucleus Zeeman interaction. Several resonance absorptions may occur depending on the strength of the crystal field [36]. A crystal field stronger than the Zeeman interaction typically leads to resonance absorptions at g > 2, whereas a weak crystal field results in signals near g ≈ 2 [37]. In the current EPR study, Eu^{2+} signals at g > 2 were observed in the ZnO samples doped with 2 and 3 mol% Eu_2O_3, suggesting that some Eu^{2+} ions are located at lattice sites with strong crystal fields, likely with octahedral symmetry. Eu^{2+} tends to substitute Zn^{2+} ions at octahedral sites within the host lattice [38]. Several lines with resolved hyperfine structure were recorded at the range of magnetic fields from 80 mT to 180 mT for the ZnO/Eu_2O_3 (2 mol%), which can be attributed to transitions of Eu^{2+}. The observed spectrum, consisting of around 12 overlapping lines, arises from the superposition of signals of Eu with natural isotopic composition. A similar spectrum was reported for Eu:YAG single crystals by Petrosyan et al. [39]. In the ZnO/Eu_2O_3 (3 mol%) sample, a broad unresolved signal was observed at g ≈ 4.2. A similar signal was previously reported by Reddy et al. in ZnO:Eu (0.1 mol%) nanopowders [40]. It is reasonable to suggest that an increased Eu_2O_3 content in the samples leads to a higher amount of Eu^{2+} ions, which in turn results in increased intensity of the EPR peak at g ≈ 4.2. Trivalent Europium ($4f^6$, $^7F_0$) does not give an EPR signal since it is diamagnetic in nature.

Table 3. Surface atomic concentrations (at.%), binding energies (eV), and corresponding oxidation states/bond types of elements in ZnO/xEu samples (x = 0, 1, 2, and 3 mol%) after tribocatalytic testing.

After O 1s Tribocatalysts	**Zn2p**		**Eu3d$_{5/2}$**		
BE, eV	**Conc., at%**	**BE, eV**	**Conc., at%**	**BE, eV**	**Conc., at%**
ZnO 530.7	24.46	1021.7			
531.6	19.19		49.06	—	0.00
533.0	7.28				
ZnO/1 mol% Eu_2O_3 530.7	28.70	1021.7			
531.7	16.12				
532.7	7.07				
ZnO/2 mol% Eu_2O_3 530.7	31.76	1021.7	47.89	~1135.6	0.21
531.7	13.59		46.08	~1135.4	0.27
532.9	8.30		46.09	~1134.5	0.16
ZnO/3 mol% Eu_2O_3 530.7	28.05	1021.7			
531.6	19.00				
532.9	6.70				

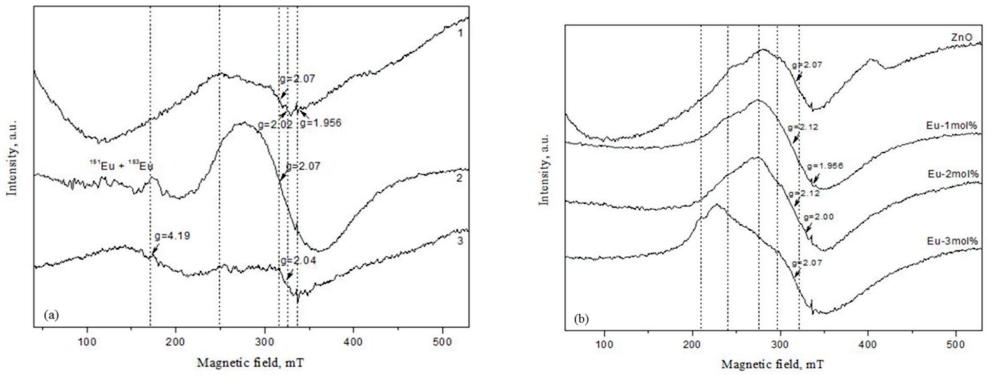

Figure 5. (**a**) EPR spectra of ZnO modified with 1 mol% Eu_2O_3 (1), 2 mol% Eu_2O_3 (2), and 3 mol% Eu_2O_3 (3); (**b**) EPR spectra of undoped ZnO and ZnO modified with 1, 2 and 3 mol% Eu_2O_3. The signal gain in the europium samples is one time greater than the undoped sample.

A broad, asymmetric signal was observed in all samples, most likely due to the overlap of several signals with close g-factors. This complicates the precise identification of all recorded signals. A resonance at g = 2.07 (observed in spectra 1 and 2 in Figure 5a) may originate from O^{2-} species formed due to traces of oxygen being present in the system [41] or from $OH^{\bullet}$ radicals adsorbed on the catalyst surface [42]. Additionally, a weak signal at g = 2.02 was recorded in spectrum 1, possibly associated with oxygen radicals, which typically exhibit g-values between 2.00 and 2.03 [42]. While in the ZnO/Eu_2O_3 (3 mol%) sample, a weak resonance line at 325 mT (g = 2.04) was observed (spectrum 3). A similar signal was reported in N-implanted ZnO films and attributed to V_0–V_{Zn} divacancy [43]. Stan et al. detected a signal at g = 2.03, which was attributed to coupled defects, such as negatively charged zinc vacancy-interstitial zinc ($V\text{-}_{Zn}$:$Z_{ni}{}^{0}$) complexes. A weak, narrow singlet at g = 1.956 was detected in all samples and can be attributed to shallow effective mass donor (SD) centers in ZnO. Some studies have assigned the resonance at g = 1.96 to bulk defects originating from negatively charged Zn vacancies [44] or to oxygen vacancy-related defects in ZnO. An increase in europium content led to a slight increase in the intensity of the signal with g_{eff} = 1.956, with similar intensities recorded for the 2 and 3 mol% doped samples.

Figure 5b presents the EPR spectra of undoped and Eu_2O_3-doped ZnO samples after tribocatalytic treatment. Some differences are observed between the EPR spectra recorded before and after mechanical activation. The EPR measurements show the absence of resonance signals attributable to paramagnetic europium species, suggesting that Eu^{2+} ions are either not present in detectable concentrations or have been oxidized to the diamagnetic Eu^{3+} state. This assumption is supported by XPS analysis, which indicates a shift in the $Eu^{3+} \leftrightarrow Eu^{2+}$ redox equilibrium toward the trivalent state. Similar to the pre-catalysis spectra, overlapping signals are observed, complicating detailed analysis via X-band EPR. Therefore, only distinct EPR signals are discussed. A signal at g = 2.07 appears in both undoped ZnO and the 3 mol% Eu_2O_3-doped sample, while a different signal with g = 2.12 is observed in ZnO doped with 1 and 2 mol% Eu_2O_3. The g = 2.07 signal was previously discussed and is attributed to O^{2-} species or $OH^{\bullet}$ radicals adsorbed on the catalyst surface. The shift from g = 2.145 to 2.12 is likely due to overlapping signals and is commonly associated with Zn vacancies [40]. Singly ionized oxygen vacancies ($g \approx 2.000$) are most likely present in all samples [43,45]. As in the pre-catalysis spectra, shallow donor (SD) centers are observed at g = 1.956. Their concentration increases in the 2 and 3 mol% Eu-doped ZnO samples, with the 3 mol% sample exhibiting approximately twice the intensity compared to the undoped and 1 mol% doped samples. As mentioned, the EPR signal with g_{eff} = 1.956 is responsible for the donor states. Since the intensity of this signal depends on the europium concentration, it can be assumed that Eu atoms are involved in the structure of these donor centers. The remaining unidentified signals are most likely due to ZnO impurities containing metal ions.

Figure 6 presents a comparison of the Raman spectra of the pure ZnO powder and the ZnO/Eu_2O_3 sample modified with 3 mol% Eu_2O_3, recorded in the 110–1300 cm^{-1} range. The Raman data confirm the hexagonal wurtzite phase composition of ZnO, consistent with the XRD patterns. The most prominent Raman peaks appear at 330 and 438 cm^{-1}, corresponding to the E2H–E2L and E2H Raman modes, respectively [46], followed by a broad feature at 1152 cm^{-1}, attributed to the 2A1(LO) and 2E2(LO) modes. No significant spectral changes are observed in the Eu_2O_3-doped powder, regardless of the dopant concentration, except for a reduction in intensity and broadening of the Raman modes. This observation is consistent with the XRD analysis. A slight redshift (~1 cm^{-1}, discernible but below the resolution of the Raman instrument used) of the observed Raman modes is also noted, which may indicate partial substitution of lattice Zn atoms by Eu [47].

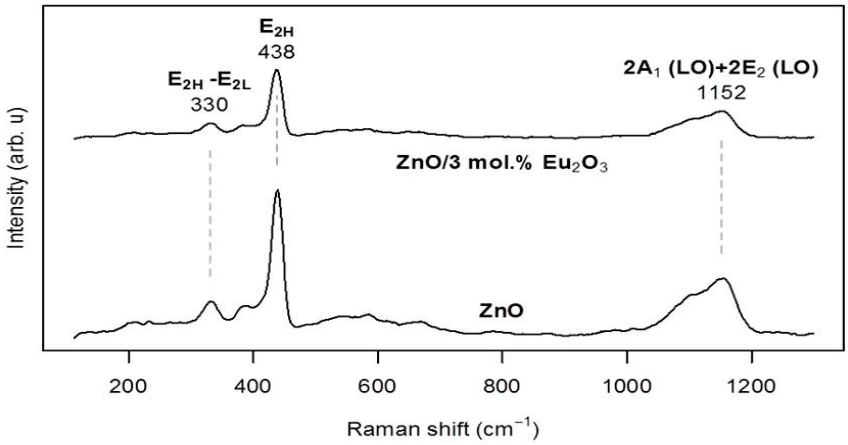

Figure 6. Raman spectra of ZnO and ZnO/3 mol%, Eu_2O_3 samples.

2.2. Optical Analysis

UV–vis absorption spectroscopy was employed to examine the optical characteristics of the tribocatalysts. Figure 7a indicates that pure ZnO exhibited an absorption band in the UV region at approximately 370 nm. The interaction between Eu and the semiconductor resulted in a slight shift of the absorption band (λ_{max} = 367 nm) in the europium-modified samples. This interaction was attributed to strong interfacial electronic coupling between ZnO and Eu_2O_3. Consequently, the loss of light energy was further minimized [48].

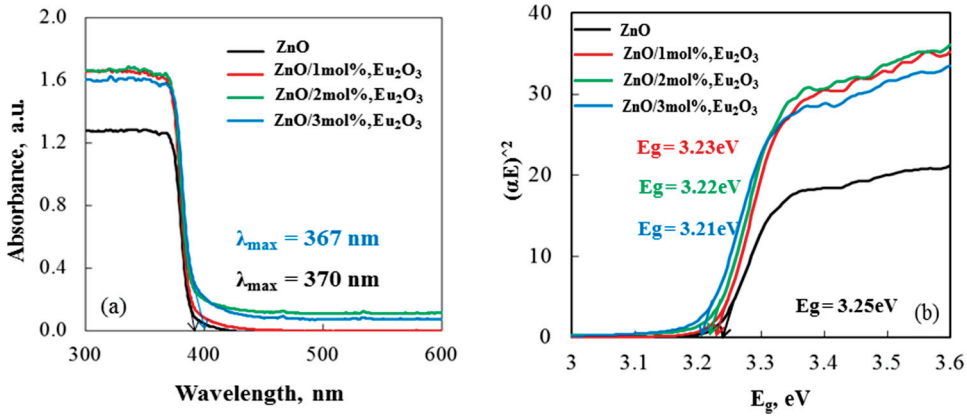

Figure 7. (**a**) UV–visible patterns of tribocatalysts and (**b**) linear plots of $(\alpha h\nu)^2$ versus E_g for tribocatalysts.

The three samples exhibited band gap energies of 3.23, 3.22, and 3.21 eV for 1, 2, and 3 mol% Eu-modified ZnO, respectively, according to the relationship E_g (eV) = 1240/λmax (nm), Figure 7b [49]. The value of the band gap energies decreased from 3.25 eV for pure ZnO to 3.21 eV for ZnO/3 mol%, Eu_2O_3. Chandrasekhar et al. [50] and Ntwaeaborwa et al. [51] reported similar findings for europium-modified ZnO semiconductors. The presence of Eu^{3+} in the ZnO lattice can explain the variations in E_g values. The incorporation of Eu^{3+} ions as substitutes at Zn site introduces 4f states into the ZnO band gap [52]. These states are situated near the conduction band edge of ZnO and, unlike non-metal and transition metal ion dopants, do not hybridize with O2p states and Zn3d states due to the strong shielding effect of the $5s^2$ and $5p^6$ orbitals [53]. Nevertheless, spectroscopic data reveal a distinctive intra-shell luminescence transition of europium-modified, indicating that weak interactions with the environment cause the 4f states of europium to become somewhat delocalized upon substitution [54]. Because the influence of Zn3d states is lessened, the observed decrease in E_g value can be understood as a lowering of the conduction band minimum of ZnO. Therefore, the lowest E_g value at 3 mol% indicates that the dopant

concentration has an optimal effect, most likely by raising the density of 4f states of Eu^{3+} replacing zinc ions in the ZnO lattice.

2.3. Tribocatalytic Decomposition of Paracetamol

The tribocatalytic decomposition of paracetamol without light, utilizing a magnetic stirrer with one PTFE magnetic bar at 300 rpm, is employed to estimate the tribocatalytic efficiency of ZnO and ZnO/Eu_2O_3 particles. Each friction test uses the same drug concentration of 15 ppm. The concentration of the drug solution was determined using the PCA molecule's distinctive absorbance at 243 nm. Figure 8a shows the tribocatalytic degradation of a paracetamol initially at a rotation speed of 300 rpm using pure and europium-modified ZnO particles. The results of the degradation process demonstrated the drug's breakdown under the tribocatalytic action. After a 24 h friction period, the ZnO/3 mol% Eu_2O_3 particles degraded 82.44% of the paracetamol.

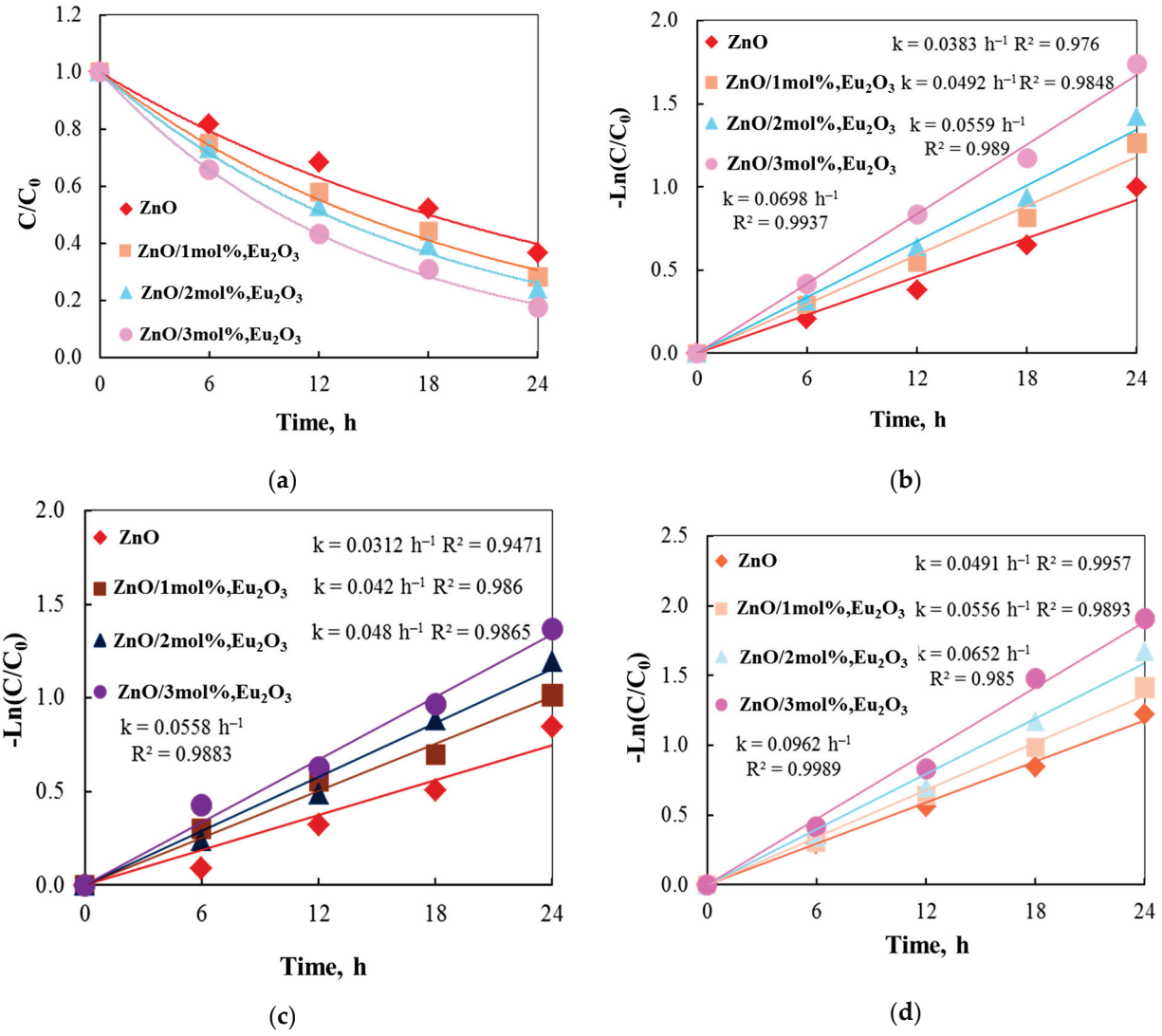

Figure 8. (**a**) Tribocatalytic degradation of paracetamol solution using ZnO and ZnO/Eu_2O_3 particles by magnetic stirring conditions at 300 rpm with one stirring rod; (**b**) kinetic fitting. The effect of various stirring speeds (**c**) 100 and (**d**) 500 rpm on the decomposition of paracetamol.

The catalytic efficiencies of ZnO/Eu_2O_3 particles are higher than those of pure ZnO. The findings indicate that tribocatalysis is significantly influenced by the morphological surface, crystallite size, and E_g values. The $Ln(C_t/C_0) = -kt$ pseudo-first-order approx-

imation yields the rate constant values (Figure 7b), which are consistent with the trend. The ZnO sample (k = 0.0383 h^{-1}) has a lower reaction rate than the ZnO/1 mol% Eu_2O_3 sample (k = 0.0492 h^{-1}). The catalyst with the highest molar concentration of europium has the highest rate constant (k = 0.0698 h^{-1}).

To investigate the factors that influence the breakdown of paracetamol, a suspension of analgesic and ZnO and ZnO/Eu_2O_3 samples was agitated at different speeds and with varying numbers of stirring rods. The data are summarized in Figure 8 and Table 4. The logarithm of the concentration ratio with ZnO and ZnO/Eu_2O_3 particles is displayed in Figure 8 using a single Teflon stirring rod at varying stirring speeds. The rate constant and the decomposition of paracetamol using ZnO/3 mol% Eu_2O_3 at 500 rpm are k = 0.0962 h^{-1} and D = 85.1% after 24 h of stirring. At 300 and 100 rpm, the decomposition ratios are k = 0.0698 h^{-1} and D = 82.4%, k = 0.0558 h^{-1} and D = 74.5%, respectively. The data suggest that a higher stirring speed could produce more friction energy, which would be advantageous for the breakdown of drugs. Increases in rotation speed can enhance the contact probability between the drug molecules and the catalyst, promoting the tribocatalytic reaction and boosting the tribocatalytic efficiency. Similarly, when Dong et al. [55] studied the tribocatalytic degradation of RhB by Bi_2WO_6, they discovered that the degradation efficiency of dyes improved with an increase in rotation speed. However, if the rotation speed is too high, the stirrer may rebound during stirring and splash the catalyst onto the beaker wall, resulting in a decrease in catalytic efficiency. The aforementioned research has demonstrated not only the significance of magnetons in the tribocatalytic experiments but also a strong correlation between the generation of tribocatalytic charges and the frequency, friction area, and charge transfer efficiency between materials.

Table 4. The values of rate constants and percentages of paracetamol degradation at 500 rpm using various amounts and types of PTFE rods.

Tribocatalysts 1 Rod		2 Rods		3 Rods	
	k, h^{-1}	D, % k, h^{-1}	D, %	k, h^{-1}	D, %
ZnO	0.0383	70.45 0.0564	74.07	0.0671	74.07
ZnO/1 mol%, Eu_2O_3	0.0492	75.62 0.0647	78.20	0.0778	81.71
ZnO/2 mol%, Eu_2O_3	0.0559	81.20 0.0795	85.02	0.0969	89.15
ZnO/3 mol%, Eu_2O_3	0.0698	85.12 0.0939	89.67	0.1054	92.15

The decomposition results obtained with varying quantities and types of stirring rods at a 500 rpm stirring speed are displayed in Table 4. The decomposition ratio with one Teflon stirring rod is the lowest, while the decomposition ratio with three Teflon stirring rods reaches the maximum percentage of paracetamol degradation. With three Teflon stirring rods, there was a noticeable increase in the decomposition ratio, which can be attributed to the increased total contact area. Two 1-mm-thick PVC belt rings were wrapped around a stirring rod to confirm the impact of total contact area on the decomposition ratio. This alteration prevents the stirring rod from making contact with the suspension's glass beaker bottom, as indicated in Table 4, which leads to a low decomposition ratio of about 25.8%. It offers proof that tribocatalytic drug breakdown is significantly influenced by the total contact area.

The contact area between the stirring rod and the catalyst, and the reactor bottom is increased by the greater number of stirring rods. Consequently, the tribocatalytic efficiency will rise as the number of stirring rods increases. Table 4 demonstrates that employing two stirring rods significantly enhances the tribocatalytic degradation efficiency of paracetamol compared to using only one stirring rod. The significance of friction between the stir bar and the vessel bottom is further illustrated by the three stirring rods.

The higher surface area, which provides more active sites for participation and permits greater adsorption of drugs in the reaction, may help to separate tribogenerated charge pairs and enhance carrier participation in the redox reaction, both of which may lead to improved tribocatalysis efficiency [56]. When ZnO absorbs mechanical energy during friction, excited e^- represents electrons, while the resulting h^+ signifies holes. O_2^- superoxide radicals are generated when oxygen molecules interact with electrons during the degradation of the drug. Following their interaction with OH^-, the holes convert into hydroxyl radicals, or $OH^\bullet$. The enhanced activity of the europium-modified ZnO sample may be attributed to the efficient electron–hole separation across the ZnO/Eu_2O_3 interface and the increased generation of O_2^- and $OH^\bullet$ radicals. The higher adsorption of hydroxyl ions onto the ZnO surface and the greater number of oxygen vacancies in the Eu-modified ZnO, resulting from the differing charge and electronegativity of europium and zinc ions, contribute to the higher efficiency [26]. The formation of $OH^\bullet$ is facilitated by the reaction between the holes and OH^-. Organic contaminants on the surface of europium-modified ZnO are degraded by strong non-selective oxidants such as hydroxyl radicals and other tribogenerated active species [57,58]. Higher catalytic efficiency is achieved when ZnO is modified with the europium oxide phase, likely due to the suppression of tribogenerated charge recombination. The incorporation of the europium phase is advantageous as it traps electrons, inhibits electron-hole recombination reactions, and increases the quantity of superoxide and hydroxyl radicals, all of which accelerate the degradation of pollutants.

A radical scavenger assay that we conducted provides evidence for the role of the superoxide and hydroxyl radicals that are involved. Figure 9 displays the data. The addition of ascorbic acid (AA) and isopropyl alcohol (IPA) scavengers, which capture the corresponding reactive species, allowed for the quantification of the roles that superoxide and hydroxyl radicals play in the degradation of paracetamol [59,60].

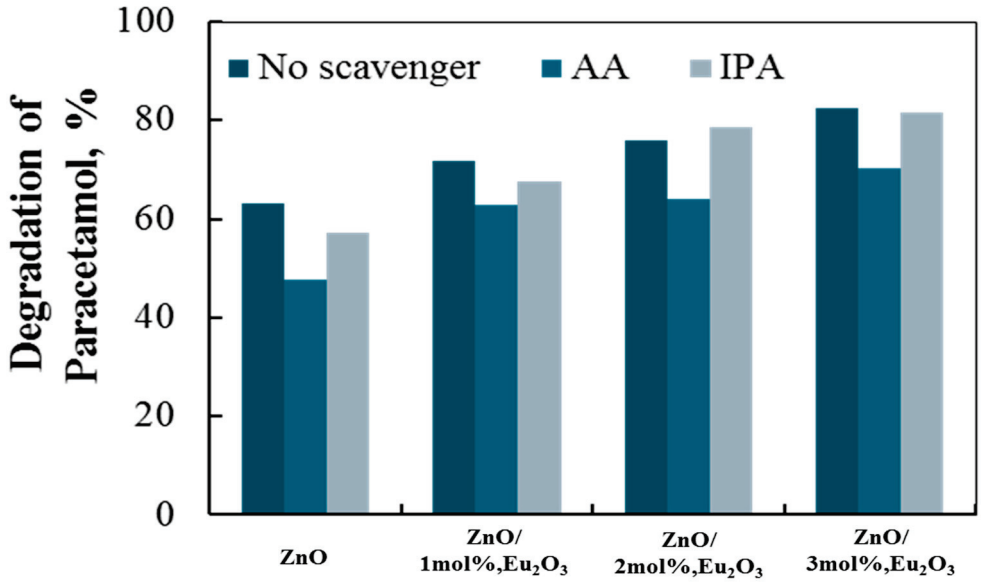

Figure 9. Scavengers' effects on the decomposition of paracetamol in the tribocatalysis process using ZnO, ZnO/1 mol% Eu_2O_3, ZnO/2 mol Eu_2O_3, and ZnO/3 mol% Eu_2O_3 particles.

Figure 9 shows that adding AA and IPA to the four tribocatalyst systems had comparable effects, with the former showing a more noticeable inhibition. This suggests that the superoxide radical has a greater impact on the paracetamol tribo-degradation rate.

A three-cycle investigation into the recyclability of tribocatalysts made of pure and europium-modified zinc oxide is depicted in Figure 10. Following three cycles in distilled water, the tribocatalytic decomposition of paracetamol decreased by approximately 2% for

all catalyst types, indicating that the catalytic performance of the tribocatalysts diminished slightly with each cycle. Despite this decrease, the stability of the drug decomposition cycle of the sol-gel samples was found to be good. These results demonstrate their potential for repeated use in the breakdown of paracetamol. The most stable and effective catalyst over many cycles is Eu_2O_3, although ZnO/3 mol% shows a slight decrease with repeated use.

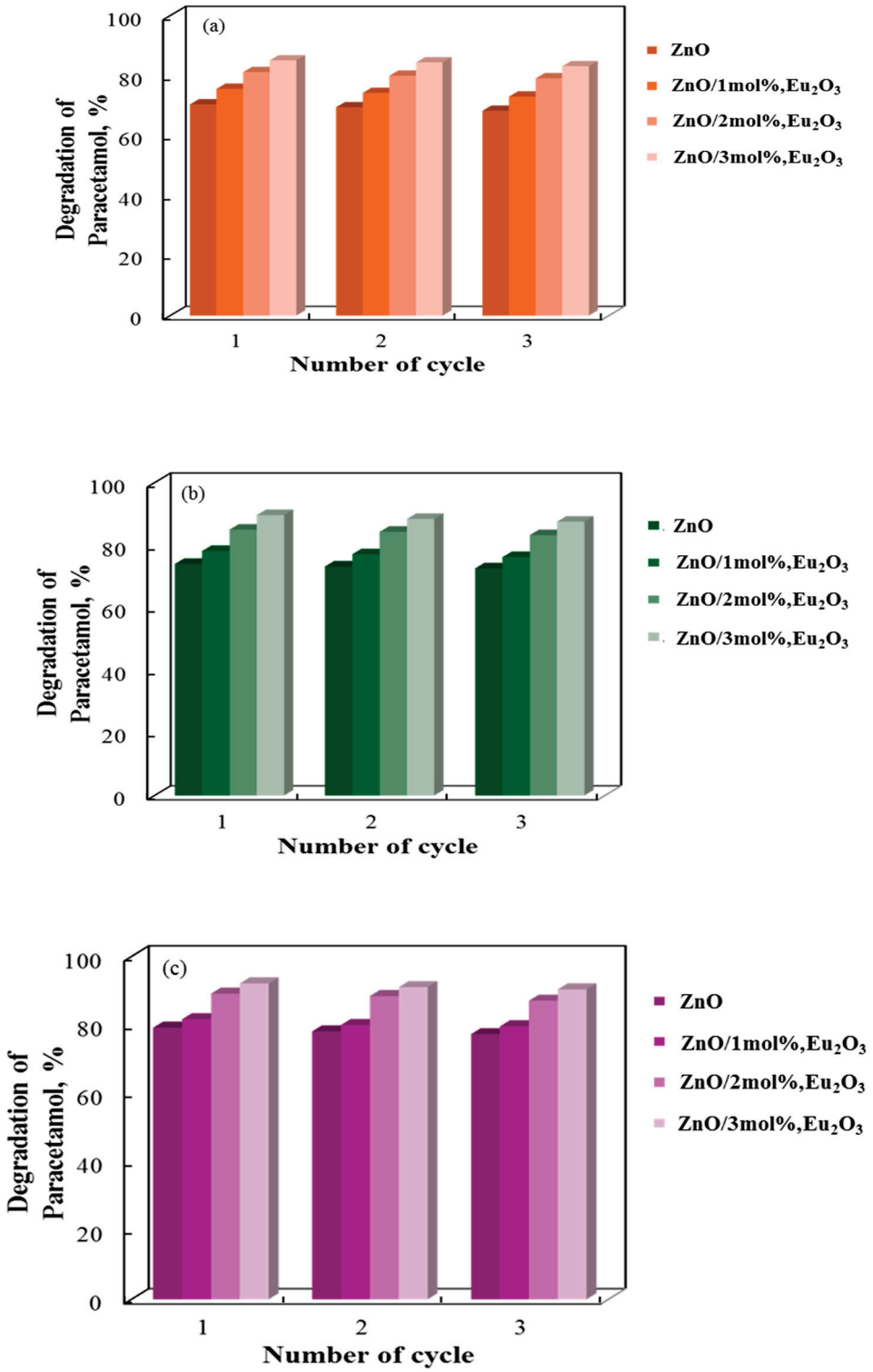

Figure 10. Decolorization rate of paracetamol at 500 rpm for three successive cycles using (**a**) 1 rod, (**b**) 2 rods, and (**c**) 3 rods.

3. Materials and Methods

3.1. Chemicals

Zinc acetate dihydrate (>99.0%), 1-propanol (>99.0%), triethylamine (>99.5%), and europium oxide (>99.0%) were from Fluka (Buchs, Switzerland). Distilled water was used in all experiments. All other chemicals and reagents were of analytical reagent grade. Paracetamol ($C_8H_9NO_2$, λ_{max} = 243 nm, Teva, Dupnitsa, Bulgaria) was chosen as the model pollutant for the tribocatalytic experiments due to its extensive application in the real world.

3.2. Synthesis of Sol-Gel ZnO and ZnO/Eu_2O_3 Particles

Four series of ZnO doped with Eu_2O_3 (0, 1, 2, and 3 mol%) powders were produced using a simple and eco-friendly sol-gel process. Zinc acetate dihydrate (0.5 g), ethylene glycol (0.15 mL), 1-propanol (20 mL), and triethylamine (0.35 mL) were mixed in a round-bottom flask with a reflux condenser and stirred (300 rpm) at room temperature for 15 min. The resulting solution was stirred for 60 min at 80 °C. ZnO tribocatalyst modified with Eu^{3+} (1 mol%) was prepared using the same method and conditions. Europium oxide was separately dissolved in 1-propanol and sonicated for 20 min to enhance dispersion. The pure reaction mixture was then added to this sonicated suspension of europium oxide, ensuring uniform doping. The resulting ZnO and ZnO/Eu_2O_3 particles were separated by centrifugation at 6000 rpm for 30 min, washed twice with pure 1-propanol, and dried in open air to yield powders. The remaining catalysts (ZnO/2 mol% Eu_2O_3 and ZnO/3 mol% Eu_2O_3) were prepared under the same optimal conditions.

3.3. Methods

A scanning electron microscope (SEM, JSM-5510, JEOL, Krefeld, Germany) was used to image the obtained samples in order to examine their morphology and microstructure. The samples were analyzed using energy-dispersive X-ray spectroscopy (EDX, detector: Quantax 200, Bruker Resolution 126 eV, Berlin, Germany) for elemental analysis or chemical characterization. Transmission Electron Microscopy (TEM) analyses were conducted on a JEOL JEM 2100 instrument (Akishima, Japan) at an accelerating voltage of 200 kV to analyze the morphology of the samples. The samples were prepared by dispersing them in ethanol for six minutes after ultrasonically grinding them. The suspensions were dripping onto standard carbon/Cu grids. The presence of all participating elements in the examined samples was further supported by elemental mapping studies using X-ray energy dispersive spectrometry (XEDS). Crystallinity and phase composition of the catalysts were analyzed using XRD (Siemens D500 with Cu Kα radiation, Karlsruhe, Germany). The average crystallite sizes were estimated using Scherrer's equation. Rietveld analysis was executed employing PowderCell [61], and the March-Dollase texturing model [62] was used to examine whether the pure and Eu-modified ZnO samples showed signs of preferential orientation. Using a Zeiss Evo 15 microscope (Bruker Resolution 126 eV, Berlin, Germany), the energy dispersive X-ray spectroscopy (EDS) analysis was performed. X-ray photoelectron spectroscopy (XPS) was carried out using an ESCALAB MkII (VG Scientific, now Thermo Scientific, Manchester, UK) electron spectrometer at a base pressure in the analysis chamber of 5×10^{-10} mbar (during the measurement, 2×10^{-9} mbar), with an AlKαX-ray source having excitation energy hα = 1486.6. The pass energy of the hemispherical analyzer was 20 eV for O 1s and Zn2p spectra, whereas for Eu3d 50 eV pas energy of the analyzer was used because of the weak spectrum intensity resulting from the low concentration of europium on the surface. The instrumental resolution is about 1 eV for the photoelectron peak, as determined from the full width at half maximum (FWHM) of the $Ag3d_{5/2}$. Data analysis was conducted using SpecsLab2 CasaXPS software (2.3.25PR1., Casa Software Ltd., Tokyo, Japan). The processing of the measured spectra includes a

subtraction of X-ray satellites and Shirley-type background [61]. The peak positions and areas are evaluated by a symmetrical Gaussian-Lorentzian curve fitting. The relative concentrations of the different chemical species are determined based on the normalization of the peak areas to their photoionization cross-sections, calculated by Scofield [62,63]. EPR measurements were performed using a standard TE011 cylindrical resonator that came with a JEOL JES-FA 100 EPR spectrometer (Tokyo, Japan). Under the following conditions, the EPR spectra were recorded at room temperature: a modulation frequency of 100 kHz, a microwave power of 6 mW, a modulation magnitude of 0.2 mT, a time constant of 0.1 s, and a sweep time of 2 min. Raman spectra of the ZnO and ZnO/Eu samples were acquired using a ThunderOptics TO-ERS-532 system, equipped with a 20× microscope objective and a 532 nm laser source operating at 30 mW power. The spectra were collected with an integration time of 2000 ms (Thunder Optics S.A.S., Montpellier, France). Raman spectral data acquisition and processing were performed using Spectragryph software (version 1.2.16.1).

3.4. Tribocatalysis for Degradation of Paracetamol

Tribocatalysis was employed to break down a 50 mL solution of paracetamol. The drug was made in a 100 mL glass beaker with distilled water and a magnetic stirrer. Without light, the tribocatalytic reaction was conducted at a steady room temperature of 23 ± 2 °C. Initially, there were 15 ppm of analgesic present. Fifty mg of catalyst (pure or Eu^{3+}-modified ZnO) was added to a glass reactor containing drug solution. Next, a magnetic bar sealed with polytetrafluoroethylene (PTFE) was used to stir the suspension magnetically. For 30 min in the dark, the resulting mixture was magnetically agitated with a PTFE to attain adsorption equilibrium between the tribocatalysts and the paracetamol solution. It then triggers the glass reactor, which initially spins at 300 revolutions per minute. Regularly, two-milliliter aliquots of the reaction solution were collected. After that, the tribocatalyst was centrifuged at 6000 rpm. This procedure was comparable to every other decomposition performance test, except for variations in the number of magnetic rods (2 and 3), magnetic stirring conditions (100 and 500 rpm), and catalyst types (ZnO/Eu (0, 1, 2, and 3 mol% powders). Friction between the catalyst and the vessel or between the stirrer and the reactor bottom may cause electron transfer during the stirring process. As a result, the vessel's material is now considered during the tribocatalysis process, as the vessel significantly influences the tribocatalytic efficiency. Polytetrafluoroethylene (PTFE) has been found to be able to absorb more electrons during the friction process than glass and polypropylene (PP) [64]. As a result, the catalyst has higher tribocatalytic efficiency when it comes into contact with the PTFE beaker and PTFE stirrer, releasing more electrons. All these studies related to the type of reaction vessel will be examined in other future experiments of ours. Thermo Scientific's Evolution 300 spectrophotometer (Madison, WI, USA) was used to acquire paracetamol's UV–vis spectra in the 200–600 nm range.

A scavenger test was used to look into the reactive species that were causing the paracetamol to degrade. As scavengers, isopropyl alcohol (IPA) and ascorbic acid (AA) were employed to absorb hydroxyl and superoxide radicals, respectively. Six milligrams of each scavenger were used independently in order to pinpoint the precise reactive species that caused the organic drug (50 mL) to degrade due to tribocatalysis.

4. Conclusions

In conclusion, three different types of ZnO sol-gel particles modified with Eu_2O_3 (0, 1, 2, and 3 mol%) are employed to achieve strong tribocatalysis for the decomposition of paracetamol by harnessing the friction energy from stirring. Among these, the ZnO/3 mol% Eu_2O_3 composite demonstrated the most efficient degradation and the highest specific

surface area. When the drug is stirred with three PTFE rods for 24 h at 500 rpm, the tribocatalytic drug decomposition ratio reaches approximately 92%. The influence of various factors, such as stirring speeds and the quantities and types of stirring rods, on the breakdown of paracetamol is assessed. The data show that electrons and holes in ZnO and ZnO/Eu_2O_3 particles are efficiently excited by mechanical energy absorbed during friction, resulting in effective drug decomposition. An environmentally friendly and promising method of using mechanical energy from the environment to combat pollution is the tribocatalytic effect. Tribocatalysis facilitates drug degradation, creating new opportunities for controlling environmental contamination.

Author Contributions: Conceptualization, N.K.; methodology, N.K.; tribocatalytic experiments, D.I.; data curation, D.I., R.M., H.K., B.I.S. and N.K.; writing—original draft preparation, N.K. All authors have read and agreed to the published version of the manuscript.

Funding: This research was funded by the Bulgarian NSF project KP-06-N89/07 (КП-06-Н89/07).

Informed Consent Statement: Informed consent was obtained from all subjects involved in the study.

Data Availability Statement: The original contributions presented in this study are included in the article. Further inquiries can be directed to the corresponding author(s).

Acknowledgments: The authors are grateful to financially supported by the Bulgarian NSF project KP-06-N89/07 (КП-06-Н89/07).

Conflicts of Interest: The authors declare no conflicts of interest.

References

1. Ashraf, M.; Ayaz, M.; Khan, M.; Adil, S.; Faroog, W.; Ullah, N.; Tahir, M. Recent Trends in Sustainable Solar Energy Conversion Technologies: Mechanisms, Prospects, and Challenges. *Energy Fuels* **2023**, *37*, 6283–6301. [CrossRef]
2. Imran, S.; Hussain, M. Emerging trends in water splitting innovations for solar hydrogen production: Analysis, comparison, and economical insights. *Int. J. Hydrogen Energy* **2024**, *77*, 975–996. [CrossRef]
3. Wu, S.; Hu, H.; Lin, Y.; Zhang, J.; Hu, Y. Visible light photocatalytic degradation of tetracycline over TiO_2. *Chem. Eng. J.* **2020**, *382*, 122842. [CrossRef]
4. Domínguez, C.; García, J.; Pedraz, M.; Torres, A.; Galán, M. Photocatalytic oxidation of organic pollutants in water. *Catal. Today* **1998**, *40*, 85–101. [CrossRef]
5. Pattnaik, A.; Sahu, J.; Poonia, A.; Ghosh, P. Current perspective of nano-engineered metal oxide based photocatalysts in advanced oxidation processes for degradation of organic pollutants in wastewater. *Chem. Eng. Res. Des.* **2023**, *190*, 667–686. [CrossRef]
6. Acher, A. Sunlight Photooxidation of Organic Pollutants in Wastewater. *Water Sci. Technol.* **1985**, *17*, 623–632. [CrossRef]
7. Yaqoob, A.; Noor, N.; Serrà, A.; Ibrahim, M. Advances and Challenges in Developing Efficient Graphene Oxide-Based ZnO Photocatalysts for Dye Photo-Oxidation. *Nanomaterials* **2020**, *10*, 932. [CrossRef]
8. Antuch, M.; Rouby, W.; Millet, P. A comparison of water photo-oxidation and photo-reduction using photoelectrodes surface-modified by deposition of co-catalysts: Insights from photo-electrochemical impedance spectroscopy. *Int. J. Hydrogen Energy* **2019**, *44*, 9970–9977. [CrossRef]
9. Ojha, N.; Pant, K.; Coy, E. Photocatalytic Conversion of Carbon Dioxide and Nitrogen Dioxide: Current Developments, Challenges, and Perspectives. *Ind. Eng. Chem. Res.* **2023**, *62*, 21885–21908. [CrossRef]
10. Lu, Z.; Wang, Z. Complete Photooxidation of Formaldehyde to CO_2 via Ni-Dual-Atom Decorated Crystalline Triazine Frameworks: A DFT Study. *Toxics* **2024**, *12*, 242. [CrossRef]
11. Saravanan, A.; Kumar, P.; Jeevanantham, S.; Karishma, S.; Kiruthika, A. Photocatalytic disinfection of micro-organisms: Mechanisms and applications. *Environ. Technol. Innov.* **2021**, *24*, 101909. [CrossRef]
12. Feng, M.; Lv, S.; Deng, J.; Guo, Y.; Wu, Y.; Shi, G.; Zhang, M. An overview of environmental energy harvesting by thermoelectric generators. *Renew. Sustain. Energy Rev.* **2023**, *187*, 113723. [CrossRef]
13. Myers, A.; Hodges, R.; Jur, J. Human and environmental analysis of wearable thermal energy harvesting. *Energy Convers. Manage.* **2017**, *143*, 218–226. [CrossRef]
14. Oturan, M.A.; Aaron, J.J. Advanced oxidation processes in water/wastewater treatment: Principles and applications. A review. *Crit. Rev. Environ. Sci. Technol.* **2014**, *44*, 2577–2641. [CrossRef]
15. Niu, S.; Wang, Z.L. Theoretical systems of triboelectric nanogenerators. *Nano Energy* **2015**, *14*, 161–192. [CrossRef]

16. Liu, C.; Wang, Y.; Zhang, N.; Yang, X.; Wang, Z.; Zhao, L.; Yang, W.; Dong, L.; Che, L.; Wang, G.; et al. A self-powered and high sensitivity acceleration sensor with V-Q-a model based on triboelectric nanogenerators. *Nano Energy* **2020**, *67*, 104228. [CrossRef]
17. Li, X.; Tong, W.; Shi, J.; Chen, Y.; Zhang, Y.; An, Q. Tribocatalysis mechanisms: Electron transfer and transition. *J. Mater. Chem. A* **2023**, *11*, 4458–4472. [CrossRef]
18. Xiao, X.; Zhang, X.; Wang, S.; Ouyang, H.; Chen, P.; Song, L.; Yuan, H.; Ji, Y.; Wang, P.; Li, Z.; et al. Honeycomb structure inspired triboelectric nanogenerator for highly effective vibration energy harvesting and selfpowered engine condition monitoring. *Adv. Energy Mater.* **2019**, *9*, 1902460. [CrossRef]
19. Zhao, P.; Soin, N.; Prashanthi, K.; Chen, J.; Dong, S.; Zhou, E.; Zhu, Z.; Narasimulu, A.; Montemagno, C.; Yu, L.; et al. Emulsion electrospinning of polytetrafluoroethylene (PTFE) nanofibrous membranes for high-performance triboelectric nanogenerators. *ACS Appl. Mater. Inter.* **2018**, *10*, 5880–5891. [CrossRef]
20. Sharma, D.; Shukla, S.; Sharma, K.; Kumar, V. A review on ZnO: Fundamental properties and applications. *Mater. Today* **2022**, *49*, 3028–3035. [CrossRef]
21. Chong, J.; Tai, B.; Zhang, Y. Tribocatalysis effect based on ZnO with various specific surface areas for dye degradation. *Chem. Phys. Lett.* **2024**, *835*, 140998. [CrossRef]
22. Lei, H.; Cui, X.; Jia, X.; Qi, J.; Wang, J.; Chen, W. Enhanced Tribocatalytic Degradation of Organic Pollutants by ZnO Nanoparticles of High Crystallinity. *Nanomaterials* **2023**, *13*, 46. [CrossRef]
23. Zhao, J.; Chen, L.; Luo, W.; Li, H.; Wu, Z.; Xu, Z.; Zhang, Y.; Zhang, H.; Yuan, G.; Gao, J.; et al. Strong tribo-catalysis of zinc oxide nanorods via triboelectrically-harvesting friction energy. *Ceram. Int.* **2020**, *46*, 25293–25298. [CrossRef]
24. Kumbhakar, P.; Mishra, S.; Kumbhakar, P.; Barik, R.; Tiwary, C.; Singh, A. Strain-Induced Tribocatalytic Activity of 2D ZnO Quantum Dots. *J. Phys. Chem. C* **2024**, *128*, 10733–10741. [CrossRef]
25. Xiao, L.; Xu, X.; Wu, Z.; Sun, T.; He, X.; Xu, X.; Qin, L.; Chen, D. Recent progress and prospect of friction-driven-tribocatalysis: From basic principle to material design. *Surf. Interfaces* **2025**, *56*, 105557. [CrossRef]
26. Mohamed, W.; Abu-Dief, A. Synthesis, characterization and photocatalysis enhancement of Eu_2O_3-ZnO mixed oxide nanoparticles. *J. Phys. Chem. Solids* **2018**, *116*, 375–385. [CrossRef]
27. Dong, X.U.; Jiang, B.; Jiao, L.; Cui, F.-D.; Xu, H.-X.; Yang, Y.-T.; Yu, R.-H.; Cheng, X.-N. Sol–gel synthesis of Y_2O_3-doped ZnO thin films varistors and their electrical properties. *Trans. Nonferrous Met. Soc. China* **2012**, *22* (Suppl. S1), s110–s114.
28. Chao, L.C.; Huang, J.W.; Chang, C.W. Annealing effects on the properties of Nd containing ZnO nanoparticles prepared by sol-gel process. *Physica B* **2009**, *404*, 1301. [CrossRef]
29. Wang, R.H.; Xin, J.H.Z.; Yang, Y.; Liu, H.F.; Xu, L.M.; Hu, J.H. The characteristics and photocatalytic activities of silver doped ZnO nanocrystallites. *Appl. Surf. Sci.* **2004**, *227*, 312. [CrossRef]
30. Aydın, C.; El-Sadek, M.S.A.; Zheng, K.; Yahia, I.S.; Yakuphanoglu, F. Synthesis, diffused reflectance and electrical properties of nanocrystalline Fe-doped ZnO via sol-gel calcination technique. *Opt. Laser Technol.* **2013**, *48*, 447–452. [CrossRef]
31. Yang, L.; Wang, Z.; Zhang, Z.; Sun, Y.; Gao, M.; Yang, J.; Yan, Y. Surface effects on the optical and photocatalytic properties of graphene-like ZnO:Eu^{3+} nanosheets. *J. Appl. Phys.* **2013**, *113*, 33514. [CrossRef]
32. Najafi, M.; Haratizadeh, H. Synthesize and optical properties of ZnO: Eu microspheres based nano-sheets at direct and indirect excitation. *Int. J. Nanosci. Nanotechnol.* **2015**, *11*, 101–113.
33. Gao, M.; Yan, C.; Li, B.; Zhou, L.; Yao, J.; Zhang, Y.; Liu, H.; Cao, L.; Cao, Y.; Yang, J.; et al. Strong red emission and catalytic properties of ZnO by adding Eu_2O_3 shell. *J. Alloys Compd.* **2017**, *724*, 537–542. [CrossRef]
34. Ivanova, D.; Kolev, H.; Stefanov, B.I.; Kaneva, N. Enhanced Tribodegradation of a Tetracycline Antibiotic by Rare-Earth-Modified Zinc Oxide. *Molecules* **2024**, *29*, 3913. [CrossRef] [PubMed]
35. Brunckova, H.; Rocha, L.A.; Nassar, E.J.; Moscardini, S.B.; Kolev, H. Luminescence properties of neodymium, samarium, and europium niobate and tantalate thin films. *Luminescence* **2022**, *37*, 642. [CrossRef]
36. Singh, V.; Sivaramaiah, G.; Rao, J.L.; Dhoble, S.J.; Kim, S.H. Mn^{2+}, Eu^{2+} and Eu^{3+} emission in co-doped $LaAl_{11}O_{18}$ phosphors. *Mater. Chem. Phys.* **2015**, *149–150*, 202–208. [CrossRef]
37. Dehelean, A.; Rada, S.; Popa, A.; Suciu, R.C.; Culea, E. Raman, photoluminescence and EPR spectroscopic characterization of europium(III) oxide-lead dioxide-tellurite glassy network. *J. lumin.* **2016**, *177*, 65–70. [CrossRef]
38. Somasundarama, K.; Girija, K.G.; Christopher, P.S.; Sudarsan, V.; Kadam, R.M.; Vatsa, R.K. Blue electroluminescence from $ZnGa_2O_4$:Eu powder samples. *J. Lumin.* **2017**, *185*, 145–150. [CrossRef]
39. Petrosyan, A.G.; Asatryan, H.R.; Hovhannesyan, K.L.; Derdzyan, M.V.; Feofilov, S.P.; Eganyan, A.V.; Sargsyan, R.S. Growth, optical and EPR studies of 151 Eu^{2+}:YAG single crystals. *Mater. Chem. Phys.* **2017**, *185*, 39–43. [CrossRef]
40. Reddy, J.A.; Kokila, M.K.; Nagabhushana, H.; Shivakumara, C.; Chakradhar, R.P.S.; Nagabhushana, B.M.; Krishna, H.R. Luminescence studies and EPR investigation of solution combustion derived Eu doped ZnO. *Spectrochim Acta Part A* **2014**, *132*, 305–312. [CrossRef]
41. Brückner, A.; Bentrup, U.; Zanthoff, H.; Maschmeyer, D. The role of different Ni sites in supported nickel catalysts for butene dimerization under industry-like conditions. *J. Catal.* **2009**, *266*, 120–128. [CrossRef]

42. Micic, O.I.; Zhang, Y.; Cromack, K.R.; Trifunac, A.D.; Thurmauer, M.C. Trapped holes on TiO_2 colloids studied by Electron Paramagnetic Resonance. *J. Phys. Chem.* **1993**, *97*, 7277–7283. [CrossRef]
43. Li, W.; Zhang, H.; Zhang, X.; Qin, G.; Li, H.; Xiong, Y.; Ye, L.; Ruan, H.; Tong, C.; Kong, C.; et al. Non-axial NO-VZn shallow acceptor complexes in nitrogen implanted p-type ZnO thin films. *Appl. Surf. Sci.* **2020**, *529*, 147168. [CrossRef]
44. Ammar, A.; Yildirim, I.; Aleinawi, M.; BulduAkturk, M.; Turhan, N.; Nadupalli, S.; Rostas, A.; Erdem, E. Multifrequency EPR spectroscopy study of Mn, Fe, and Cu doped nanocrystalline ZnO. *Mat. Res. Bull.* **2023**, *160*, 112117. [CrossRef]
45. Krasilinikov, V.; Dyachkova, T.; Tyutyunnik, A.; Gyrdasova, O.; Melkozerova, M.; Baklanova, I.; Perevozchikova, Y.A.; Emelyanova, S.M.; Weber, H.; Marchenkov, V. Magnetic and optical properties as well as EPR studies of polycrystalline ZnO synthesized from different precursors. *Mat. Res. Bull.* **2018**, *97*, 553–559. [CrossRef]
46. Decremps, F.; Pellicer-Porres, J.; Saitta, A.; Chervin, J.; Polian, A. High-pressure Raman sprectroscopy study of wurtzite ZnO. *Phys. Rev. B* **2002**, *65*, 092101. [CrossRef]
47. Kumar, S.; Kumar, T.; Kaur, H.; Kumar, A.; Kumar, A. Optimizing photocatalysis: Tuning europium concentration in zinc oxide nanoparticles for superior performance. *Phys. B Condens. Matters* **2025**, *697*, 416699.
48. AlAbdulaal, T.; Ganesh, V.; AlShadidi, M.; Hussien, M.; Bouzidi, A.; Algarni, H.; Zahran, H.; Abdel-wahab, M.; Yahia, I.; Nasr, S. The Auto-Combustion Method Synthesized Eu_2O_3- ZnO Nanostructured Composites for Electronic and Photocatalytic Applications. *Materials* **2022**, *15*, 3257. [CrossRef]
49. Kumar, M.; Chauhan, M.; Akhtar, M.; Umar, A. Effect of cerium ions in Ce-Doped ZnO nanostructures on their photocatalytic and picric acid chemical sensing. *Ceram. Int.* **2021**, *47*, 3089–3098. [CrossRef]
50. Chandrasekhar, M.; Nagabhushana, H.; Sharma, S.; Sudheer kumar, K.; Dhananjaya, N.; Sunitha, D.; Shivakumara, C.; Nagabhushana, B. Particle size, morphology and color tunable ZnO:Eu^{3+} nanophosphors via plant latex mediated green combustion synthesis. *J. Alloys Compd.* **2014**, *584*, 417–424. [CrossRef]
51. Ntwaeaborwa, O.; Mofokeng, S.; Kumar, V.; Kroon, R. Structural, optical and photoluminescence properties of Eu^{3+} doped ZnO nanoparticles. *Spectrochim. Acta A* **2017**, *182*, 42–49. [CrossRef] [PubMed]
52. Röder, R.; Geburt, S.; Zapf, M.; Franke, D.; Lorke, M.; Frauenheim, T.; Luisa da Rosa, A.; Ronning, C. Transition metal and rare earth element doped zinc oxide nanowires for optoelectronics. *Phys. Status Solidi B* **2019**, *256*, 1800604. [CrossRef]
53. Kumar, V.; Som, S.; Kumar, V.; Kumar, V.; Ntwaeaborwa, O.; Coetsee, E.; Swart, H. Tunable and white emission from ZnO:Tb^{3+} nanophosphors for solid state lighting applications. *Chem. Eng. J.* **2014**, *255*, 541–552. [CrossRef]
54. Marin, R.; Oussta, F.; Katea, S.; Prabhudev, S.; Botton, G.; Westin, G.; Hemmer, E. Europium-doped ZnO nanosponges—Controlling optical properties and photocatalytic activity. *J. Mater. Chem. C* **2019**, *7*, 3909–3919. [CrossRef]
55. Wu, M.; Xu, Y.; He, Q.; Sun, P.; Weng, X.; Dong, X. Tribocatalysis of homogeneous material with multi-size granular distribution for degradation of organic pollutants. *J. Colloid Interface Sci.* **2022**, *622*, 602–611. [CrossRef] [PubMed]
56. Xu, Y.; Yin, R.; Zhang, Y.; Zhou, B.; Sun, P.; Dong, X. Unveiling the Mechanism of Frictional Catalysis in Water by $Bi_{12}TiO_{20}$: A Charge Transfer and Contaminant Decomposition Path Study. *Langmuir* **2022**, *38*, 14153–14161. [CrossRef]
57. Dash, D.; Panda, N.; Sahu, D. Photoluminescence and photocatalytic properties of europium doped ZnO nanoparticles. *Appl. Surf. Sci.* **2019**, *494*, 666–674. [CrossRef]
58. Kumar, M.; Singh, G.; Chauhan, M. Europium (Eu^{3+})—Doped ZnO nanostructures: Synthesis, characterization, and photocatalytic, chemical sensing and preliminary assessment of magnetic properties. *Ceram. Int.* **2021**, *47*, 17023–17033. [CrossRef]
59. Kraus, W.; Nolze, G. POWDER CELL—A program for the representation and manipulation of crystal structures and calculation of the resulting X-ray powder patterns. *J. Appl. Crystallogr.* **1996**, *29*, 301–303. [CrossRef]
60. Dollase, W.A. Correction of intensities for preferred orientation in powder diffractometry: Application of the March model. *J. Appl. Crystallogr.* **1986**, *19*, 267–272. [CrossRef]
61. Shirley, D. High-Resolution X-Ray Photoemission Spectrum of the Valence Bands of Gold. *Phys. Rev. B* **1972**, *5*, 4709–4714. [CrossRef]
62. Scofield, J. Hartree-Slater subshell photoionization cross-sections at 1254 and 1487 eV. *J. Electron Spectrosc. Relat. Phenom.* **1976**, *8*, 129. [CrossRef]
63. Moulder, F.; Sticke, W.F.; Sobol, P.E.; Bombel, K.D. *Handbook of X-Ray Photoelectron Spectroscopy*, 2nd ed.; Castain, J., Ed.; Physical Electron Division; Perkin-Elmer Corporation: Eden Prairie, MN, USA, 1992.
64. Jia, X.; Wanga, H.; Lei, H.; Mao, C.; Cui, X.; Liu, Y.; Jia, Y.; Yao, W.; Chen, W. Boosting tribocatalytic conversion of H_2O and CO_2 by Co_3O_4 nanoparticles through metallic coatings in reactors. *J. Adv. Ceram.* **2023**, *12*, 1833–1843. [CrossRef]

molecules

MDPI

Article

Insight into the Local Surface Plasmon Resonance Effect of Pt-SnS_2 Nanosheets in Tetracycline Photodegradation

Mao Feng [1], Tianhao Zhou [2], Jiaxin Li [2], Mengqing Cao [2], Jing Cheng [2], Danyang Li [2,3,*], Jian Qi [4,5,*] and Feifei You [2,*]

[1] Textile School, Zhejiang Fashion Institute of Technology, Ningbo 315211, China; xgf@msn.com
[2] College of Textile and Clothing, Yancheng Institute of Technology, Yancheng 224051, China; 17311504196@163.com (T.Z.); 19705102579@163.com (J.L.); 18164327219@163.com (M.C.); 19705100129@163.com (J.C.)
[3] Sichuan Provincial Engineering Research Center of Functional Development and Application of High Performance Special Textile Materials, Chengdu Textile College, Chengdu 611731, China
[4] State Key Laboratory of Biochemical Engineering, Institute of Process Engineering, Chinese Academy of Sciences, Beijing 100190, China
[5] School of Chemical Engineering, University of Chinese Academy of Sciences, Beijing 100049, China
* Correspondence: strawberry4173@163.com (D.L.); jqi@ipe.ac.cn (J.Q.); ffyouycit@163.com (F.Y.)

Abstract: Constructing highly efficient catalysts for the degradation of organic pollutants driven by solar light in aquatic environments is a promising and green strategy. In this study, a novel hexagonal sheet-like Pt/SnS_2 heterojunction photocatalyst is successfully designed and fabricated using a hydrothermal method and photodeposition process for photocatalytic tetracycline (TC) degradation. The optimal Pt/SnS_2 hybrid behaves with excellent photocatalytic performance, with a degradation efficiency of 91.27% after 120 min, a reaction rate constant of 0.0187 min^{-1}, and durability, which can be attributed to (i) the formation of a metal/semiconductor interface field caused by loading Pt nanoparticles (NPs) on the surface of SnS_2, facilitating the separation of photo-induced charge carriers; (ii) the local surface plasmon resonance (LSPR) effect of Pt NPs, extending the light absorption range; and (iii) the sheet-like structure of SnS_2, which can shorten the transmission distance of charge carriers, thereby allowing more electrons (e^-) and holes (h^+) to transfer to the surface of the catalyst. This work provides new insights with the utilization of sheet-like structured materials for highly active photocatalytic TC degradation in wastewater treatment and environmental remediation.

Keywords: sheet structure; Pt/SnS_2; tetracycline; photodegradation; heterogeneous junction

1. Introduction

Antibiotics are crucial for preventing and treating bacterial infections in humans and infectious diseases in livestock [1,2]. Tetracycline (TC), as a broad-spectrum antibiotic, is renowned for its potent antibacterial properties and better cost-effectiveness [3,4]. Unfortunately, due to the chemical stability and resistance to biodegradation of TC, the residual TC will eventually be released into the soil and aquatic environments, causing serious pollution to the environment, and then posing significant threats to ecosystems and human health [5,6]. Despite various wastewater treatment methods such as adsorption, biological treatment, membrane separation, and advanced oxidation processes, the drawbacks of secondary pollution, high energy consumption, low efficiency, and complicated treatment processes restrict the widespread application of these strategies [7,8]. Therefore, developing effective, environmentally friendly, and economical strategies to remove TC antibiotic residues in aquatic environments is an important and urgent issue of crucial significance to the ecological environment, people's health, and the achievement of sustainable development [9].

So far, photocatalytic TC degradation driven by inexhaustible green solar energy is considered one of the most promising solutions owing to its high efficiency and stability,

low toxicity and cost, sustainability, and recyclability [10–12]. In a nutshell, photocatalysts generate photo-generated e^-/h^+ pairs with redox properties under light illumination, which can transfer to the surface of the photocatalyst and react with H_2O and O_2 to produce active species such as hydroxyl radicals (·OH) and superoxide anion radicals ($\cdot O_2{}^-$), and then the radicals are exploited to degrade TC to form harmless products [13,14]. The key factors enhancing the photodegradation efficiency include increasing light capture and absorption, hindering the fast recombination of photo-induced charge carriers, and improving mass transport. Thus, the delicate design of the macro-structure and elaborate choice of micro-composition are highly required to achieve satisfactory degradation efficiency.

Two-dimensional (2D) sheet-like materials possess unique merits in the field of photocatalysis [15–25], such as shortening the transport path of charge carriers to make more photo-excited e^- and h^+ pairs to participate in reactions on the surfaces of the catalysts, exposing specific crystal planes to provide more reactive sites, and preventing catalysts from aggregating together during the reaction process [26–37]. Additionally, the semiconductors with 2D structures, such as TiO_2 [38], g−C_3N_4 [39], Fe_2O_3 [40], ZnO [41], and SnS_2 [42], etc., are considered to be promising candidates for the efficient photocatalytic degradation of TC. Among them, SnS_2, an n-type semiconductor with a fascinating band gap of ~2.2 eV and the advantages of being non-toxic, harmless, easy to prepare, inexpensive, and environmentally friendly, has been extensively studied for the photodegradation of water pollutants [43,44]. However, pure SnS_2 tends to suffer from the weakness of rapid carrier recombination, restricting its photocatalytic efficiency. In view of this, constructing heterojunctions as well as decorating noble metal NPs is an effective method to overcome this intrinsic limitation. Noble metals, such as Ag, Au, Pt, and Pd, have been verified to display unique LSPR effects and are extensively employed as co-catalysts to enhance photocatalytic efficiency [45]. The noble metal NPs can absorb and scatter visible light, causing a strong local electromagnetic field, which benefits the excitation, separation, and transfer of photo-induced carriers, improving the photocatalytic activity. Vishal et al. [46] successfully designed and synthesized a novel ternary Z-Scheme Ag/HAp/SnS_2 catalyst for the photodegradation of metronidazole, which behaved with excellent photodegradation efficiency because of the formation of heterogeneous junctions and Ag NPs acting as a charge transfer medium and e^- accumulators delaying e^-/h^+ recombination. Li et al. [47] successfully prepared a hollow-structured Pt/TiO_2 hybrid as a catalyst for photocatalytic TC degradation, exhibiting great photodegradation performance and durability attributed to the formation of Schottky junctions and the LSPR effect of Pt.

In this work, Pt NPs loaded on sheet-like-structured SnS_2 hybrids were designed and synthesized through a simple hydrothermal process and photodeposition reaction toward TC photodegradation. Pt NPs extended the light absorption range due to the LSPR effect as well as captured the e^- of SnS_2 with plasmonic hot h^+ caused by tough electron oscillation of LSPR excitation. Additionally, Pt NPs also played the role of e^- grooves, which could promote the separation of charge carriers and enrich e^-. Benefiting from the Schottky junction constructed between Pt and SnS_2 and the natural advantages of the sheet-like structure of a short carrier transfer path and more exposed active reaction sites, the optimal specimen showed outstanding photocatalytic TC degradation activity with a degradation efficiency of 91.27% under light illumination for 120 min, a rate constant of 0.0194 min^{-1}, and durability in five cycles without apparent activity reduction. Thus, we believe that the sheet-like-structured Pt/SnS_2 heterogeneous junction catalyst provides a different strategy for the construction of highly efficient photocatalysts for the degradation of water pollutants.

2. Results and Discussion

2.1. Morphological and Structural Characterization

The synthesis procedure of a sheet-like Pt/SnS_2 hybrid is illustrated in Figure 1a. Briefly, the hard template method was used to synthesize the SnO_2 hollow sphere, with CMS and $SnCl_4$ as a sacrificial template and metal ion precursor, and then sheet-like-structured SnS_2 was obtained through sulfuration treatment in the presence of TAA. After that, 2D

heterogeneous junction Pt/SnS_2 hybrids were prepared via a subsequent photodeposition process. As shown in the transmission electron microscopy (TEM) image (Figure 1b), the SnO_2 hollow spheres display a coarse surface with an outer diameter of 600–700 nm. After sulfuration, it could be obviously observed that the SnO_2 hollow sphere became the hexagonal sheet-like-structured SnS_2 (Figure 1c). It must be pointed out that the structure has changed from three-dimensional (3D) to two-dimensional (2D), resulting in a significant increase in size. Figure 1d demonstrates the TEM of the Pt/SnS_2 hybrid, and the Pt NPs with an average diameter of 10.56 nm are uniformly dispersed on the surface of the SnS_2 sheet. The high-resolution TEM (HRTEM) image of the Pt/SnS_2 hybrid displayed in Figure 1e indicates that the heterojunction formed by SnS_2 and Pt and the Pt NPs are tightly anchored at the surfaces of SnS_2. Two lattice fringes were measured with the interplanar distances of 0.18 and 0.23 nm, which corresponded to the (110) plane of SnS_2 [48] and the (111) plane of Pt [49], respectively. Furthermore, the corresponding high-angle annular dark-field scanning transmission electron microscopy (HAADF−STEM) and elemental mapping images (Figure 1f–i) of the Pt/SnS_2 hybrid verified that the elements of Sn, S, and Pt were well dispersed throughout the catalyst and further confirmed the uniform distribution of Pt nanoparticles loaded on the surfaces of sheet-like Pt/SnS_2, indicating the formation of ample intimate heterointerfaces between Pt and SnS_2.

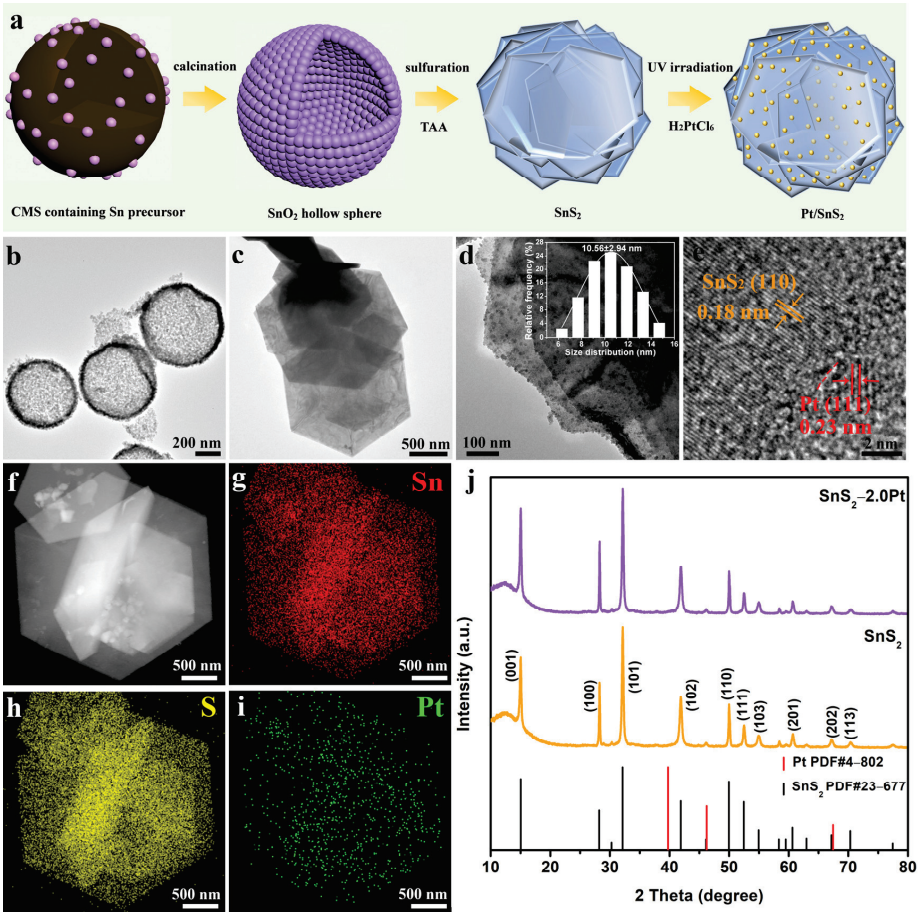

Figure 1. (**a**) Schematic illustration of the synthesis process of sheet-like-structured SnS_2 and Pt/SnS_2 hybrids; TEM images of (**b**) SnO_2 hollow sphere, (**c**) SnS_2 and (**d**) SnS_2-2.0Pt with inset of particle size distribution of Pt NPs; HRTEM image of (**e**) SnS_2-2.0Pt; (**f**) HAADF−STEM and (**g**–**i**) elemental distribution images of SnS_2−2.0Pt; and (**j**) XRD patterns of SnS_2 and SnS_2−2.0Pt with standard diffraction peaks of SnS_2 and Pt (vertical lines).

The crystallographic properties and phase composition of the SnS_2 and SnS_2−2.0Pt hybrids were investigated by X-ray diffraction (XRD) patterns (Figure 1j). The typical diffraction

spectrum with specific peaks of pure SnS_2 is indexed by hexagonal SnS_2 (PDF#23-0677) [48], and the diffraction peaks located at 15.029, 28.199, 32.124, 41.886, 49.960, 52.451, 54.960, 60.619, 67.152, and 70.333° are well attributed to (001), (100), (101), (102), (110), (111), (103), (201), (202), and (113) crystal facets with lattice constants of a = b = 3.6486 Å and c = 5.8992 Å. The absence of no impurity peaks demonstrates that pure SnS_2 has been successfully fabricated. As for SnS_2−2.0Pt, loading Pt NPs does not influence the crystalline structure of SnS_2. The deposition of Pt NPs at SnS_2−2.0Pt concentrations was not detected in the XRD pattern with JCPDS card no. 4−802 because of the small particle size of Pt NPs with highly uniform dispersion onto the sheet-like SnS_2. Nevertheless, the energy-dispersive spectroscopy of SnS_2−2.0Pt illustrated in Figure S1 displays that Pt NPs do exist.

2.2. XPS Analysis

An X-ray photoelectron spectroscopy (XPS) test was used to investigate the element composition and valence state of as-prepared samples. Figure 2a depicts the survey XPS spectra of SnS_2 and SnS_2−2.0Pt, and the peaks of Pt only can be observed in SnS_2−2.0Pt, proving once again the successful modification of Pt onto SnS_2. The peaks at 486.9 and 495.3 eV in Figure 2b mainly focus on Sn $3d_{5/2}$ and Sn $3d_{3/2}$, belonging to the binding energies of Sn^{4+} states [50]. And the high-resolution XPS scans of the S 2p spectrum exhibit two peaks with the binding energies of 161.9 and 163.1 eV (Figure 2c), corresponding to S $2p_{3/2}$ and S $2p_{1/2}$, respectively, confirming the chemical state of S with −2 valence in the SnS_2 sheet. However, compared to the pure SnS_2, the binding energies of S 2p and Sn 3d for SnS_2−2.0Pt showed a slightly negative shift toward a lower direction of 0.5 eV (S 2p) and 0.5 eV (Sn 3d), indirectly confirming the closed interaction between Pt NPs and SnS_2, which shows that the e^- of SnS_2 migrate to Pt at the interface. As shown in Figure 2d, the Pt 4f XPS spectrum of SnS_2−2.0Pt can be divided into two double peaks. The peaks located at 71.7 eV and 75.1 eV belong to the Pt $4f_{7/2}$ and Pt $4f_{5/2}$ of metal Pt^0, while the peaks at 73.0 eV and 76.3 eV correspond to the Pt $4f_{7/2}$ and Pt $4f_{5/2}$ of Pt^{2+} [51–54], existing in the interfaces of Pt and SnS_2 or the oxidized Pt atoms [55]. Moreover, the ratio of Pt^0/Pt is 70.18% (Table S1), demonstrating that Pt is mainly presented in the metallic form.

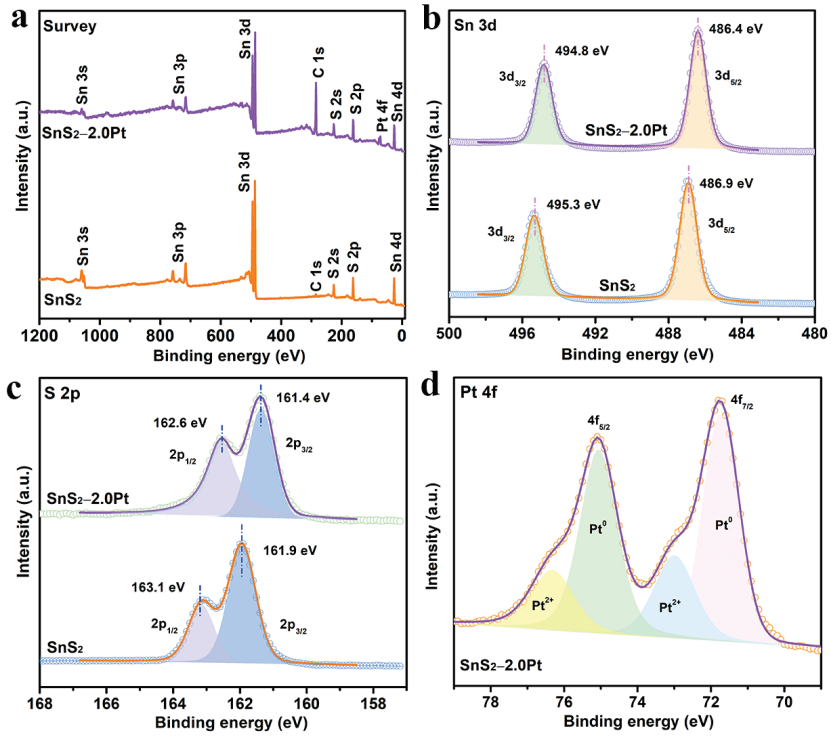

Figure 2. XPS spectra of SnS_2 and SnS_2−2.0Pt: (**a**) survey; high-resolution XPS spectra of (**b**) Sn 3d, (**c**) S 2p, and (**d**) Pt 4f.

2.3. Photocatalytic TC Degradation Evolution

The photocatalytic property tests of TC degradation for all as-prepared samples were carried out under 300 W Xe lamp irradiation. The standard curve of absorbance vs. varied concentrations of TC is displayed in Figure S2. The initial TC solution containing catalysts was stirred for 30 min in a dark environment, aiming to achieve adsorption/desorption equilibrium between TC and the catalyst before illumination. Firstly, the blank experiment was conducted. The test result (Figure 3a) showed that the TC was difficult to degrade under the condition of no light irradiation, while the concentration of TC significantly decreased in the existence of light and the catalyst. The pure SnS_2 demonstrated a degradation efficiency of 52.15% for TC within 120 min. And for Pt/SnS_2 hybrids, there was a rise in the Pt NP amount loaded on the SnS_2 sheet. The degradation activity was improved; however, the excess loading amount of Pt NPs caused a decrease in the performance of TC degradation. The degradation efficiency of TC was 76.32%, 84.76%, 91.27%, and 83.65% for SnS_2−1.0Pt, −1.5Pt, −2.0Pt, and −2.5Pt, respectively, and SnS_2−2.0Pt showed optimal photocatalytic TC degradation performance behaviors.

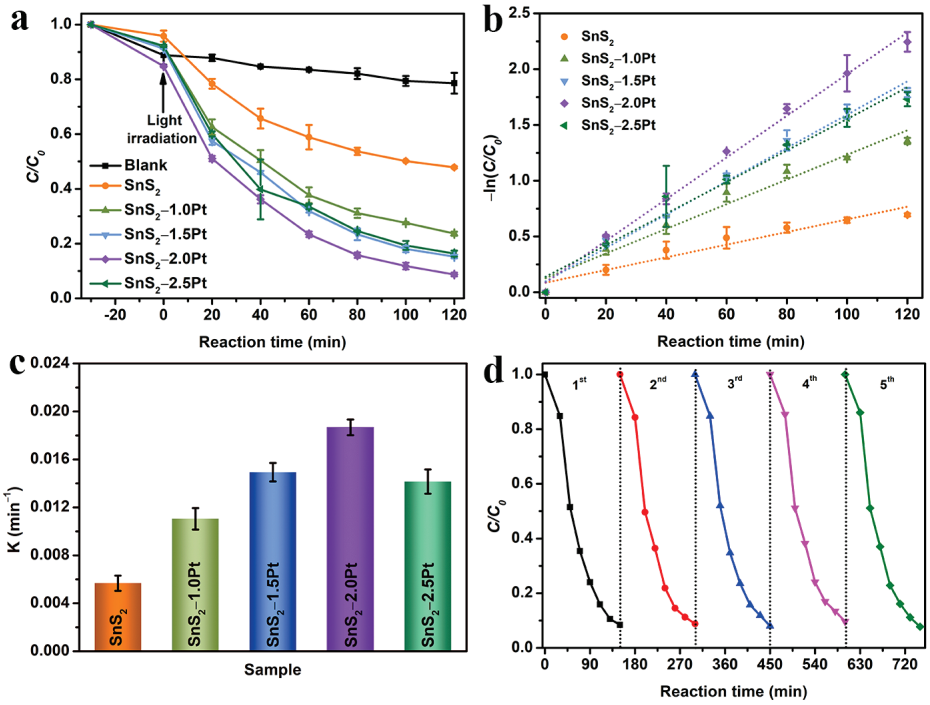

Figure 3. (**a**) Photocatalytic activities of all as-prepared samples during the degradation of TC, (**b**) kinetic curves, (**c**) the reaction rate constant, and (**d**) durability tests of SnS_2−2.0Pt.

Then, the reaction kinetics of the catalytic process for all as-prepared samples was studied using the first-order reaction kinetic equation of $-\ln(C_t/C_0) = kt$, where t is reaction time, C_t stands for the concentration of TC after t min light irradiation, C_0 is the concentration of TC after adsorption/desorption equilibrium in a dark environment, and k is the reaction rate constant (min^{-1}). The fitting data (Figure 3b) demonstrate a very good linear relationship between $-\ln(C_t/C_0)$ and t, and the R^2 values of SnS_2, SnS_2−1.0Pt, −1.5Pt, −2.0Pt, and −2.5Pt are 0.9301, 0.9619, 0.9845, 0.9927, and 0.9699. And the slopes of the fitted lines are represented by the value of k, which is 0.0057, 0.0111, 0.0149, 0.0187, and 0.0142 min^{-1} for SnS_2, SnS_2−1.0Pt, −1.5Pt, −2.0Pt, and −2.5Pt (Figure 3c). Notably, SnS_2−2.0Pt demonstrates the best performance of TC photodegradation among all samples and also possesses strong competitiveness compared with the published papers with the SnS_2-based materials under similar reaction conditions [48,56–60] (Table 1). In addition, Figure 3d shows the recyclability and stability of SnS_2−2.0Pt, in which the degradation rate of TC has no obvious change during five cycles, suggesting the stability of SnS_2−2.0Pt

for photocatalytic TC degradation. And the high stability of the SnS_2-2.0Pt sample crystal structure and morphology can also be proved by the XRD pattern and TEM image (Figure S3). Furthermore, the pH value of the initial TC solution as a major effect parameter was studied during the process of TC degradation. As shown in Figure S4, $SnS_2-2.0Pt$ demonstrated excellent performance under a wide pH range with a TC degradation efficiency of 92.50%, 91.56%, 88.17%, and 83.28 under the initial solution pH values of 3, 5, 9, and 11, respectively. The degradation rate decreased slightly but not significantly in an alkaline environment, indicating that $SnS_2-2.0Pt$ could exhibit good performance in a wide range of pH values.

Table 1. Comparison of TC photodegradation activity of previously published papers with SnS_2-based catalysts.

Catalyst	Initial Concentration of TC (mg/L)	Dosage (g/L)	Reaction Time (min)	Degradation (%)	Kinetic Constant (min^{-1})	Ref.
Pt/SnS_2	**20**	**0.33**	**120**	**91.27**	**0.0187**	**This work**
Fe/SnS_2/Kaolinite [a]	40	0.50	60	80.38	0.0257	48
Zn_2SnO_4/SnS_2	10	0.10	120	83.00	0.0176	56
$BiVO_4/SnS_2$	10	0.20	150	80.80	0.0100	57
$LaFeO_3/SnS_2$	50	0.33	120	28.80	0.0028	58
Bi_2MoO_{6-x}/SnS_2	20	0.20	90	89.00	0.0139	59
Ti_3C_2/SnS_2	10	0.50	90	87.70	0.0156	60

[a] A total of 8 mM of H_2O_2 was added to the reaction system.

2.4. Photoelectronic Tests

In order to investigate the reasons why the $SnS_2-2.0Pt$ sample behaved with such properties during the photodegradation of TC, a series of photoelectronic characterizations were carried out. Figure 4a shows the steady-state photoluminescence (PL) spectra of SnS_2 and $SnS_2-2.0Pt$ with the peak position located at ~550 nm. And $SnS_2-2.0Pt$ displays a weaker peak intensity compared to that of pure SnS_2, suggesting that the heterogeneous structures constructed between SnS_2 and Pt NPs hinder the recombination of photo-induced e^-/h^+ pairs [61]. In addition, time-resolved PL was used to study the characteristics of photo-excited charge carriers. As illustrated in Figure 4b, the average lifetimes ($\tau_{Ave.}$) of SnS_2 and $SnS_2-2.0Pt$ were calculated to be 0.30 and 0.26 ns using the biexponential function, respectively. The shorter average fluorescence lifetime of $SnS_2-2.0Pt$ demonstrated the improved transfer and separation efficiency of charge carriers [62]. Moreover, the electrochemical impedance spectra (EIS) exhibited in Figure 4c show the fitted semicircle diameter values of 69.66 and 19.99 kΩ for SnS_2 and $SnS_2-2.0Pt$, respectively, and smaller semicircles of $SnS_2-2.0Pt$ indicate lower charge carrier transfer resistance. Furthermore, $SnS_2-2.0Pt$ shows higher photocurrent density than that of SnS_2 (Figure 4d), demonstrating a promotion of the generation and separation efficiency of charge carriers due to the heterojunctions in $SnS_2-2.0Pt$. All these characterization results confirm that the generation, separation, and transfer of photo-induced e^-/h^+ pairs can be enhanced in $SnS_2-2.0Pt$ during photocatalytic TC degradation [63,64], resulting in higher photocatalytic activity.

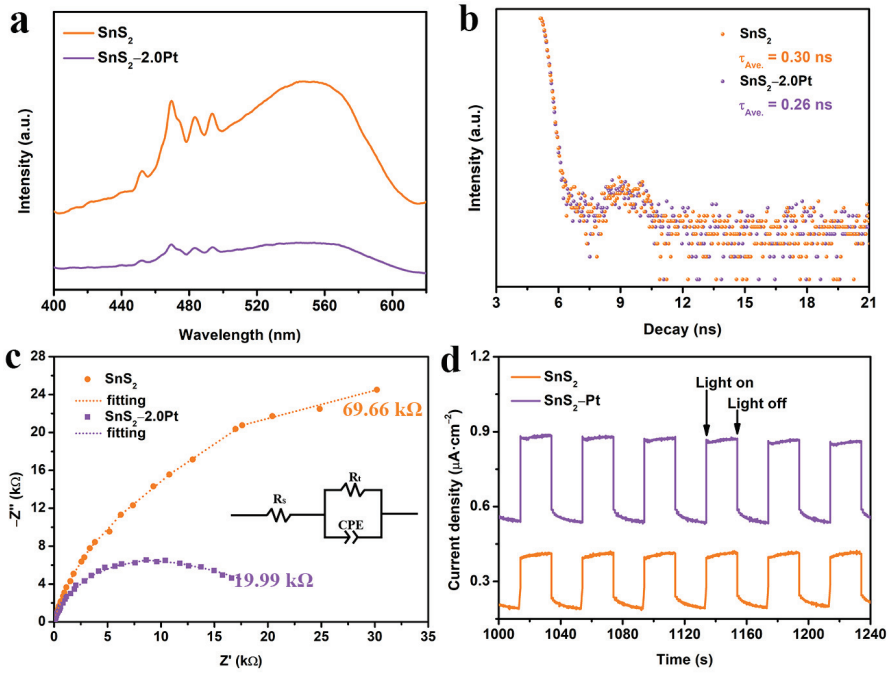

Figure 4. Photoelectronic characterizations of SnS_2 and SnS_2−2.0Pt: (**a**) steady-state PL spectra, (**b**) time-resolved PL spectra, (**c**) EIS Nyquist plots and the fitting circuit diagram (inset), and (**d**) photocurrent density−time curves.

2.5. Mechanism Analysis

Free-radical trapping experiments were implemented to examine the main active species in TC photodegradation. Normally, the active substances, e^-, hydroxyl radicals (·OH), h^+, superoxide radicals ($\cdot O_2^-$), and singlet oxygen ($^1O_2$), were generated during the process of photocatalytic TC degradation, which could be captured using the scavengers of IPA, $K_2S_2O_8$, EDTA, BQ, and FFA, respectively. As displayed in Figure 5a,b, the TC degradation efficiency decreased after adding IPA, $K_2S_2O_8$, EDTA, BQ, and FFA, with the degradation efficiency of 75.30%, 82.72%, 76.11%, 17.56%, and 28.60%, respectively. BQ was a great obstacle to TC degradation, followed by FFA, and IPA, $K_2S_2O_8$, and EDTA illustrated a relatively small impact on TC degradation. Thus, $\cdot O_2^-$ played a dominant role in the degradation process of TC, followed by $^1O_2$, and e^-, ·OH, and h^+ played an auxiliary role [65,66].

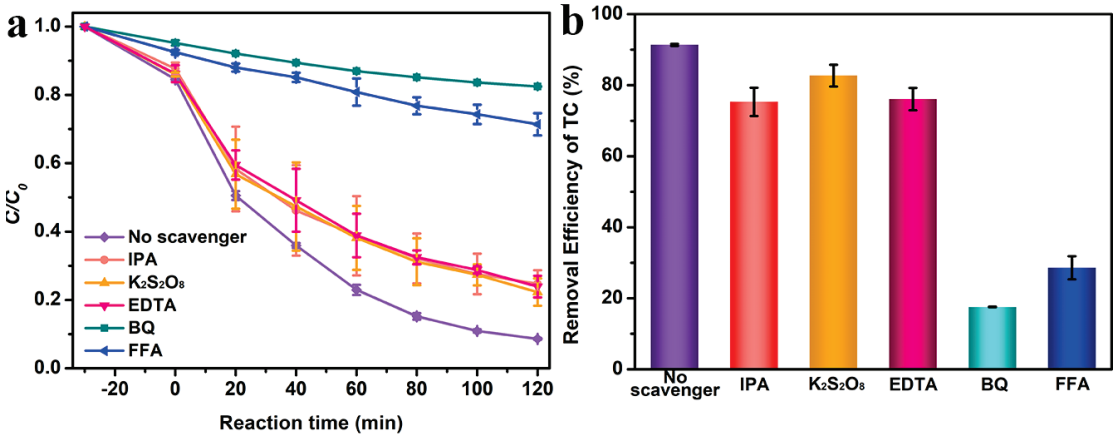

Figure 5. (**a**) Photocatalytic activities of the degradation of TC and (**b**) TC removal efficiency with the SnS_2−2.0Pt catalyst in the presence of various scavengers.

To unveil the catalytic reaction mechanism, corresponding tests were conducted to define the energetic band structure. The UV−Vis light absorption spectra of SnS_2 and

SnS_2−1.0Pt, −1.5Pt, −2.0Pt, and −2.5Pt are revealed in Figure 6a. The light absorption edge is approximately 580 nm for pure SnS_2. After loading Pt NPs on SnS_2, the light absorption of Pt/SnS_2 hybrids is significantly enhanced compared to that of pure SnS_2, which contributes to the LSPR effect of Pt. The Tauc plots can be obtained through the UV−Vis light absorption data. And then the energy band gap (E_g) of as-prepared samples can be determined according to the intercept of the straight lines of the Tauc curves on the *x*-axis. As exhibited in Figure 6b, the E_g values of SnS_2 and SnS_2−2.0Pt are 2.14 and 1.98 eV, respectively. In addition, the Mott−Schottky measurement is used to confirm the location of the flat band (E_f). Figure 6c demonstrates the Mott−Schottky plots under various frequencies of SnS_2, whose slopes are positive, indicating an n-type semiconductor of SnS_2. As for the n-type semiconductor, compared to the position E_f, the conduction band (E_{CB}) potential is negative 0.1 V [67]. According to the intercept of the straight section of the Mott−Schottky curves with various frequencies on the *x*-axis, the E_f potential of SnS_2 is −0.60 V (vs. NHE). And the position of the E_{CB} of SnS_2 is −0.70 V (vs. NHE). The valence band potential (E_{VB}) of SnS_2 is calculated to be 1.44 V (vs. NHE) from the following formula: $E_{VB} = E_g + E_{CB}$ [68]. Thus, the proposed main mechanism of TC photodegradation for the Pt/SnS_2 hybrid is illustrated (Figure 6d) and the related reactions are as follows: Under light irradiation, the e^- are excited and move from the valence band (VB) to the conduction band (CB) of SnS_2; in the meantime, an equal quantity of h^+ is produced in the VB of SnS_2 (Reaction 1). Because of the tough electron oscillation induced by LSPR excitation, the generated plasmonic hot h^+ can capture the e^- in the CB of SnS_2, which can effectively suppress the recombination of photo-excited e^-/h^+ pairs. Then, the oxygen is reduced to $\cdot O_2^-$ (Reaction 2) by the e^-. Subsequently, the $^1O_2$ can be generated through $\cdot O_2^-$ reacting with h^+ (Reaction 3). Finally, TC is degraded by the active species (Reaction 4).

$$Pt/SnS_2 + light \rightarrow e^- + h^+ \quad (1)$$

$$O_2 + e^- \rightarrow \cdot O_2^- \ (-0.33 \text{ V vs. NHE}) \quad (2)$$

$$\cdot O_2^- + h^+ \rightarrow {}^1O_2 \ (0.67 \text{ V vs. NHE}) \quad (3)$$

$$\cdot O_2^-/{}^1O_2 + TC \rightarrow CO_2 + H_2O + \text{other products} \quad (4)$$

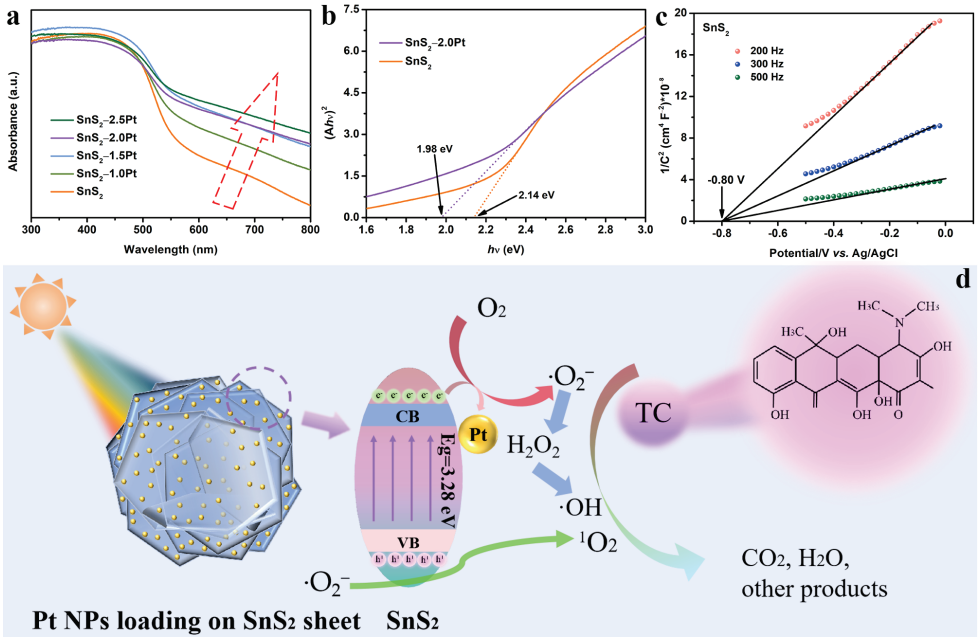

Figure 6. (a) UV−Vis spectra of all samples, (**b**) Tuac curves of SnS_2 and SnS_2−2.0Pt, (**c**) Mott−Schottky plots of SnS_2 and (**d**) the main proposed photocatalytic TC degradation mechanism diagram of the sheet-like SnS_2−2.0Pt heterogeneous catalyst.

3. Materials and Methods

3.1. Materials

Thioacetamide (TAA) and sodium sulfate anhydrous (Na_2SO_4) were purchased from Shanghai Aladdin Biochemical Technology CO., Ltd., Shanghai, China. Tin (IV) chloride pentahydrate ($SnCl_4 \cdot 5H_2O$), chloroplatinic acid (H_2PtCl_6), absolute ethanol, methyl alcohol, isopropyl alcohol (IPA), TC, potassium persulfate ($K_2S_2O_8$), ethylene diamine tetraacetate dehydrate (EDTA), furfuryl alcohol (FFA) and p-ben-zoquinone (BQ) were purchased from Shanghai Macklin Biochemical Technology CO., Ltd., Shanghai, China. Sucrose was supplied from Xilong Science Co., Ltd., Shantou, China. All the above chemicals were analytical reagent grade and were utilized directly without further purification.

3.2. Preparation of Photocatalysts

3.2.1. Preparation of Carbonaceous Microsphere (CMS) Templates

The details can be seen in Supporting Information.

3.2.2. Preparation of SnO_2 Hollow-Structured Microspheres

The synthesis process can be found in Supporting Information.

3.2.3. Preparation of Sheet-Like SnS_2

Firstly, 1.0 g TAA and 100.0 mg SnO_2 hollow spheres were gradually added into 30.0 mL deionized (DI) water, and the suspension was vigorously stirred with a magnetic stirrer for 30 min at room temperature to form a mixed homogeneous solution. Next, the obtained suspension was placed in a 50 mL stainless steel autoclave and crystallized in a 180 °C oven for 3 days. After the stainless steel autoclave was naturally cooled to room temperature, the product was separated by centrifugation and washed several times with deionized water and ethanol in sequence. Finally, the product was dried in a 60 °C oven for 24 h to obtain the yellow powder.

3.2.4. Synthesis of Pt/SnS_2 Hybrids

Firstly, 2 mg/mL H_2PtCl_6 aqueous solution was prepared. Subsequently, 40 mL of deionized water, 10 mL of methanol, and different volumes of H_2PtCl_6 solutions of 1.05, 1.57, 2.10, and 2.62 mL were poured into the beakers in sequence, and this was stirred for 30 min to form a uniform solution. Then, 100 mg of SnS_2 (Pt/SnS_2 mass ratios were 1.00, 1.50, 2.00, and 2.50%, respectively) was added to the above solution with constant magnetic stirring for 2 h under a Xe lamp. Finally, after centrifugal separation, the obtained gray solid powder was washed with deionized water and ethanol, collected, and then dried in a 60 °C oven for 24 h. According to the different deposition amounts of Pt on SnS_2, the synthesized samples are denoted as $SnS_2-1.0Pt$, $SnS_2-1.5Pt$, $SnS_2-2.0Pt$, and $SnS_2-2.5Pt$.

3.3. Characterization

This part can be seen in Supporting Information.

3.4. Evolution of Photocatalytic TC Degradation

Under the irradiation of a 300 W Xe lamp (HF−GHX−XE−300, Shanghai Hefan Instrument Co., Ltd., Shanghai, China), the photocatalytic reactions of the as-prepared samples were evaluated by photodegradation of TC aqueous solution (20 mg/L). The synthesized sample (20 mg) was dispersed into an aqueous TC solution (60 mL), and the suspension was stirred in a dark environment for 30 min to reach adsorption/desorption equilibrium before turning on the light. Subsequently, the photocatalytic suspension system was sampled (3 mL) at specific time intervals during the process of light illumination and then centrifugated to remove the photocatalyst (10,000 rpm/min, 2 min). Finally, the absorbance of the residual TC was measured using a UV−Vis spectrophotometer at 357 nm [42]. For comparison, the degradation of TC under light illumination without a photocatalyst, the

degradation of TC with a photocatalyst under no light, and the degradation of TC in the absence of a photocatalyst and light were also investigated.

4. Conclusions

In summary, Pt NPs loaded on SnS_2 sheet hybrids were successfully designed and synthesized via a simple hydrothermal approach and photodeposition process for photocatalytic TC degradation. Benefiting from the formation of a metal/semiconductor interface field between SnS_2 and Pt enhancing the separation of photo-induced charge carriers, the LSPR effect of Pt strengthening the light absorption, and the sheet-like structure shortening the transfer path of charge carriers, the best catalyst displayed an excellent photocatalytic activity of TC degradation with a degradation efficiency of 91.27%, and a reaction rate constant of 0.0187 min^{-1}, and durability. Our finding not only proposes a feasible strategy for utilizing the combined capabilities of sheet-like structures and the LSPR effect of Pt NPs but also paves a new avenue for the design of efficient and sustainable photodegradable materials for wastewater treatment technologies.

Supplementary Materials: The following supporting information can be downloaded at https://www.mdpi.com/article/10.3390/molecules29225423/s1: Figure S1: The energy-dispersive spectroscopy of SnS2−2.0Pt; Figure S2: The standard curve of absorbance vs. various concentrations of TC; Figure S3: (a) XRD patterns of fresh and used SnS2−2.0Pt and (b) a TEM image of used SnS2−2.0Pt; Figure S4: Photocatalytic TC degradation curves under various pH values of initial of TC; Table S1: A summary of peak area ration and the full width at half maximum of each peak for SnS2−2.0Pt according to XPS peak-fitting results.

Author Contributions: M.F.: methodology, investigation, validation, formal analysis, writing—original draft. T.Z.: methodology, data curation. J.L.: methodology, data curation. M.C.: methodology, data curation. J.C.: methodology, data curation. D.L.: conceptualization, formal analysis, funding acquisition, writing—review and editing. J.Q.: conceptualization, supervision, validation, resources, funding acquisition, writing—review and editing. F.Y.: conceptualization, supervision, funding acquisition, writing—review and editing. All authors have read and agreed to the published version of the manuscript.

Funding: This work was financially supported by funding for school-level research projects of Yancheng Institute of Technology (Nos. xjr2021056 and xjr2021054), A Project Supported by Scientific Research Fund of Zhejiang Provincial Education Department (Project No. Y202456623), the Opening Project of Sichuan Provincial Engineering Research Center of Functional Development and Application of High Performance Special Textile Materials (Chengdu Textile College) (Project No. 2024FDAST-C11), and the National Natural Science Foundation of China (No. 51972306).

Institutional Review Board Statement: Not applicable.

Informed Consent Statement: Not applicable.

Data Availability Statement: Data are contained within the article and Supplementary Materials.

Conflicts of Interest: There are no conflicts of interest to declare.

References

1. Kalelkar, P.P.; Riddick, M.; García, A.J. Biomaterial-Based Antimicrobial Therapies for the Treatment of Bacterial Infections. *Nat. Rev. Mater.* **2022**, *7*, 39–54. [CrossRef] [PubMed]
2. Zhu, Y.; Hao, W.; Wang, X.; Ouyang, J.; Deng, X.; Yu, H.; Wang, Y. Antimicrobial Peptides, Conventional Antibiotics, and Their Synergistic Utility for the Treatment of Drug-Resistant Infections. *Med. Res. Rev.* **2022**, *42*, 1377–1422. [CrossRef] [PubMed]
3. Ren, H.; Pan, Y.; Zhong, J.; Wang, J.; Lu, Z.; He, Q.; Zhou, S.; Liao, X.; Liu, Y.; An, T. An Antibiotic-Destructase-Activated Fenton-Like Catalyst for Synergistic Removal of Tetracycline Residues from Aquatic Environment. *Chem. Eng. J.* **2023**, *459*, 141576. [CrossRef]
4. Tang, H.; Liu, Z.; Hu, B.; Zhu, L. D-Ring Modifications of Tetracyclines Determine Their Ability to Induce Resistance Genes in the Environment. *Environ. Sci. Technol.* **2023**, *58*, 1338–1348. [CrossRef]
5. Stapleton, M.J.; Ansari, A.J.; Hai, F.I. Antibiotic Sorption onto Microplastics in Water: A Critical Review of the Factors, Mechanisms and Implications. *Water Res.* **2023**, *233*, 119790. [CrossRef]

6. Chen, X.; Yang, Y.; Ke, Y.; Chen, C.; Xie, S. A Comprehensive Review on Biodegradation of Tetracyclines: Current Research Progress and Prospect. *Sci. Total Environ.* **2022**, *814*, 152852. [CrossRef]
7. Liao, Q.; Rong, H.; Zhao, M.; Luo, H.; Chu, Z.; Wang, R. Interaction between Tetracycline and Microorganisms During Wastewater Treatment: A Review. *Sci. Total Environ.* **2021**, *757*, 143981. [CrossRef]
8. Zhang, X.; Cai, T.; Zhang, S.; Hou, J.; Cheng, L.; Chen, W.; Zhang, Q. Contamination Distribution and Non-Biological Removal Pathways of Typical Tetracycline Antibiotics in the Environment: A Review. *J. Hazard. Mater.* **2024**, *463*, 132862. [CrossRef]
9. Nasrollahi, N.; Vatanpour, V.; Khataee, A. Removal of Antibiotics from Wastewaters by Membrane Technology: Limitations, Successes, and Future Improvements. *Sci. Total Environ.* **2022**, *838*, 156010. [CrossRef]
10. He, Z.; Siddique, M.S.; Yang, H.; Xia, Y.; Su, J.; Tang, B.; Wang, L.; Kang, L.; Huang, Z. Novel Z-Scheme In_2S_3/Bi_2WO_6 Core-Shell Heterojunctions with Synergistic Enhanced Photocatalytic Degradation of Tetracycline Hydrochloride. *J. Clean. Prod.* **2022**, *339*, 130634. [CrossRef]
11. Zhu, D.; Xue, S.; Yang, S.; Zuo, Q.; Wang, H.; Lu, Q.; Ruan, G.; Zhao, C.; Du, F. Layered Bimetallic Oxide Composite Film: A Highly Efficient and Reusable Photocatalytic Film for Removal of Tetracycline Antibiotics. *Chem. Eng. J.* **2023**, *476*, 146681. [CrossRef]
12. Yang, J. FeOOH Nanosheets Coupled with ZnCdS Nanoparticles for Highly Improved Photocatalytic Degradation of Organic Dyes and Tetracycline in Water. *Molecules* **2024**, *29*, 2913. [CrossRef] [PubMed]
13. Hao, Z.; Hou, W.; Fang, C.; Huang, Y.; Liu, X. Sulfite Activation by Cobaltosic Oxide Nanohydrangeas for Tetracycline Degradation: Performance, Degradation Pathways and Mechanism. *J. Hazard. Mater.* **2022**, *439*, 129618. [CrossRef] [PubMed]
14. El Messaoudi, N.; Ciğeroğlu, Z.; Şenol, Z.M.; Elhajam, M.; Noureen, L. A Comparative Review of the Adsorption and Photocatalytic Degradation of Tetracycline in Aquatic Environment by g-C_3N_4-Based Materials. *J. Water Process Eng.* **2023**, *55*, 104150. [CrossRef]
15. Liu, Y.; Luo, J.; Li, J.; Wang, X.; Song, H. Coupling Agent Grafting Assisted Synthesis of C_3N_4-ZrO_2 Heterojunction Composites with Enhanced Photocatalytic Performance. *China Pet. Process. Petrochem. Technol.* **2023**, *25*, 123–132.
16. Liu, X.; Cheng, H.; Wang, Z.; Zhang, J.; Lan, Y.; Wang, X. Assembling Superfine Bi_3TaO_7 Particles into 2D Fe_2O_3 Nanosheets for Enhanced Usability to Aqueous Tetracycline Residues. *China Pet. Process. Petrochem. Technol.* **2022**, *24*, 147–158.
17. Liu, Y.; Zhao, H.; Li, H.; Cai, T. One-step Synthesis and Photocatalytic Degradation Performance of Sulfur-doped Porous g-C_3N_4 Nanosheets. *China Pet. Process. Petrochem. Technol.* **2022**, *24*, 81–89.
18. He, J.; Shi, C.; Yang, Z.; Hou, Q.; Zhang, R.; Zhu, T.; Pan, P.; Zhang, P. Visible-Light Photocatalytic Activity of TiO_2 Nanorods and Its Application to Degrading Organic Pollutants. *China Pet. Process. Petrochem. Technol.* **2022**, *24*, 138–146.
19. Liu, C.; Jin, T.; Qian, J.; Xu, X.; Meng, X.; Chen, Z. Synthesis and Photocatalytic Property of CuS-Ag/g-C_3N_4. *Chin. J. Rare Met.* **2023**, *47*, 1104–1112.
20. Yu, F.; Li, Y.; Liu, Z.; Cui, J.; Zhou, Y. Synthesis and Photocatalytic Properties of Na Doped g-C_3N_4 Nanotubes. *Chin. J. Rare Met.* **2022**, *46*, 889–895.
21. Xu, Y.; Liu, C.; Jin, T.; Chen, F.; Qian, J.; Qiu, Y.; Meng, X.; Chen, Z. Preparation and Photocatalytic Properties of MoS_2/CQDs/g-C_3N_4 Composites. *Chin. J. Rare Met.* **2024**, *48*, 682–694.
22. Miao, H.; Zhang, W.; Wang, T.; Yang, Z.; Kong, C. g-C_3N_4-based Nanocomposites for the Photocatalytic Degradation of VOCs: A review. *Prog. Nat. Sci. Mater. Int.* **2023**, *33*, 407–424. [CrossRef]
23. Ye, L.; Peng, X.; Wen, Z.; Huang, H. Solid-state Z-scheme Assisted Hydrated Tungsten Trioxide/$ZnIn_2S_4$ Photocatalyst for Efficient Photocatalytic H_2 Production. *Mater. Futures* **2022**, *1*, 035103. [CrossRef]
24. Gao, R.; Bai, J.; Shen, R.; Hao, L.; Huang, C.; Wang, L.; Liang, G.; Zhang, P.; Li, X. 2D/2D Covalent Organic Framework/CdS Z-scheme Heterojunction for Enhanced Photocatalytic H_2 Evolution: Insights into Interfacial Charge Transfer Mechanism. *J. Mater. Sci. Technol.* **2023**, *137*, 223–231. [CrossRef]
25. Shang, W.; Liu, W.; Cai, X.; Hu, J.; Guo, J.; Xin, C.; Li, Y.; Zhang, N.; Wang, N.; Hao, C.; et al. Insights into Atomically Dispersed Reactive Centers on g-C_3N_4 Photocatalysts for Water Splitting. *Adv. Powder Mater.* **2023**, *2*, 100094. [CrossRef]
26. Mo, X.; Zhang, X.; Lin, B.; Ning, C.; Li, M.; Liao, H.; Chen, Z.; Wang, X. Boosting Interfacial S-scheme Charge Transfer and Photocatalytic H_2-production Activity of 1D/2D WO_3/g-C_3N_4 Heterojunction by Molecular Benzene-rings Integration. *J. Mater. Sci. Technol.* **2023**, *145*, 174–184. [CrossRef]
27. Zhao, G.; Ma, W.; Wang, X.; Xing, Y.; Hao, S.; Xu, X. Self-water-absorption-type Two-dimensional Composite Photocatalyst with High-efficiency Water Absorption and Overall Water-splitting Performance. *Adv. Powder Mater.* **2022**, *1*, 100008. [CrossRef]
28. Chu, X.; Sathish, C.; Li, M.; Yang, J.; Li, W.; Qi, D.; Chu, D.; Vinu, A.; Yi, J. Anti-Stoke Effect Induced Enhanced Photocatalytic Hydrogen Production. *Battery Energy.* **2023**, *2*, 20220041. [CrossRef]
29. Yang, N.; He, T.; Chen, X.; He, Y.; Zhou, T.; Zhang, G.; Liu, Q. TiO_2-based Heterojunctions for Photocatalytic Hydrogen Evolution Reaction. *Microstructures* **2024**, *4*, 2024042. [CrossRef]
30. He, J.; Zhang, G.; Jiang, Y.; Jia, J.; Cao, J. Design and Synthesis of Two Dimensional-$ZnIn_2S_4$ Nanosheets with Sulfur Vacancies for Improving Photocatalytic Hydrogen Production Performance. *Prog. Nat. Sci. Mater. Int.* **2023**, *33*, 607–615. [CrossRef]
31. Li, L.; Dai, X.; Lu, M.; Guo, C.; Wabaidur, S.; Wu, X.; Lou, Z.; Zhong, Y.; Hu, Y. Electron-enriched Single-Pd-sites on g-C_3N_4 Nanosheets Achieved by in-situ Anchoring Twinned Pd Nanoparticles for Efficient CO_2 Photoreduction. *Adv. Powder Mater.* **2024**, *3*, 100170. [CrossRef]

32. Li, J.; Wang, Y.; Wang, Y.; Guo, Y.; Zhang, S.; Song, H.; Li, X.; Gao, Q.; Shang, W.; Hu, S.; et al. MXene Ti_3C_2 Decorated g-C_3N_4/ZnO Photocatalysts with Improved Photocatalytic Performance for CO_2 Reduction. *Nano Mater. Sci.* **2023**, *5*, 237–245. [CrossRef]
33. Wei, H.; Meng, F.; Zhang, H.; Yu, W.; Li, J.; Yao, S. Novel Oxygen Vacancy-enriched Bi_2MoO_{6-x}/MoS_2 S-scheme Heterojunction for Strengthening Photocatalytic Reduction CO_2 and Efficient Degradation of Levofloxacin Hydrochloride: Mechanism, DFT Calculations. *J. Mater. Sci. Technol.* **2024**, *185*, 107–120. [CrossRef]
34. Asrami, M.; Jourshabani, M.; Park, M.; Shin, D.; Lee, B. A Unique and Well-designed 2D Graphitic Carbon Nitride with Sponge-like Architecture for Enhanced Visible-light Photocatalytic Activity. *J. Mater. Sci. Technol.* **2023**, *159*, 99–111. [CrossRef]
35. Chen, L.; Maigbay, M.; Li, M.; Qiu, M. Synthesis and Modification Strategies of g-C_3N_4 Nanosheets for Photocatalytic Applications. *Adv. Powder Mater.* **2024**, *3*, 100150. [CrossRef]
36. Raza, S.; Ghasali, E.; Orooji, Y.; Lin, H.; Karaman, C.; Dragoi, E.N.; Erk, N. Two Dimensional (2D) Materials and Biomaterials for Water Desalination; Structure, Properties, and Recent Advances. *Environ. Res.* **2023**, *219*, 114998. [CrossRef]
37. Liu, Y.; Gu, D.; Tao, X.; Ouyang, Y.; Duan, C.; Liang, G. Two-Dimensional Polarized Blue P/SiS Heterostructures as Promising Photocatalysts for Water Splitting. *Molecules* **2024**, *29*, 4355. [CrossRef]
38. Guo, Z.; Zheng, J.; Li, B.; Da, Z.; Meng, M. Fabrication of Mixed Matrix Membranes Blending with the TiO_2/Bi_3O_4Cl 2D/2D Heterojunction for Photocatalytic Degradation of Tetracycline. *Appl. Surf. Sci.* **2022**, *574*, 151549. [CrossRef]
39. Gan, W.; Fu, X.; Guo, J.; Zhang, M.; Li, D.; Ding, C.; Lu, Y.; Wang, P.; Sun, Z. Ag Nanoparticles Decorated 2D/2D TiO_2/g-C_3N_4 Heterojunction for Efficient Removal of Tetracycline Hydrochloride: Synthesis, Degradation Pathways, and Mechanism. *Appl. Surf. Sci.* **2022**, *606*, 154837. [CrossRef]
40. Fang, H.; Zhou, C.; Xu, S.; Shi, J.; Hu, Y.; Liu, G. S-Scheme Photocatalyst Mo_2C/α-Fe_2O_3 with Vacant Oxygen for Highly Efficient Tetracycline Degradation in Peroxymonosulfate-Mediated Photocatalytic System. *J. Alloys Compd.* **2023**, *958*, 170547. [CrossRef]
41. Yazdi, A.A.; Pirbazari, A.E.; Saraei, F.E.K.; Esmaeili, A.; Pirbazari, A.E.; Kohnehsari, A.A.; Derakhshesh, A. Design of 2D/2D β-$Ni(OH)_2$/ZnO Heterostructures Via Photocatalytic Deposition of Nickel for Sonophotocatalytic Degradation of Tetracycline and Modeling with Three Supervised Machine Learning Algorithms. *Chemosphere* **2024**, *352*, 141328. [CrossRef] [PubMed]
42. Raja, A.; Son, N.; Pandey, S.; Kang, M. Fabrication of Solar-Driven Hierarchical $ZnIn_2S_4$/rGO/SnS_2 Heterojunction Photocatalyst for Hydrogen Generation and Environmental Pollutant Elimination. *Sep. Purif. Technol.* **2022**, *293*, 121119. [CrossRef]
43. Sun, H.; Tillotson, M.R.; Wang, D.; Zhao, X. A Novel Z-Scheme SnS/NiAl-LDH/g-C_3N_4 Heterojunction for Piezo-Photocatalytic Degradation of Tetracycline: Performance and Mechanism. *Surf. Interfaces* **2024**, *52*, 104861. [CrossRef]
44. Wang, R.; Zhang, Y.; Sun, X.; Zhang, Q.; Cheng, Z.; Xue, W.; Zeng, Q. Resourceful Treatment of Complex Uranium-Organic Wastewater by a Hybrid Tandem Photocatalytic Fuel Cell with SnS_2 Nanoplate Modified Carbon Felt Cathode. *J. Hazard. Mater.* **2024**, *480*, 135861. [CrossRef]
45. Chen, M.; Ye, Z.; Wei, L.; Yuan, J.; Xiao, L. Shining at the Tips: Anisotropic Deposition of Pt Nanoparticles Boosting Hot Carrier Utilization for Plasmon-Driven Photocatalysis. *J. Am. Chem. Soc.* **2022**, *144*, 12842–12849. [CrossRef]
46. Gadore, V.; Mishra, S.R.; Ahmaruzzaman, M. Bandgap Engineering Approach for Synthesising Photoactive Novel Ag/HAp/SnS_2 for Removing Toxic Anti-Fungal Pharmaceutical from Aqueous Environment. *J. Hazard. Mater.* **2024**, *461*, 132458. [CrossRef]
47. Li, D.; Li, Y.; Liao, D.; Cao, M.; Zhang, L.; Zhang, S.; Chen, L.; Chen, Y.; Wang, H.; Qi, J. Enhanced Light Harvesting Ability in Hollow Pt/TiO_2 Nanoreactor for Boosting Tetracycline Photodegradation. *Prog. Nat. Sci. Mater. Int.* **2024**, *34*, 767–775. [CrossRef]
48. Li, J.; Cao, Z.; Wang, Q.; Cheng, H. Highly Dispersed Fe/SnS_2/Kaolinite Composite for the Enhanced Photo-Fenton Degradation of Tetracycline Hydrochloride. *J. Alloys Compd.* **2024**, *976*, 173061. [CrossRef]
49. Wang, J.-T.; Cai, Y.-L.; Liu, X.-J.; Zhang, X.-D.; Cai, F.-Y.; Cao, H.-L.; Zhong, Z.; Li, Y.-F.; Lü, J. Unveiling the Visible–Light–Driven Photodegradation Pathway and Products Toxicity of Tetracycline in the System of Pt/$BiVO_4$ Nanosheets. *J. Hazard. Mater.* **2022**, *424*, 127596. [CrossRef]
50. Kumar, G.; Kumar, J.; Bag, M.; Dutta, R.K. Solar Light Induced Photocatalytic Process for Reduction of Hexavalent Chromium and Degradation of Tetracycline and Methylene Blue by Heterostructures Made of SnS_2 Nanoplates Surface Modified by $ZnWO_4$ Nanorods. *Sep. Purif. Technol.* **2022**, *292*, 121040. [CrossRef]
51. Yan, J.; Wu, R.; Jin, G.; Jia, L.; Feng, G.; Tong, X. The Hybrid Pt Nanoclusters/Ru Nanowires Catalysts Accelerating Alkaline Hydrogen Evolution Reaction. *Adv. Powder Mater.* **2024**, *3*, 100214. [CrossRef]
52. Gao, M.; Zhou, W.; Mo, Y.; Sheng, T.; Deng, Y.; Chen, L.; Wang, K.; Tan, Y.; Zhou, H. Outstanding Long-cycling Lithium-sulfur Batteries by Core-shell Structure of S@Pt Composite with Ultrahigh Sulfur Content. *Adv. Powder Mater.* **2022**, *1*, 100006. [CrossRef]
53. Shi, Y.; Feng, Y.; Wang, Z.; Wang, X.; Jiang, Y.; Deng, J.; Dai, H.; Liu, Y. Light-driven Photothermocatalytic Performance of the Pt/Co_3O_4 Catalyst for Toluene Oxidation. *Prog. Nat. Sci. Mater. Int.* **2023**, *33*, 526–533. [CrossRef]
54. Shu, C.; Cao, J.; Gan, Z.; Qiu, P.; Chen, Z.; Lian, G.; Chen, Z.; Deng, C.; Tang, W. Synergistic Effect between Co Single Atoms and Pt Nanoparticles for Efficient Alkaline Hydrogen Evolution. *Mater. Futur.* **2024**, *3*, 035101. [CrossRef]
55. Ma, X.; Li, D.; Jiang, Y.; Jin, H.; Bai, L.; Qi, J.; You, F.; Yuan, F. Fiber-Like ZnO with Highly Dispersed Pt Nanoparticles for Enhanced Photocatalytic CO_2 Reduction. *J. Colloid Interf. Sci.* **2022**, *628*, 768–776. [CrossRef]
56. Huang, P.; Chen, F.; Tang, Y.; Sun, W.; Song, Y.; Sun, Y. Zn_2SnO_4 Decorated SnS_2 Flower-Like Ball for Enhanced Photocatalytic Degradation of Tetracycline under Visible Irradiation: The Role of Zn_2SnO_4 in Photoinduced Electrons Transfer. *Mat. Sci. Semicon. Proc.* **2024**, *173*, 108182. [CrossRef]

57. Singla, S.; Basu, S.; Devi, P. Solar Light Responsive 2D/2D $BiVO_4/SnS_2$ Nanocomposite for Photocatalytic Elimination of Recalcitrant Antibiotics and Photoelectrocatalytic Water Splitting with High Performance. *J. Ind. Eng. Chem.* **2023**, *118*, 119–131. [CrossRef]
58. Luo, J.; Li, R.; Chen, Y.; Zhou, X.; Ning, X.; Zhan, L.; Ma, L.; Xu, X.; Xu, L.; Zhang, L. Rational Design of Z-Scheme $LaFeO_3/SnS_2$ Hybrid with Boosted Visible Light Photocatalytic Activity Towards Tetracycline Degradation. *Sep. Purif. Technol.* **2019**, *210*, 417–430. [CrossRef]
59. Zou, X.; Sun, B.; Wang, L.; Bai, H.; Meng, X.; Li, C.; Li, Z. Enhanced Photocatalytic Degradation of Tetracycline by SnS_2/Bi_2MoO_{6-X} Heterojunction: Multi-Electric Field Modulation through Oxygen Vacancies and Z-Scheme Charge Transfer. *Chem. Eng. J.* **2024**, *482*, 148818. [CrossRef]
60. Bao, Y.; Liu, Y.; Zhang, Z.; Pan, J.; Li, X.; Zhao, B.; Wang, R.; Liu, J. Constructing 2D/2D Ultrathin Ti_3C_2/SnS_2 Schottky Heterojunctions toward Efficient Tetracycline Degradation. *Chemosphere* **2022**, *307*, 136118. [CrossRef]
61. Chen, X.; Han, Z.; Lu, Z.; Qu, T.; Liang, C.; Wang, Y.; Zhang, B.; Han, X.; Xu, P. Construction of Strongly Coupled 2D-2D SnS_2/CdS S-Scheme Heterostructures for Photocatalytic Hydrogen Evolution. *Sustain. Energy Fuels* **2023**, *7*, 1311–1321. [CrossRef]
62. Zhang, J.; Fang, Y.; Zhang, Y.; Lin, Y.; Gui, Y.; Liu, L. Photocatalytic Degradation of Volatile Organic Compounds over WO_2/SnS_2 Nanofibers. *ACS Appl. Nano Mater.* **2023**, *6*, 22301–22310. [CrossRef]
63. Qiang, T.; Chen, L.; Xia, Y.; Qin, X. Dual Modified MoS_2/SnS_2 Photocatalyst with Z-Scheme Heterojunction and Vacancies Defects to Achieve a Superior Performance in Cr (VI) Reduction and Dyes Degradation. *J. Clean. Prod.* **2021**, *291*, 125213. [CrossRef]
64. Gadore, V.; Mishra, S.R.; Ahmaruzzaman, M. Green and Environmentally Sustainable Fabrication of SnS_2 Quantum Dots/Chitosan Nanocomposite for Enhanced Photocatalytic Performance: Effect of Process Variables, and Water Matrices. *J. Hazard. Mater.* **2023**, *444*, 130301. [CrossRef]
65. Wu, S.; Hu, H.; Lin, Y.; Zhang, J.; Hu, Y.H. Visible Light Photocatalytic Degradation of Tetracycline over TiO_2. *Chem. Eng. J.* **2020**, *382*, 122842. [CrossRef]
66. Liu, C.; Dai, H.; Tan, C.; Pan, Q.; Hu, F.; Peng, X. Photo-Fenton Degradation of Tetracycline over Z-Scheme Fe-g-C_3N_4/Bi_2WO_6 Heterojunctions: Mechanism Insight, Degradation Pathways and DFT Calculation. *Appl. Catal. B Environ.* **2022**, *310*, 121326. [CrossRef]
67. You, F.; Zhou, T.; Li, J.; Huang, S.; Chang, C.; Fan, X.; Zhang, H.; Ma, X.; Gao, D.; Qi, J. Rich Oxygen Vacancies in Confined Heterostructured TiO_2@In_2S_3 Hybrid for Boosting Solar-Driven CO_2 Reduction. *J. Colloid Interf. Sci.* **2024**, *660*, 77–86. [CrossRef]
68. Li, D.; Zhang, H.; Xie, S.; Zhang, H.; Wang, H.; Ma, X.; Gao, D.; Qi, J.; You, F. Lattice Distortion in a Confined Structured ZnS/ZnO Heterojunction for Efficient Photocatalytic CO_2 Reduction. *ACS Appl. Mater. Interfaces* **2023**, *15*, 36324–36333. [CrossRef]

molecules

MDPI

Review

NMR Relaxation to Probe Zeolites: Mobility of Adsorbed Molecules, Surface Acidity, Pore Size Distribution and Connectivity

Marina G. Shelyapina

Department of Nuclear Physics Research Methods, Saint Petersburg State University, 7/9 Universitetskaya nab., Saint Petersburg 199034, Russia; marina.shelyapina@spbu.ru

Abstract: Unique structural and chemical properties, such as ion exchange, developed inner surface, etc., as well as the wide possibilities and flexibility of regulating these properties, cause a keen interest in zeolites. They are widely used in industry as molecular sieves, ion exchangers and catalysts. Current trends in the development of zeolite-based catalysts include the adaptation of their cationic composition, acidity and porosity for a specific catalytic process. Recent studies have shown that mesoporosity is beneficial to the rational design of catalysts with controlled product selectivity and an improved catalyst lifetime due to its efficient mass-transport properties. Nuclear magnetic resonance (NMR) has proven to be a reliable method for studying zeolites. Solid-state NMR spectroscopy allows for the quantification of both Lewis and Brønsted acidity in zeolite catalysts and, nowadays, ^{27}Al and ^{29}Si magic angle spinning NMR spectroscopy has become firmly established in the set of approved methods for characterizing zeolites. The use of probe molecules opens up the possibility for the indirect measurement of the characteristics of acid sites. NMR relaxation is less common, although it is especially informative and enlightening for studying the mobility of guest molecules in the porous matrix. Moreover, the NMR relaxation of guest molecules and NMR cryoporometry can quantify pore size distribution on a broader scale (compared to traditional methods), which is especially important for systems with complex pore organization. Over the last few years, there has been a growing interest in the use of 2D NMR relaxation techniques to probe porous catalysts, such as 2D T_1–T_2 correlation to study the acidity of the surface of catalysts and 2D T_2–T_2 exchange to study pore connectivity. This contribution provides a comprehensive review of various NMR relaxation techniques for studying porous media and recent results of their applications in probing micro- and mesoporous zeolites, mainly focused on the mobility of adsorbed molecules, the acidity of the zeolite surface and the pore size distribution and connectivity of zeolites with hierarchical porosity.

Keywords: nuclear magnetic resonance; spin relaxation; zeolites; microporous materials; mesoporous materials; hierarchical porosity; Lewis acid sites; Brønsted acid sites; diffusion; NMR cryoporometry; pore connectivity

1. Introduction

Zeolites form a large group of crystalline aluminosilicates. Their crystal structures can be represented as open three-dimensional frameworks assembled from $[SiO_4]^{4-}$ and $[AlO_4]^{5-}$ tetrahedra, connected by vertices that form regular cavities and channel systems in one, two or three dimensions depending on the zeolite framework topology. At the moment, 256 different topologies of the zeolite framework are known [1]. Selected zeolite structures and brief information about their channels, taken from the International Zeolite Association database [1], are shown in Figure 1.

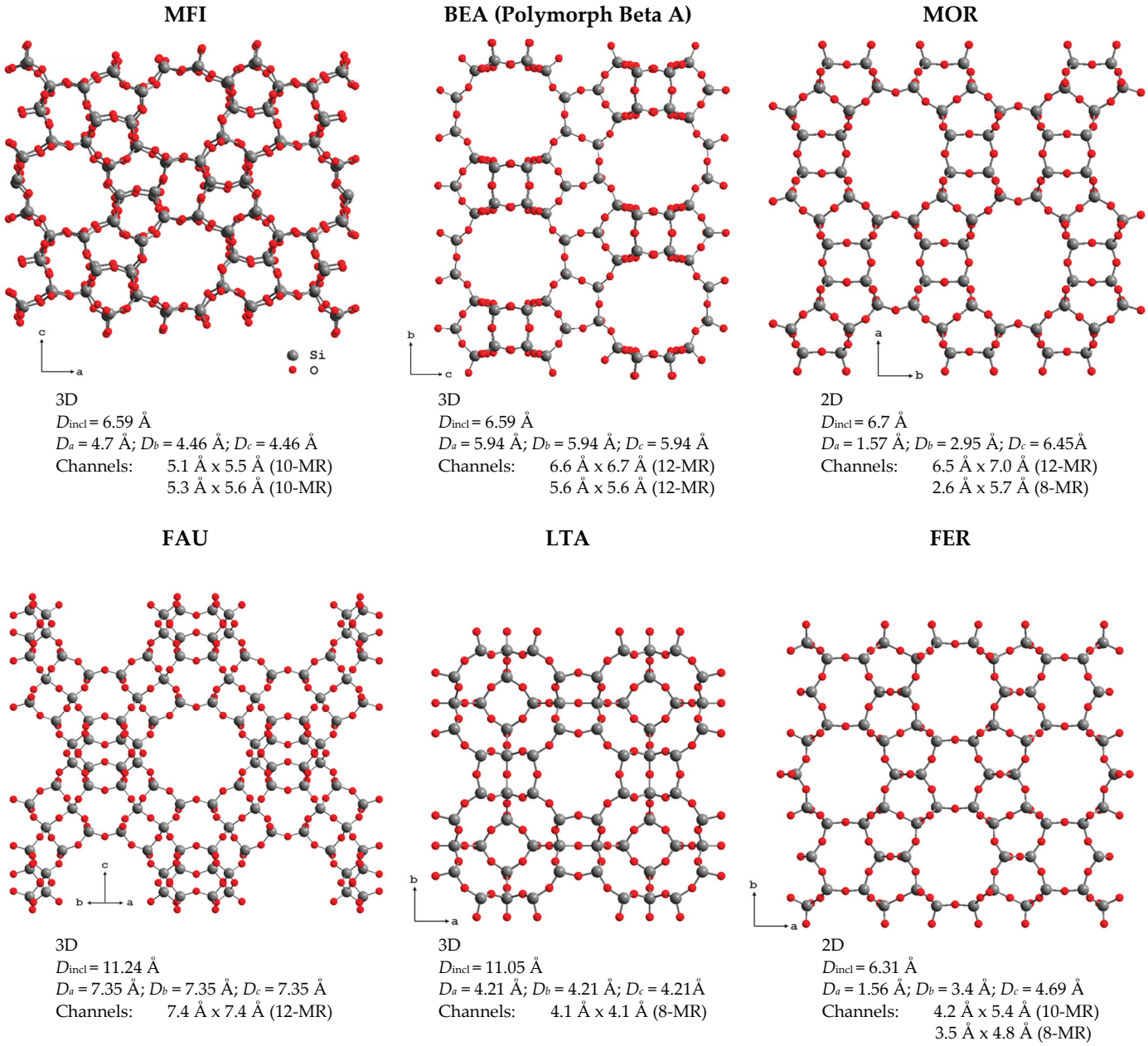

Figure 1. Selected zeolite frameworks and information about their pore structure: channel dimensionality; the maximum diameter of a sphere that can be included (D_{incl}) and that diffuses in a specific direction x (D_x); the channel size and the N-membered ring it is formed by (in parenthesis).

The size of the formed voids varies from 0.3 to 1.0 nm. This means that, according to the International Union of Pure and Applied Chemistry (IUPAC), 3D zeolites are microporous materials (the IUPAC classification of porous materials according to their pore sizes d is as follows: microporous if $d < 2$ nm, mesoporous if $2 < d < 50$ nm and macroporous if $d > 50$ nm). Depending on the framework type, zeolites can be stable in different ranges of the Si/Al ratio. The substitution of Al^{3+} for Si^{4+} results in the negative charge of the zeolite framework that is compensated by extra-framework cations, such as Na^+, K^+, NH_4^+, Ca^{2+}, etc., located in the zeolite voids, or protons that form various OH groups on the zeolite inner surface [2].

The unique structural and chemical properties of zeolites, such as ion exchange, their developed inner surface and their ordered pore structure, as well as the wide possibilities and flexibility of regulating these properties either during synthesis or as a result of post-

synthetic processing, cause a wide interest in zeolites and, nowadays, this interest is only increasing, especially in view of the accepted strategies for sustainable development and the transition to resource-saving energy [3]. It should be noted that zeolites are quite common minerals and are widely used in industry as molecular sieves and ion exchangers [4]. Another important application of zeolites that is demanded in the market is catalysis. Until recently, synthetic zeolites have dominated in this field [5,6]. Current trends in the development of zeolite-based catalysts include the adaptation of their cationic composition [4,7–9], porosity [10–12] and acidity [13–15] for specific catalytic processes.

Synthetic ZSM-5 (MFI), beta-zeolite (BEA), mordenite (MOR), zeolite Y (FAU) and ferrierite (FER) form the so-called "big five" zeolites, which are widely used in industry as catalysts [16]. The main reasons for their use are their unique pore structure, which ensures a perfect match with the requirements of the target reactions, and the presence of active sites and accessibility of these sites to guest molecules [17]. Brønsted and Lewis acid sites play key roles in the efficiency and selectivity of many catalytic processes. The reactivity of these acid sites is determined by the density, spatial arrangement and local environment of the aluminum atoms in the zeolite framework. In addition, ion exchange [4,7,18,19], the incorporation of metallic nanoparticles [8,20–22] or oxo-cation clusters [23–26] and isomorphous substitution with the introduction of different heteroelements [8,27,28] into zeolites allows for the tailoring of the nature and catalytic function of the formed acid sites.

At the same time, the transport properties of the zeolite matrix, as well as the type and strength of the interaction of the adsorbed molecules with the inner surface of the zeolite, are of great importance [29,30]. Recent studies have shown that mesoporosity is beneficial for the rational design of catalysts with controlled product selectivity [31,32] and helps to improve the catalyst's lifetime [33,34] due to its efficient mass-transport properties.

To tailor the structure and properties of zeolite-based catalysts for specific applications, a comprehensive study of their physicochemical properties is necessary. Nuclear magnetic resonance (NMR) has proven to be a reliable method for studying zeolites [35–38]. Magic angle spinning (MAS) NMR on the ^{29}Si and ^{27}Al nuclei allows for the quantification of the silica to alumina ratio in the material, which is considered to be an analog of the acidity of the zeolite [13,39]. Moreover, ^{27}Al MAS NMR enables the aluminum that is a part of the zeolite framework (tetra-co-ordinated Al) to be distinguished from the disordered, so-called penta-co-ordinated Al, and the extra-framework Al species (six-co-ordinated Al) [40,41]; the penta- and six-co-ordinated species, in turn, are issues of Brønsted [42] and Lewis acidity [39,43], respectively. Solid-state ^{1}H MAS NMR spectroscopy provides a direct quantitative determination of the density of Brønsted acid sites [44], distinguishing the bridge Si–OH–Al and terminal Al–OH or Si–OH groups from the observed ^{1}H chemical shift.

The application of probe molecules opens up the possibility of indirect studying of the zeolite surface acid sites and its pore structure. In particular, ^{1}H chemical shift can be used for detailed study of the interactions of adsorbed water molecules with the zeolite surface [45]. In the case of organic probe molecules (such as phosphine oxides [46–49], pyridine [50,51], acetone [52,53], carbon dioxide [54], etc.), a wide range of experiments involving ^{31}P, ^{15}N and ^{13}C MAS NMR are successfully applied to study zeolite acidity.

^{129}Xe NMR is another powerful tool for determining both the porosity and pore connectivity of zeolites [55–57]. Being sensitive to the chemical composition and the physical structure of its environment, ^{129}Xe is an ideal probe gas for NMR. However, in practice, for better sensitivity, ^{129}Xe has to be hyperpolarized via spin exchange optical pumping (SEOP) [58,59], dynamic nuclear polarization (DNP) [60] or by the so-called brute force method in high magnetic fields and very low temperatures (on the order of millikelvins) [61].

In recent years, zero- to ultralow-field, below 10 μT, NMR have appeared. In contrast to conventional high-field NMR, in ultralow-field NMR experiments, chemical shifts vanish and spectra are governed by indirect nuclear spin–spin couplings [62]. Without magnetic field inhomogeneity, the high resolved spectra enable monitoring of the chemical

reaction in the liquid phase [63]. Several studies demonstrate that ultralow-field NMR is a promising tool for probing liquid–surface adsorption dynamics of molecules inside porous materials [64,65]; however, there have been few such studies.

It should be noted that the vast majority of NMR studies of zeolites are focused on NMR spectroscopy; meanwhile, another NMR technic, relaxation, is especially informative for studying the mobility of guest molecules confined in pores [45,66–69]. Over the last few years, there has been a growing interest in the use of NMR relaxation in a relatively low magnetic field to probe the surface acidity of mirco- and mesoporous catalysts [70–72], pore size distribution [73–75] and pore connectivity [74,76]; the latter is especially valuable for systems with hierarchical porosity.

This review presents various NMR relaxation techniques for probing zeolites, both traditional methods for studying the mobility of adsorbed molecules via relaxation time measurements (including diffusometry) and, less frequent in the past but becoming more and more popular, NMR cryoporometry, 2D T_1–T_2 correlation and 2D T_2–T_2 exchange experiments.

2. Basic NMR Pulse Sequences for Relaxation Measurements

Before discussing application to zeolites, let us provide the basic concepts of NMR relaxation and describe the main pulse sequences for determining the nuclear relaxation times.

Let us consider a sample consisting of nuclei with spin $I > 0$ and, therefore, having magnetic moment. In a constant magnetic field $\vec{B}_0$ (let us suppose it is along the z-axis of the laboratory frame), the nuclear magnetization $\vec{M}$ (the sum of all nuclear spins) is in the equilibrium state and parallel to the magnetic field $\vec{B}_0$. If one applies a radiofrequency (rf) pulse, which is oscillating at or near to the so-called Larmor frequency $\omega_0 = \gamma B_0$ (γ is a gyromagnetic ratio for the nuclei under study) and perpendicular to $\vec{B}_0$, for example, along the x-axis of the laboratory frame, it turns the nuclear magnetization around this axis. The pulse duration and amplitude determine the deviation angle of the nuclear magnetization from its equilibrium state: 90° pulse means that it turns the nuclear magnetization in a plane perpendicular to the z-axis; 180° pulse means that it inverts the nuclear magnetization. After the rf pulse is switched off, the nuclear magnetization relaxes to its equilibrium state, wherein the recovery of the longitudinal component of the nuclear magnetization (parallel to $\vec{B}_0$) and the disappearance of the transverse component (perpendicular to $\vec{B}_0$) obey exponential laws but with different characteristic times: spin–lattice (T_1) and spin–spin (T_2) relaxation times, respectively.

The issues of these relaxation processes are interactions of the nuclear spin with neighboring spins and with fluctuating local electric and magnetic fields. More details on the theoretical background of NMR relaxation can be found anywhere [77]. The values of T_1 and T_2 for a specific nucleus, their temperature and/or frequency dependences characterize both the local structure and dynamics of the system under study.

2.1. T_1 and $T_{1\rho}$ Measurements

Among methods for measuring spin–lattice relaxation times T_1, the most popular are inversion-recovery and saturation-recovery pulse sequences. The inversion-recovery method comprises a 180° pulse, inverting the nuclear magnetization $\vec{M}$, followed by a 90° pulse in time τ to measure the recovering magnetization. For the recovery time, the magnetization starts out inverted and, with τ increasing, passes through zero, recovering its equilibrium value M_0; see Figure 2a. The evolution of the z-projected nuclear magnetization is described by the following equation:

$$M_z(\tau) = M_0\left[1 - 2\exp\left(-\frac{\tau}{T_1}\right)\right]. \quad (1)$$

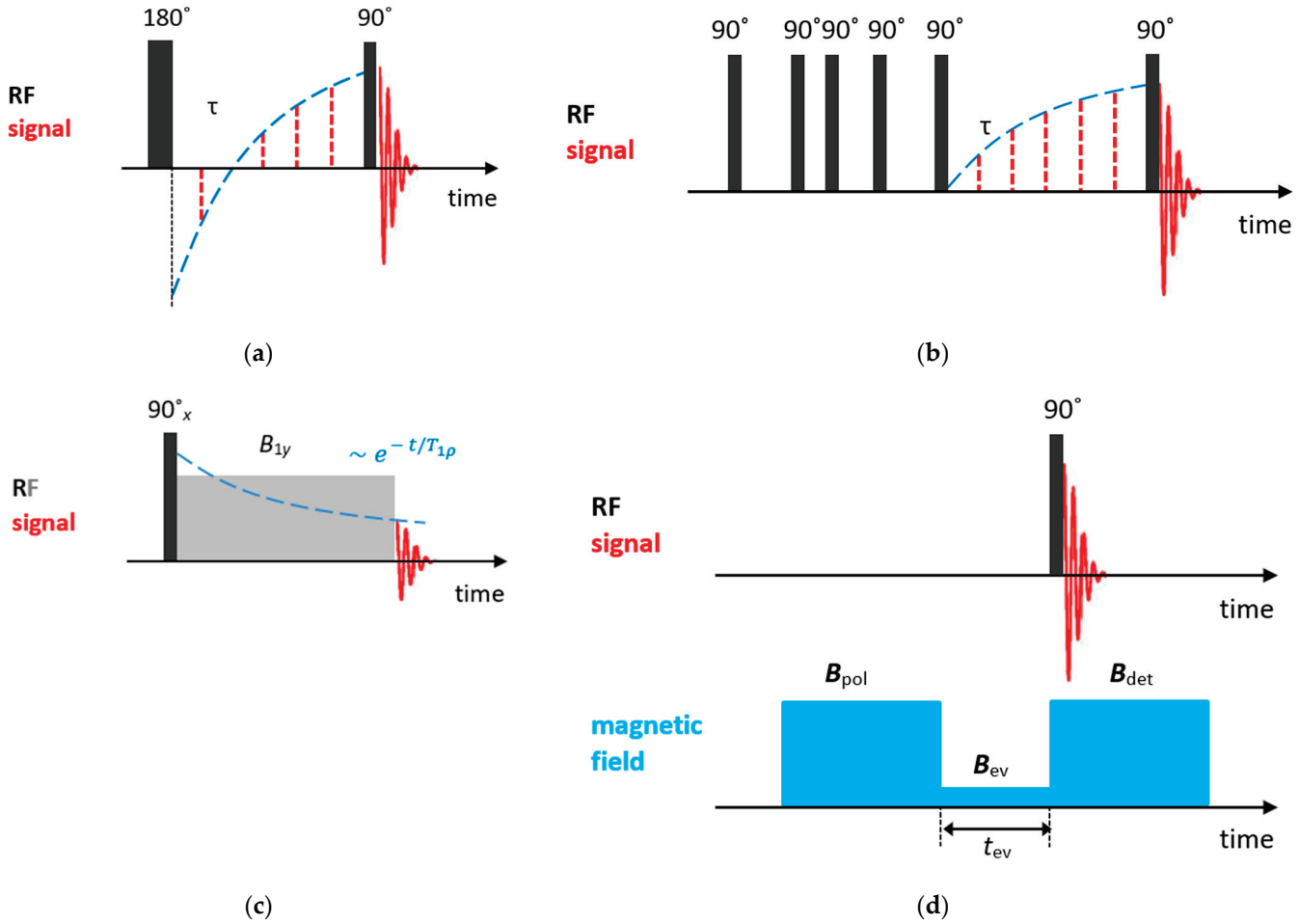

Figure 2. Basic NMR sequences for T_1 and $T_{1\rho}$ measurements: (**a**) inversion-recovery; (**b**) saturation-recovery; (**c**) spin-locking; (**d**) field cycling.

However, it should be noted that, before applying the 180° pulse, the spin system must be in equilibrium that is achieved at $t > 5T_1$. For systems with long T_1, this method can be rather time-consuming.

In the saturation-recovery experiment, Figure 2b, two 90° pulses separated by τ are applied. The first pulse destroys the nuclear magnetization and the signal measured after the second pulse is described by:

$$M_z(\tau) = M_0\left[1 - \exp\left(-\frac{\tau}{T_1}\right)\right]. \quad (2)$$

In this method, the requirement for the equilibrium of the nuclear magnetization before the first pulse is not so strict and, therefore, this method is more time-saving.

Actually, there are many other methods for determining T_1; the choice between them depends on the studied system or process and on the NMR equipment available to a researcher. For systems with long T_1 and weak NMR signal, the progressive saturation method, which is closely related to the saturation-recovery experiment, can be used [78]. For a quantitative NMR analysis, widely used in organic chemistry in those areas where an express analysis is required (e.g., in reaction monitoring, mechanistic analysis and purity determination), for the estimation of T_1, a newly proposed Faster Longitudinal relaxation Investigated by Progressive Saturation (FLIPS) is a good choice [79]. More details concerning a comparative analysis between various techniques for measuring T_1 can be found in Ref. [80].

As will be discussed further, relaxation times are temperature- and frequency-dependent. From the temperature dependence of relaxation times, especially T_1, one can determine parameters of molecular motion. However, for systems with relatively slow molecular dynamics, such as liquids confined in zeolite voids, more informative is the so-called relaxation time $T_{1\rho}$, which characterizes the equilibration of the nuclear magnetization along the rf field $\vec{B}_1$ in the rotating frame. $T_{1\rho}$ can be measured by applying the spin-locking techniques. The experiment involves three stages; see Figure 2c. First, the nuclear magnetization is oriented by the rf field B_{1x} (usually by applying a 90° pulse). Second, the spin system evolves in the rf field B_{1y} (the locking pulse that keeps the magnetization along the y-axis), with the characteristic relaxation time $T_{1\rho}$. Finally, after the magnetic field B_{1y} is switched off, the rest nuclear magnetization is recorded. For more details, see Ref. [77].

Frequency dependences of relaxation times provide additional information on molecular motion; however, usually only fixed-frequency NMR spectrometers are available. Nevertheless, it can be accessed through a field cycling relaxometry that requires special settings [81].

In the field cycling experiment, the magnetic field is periodically switched; Figure 2d. First, to attain the equilibrium magnetization of nuclear spins, a high polarization field $\vec{B}_{\mathrm{pol}}$ is applied. Second, the magnetic field is quickly switched to a variable evolution field $\vec{B}_{\mathrm{ev}}$, to allow the nuclear magnetization to relax toward its new equilibrium value. To trace this equilibration, the magnetic field is quickly switched back to a suitable detection field $\vec{B}_{\mathrm{det}}$. Finally, to register the nuclear magnetization at a given $\vec{B}_{\mathrm{ev}}$ and evolution time t_{ev}, a 90° pulse is applied. This field cycle is repeated for various evolution times and evolution fields to store the frequency-dependent magnetization decay. A more detailed description can be found in Ref. [81].

2.2. T_2 Measurements

The spin–spin relaxation time T_2 quantifies the rate of the decay of the transversal component of the nuclear magnetization recovering to its equilibrium state. If one neglects the inhomogeneity of the magnetic field, the simplest way to measure the T_2 time is to record the free induction decay (FID) signal after a 90° pulse. However, under the condition of magnetic field inhomogeneity, which is always the case, the measured value, T_2^*, is shorter than the real T_2 value, and additional efforts are needed to determine spin–spin relaxation times. The simplest way to measure it is the Hahn spin echo (SE) pulse sequence [82], in which, after the first 90° pulse, after a time of τ, during which the dephasing of nuclear magnetization precessions occurs due to the magnetic field inhomogeneity, a 180° pulse follows and, after another time of τ, the precession is phased and a spin echo signal appears; see Figure 3a. The echo amplitude at time 2τ is given by the simple expression:

$$S^{\mathrm{SE}}(2\tau) = S_0 \exp\left(-\frac{2\tau}{T_2}\right). \tag{3}$$

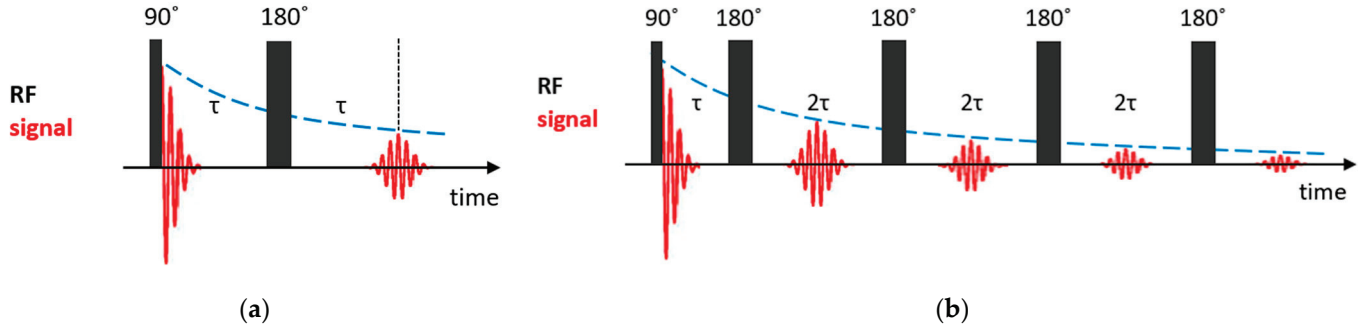

(**a**) (**b**)

Figure 3. Basic NMR sequences for T_2 measurements: (**a**) Hahn spin echo; (**b**) CPMG pulse train.

In this method, the requirement of the equilibrium for the nuclear magnetization before the first pulse is not so strict. However, in the presence of translational diffusion, an additional contribution to the echo decay appears. The effect of diffusion can be suppressed by applying a Carr–Purcell–Meiboom–Gill (CPMG) pulse train [83,84], in which a series of 180° pulses follows after a two-pulse Han echo sequence at intervals of 2τ; see Figure 3b. To compensate imperfections in the 180° pulses, the subsequent 180° pulses are shifted in phase by 90° relative to the first 90° pulse. The amplitude of the echo signal at times $2\tau n$ is described by the following expression:

$$S^{\mathrm{CPMG}}(2\tau n) = S_0 \exp\left(-\frac{2\tau n}{T_2}\right) \exp\left(-\frac{D\gamma^2 G_0^2 (2\tau)^3 n}{3}\right), \quad (4)$$

where D is the diffusion coefficient and G_0 is the magnetic field gradient. By decreasing τ, one can make the diffusional decay arbitrarily small. Currently, CPMG is a fundamental component of pulse sequences used in NMR to study dynamic processes.

2.3. Self-Diffusion Measurements

As was mentioned previously, in the Hahn echo experiment, molecular diffusion results in spin echo attenuation (it should be noted that, in NMR, one normally deals with self-diffusion, which is often referred to simply as diffusion). Thus, a gradient-assisted experiment can be designed in such a way to explore the diffusion coefficients. In the pulsed gradient spin echo (PGSE) method [85], which is based on the Hahn spin echo sequence, two gradient pulses g of equal phase and length are applied for spatially encoding the nuclear spins along the gradient direction. The first gradient pulse follows the 90° pulse after a short delay t_1 and the second gradient pulse is applied after the 180° rf pulse with a time interval between the two gradient pulses Δ (the diffusion delay) and acts to spatially decode the spins in the sample. The PGSE pulse sequence is shown in Figure 4a. This technique of the spatially encoding nuclei with the magnetic field gradient extended to three dimensions is used in magnetic resonance imaging.

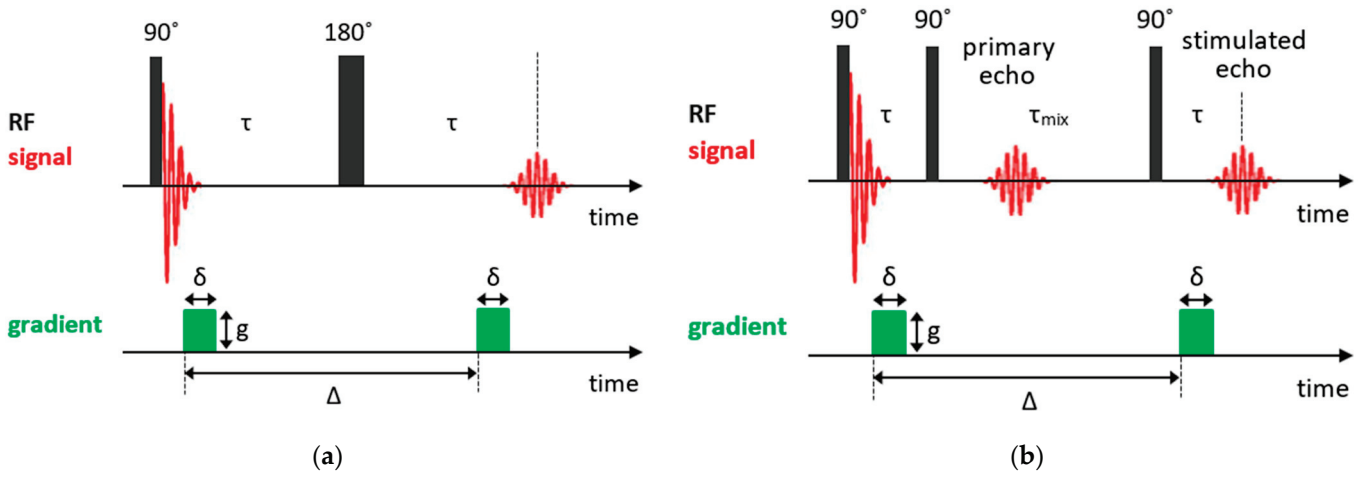

Figure 4. Basic NMR sequences for diffusion measurements: (**a**) PGSE experiment; (**b**) PFG STE experiment.

For systems with short T_2, which is often the case of solids or confined liquids, more effective is the stimulated echo (STE) pulse sequence, in which the 180° pulse is split into two 90° pulses. So, the STE pulse sequence consists of three 90° rf pulses: the first 90° pulse creates the transverse nuclear magnetization, which begins to out-phase; the second 90° pulse applied in time τ turns the out-phased magnetization along the z-axis and, during the mixing time $t_m \gg \tau$, the magnetization decays due to both the spin-lattice relaxation and diffusion in the field gradient; finally, the third 90° pulse in time $t_m + \tau$ transforms the

magnetization again to the transverse one; and, at time $t_m + 2\tau$, an echo signal appears. Similar to the PGSE experiment, the transverse magnetization is coded by the first gradient pulse and then decoded by the second pulse after a delay, during which diffusion occurs. The magnetic field gradient pulses of amplitude g and duration δ are applied after the first and third 90° pulses, with an interval between gradient pulses Δ. The pulsed-field gradient stimulated echo (PFG STE) experiment is shown in Figure 4b. The dependence of the echo signal attenuation is expressed as follows:

$$S^{\mathrm{PGF-STE}}(t_m, \tau, g) = S_0 \exp\left(-\frac{2\tau}{T_2}\right) \exp\left(-\frac{t_m}{T_1}\right) \exp\left(-\frac{\gamma^2 g^2 \delta^2 D(\Delta - \delta/3)}{3}\right). \quad (5)$$

It should be noted that gradient pulses induce eddy currents that distort the recorded signal. These currents must be allowed to dissipate before the FID acquisition. There are several strategies to take it into account, for example, the longitudinal eddy-corrected delay (LED) experiment [86] that can be further extended to the bipolar pulse LED (BPPLED) method [87]. However, these problems are more acute for magnetic resonance imaging and will not be discussed here.

The PFG NMR sequence can be combined with various 2D NMR techniques to benefit from additional analytical dimension (3D diffusion-ordered spectroscopy (DOSY) experiments), but it is beyond the present review; more information can be found anywhere [88].

As it follows from Equation (5), for a given mean molecular displacement, the signal attenuation becomes more essential with increasing intensity and duration of the gradient pulse. For systems with relatively slow molecular diffusion, the static field gradient (SFG) experiment can be more effective [89]. The observed echo amplitude in this case can be described by the following expression:

$$S^{\mathrm{SGF-STE}}(t_m, \tau, g) = S_0 \exp\left(-\frac{2\tau}{T_2}\right) \exp\left(-\frac{t_m}{T_1}\right) \exp\left(-\gamma^2 g^2 D\left(\frac{2}{3}\tau^3 + \tau^2 t_m\right)\right). \quad (6)$$

As one can see from Equations (5) and (6), to determine the diffusion coefficient, one needs to know both T_1 and T_2, which can be determined by applying the methods described above.

2.4. T_1–T_2 Correlation and T_2–T_2 Exchange Experiments

Recently, T_1–T_2 correlation and T_2–T_2 exchange experiments became popular for characterizing the pore structure and functionality of porous materials [90]. On the one hand, this is explained by the rather modest requirements for the NMR equipment and, on the other, by the development of numerical processing methods.

In the T_1–T_2 correlation experiment, data can be acquired using an NMR pulse sequence, shown in Figure 5a, which is composed of an inversion recovery pulse sequence followed by a CPMG echo train [91]. The recovery time τ and the echo time τ_e are two independent variables.

The acquired 2D NMR relaxation data, which are the normalized spin echo magnitudes, may be described by the following expression through the Fredholm integral equation of the first kind [91,92]:

$$\frac{S(\tau, n\tau_e)}{S(\tau \to \infty, 0)} = \iint \exp\left(\frac{-n\tau_e}{T_2}\right) \left[1 - 2\exp\left(\frac{-\tau}{T_1}\right)\right] F(T_1, T_2) dT_1 dT_2 + E(\tau, n\tau_e), \quad (7)$$

where $F(T_1, T_2)$ represents the desired 2D distributions of T_1 and T_2 relaxation times and $E(\tau, n\tau_e)$ is the experimental noise. The data analysis relies on inversion of the integral to extract $F(T_1, T_2)$ from the measured signal amplitude.

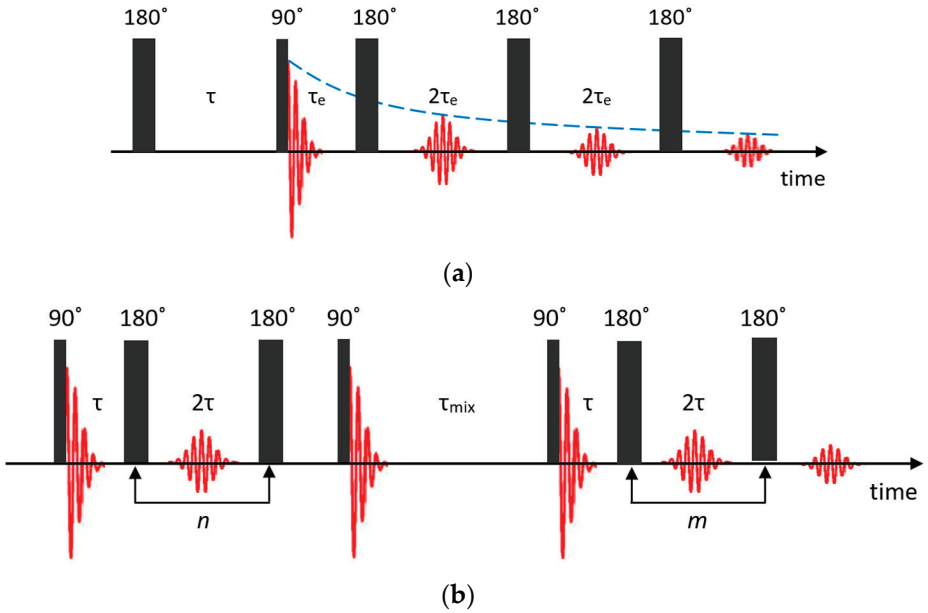

Figure 5. Pulse sequences used for the T_1–T_2 correlation (**a**) and T_2–T_2 exchange (**b**) experiments.

The T_2–T_2 exchange experiment comprises two CPMG echo trains A and B, during which the spin–spin relaxation first evolves and afterwards is detected [93,94]; see Figure 5b. These two echo trains are separated by a mixing period τ_{mix} that is often referred to as the storage interval. The acquired magnetization from two isolated populations can be written as follows [95]:

$$\frac{S(t_A, t_B, \tau_{\mathrm{mix}})}{S(\tau \to \infty, 0)} = \iint \exp\left(\frac{-t_A}{T_2^A}\right) \exp\left(\frac{-t_B}{T_2^B}\right) F(T_2^A, T_2^B, \tau_{\mathrm{mix}}) dT_2^A dT_2^B + E(t_A, t_B), \quad (8)$$

where $F\left(T_2^A, T_2^B, \tau_{\mathrm{mix}}\right)$ is the probability density of the signal components with the relaxation times T_2^A and T_2^B, $E(t_A, t_B)$ is the experimental noise, and $t_A = n\tau$ and $t_B = m\tau$ are the relaxation-encoding time intervals that correspond to the durations of two CPMG echo trains. During the mixing period, nuclear magnetization relaxes with a characteristic time T_1 to its thermodynamic equilibrium along the external magnetic field. Therefore, exchange of magnetization from one site to another must be considered during all the three periods t_A, t_B and τ_{mix} [96] and the total signal amplitude is reduced by $\exp\left(-\tau_{\mathrm{mix}}/T_1^{AB}\right)$.

On the T_2–T_2 map, the majority of the signal lies on the diagonal line $T_2^A = T_2^B$. An exchange between regions with different T_2 results in the appearance of symmetric pairs of off-diagonal peaks, whose intensity relative to the main peaks quantifies the exchange occurring within the mixing time.

3. NMR Relaxation and Diffusometry to Study Molecular Dynamics in Zeolites

The details of the dynamics of molecules adsorbed in zeolite pores govern most of the properties of these substances, which are important for applications. As was mentioned above, the selectivity of the catalytic reaction is determined by the geometry of the zeolite cavities, among others, since it affects the mechanism of the molecule reorientation. The interactions of adsorbed molecules with charge-compensating cations, hydroxyls of different natures or zeolite framework defects restrict the mobility of molecules confined in zeolite cavities and indirectly impact the overall catalytic activity of the material. And NMR, whose parameters are sensitive to fluctuations in local magnetic and electric fields at the nuclear sites due to reorientational and translational motion of molecules, provides a unique tool to probe the dynamics of adsorbed molecules in a wide range of jump rates τ_c^{-1} from 10^4 to 10^{11} s^{-1} that can be expanded up to 10^{-1} s^{-1} to probe slow motions in solids when applying special techniques [97,98].

3.1. Nuclear Dipole Relaxation and Bloembergen–Purcell–Pound Model

For many of the systems considered here, the main issues of NMR relaxation are fluctuating strengths of nuclear dipole coupling. Being dependent on the relative position of the interacting nuclear spins, these interactions are altered by atomic motion that creates fluctuations in the magnetic field at nuclei and, therefore, fluctuations in the Larmor frequency $\Delta\omega$ [77]. This process can be described in terms of a correlation function $G(t)$ that contains the information on dynamic processes:

$$G(t) = \langle \Delta\omega(0) \cdot \Delta\omega(t) \rangle = G(0) \cdot g(t), \tag{9}$$

where the angle brackets mean the ensemble averaging. For isotropic random motion $g(t)$ is:

$$g(t) = g(t) = e^{-|t|/\tau_c}, \tag{10}$$

where τ_c is the correlation time. Applying Fourier transform to $g(t)$, one obtains the frequency-domain spectral relaxation function $j(\omega)$ that is used to describe NMR relaxation processes. In terms of $j(\omega)$, the dipole contribution to the spin–lattice relaxation time is:

$$\frac{1}{T_1} = G(0) \cdot \left[\frac{1}{3} j(\omega_0) + \frac{4}{3} j(2\omega_0) \right], \tag{11}$$

where ω_0 is the resonance frequency. The factor $G(0)$ contains information on the mutual arrangement of nuclear spins.

For liquids, the temperature dependence of T_1 can be well described within the Bloembergen–Purcell–Pound (BPP) model [99] that assumes the correlation time τ_c obeys the Arrhenius law:

$$\tau_c = \tau_0 \exp\left(\frac{E_a}{k_B T} \right), \tag{12}$$

where E_a is the activation energy of nuclear motion, k_B is the Boltzmann constant and τ_0 is a pre-exponential factor. In this case the spectral density is:

$$j(\omega) = \frac{2\tau_c}{1 + (\omega\tau_c)^2}. \tag{13}$$

The BPP model suggests a V shape of the $T_1(1/T)$ dependence with a minimum at $\omega_0\tau_\mathrm{c} \approx 1$ [77]. For slow spin motion, which is often the case for confined liquids, the minimum is shifted towards a high temperature and is often outside the accessible temperature range. To probe slow spin motion, a spin-locking technique (relaxation in the rotating frame) can be applied. The application of the locking pulse ω_1 allows for the displacement of the minimum into the experimentally accessible temperature window. The spin–lattice relaxation in this case is characterized by $T_{1\rho}$, which can be written as follows [77]:

$$\frac{1}{T_{1\rho}} = G(0) \cdot \left[\frac{1}{2} j(\omega_1) + \frac{5}{6} j(\omega_0) + \frac{1}{3} j(2\omega_0) \right]. \tag{14}$$

Note that Equation (14) is obtained at the exact resonance condition and for $\omega_1 \ll \omega_0$.

The dipole contribution to the spin–spin relaxation time within the BPP model can be expressed as follows:

$$\frac{1}{T_2} = G(0) \cdot \left[\frac{1}{2} j(0) + \frac{5}{6} j(\omega_0) + \frac{1}{3} j(2\omega_0) \right]. \tag{15}$$

To study molecular mobility, relaxation times are measured as a function of temperature (less often, as a function of frequency, for example, applying the field cycling techniques). By fitting the experimental data using Equations (11)–(15), one obtains parameters of molecular motion $\{E_a, \tau_c\}$. However, for solids, very often the temperature behavior of nuclear spins differs from the simple BPP model. The main issues are the distribution

of correlation times and/or activation energy [100–102], the exchange between different fractions of adsorbed liquids (for example, on the surface and inside the voids) [103–105], the contribution of ion currents [106–108] or the interaction with paramagnetic ions [109] if present.

3.2. NMR Diffusometry

As noted above, depending on the zeolite topology, zeolite voids form a system of 1D, 2D or 3D channels.

Let us denote the last exponential factor in Equations (5) and (6) as $S_{\mathrm{ND}}(t_m, \tau, g)$. It accounts for the diffusional signal decay in the case of unrestricted diffusion in 3D space. Let us rewrite this factor for an SFG STE case as:

$$S_{3\mathrm{D}} = \exp(-kD), \tag{16}$$

with $k = (\gamma g \tau)^2 (2\tau/3 + t_m)$. For diffusion in randomly oriented capillaries (1D diffusion) or in thin films (2D diffusion), the signal attenuation can be written as follows [110]:

$$S_{1\mathrm{D}} = \int_0^1 \exp\left(-kDx^2\right) dx, \tag{17}$$

$$S_{2\mathrm{D}} = \exp(-kD) \int_0^1 \exp\left(kDx^2\right) dx. \tag{18}$$

In the limit $kD \ll 1$, the 1D and 2D attenuations are singly exponential and are equal to $\exp(-kD/3)$ and $\exp(-2kD/3)$, respectively. Hence, for correctly determining the diffusion coefficient, it is necessary to take into account the dimension of the space, in which diffusion occurs.

Figure 6 shows the temperature dependence of the self-diffusion coefficient of water in zeolites with mordenite structure, as determined from ^{1}H SFG STE [68]. The self-diffusion coefficient in sodium mordenite above and below 300 K was determined assuming intercrystallite (3D model; Equation (16)) and intracrystallite (1D model; Equation (17)) motion, respectively. Mordenite can be classified as a zeolite with a 2D network of voids: two types of channels are oriented along the *c*-axis and are interconnected through side pockets; see Figure 1. However, depending on the cationic form and the Si/Al ratio, the side pockets can be blocked by trapped molecules [68,111] or cations [112,113] and often mordenite is considered as a zeolite with a 1D channel system. Moreover, according to molecular dynamics (MD) simulation, at a low temperature, the water diffusion in voids of the fully silicated mordenite exhibits a 1D character, although, upon heating above 243 K, it passes from a 1D mode to 2D [114]. However, for the sodium form with Na^+ located in the small mordenite channels, the side pockets can be partly blocked. Figure 6, therefore, clearly demonstrates how the model choice affects the magnitude of the self-diffusion coefficient derived from the same experiment.

The activation energy of water diffusion can be determined from the Arrhenius law:

$$D = D_0 \exp\left(-\frac{E_a}{k_B T}\right) \tag{19}$$

and is less sensitive to the model choice.

In the experiment, the diffusional displacement of a particle is measured within a fixed time interval t_d (in the STE method, $t_d = t_m$) that provides an exceptional opportunity to estimate the size and geometry of obstacles in the case of restricted diffusion, e.g., within porous media [115–117] or within crystallites [118,119]; Figure 7a. More information on this issue can be found in Refs. [116,120–122].

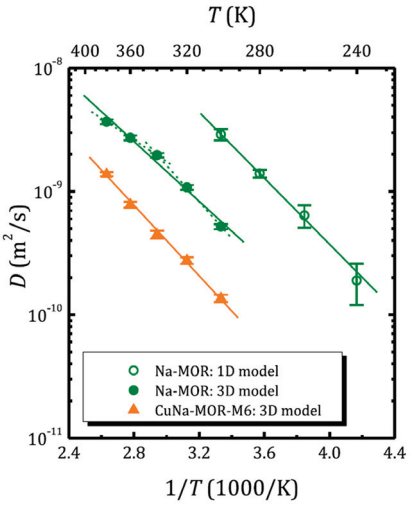

Figure 6. Water self-diffusion coefficient versus inverse temperature in sodium- and copper-exchanged mordenite (the ^{1}H SFG STE experiment). The open and solid symbols correspond to the diffusion coefficient obtained applying the 1D and 3D diffusion model, respectively. Reproduced with permission from Krylova, E.A. et al. *Micropor. Mesopor. Mat.*; Elsevier Inc., 2018 [68].

According to the Einstein equation that relates diffusion and mobility of a particle, in the case of free diffusion in a 3D space, the mean square displacement $\langle r^2 \rangle$ of the observed particle depends on time as follows:

$$\langle r^2 \rangle = 6Dt, \tag{20}$$

where the diffusion coefficient takes a value averaged over the time interval t. If, on a shorter time scale $< t$, the diffusion coefficient of the observed particle (or the mechanism of motion) changes, the apparent diffusion coefficient (D_{app}) will differ from the one measured on a short time scale. Such a diffusion is called restricted or anomalous (opposite to the normal Einstein diffusion) [120,123].

The character of the $D_{app}(t_d)$ dependence is related to the shape of the diffusion area; however, a qualitative analysis can be conducted using a simple interpolation expression [122]:

$$D_{app}(t_d) = \frac{D_f\left(1 - \frac{4}{9}\sqrt{\pi}\right)S}{V}\sqrt{D_f t_d}, \tag{21}$$

where D_f is the free diffusion coefficient and S/V is the surface-to-volume ratio of a cavity. Hence, by measuring $D_{app}(t_d)$, one can estimate the effective size of the limited diffusion area.

For partially permeable pores, the $D_{app}(t_d)$ dependence has a form shown in Figure 7b. In this case, the permeability of pore networks P can be estimated using a simple equation [125]:

$$\frac{1}{D_p} = \frac{1}{D_f} + \frac{1}{Pd}, \tag{22}$$

where d is the size of restricted area, which can be determined from Equation (21), and D_p is the hindered self-diffusion coefficient in a region, where the total average of intrapore diffusion is achieved due to the permeability of the pore wall [116].

Beckert et al. [126] applied SFG STE to study the time-dependent mean diffusion path lengths of H_2O molecules (via ^{1}H NMR) and Li^+ cations (via ^{7}Li NMR) in hydrated zeolite Li-LSX with faujasite (FAU) topology characterized by a 3D channel system; see Figure 1. They found the diffusivities decrease with increasing observation time due to transport resistances on the diffusion paths of water molecules and lithium cations. Drawing on the sample Scanning Electron Microscopy (SEM) microphotographs, possible issues of

transport resistances are the outer surface of the zeolite particles and the boundary between the individual crystallites. Figure 8 shows water and Li^+ diffusivities plotted versus $\sqrt{t_d}$. For both species, there are two regimes of the time dependence, "short-range" and "long-range", that correlate with two types of resistance: "short-range" measurements refer to the intracrystalline diffusion and the resistance is related to barriers formed at the interfaces between the individual crystallites; "long-range" measurements refer to diffusion within the crystallite agglomerates, with transport resistances occurring at their external surface. Crystallite and particle sizes estimated using Equation (21) from ^1H and ^7Li measurements agree with each other and are consistent with the SEM images.

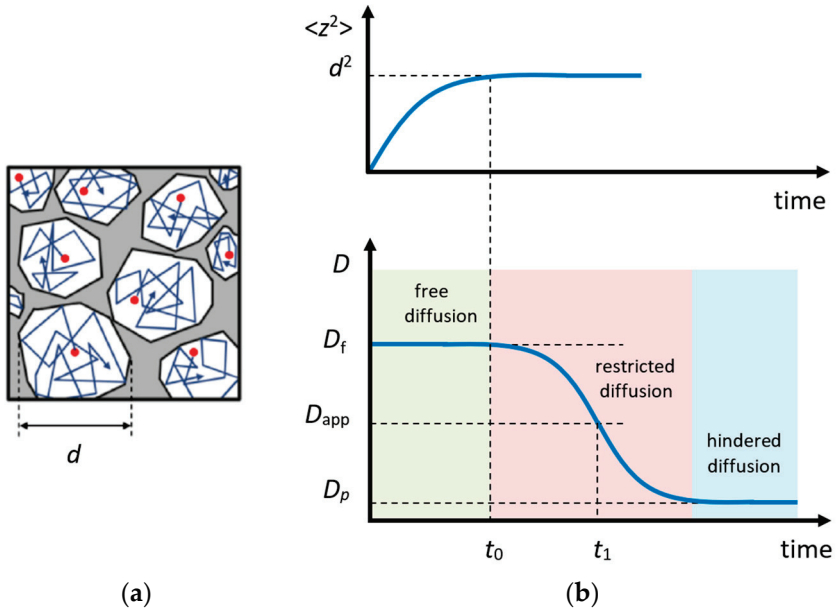

Figure 7. Restricted diffusion model: (**a**) motion of particles in a restricted area; (**b**) the mean square displacement of the particle in a restricted area (above) and the apparent diffusion coefficient (below) depending on time. Adapted with permission from Shelyapina M.G. et al. *Int. J. Hydrogen Energy*; Hydrogen Energy Publications, LLC. Published by Elsevier Ltd., 2015 [124].

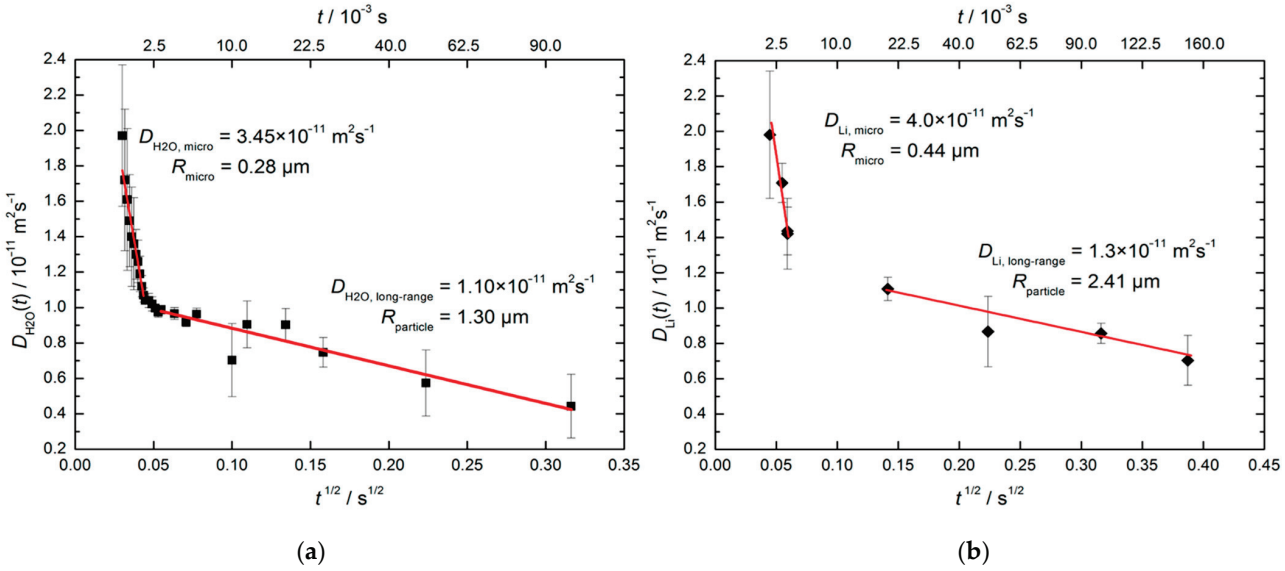

Figure 8. Effective diffusivities of water at 298 K (**a**) and of Li^+ at 373 K (**b**) in hydrated zeolite Li-LSX. The straight lines show the fit of Equation (21) to the experimental data in the short- and long-time ranges. Reproduced with permission from Beckert, S. et al. *J. Phys. Chem. C*; American Chemical Society, 2013 [126].

3.3. Water Dynamics in Zeolites

The partial substitution of Al for Si creates a negative charge in the zeolite framework compensated by cations and producing a strong electrostatic field that leads to vigorous interaction with polar molecules such as water [127–129]. Water is a promoter of many physical and chemical processes in zeolites, involving ion exchange that is carried out in aqueous solution. Water improves the efficiency of the ion-exchange process by coordinating cations and increasing their mobility [130] and affects the distribution and interaction of exchangeable cations with the zeolite framework [68,131,132]. In addition to high polarity, the water molecule is capable of forming up to four hydrogen bonds that result in a very high internal cohesiveness of bulk water [133]. In confined geometries, water molecules can interact both with pore surfaces and other water molecules, resulting in new elements of water structure due to the competing interactions. Zeolites provide clear examples of the effect of nanoconfinement on the water structure and behavior [45,134,135].

Water in zeolites have been extensively studied by various NMR methods for many years. Comprehensive reviews were conducted by Klinowskii [36] and Grey [35]. Here, we provide a short overview of recent results, focusing on relaxation studies.

The temperature dependences of the proton spin–lattice relaxation time, T_1, allow us to determine the activation energy and correlation times, the characteristic parameters of water molecule motion. However, molecular motion, as a rule, includes both translational and reorientation components and, for liquids confined in zeolite voids, this dependence differs from the standard BPP model (where $T_1^{-1}(1/T)$ has a symmetric Λ shape) and can be rather intricate due to contributions from different types of motion and rearrangements of water structure. An example of such a complex temperature dependence of the proton spin–lattice relaxation rate $R_1 = T_1^{-1}$ of water in mordenite and ZSM-5 zeolites with hierarchical porosity (2D zeolite lamella separated by amorphous SiO_2 pillars preventing structure collapse and forming mesoporosity) [45] is shown in Figure 9a. As was mentioned above, for slow spin motions, the maximum of $T_1^{-1}(1/T)$ is shifted towards a high temperature and often lies beyond the accessible temperature range, which is the case for water confined in zeolites, as normally, above 300 K, zeolites start to desorb water. This further complicates the task of finding the parameters of molecular motion and, to determine them, the use of auxiliary tools, such as spin-locking [45,108] (that allows for the shifting of the maximum of the $T_{1\rho}^{-1}(1/T)$ dependence towards the desirable temperature window; see Figure 9b), NMR diffusometry and NMR spectroscopy (motional narrowing the spectral line) [45,136], as well as molecular dynamics simulation [114,137,138], is very helpful. The latter makes it possible to qualitatively estimate the correlation times for various types of motion that can be used to narrow down the search range for parameters of the model when fitting experimental data within expressions like Equations (11)–(15).

The activation energy values for various types of water motion in microporous and mesoporous zeolites, determined by various NMR methods, are listed in Table 1. It should be noted that, for confined water, the Arrhenius law (Equation (12)) does not hold at low temperatures, and the activation energy depends on temperature; therefore, the temperature ranges in which the studies were performed are specified in Table 1.

Paczwa et al. [139] combining ^{1}H T_1 and $T_{1\rho}$ studied water mobility in natural natrolite from Khibiny deposit (Kola Peninsula, Russia) in a temperature range from 190 to 400 K. The natrolite structure contains two types of narrow channels (see Table 1) running parallel and perpendicular to the *c*-axis. As soon as the sizes of the channels are comparable with the diameter of water molecules (approximately 2.8 Å), the path and mechanism of water diffusion in natrolite are not evident. The proton relaxation studies suggested 2D water diffusion above 250 K with different activation energy. An additional contribution to the spin–lattice relaxation at low temperatures the authors associated with a contribution from paramagnetic impurities that commonly present in natural zeolites [4,12]. However, according to other studies, a flattening of the low-temperature branch of the $T_1(1/T)$ curve can be also associated with the translational motion of charged particles [108,124,140] or rotational motion of confined water molecules [114,141].

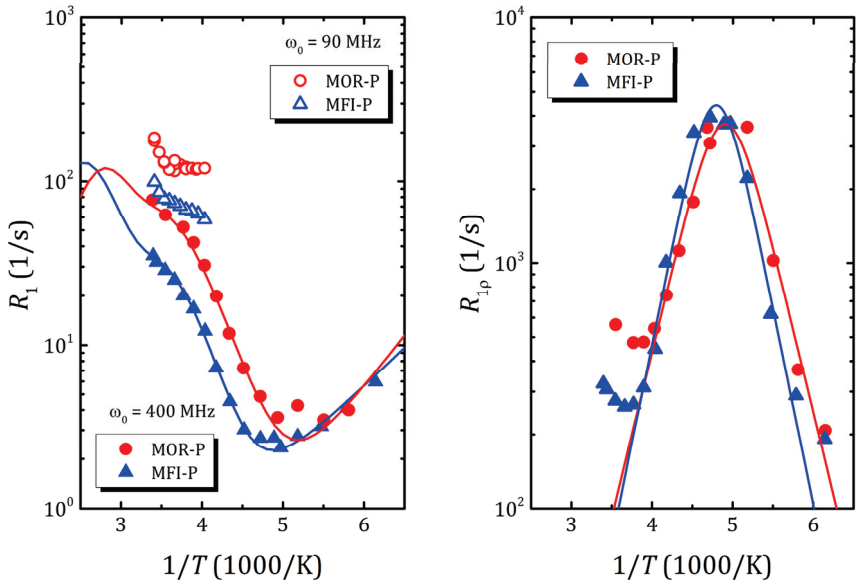

Figure 9. ^{1}H spin–lattice relaxation rate in laboratory frame (**a**) and rotating frame (**b**) versus inverse temperature in pillared mordenite (triangles) and pillared ZSM-5 (circles). Reproduced with permission from Shelyapina, M.G. et al. *Int. J. Mol. Sci.*; published by MDPI, Basel, Switzerland. Creative Common CC BY license, 2023 [45].

Table 1. Activation energy of intracrystalline water motion in micro- and mesoporous zeolites with different zeolite framework types as derived from various NMR experiments.

Zeolite	Si/Al	Micropore Size [1] (Å)	Mesopore Size (Å)	NMR Experiment	Temperature Range (K)	Type of Motion	Ea (kJ/mol)	Ref.
Natrolite (natural)	1.5	2.5 × 4.1 2.6 × 3.9	–	^{1}H T_1	190–400	Translational ∥ [001]	28	[139]
				^{1}H $T_{1\rho}$	220–380	Translational ⊥ [001]	37.3	[139]
Na,Ca-mordenite (natural)	5	7.0 × 6.5 3.4 × 4.8	–	^{1}H T_1	96–351	Translational ∥ [001]	20	[142]
				^{1}H $T_{1\rho}$	96–351	Translational	30	[142]
				^{27}Al T_1	200–365	Translational ∥ [001]	21.6	[143]
				^{23}Na T_1	200–365	Translational ∥ [001]	22.7	[143]
Na-mordenite	5.87	7.0 × 6.5	–	^{1}H SFG	240–300	Translational ∥ [001]	25.6	[68]
Faujasite-NaX	~1.18 [2]	7.4 × 7.4	–	^{1}H PFG	254–353	Translational ∥ [111]	18.7	[66]
Faujasite-HY	2.39	7.4 × 7.4	–	^{1}H T_1	293–873	Translational ∥ [111]	25.6	[144]
Mesoporous NaA	NR [3]	4.1 × 4.1	5.0	^{1}H PFG	250–310	Translational	56.2	[66]
Pillared mordenite	8.4 [4]	7.0 × 6.5	4.0	^{1}H T_1	173–293	Translational	23.6	[141]
				^{1}H T_1	173–293	Rotational	12	[45]
				^{1}H T_1	173–293	Freezing	29	[45]
				^{1}H $T_{1\rho}$	173–293	Freezing	28.9	[45]

Table 1. *Cont.*

Zeolite	Si/Al	Micropore Size [1] (Å)	Mesopore Size (Å)	NMR Experiment	Temperature Range (K)	Type of Motion	Ea (kJ/mol)	Ref.
Pillared ZSM-5	8.8 [4]	0.55	4.4	^{1}H T_1	173–291	Translational	26.0	[45]
				^{1}H T_1	173–291	Rotational	9	[45]
				^{1}H T_1	173–291	Freezing	30	[45]
				^{1}H $T_{1\rho}$	173–291	Freezing	30.7	[45]

[1] The size of micropores (channels) was taken from Ref. [1]. [2] Not reported; the Si/Al ratio was taken from Ref. [1]. [3] Not reported. [4] Data are taken from Ref. [38] for lamellar zeolites before pillaring with SiO_2.

The same group [142] reported on the proton relaxation study of translational motion in natural mordenite from Nidym, Siberia. Two essentially different values of the activation energy of water motion in mordenite determined from T_1 and $T_{1\rho}$ temperature dependencies, 20 and 30 kJ/mol, respectively, the authors related with translational diffusion in larger and narrower mordenite channels [142]. However, the latter can be also associated with the translational motion through the side pockets, as predicted by molecular dynamics simulation [114]. Sergeev et al. showed that water mobility can be indirectly evaluated from spin–lattice relaxation of quadrupole ^{27}Al and ^{23}Na nuclei consisting zeolite that is governed by quadrupole coupling, which, in its turn, is modulated by translational motion of water molecules [143], wherein different methods, including diffusometry [68], give close activation energies of translational motion of water in mordenite channels, about 23 kJ/mol.

Zeolites with faujasite topology (zeolite X, zeolite Y and ultrastable zeolite Y (USY)) exhibit the most open framework of all natural zeolites; voids fill about half of the unit cell space; see Figure 1. Wide intersecting channels are formed parallel to the $< 111 >$ directions of the cubic cell. Water molecules reside predominantly in the large cavities. In zeolites of the faujasite type, Si/Al ranges from 1.2 to 1.5 for X and from 1.5 to 2.5 for Y. The positions of Al and, hence, charge-compensating cations are also governed by the Si/Al ratio: in zeolites X in 6-MR rings, Al atoms are located in meta-positions, while, in zeolites Y, they are in para-positions. All this affects the water mobility confined in faujasite voids.

Katsiotis et al. [144] applied ^{1}H NMR relaxation to study protonated zeolite Y. They found that T_1 displays a typical temperature dependence with a minimum at 423 K that can be fitted within the BPP model, providing a nominal activation energy E_a = 25.6 kJ/mol; however, the temperature dependence of the spin–spin relaxation time T_2, which, instead of increasing with temperature rising, rapidly decreases up to 423 K and, after, remains constant, suggests a more complex mechanism. The authors suppose that, as intracage water dissociates by heating, proton motion mediated through the hydroxonium H_3O^+ vehicle mechanism becomes restricted, slowing down the relaxation behavior. On the other hand, the increase in the T_1/T_2 ratio means the enhancement of bonding of the proton with framework Al.

Recent studies of water mobility in hierarchical zeolites [45,141] confirmed that water in such a complex nanoconfinement (two-dimensional zeolite lamellae separated by amorphous SiO_2) experiences complex temperature behavior. Two studied systems, pillared mordenite and pillared ZSM-5, show rather similar results. The temperature dependence of ^{1}H T_1, see Figure 9a, suggests the presence of three different processes: freezing, fast rotation and translational motion of water. According to the ^{1}H NMR spectral line narrowing, the water freezing occurs near 180 K [45], which, by applying the Waugh–Fedin expression [136], provides an estimate of the activation energy of about 30 kJ/mol. The activation energy of water rotational motion was found between 9 and 12 kJ/mol (depending on the zeolite framework topology), which is lower than in bulk water, and can be related with a low water density in mesopores. For translational motion, it was found to be 23.6 and 26.0 kJ/mol for pillared mordenite and ZSM-5, respectively, which is very close to the values in microporous zeolites but essentially lower than for water in mesoporous silicas

or zeolites with a similar size of mesopores but with disordered mesoporosity; see Table 1. Similar to silicas in pillared zeolites, only a part of water interacts with silanol groups on SiO_2 pillars, forming mesoporosity. This water fraction is characterized by fast rotational but slow translational motion. The rest of water is involved in translational motion in ordered zeolite micropores. All this allowed the authors to suppose that the diffusion process in zeolites with a hierarchically organized pore structure is affected both by mesoporosity and by the mutual arrangement of meso- and micropores; moreover, the translational motion of water molecules is determined mainly by the zeolite micropores [45].

4. Probe of Acidity: 2D T_1–T_2 Correlation Maps

Over the past decade, there has been a rapid development in the use of NMR relaxation as a method for determining surface affinity and adsorbate behavior in catalytically active porous media, including zeolites.

For confined liquids, where the exchange that molecules experience between the surface layer of thickness ε cannot be neglected, the observed nuclear spin relaxation rates $T_{1,2}^{-1}$ can be represented as follows [145–147]:

$$\frac{1}{T_{1,2}} \approx \frac{1}{T_{1,2}^{\text{bulk}}} + \frac{1}{\frac{d_\text{p}}{2\alpha\rho_{1,2}} + \frac{d_\text{p}^2}{8\alpha D}} = \frac{1}{T_{1,2}^{\text{bulk}}} + \frac{2\alpha\rho_{1,2}}{d_\text{p}} \cdot \frac{1}{1 + \frac{\rho_{1,2} d_\text{p}}{8\alpha D}}, \tag{23}$$

where $\rho_{1,2} = \varepsilon \cdot \left(T_{1,2}^{\text{surf}}\right)^{-1}$ is the surface relaxivity, $T_{1,2}^{\text{bulk}}$ and $T_{1,2}^{\text{surf}}$ are the corresponding relaxation times for the bulk liquid and molecules adsorbed on the surface, D is the self-diffusion coefficient of the unrestricted bulk liquid, d_p is the pore diameter and α is a parameter that characterizes the pore shape ($\alpha = 1$, 2 or 3 for planar, cylindrical or spherical pores, respectively). Note that Equation (23) was obtained for long times t and under conditions of the fast exchange with a rate w: $t \gg T_{1,2}^{surf} \gg 1/w$. Let us consider two extreme cases. In the case of the diffusion-limited relaxation, $4D/d_\text{p} \ll \rho_{1,2}$, Equation (23) can be simplified:

$$\frac{1}{T_{1,2}} \approx \frac{1}{T_{1,2}^{\text{bulk}}} + \frac{8\alpha D}{d_\text{p}^2}. \tag{24}$$

In the case of the surface-limited relaxation, when $4D/d_\text{p} \gg \rho_{1,2}$, it can be written as:

$$\frac{1}{T_{1,2}} \approx \frac{1}{T_{1,2}^{\text{bulk}}} + \frac{2\alpha\rho_{1,2}}{d_\text{p}}, \tag{25}$$

and, for spherical pores of volume V and surface S, one obtains the generally applied expression:

$$\frac{1}{T_{1,2}} \approx \frac{1}{T_{1,2}^{\text{bulk}}} + \rho_{1,2}\frac{S}{V}. \tag{26}$$

It means that, for the confined geometry, there is a linear correlation between the observed relaxation rates $T_{1,2}$ and d_p or d_p^2, depending on the relaxation limiting conditions. On the one hand, it opens opportunities to use NMR relaxation as a tool to probe the morphology of porous media, as will be discussed further. On the other hand, the surface relaxivities of molecules adsorbed on microporous materials are a measure for host–guest interactions. For instance, relaxation measurements were used to investigate confinement effects on CO_2 and CH_4 admission in ZIF-8 metal organic framework and ZSM-58 zeolite [148]. By plotting T_1^{-1} of ^{1}H or ^{13}C as a function of inverse gas density, it was found that, for ZIF-8, the surface relaxation is independent of the adsorbed gas density, while, in ZSM-58 with small eight-ring windows, the density dependence of the relaxation rates of adsorbed methane indicates stronger host–guest interactions at low gas loadings.

The ratio T_1/T_2 has been found to be very worthwhile to prove molecular mobility at the solid/liquid interface. Due to the decrease in rotational and translational molecular

mobility upon adsorption on the surface, the surface relaxation times became shorter, $T_{1,2}^{\text{bulk}} \gg T_{1,2}^{\text{surf}}$. Then, the ratio of the surface spin–lattice and spin–spin relaxation times is:

$$\frac{T_1}{T_2} \approx \frac{\rho_1}{\rho_2} = \frac{T_2^{\text{surf}}}{T_1^{\text{surf}}}. \tag{27}$$

This ratio is sensitive to surface affinity [70] and can be used as a noninvasive method for determining surface acidity affinity of porous zeolites [71]. It was shown that the T_1/T_2 ratio correlates with the desorption energy of liquids absorbed into zeolite matrix [71,72].

In studies of molecular structures and dynamics, modern NMR spectroscopy relies on multidimensional correlations. Likewise, the multidimensional correlation functions of T_1 and T_2 can also be used to identify molecular species and to probe their dynamics. For this purpose, T_1–T_2 correlation data are acquired by applying a 2D NMR pulse sequence, as shown in Figure 5a. The resulting maps evidence the relationship between the ratio of relaxation times of the adsorbed liquid and the properties of the surface of a porous medium.

Robinson et al. [71] proposed the T_1/T_2 ratio as a probe for zeolite acidity. Figure 10a shows the 2D T_1–T_2 correlation map for pyridine adsorbed in the pores of microporous ZSM-5 zeolites with different SiO_2/Al_2O_3 ratios. Correlation peaks indicate the relative probability density of each pyridine/zeolite system. Increasing T_1/T_2 can be interpreted as indicative of surface host–guest interaction strength. The authors suggested that the position of these peaks is conditioned by the relative surface affinities of pyridine within zeolite matrices. Indeed, for the studied series of ZSM-5 zeolites, the T_1/T_2 ratio plotted versus enthalpy of pyridine desorption ΔH_{des} shows a linear correlation between these two parameters. ΔH_{des}, in its turn, increases with decreasing SiO_2/Al_2O_3 (increasing the number of Brønsted acid sites); see Figure 10b.

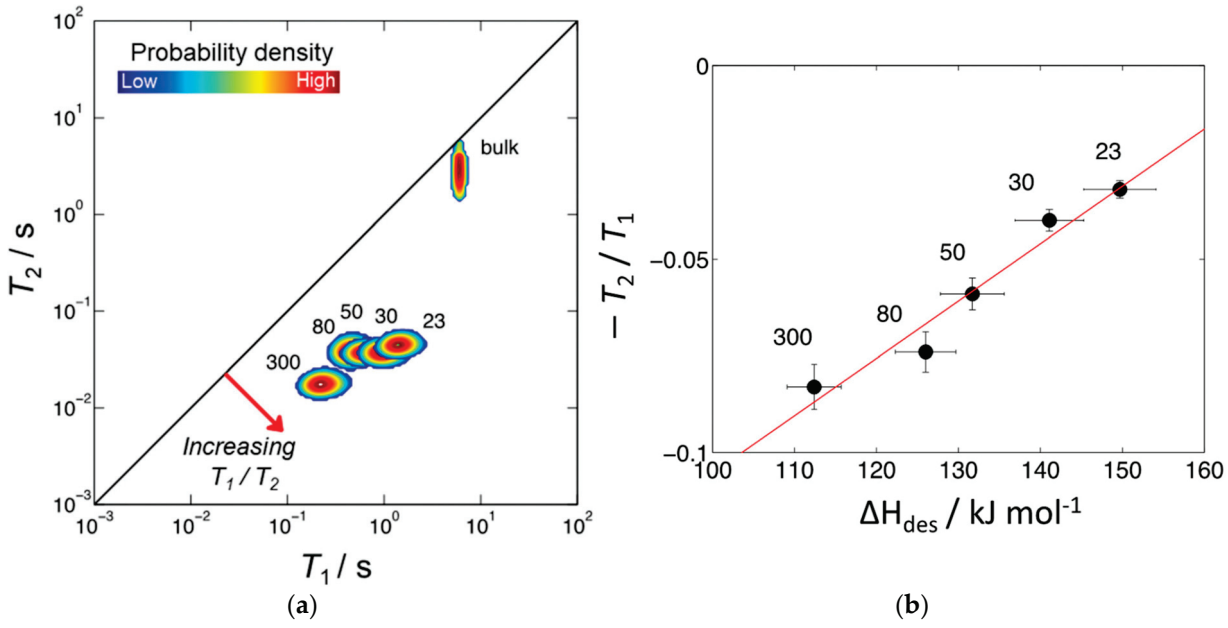

Figure 10. (**a**) ^{1}H T_1–T_2 correlation plots for pyridine in HZSM-5 with varying SiO_2/Al_2O_3 ratios. The diagonal line indicates the parity ratio $T_1/T_2 = 1$; bulk pyridine data are also shown; (**b**) $-T_1/T_2$ plotted versus enthalpy of pyridine adsorption; the red line shows a linear fit. SiO_2/Al_2O_3 values are indicated next to each correlation peak or point. Reproduced with permission from Robinson, N. et al. *Phys. Chem. Chem. Phys.*; published by the Royal Society of Chemistry. Creative Common CC BY license, 2021 [71].

Further relaxation studies of adsorbed water in ZSM-5 and chabazite conducted by d'Agostino et al. [149] confirmed that the T_1/T_2 ratio can be used as an indicator of host–guest surface interactions within a given zeolite framework that are related with Brønsted acidity. However, the authors note that, when comparing zeolite frameworks with different pore sizes, besides host–guest interactions, it is necessary to take into account the confinement effects. A more dramatic increase in T_1/T_2 with increasing Al content for chabazite, which is characterized by a smaller pore size (3.8 × 3.8 Å) compared to ZSM-5 (sinusoidal channels: 5.3 × 5.6 Å; straight channels: 5.5 × 5.1 Å), indicates reduced mobility of water molecules (kinetic diameter: 2.7 Å) due to an increased interaction with the chabazite surface [149].

The guest–host interaction for toluene adsorbed into H-Beta and Pd-modified H-Beta zeolites was probed by NMR relaxation by Zue et al. [150]. For both compounds, the dealumination results in an increase in the T_1/T_2 ratio, confirming the enhanced interaction between toluene molecules and the zeolite surface. In addition, the Pt loading leads to a considerable increase in T_1/T_2 that authors interpreted as an ability of dealuminated Pd-modified H-Beta zeolites to interact with toluene, providing partial oxidation of the adsorbed toluene to benzyl alcohol facilitated by the zeolite hydroxyls.

Forster et al. [151] applied NMR relaxation measurements to evaluate the effect of the reaction solvent (water, methanol and ethanol) upon the catalytic activity of Sn- and Ga-doped zeolite Y for the isomerization of glucose to fructose. NMR relaxation suggested that the lack of catalytic activity in water is due to the strong adsorption of water molecules within the zeolite pores, which makes the Lewis acid sites active for the sugar isomerization inaccessible for reactants. Ethanol, compared to methanol, is more easily adsorbed in zeolite pores, where Lewis acid sites transform glucose to fructose. Ethanol being retained in the pores prevents solvated fructose from further reaction on Brønsted acid sites situated outside of the pore space.

Besides probing surface acidity, 2D T_1–T_2 measurements can be used for mineral deposit analysis, in particular, such complex porous media as clay minerals containing multiple components [152–154]. While 1D T_2 distribution recorded at low field (commonly used frequencies are 2–20 MHz for ^{1}H) now is routine for rock core analysis [155], 2D T_1–T_2 correlation maps provide more comprehensive data on fluid saturation and its states [152]. So far, to our knowledge, no such study has been conducted for natural zeolites.

5. NMR Cryoporometry

In recent years, NMR cryoporometry (NMRC) has been increasingly used to study the pore size distribution on a scale from sub-nanometers to several micrometers. Comprehensive reviews that discover the main principles of this method can be found in Refs. [146,156].

The main idea of NMR cryoporometry is to detect the temperature shift of phase transitions of a matter due to confinement within the porous matrix. These shifts can be interpreted in terms of pore geometry and, consequently, information can be obtained about pore sizes and their distribution and, in favorable cases, about the shape of the pores. As compared to gas adsorption technics that use the Kelvin equation (constant temperature), NMR cryoporometry relies on the Gibbs–Thomson equation (constant pressure). So, for example, for a case of cylindrical pores with radius r, the shift of the melting point T_m can be expressed as [157]:

$$\Delta T_m \equiv T_m - T^0 = -\frac{4\sigma_{sl} T_m}{r \Delta H_f \rho_s}, \quad (28)$$

where σ_{sl} is the surface energy of the solid–liquid interface, ΔH_f is the bulk enthalpy of fusion and ρ_s is the density of the solid. In a similar way, the shift in the freezing point can be defined as $\Delta T_f \equiv T_f - T^0$. This equation can be simplified for specific cases. For

example, for cylindrical pores in the large pore limit (>10 nm), it is possible to obtain the following simple expressions [156]:

$$\begin{aligned} \Delta T_{\mathrm{m}} &\equiv -\tfrac{K_{\mathrm{c}}}{r}, \\ \Delta T_{\mathrm{f}} &\equiv -\tfrac{2K_{\mathrm{c}}}{r}. \end{aligned} \tag{29}$$

For other models of pore shapes, the Gibbs–Thomson relationship is provided in Table 2 and illustrated in Figure 11. As soon as the $\Delta T_{\mathrm{m}}/\Delta T_{\mathrm{f}}$ ratio is sensitive to the pore shape, it can be used to assess the pore geometry.

Table 2. The freezing and melting temperature shift ΔT_{f} and ΔT_{m}, respectively, for various pore geometries in the limits of large pores [156].

Pore Shape	$\lvert \Delta T_{\mathrm{f}} \rvert$ (K)	$\lvert \Delta T_{\mathrm{m}} \rvert$ (K)
Sphere	$3K_{\mathrm{c}}/r$	$2K_{\mathrm{c}}/r$
Cylinder	$2K_{\mathrm{c}}/r$	K_{c}/r
Slit	K_{c}/r	0

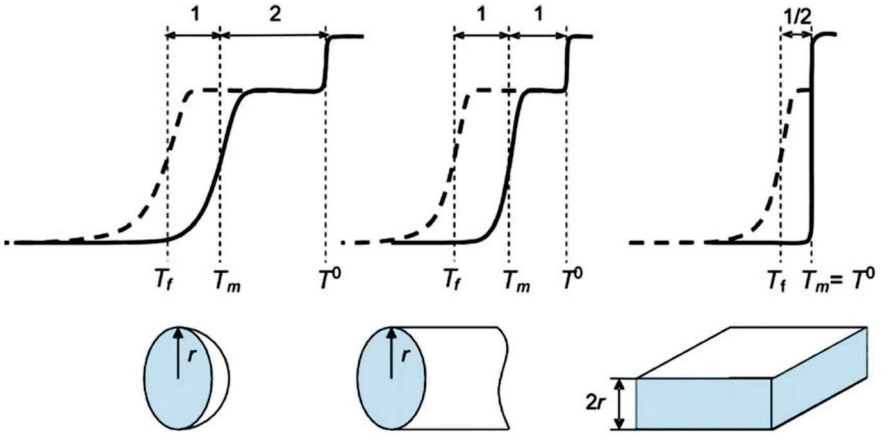

Figure 11. Scratch to illustrate relationship between the freezing–melting hysteresis form and model pore geometries in the large pore limit (>10 nm); dashed and solid lines correspond to freezing and melting, respectively. Reproduced with permission from Petrov, O.V., Furó, I. *Prog. Nucl. Magn. Reson. Spectrosc.*; Elsevier B.V. 2008, [156].

In an NMR cryoporometry experiment, the signal intensity is proportional to the pore volume $v(x)$. If the pores are filled with liquid, its melting temperature T_{m} is related to the pore size distribution. Hence, the measurement of pore size distributions is accessed by differentiating and remapping the melting curve data using the following expression [158]:

$$\frac{\mathrm{d}v(x)}{\mathrm{d}x} = \frac{K_{\mathrm{c}}}{x^2}\frac{\mathrm{d}v}{\mathrm{d}T_{\mathrm{m}}(x)}. \tag{30}$$

So, for NMR cryoporometry measurements, a porous material with an adsorbed probe liquid is cooled until all the liquid in the pores is frozen; after that, the sample is slowly heated. Hence, to determine a pore size distribution, it is enough to record the intensity of the liquid signal as a function of temperature.

Normally, NMR cryoporometry detects ^{1}H T_2 signals from adsorbed substances (typically water or organic molecules). The solid phase is characterized by short spin–spin relaxation times T_2 of the order of microseconds, while liquid phases have characteristic T_2 values from milliseconds to seconds. This usually makes it easy to distinguish signals from solid and liquid fractions, although there may be exceptions in the case of a soft plastic crystalline phase with a relatively long spin–spin relaxation time, as in the case

of cyclohexane. The temperature behavior of T_2 of the liquid fraction can be obtained by measuring an echo train using the CPMG pulse sequence.

Figure 12 shows pore size distribution in cement paste determined by NMR cryoporometry and NMR relaxometry [159]; for both cases, water was used as adsorbate. These two methods exhibit good agreement for micro- and mesopores but, for macropores, a certain discrepancy between two methods is observed.

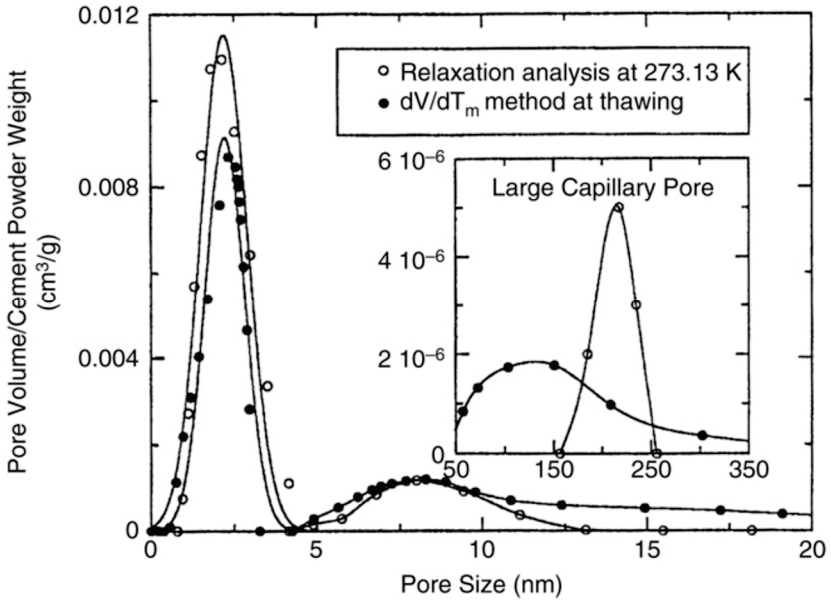

Figure 12. Pore size distribution for a cement paste determined by NMR cryoporometry (solid symbols) and NMR relaxometry (open symbols). Reproduced with permission from Jehng, J.Y. et al. *Magn. Reson. Imaging*; Elsevier Science Inc., 1996 [159].

The main advantages of NMR cryoporometry over standard gas adsorption and thermo-porosimetry are a wide variety of substances that can be used as a probe liquid and that predrying of the samples is not essential and, hence, it can be used for those materials whose pore structure would suffer if predried (wet clays and hydrogels). For zeolites, the latter is not so crucial, and traditional methods are more in demand.

Webber et al. [73] reported the results of NMR cryoporometry to probe the micro- and mesopore size distributions in USY zeolites compared to Barrett–Joyner–Halenda (BJH) model for N_2 adsorption to construct a pore size distribution. They found that both methods account for the mesopore volume, while the micropore volume is underestimated relative to the *t*-plot method. However, the pore size distribution obtained within NMR cryoporometry is better resolved in a small mesopore range compared to a smoothed one derived using BJH.

Recently, Fleury et al. [74] reported results of the pore size distribution in microporous and partly mesoporous UZY zeolite probed by NMR cryoporometry and mercury intrusion experiments. Whereas both technics yield the same average meso- and macropore size, only NMR cryoporometry detects the larger macropores.

6. Pore Connectivity: 2D T_2–T_2 Exchange Maps

Two-dimensional relaxation exchange NMR experiments are very helpful to evidence molecular transport between different relaxation environments and can be used to probe connectivity in systems with complex hierarchical porosity [95]. Relaxation exchange experiments help to evidence diffusive coupling between two relaxation environments [76].

The magnetization recorded in 2D relaxation exchange NMR is described by Equation (8). By applying 2D inverse Laplace transform, one can determine the probabilities $F\left(T_2^A, T_2^B\right)$.

Let us consider two reservoirs of magnetization, M_A and M_B, that correspond to nuclei in pores of different sizes, for example, micro- and mesopores. And let us assume that there is an exchange between these two reservoirs. In this case, the relaxation of the magnetization is governed by the system of coupled differential equations [160]:

$$\begin{aligned} \frac{dM_A}{dt} &= -k_A M_A + k_B M_B + \frac{1}{T_{1,2}^A}\left(M_A^{eq} - M_A\right), \\ \frac{dM_B}{dt} &= -k_B M_B + k_A M_A + \frac{1}{T_{1,2}^B}\left(M_B^{eq} - M_B\right), \end{aligned} \tag{31}$$

where k_A and k_B are the exchange rates from A to B and from B to A and $M_{A,B}^{eq}$ is the equilibrium magnetization for each reservoir, which is equal to zero for spin–spin relaxation. The analytical solution of this system of equations can be found in Ref. [161]. The obtained 2D T_2–T_2 map is schematically shown in Figure 13a. Off-diagonal peaks at an exchange time τ_e indicate diffusive exchange between two reservoirs A and B (relaxation populations). The diagonal peaks appear at T_2^+ and T_2^- that differ from the "real" T_2^A and T_2^B relaxation times if there is an exchange. Recording a series of T_2–T_2 maps at various exchange times τ_e, one can plot the amplitudes of the diagonal P^{++}, P^{--} and off-diagonal P^{+-}, P^{-+} peaks as a function of τ_e and determine the exchange rates k_A and k_B. The numerical expression of these amplitudes can be found in Ref. [161].

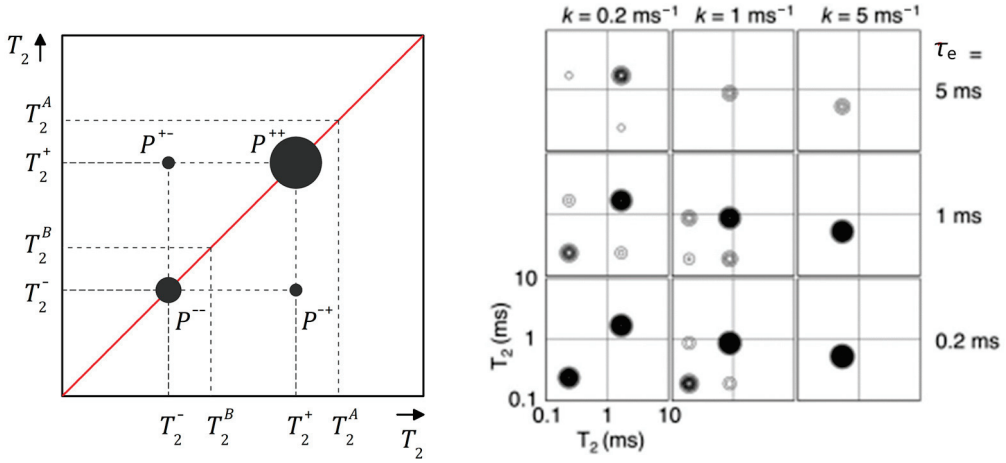

(**a**) (**b**)

Figure 13. (**a**) A schematic T_2–T_2 map showing diagonal and off-diagonal peaks at a certain exchange time τ_e; (**b**) calculated T_2–T_2 maps for slow (**left**), intermediate (**middle**) and fast (**right**) exchange rates k and short (**bottom**), intermediate (**middle**) and long exchange time τ_e. Reproduced with permission from Monteilhet, L. et al. *Phys. Rev. E*; The American Physical Society, 2006 [161].

Figure 13b shows results of simulation of T_2–T_2 maps conducted by Monteilhet et al. [161] assuming a two-sites model and with $k_A = k_A = k$ (two reservoirs of equal size) within the above described model. It allows us to follow how the peak positions and intensities depend on the exchange rate k and the exchange time τ_e. The simulation was conducted for $M_A^{eq} = M_B^{eq} = 0.5$, $T_2^A = T_1^A/4 = 0.25$ ms and $T_2^B = T_1^B/4 = 2.5$ ms. For slow exchange and short exchange time (Figure 13b, bottom left), the 2D spectrum consists of two intensive diagonal peaks P^{++} and P^{--} of comparable amplitude close to $\left(T_2^A, T_2^A\right)$ and $\left(T_2^B, T_2^B\right)$ points on the 2D T_2–T_2 map (in the limit $k \to 0$ and $\tau_e \to 0$, the peaks are of equal amplitude and centered exactly on these positions). With the exchange rate increasing, the peaks shift along the diagonal, their intensities change and one becomes dominating and, simultaneously, off-diagonal peaks appear. In the case of fast exchange, only one diagonal peak corresponding to the average T^2 value is observed and off-diagonal peaks disappear. With the exchange time τ_e increasing, the total intensity of the peaks goes down due to spin–lattice relaxation losses. This is particularly true for the lower diagonal

peaks (short T_2 and short T_1). However, the fraction of the intensity of the off-diagonal peaks increases.

In a real experiment, the integral peak intensities P^{ij} (where i, j mean $+$ or $-$) are determined at different exchange times and, within the described above model, the exchange rate k can be found by fitting the experimental data by the following the equation [93,162]:

$$\frac{P^{+-} + P^{-+}}{P^{\text{tot}}} = A\left(1 - e^{\frac{\tau_e}{k}}\right), \tag{32}$$

where P^{tot} is the summed amplitude of all peaks and A characterizes the amount of molecules exchanged.

The above described NMR 2D T_2–T_2 exchange experiment provides additional information about the dynamics of liquids confined in different interconnected pores, which is especially useful for exploring systems with hierarchical porosity. Fleury at al. [74] applied 2D relaxation experiments with squalane and propanol to evaluate exchange rates between zeolite microporosity and surrounding mesopores in mesoporous USY zeolites; Figure 14. They studied two samples: CBV400 (a slightly dealuminated USY zeolite with a fairly low mesopore volume) and CBV720 (a strongly dealuminated form of USY, with a significantly higher internal mesoporosity and a higher external crystalline surface). Microporous USY zeolites belong to the framework type FAU, with 3D channels of 7.4 × 7.4 Å; see Figure 1. Squalane is the largest alkane molecule that, close to solid surfaces, can have a diameter of about 5 Å that allows it to penetrate into the micropores and to exchange between meso- and/or micropores. 2-propanol as a probe allows the porous network to be explored in another way: having a hydroxyl group, this molecule strongly interacts with the zeolite surface and, therefore, the surface diffusion mechanism becomes important.

The 2D T_1–T_2 maps for squalane indicate multiple T_1/T_2 ratios that can be attributed to macropores ($T_1/T_2 = 1$ means molecules very weakly interact with the zeolite surface and behave as in the bulk), to mesopores (T_1/T_2 = 4 indicates molecules interact with the zeolite surface), and to micropores (T_1/T_2 = 20 and 40 for CBV400 and CBV720, respectively, which is typical for pseudo-solid behavior when rotational motions are severely limited). Comparing these different pore fractions estimated from T_2 relaxation to the reference value measured by NMR cryoporometry (T_2 measurements essentially underestimate microporosity and overestimate mesoporosity), the authors made a conclusion about strong exchange between micro- and mesopores [74]. A stronger underestimation of microporosity from T_2 for a given molecule means a stronger connectivity between micro- and mesopores.

Relaxation exchange experiments provide direct evidence of diffusive coupling between two relaxation environments that can be used to probe pore connectivity [76]. Figure 14a,c show 2D T_2–T_2 maps for squalane confined in CBV400 and CBV720, respectively [74]. Symmetric off-diagonal peaks evidence diffusive coupling between the micro- and mesopores, while a single asymmetric peak points out diffusive coupling between meso- and macropores. Analysis of off-diagonal peak intensities as a function of the exchange time results in squalane molecule exchange between the micro- and mesopores with a timescale of about 6 ms for both zeolites but a larger amount of molecules exchanged for CBV720 that correlates with the data on microporosity.

For 2-propanol (Figure 14b,d), only exchange peaks between micro- and mesopores were observed. Analysis of the off-diagonal terms applying Equation (32) results in k = 2 and 4 ms for CBV400 and CBV720, respectively; however, the amount of exchanged 2-propanol molecules in CBV400 is one order of magnitude greater than in CBV720, which the authors associated with the high surface residence time of 2-propanol in micropores of CBV720 due to the strong interaction of polar molecules with the zeolites framework.

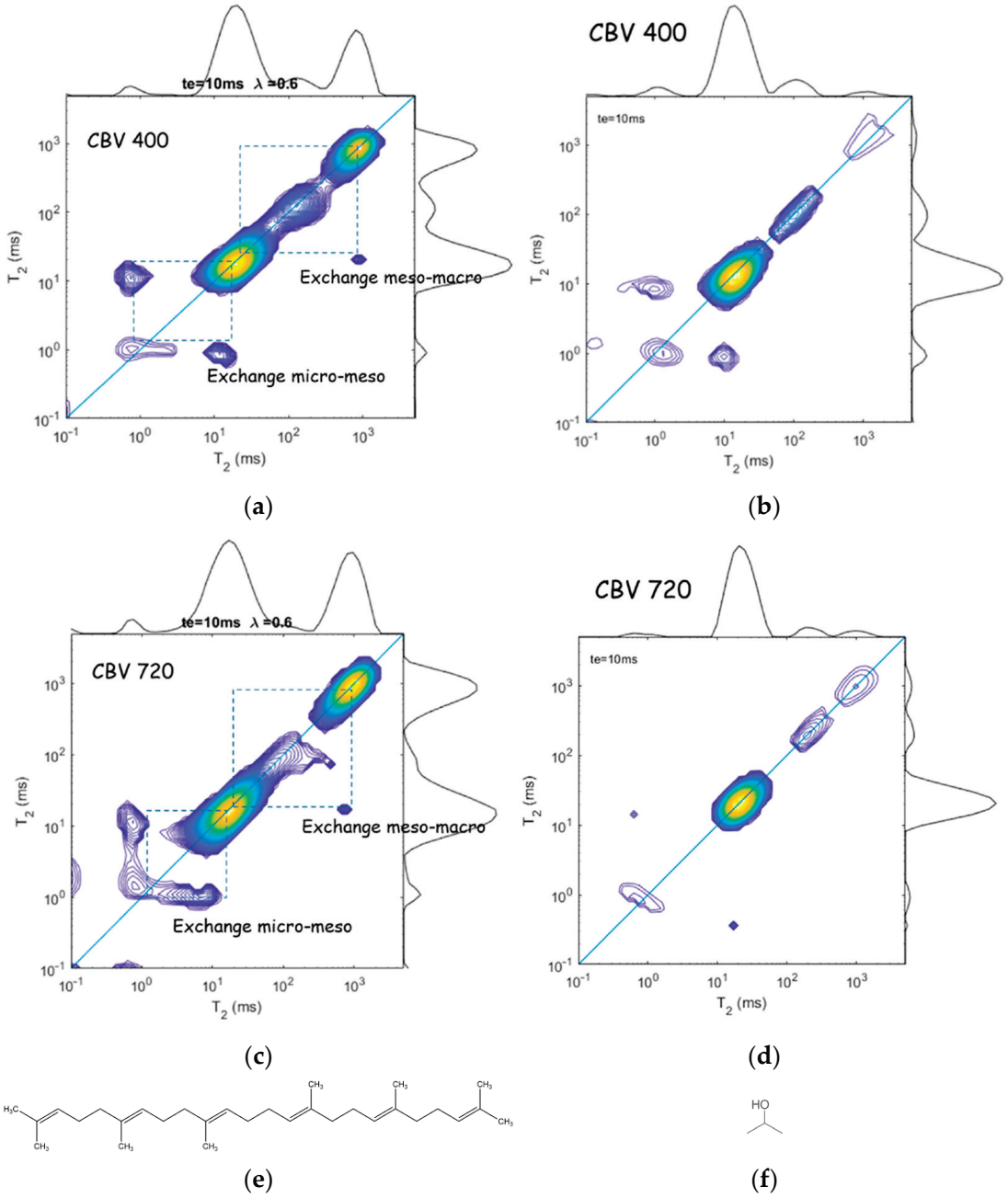

Figure 14. Relaxation exchange experiments with squalane (**a**,**c**) and 2-propanol (**b**,**d**) adsorbed by UZY zeolites with low (**a**,**c**) and high (**b**,**d**) mesoporosity. The off-diagonal amplitudes indicate the diffusive coupling between micro- and mesopores, as well as between meso- and macropores. (**e**,**f**) show squalane and 2-propanol molecules, respectively. Adopted with permission from Fleury, M. et al. *Micropor. Mesopor. Mat.*; Elsevier Inc., 2023 [74].

It should also be added that the two-sites model is normally used to analyze experimental data; however, it is not always applicable to real systems. A more carful theoretical study within the three-sites model conducted by Gao and Blümich [96] shows that (i) the exchange map can be asymmetric in the case of microscale vortex motion, (ii) the peaks shift in the apparent 2D two-site T_2–T_2 exchange maps, and (iii) there can be negative peak amplitudes (it can indicate that more molecules move from one site to another in the evolution or detection periods than in the mixing period).

Despite its visibility and great potential for the study of systems with complex pore organization, up to now, T_2–T_2 relaxation exchange NMR is little used for the study of

zeolites. Nevertheless, in the last few years, a number of publications have appeared on the study of related systems. For instance, Elgersma et al. applied it to measure the liquid–solid mass transfer coefficient for water flowing through in packed beds of porous silica (or silica/titania) pellets [163,164]. The authors proposed this method for the screening and optimization of catalyst pellets and reactor operating conditions.

7. Conclusions

The main goal of this review was to demonstrate the great potential of NMR relaxation techniques to bring insight into various properties of zeolites and zeolite-based catalysts with complex pore architecture. In recent years, various low-field NMR relaxation methods along with fast field cycling and ultralow-field NMR have emerged as a complementary approach to traditional high-field NMR techniques. These methods result in not only cost saving but open up new opportunities.

One of the advantages of the NMR relaxation techniques described above is relatively modest requirements for the instrument base compared to solid-state NMR spectroscopy: they do not require high field for better resolution, fast rotation of the sample or special setup to prepare hyperpolarized ^{129}Xe. Besides the traditional application to study the mobility of adsorbed molecules, both rotational and/or translational motion, by measuring the temperature dependences of relaxation times and self-diffusion coefficients, NMR relaxation provides access to surface acid sites and, by combining different NMR techniques, it is possible to obtain valuable information on textural properties of catalysts at different scales, which is of special interest for systems with hierarchical pore structure.

Although, generally, NMR relaxation gives rather integral characteristics as compared to multiple-quantum and 2D MAS NMR, in some cases, the information extracted is comparable and even surpasses that obtained by other methods. In particular, NMR cryoporometry disposes a wide variety of substances that can be used as a probe liquid and gives access to a larger scale of pore sizes compared to standard gas adsorption and thermo-porosimetry methods. However, despite its obvious advantages and a number of fascinating studies that have appeared in the last few years, NMR relaxation is still not in sufficient demand for probing porous systems and zeolites in particular. We hope that this review will expand the range of researchers who include this method among other useful tools for characterizing zeolites and zeolite-based materials with complex topology of voids and active sites on their surface.

Funding: This study was supported by the Russian Science Foundation (project No. 23-23-00448).

Conflicts of Interest: The author declares no conflicts of interest.

References

1. Baerlocher, C.; McCusker, L.B. Database of Zeolite Structures. Available online: http://www.iza-structure.org/databases/ (accessed on 30 May 2024).
2. Breck, D.W. *Zeolite Molecular Sieves: Structure, Chemistry, and Use*; John Wiley and Sons: Hoboken, NJ, USA, 1974; ISBN 0471099856.
3. Van Speybroeck, V.; Hemelsoet, K.; Joos, L.; Waroquier, M.; Bell, R.G.; Catlow, C.R.A. Advances in Theory and Their Application within the Field of Zeolite Chemistry. *Chem. Soc. Rev.* **2015**, *44*, 7044–7111. [CrossRef] [PubMed]
4. Rodríguez-iznaga, I.; Shelyapina, M.G.; Petranovskii, V. Ion Exchange in Natural Clinoptilolite: Aspects Related to Its Structure and Applications. *Minerals* **2022**, *12*, 1628. [CrossRef]
5. Sun, Q.; Wang, N.; Yu, J. Advances in Catalytic Applications of Zeolite-Supported Metal Catalysts. *Adv. Mater.* **2021**, *33*, 2104442. [CrossRef] [PubMed]
6. Sánchez-López, P.; Kotolevich, Y.; Yocupicio-Gaxiola, R.I.; Antúnez-García, J.; Chowdari, R.K.; Petranovskii, V.; Fuentes-Moyado, S. Recent Advances in Catalysis Based on Transition Metals Supported on Zeolites. *Front. Chem.* **2021**, *9*, 716745. [CrossRef] [PubMed]
7. Zhukov, Y.M.; Shelyapina, M.G.; Zvereva, I.A.; Efimov, A.Y.; Petranovskii, V. Microwave Assisted versus Convention Cu^{2+} Exchange in Mordenite. *Microporous Mesoporous Mater.* **2018**, *259*, 220–228. [CrossRef]
8. Shelyapina, M.G.; Gurgul, J.; Łątka, K.; Bogdanov, D.; Kotolevich, Y.; Petranovskii, V.; Fuentes, S.; Sánchez-López, P.; Bogdanov, D.; Kotolevich, Y.; et al. Mechanism of Formation of Framework Fe^{3+} in Bimetallic Ag-Fe Mordenites—Effective Catalytic Centers for DeNOx Reaction. *Microporous Mesoporous Mater.* **2019**, *299*, 109841. [CrossRef]

9. Antúnez-García, J.; Galván, D.H.; Petranovskii, V.; Murrieta-Rico, F.N.; Yocupicio-Gaxiola, R.I.; Shelyapina, M.G.; Fuentes-Moyado, S. The Effect of Chemical Composition on the Properties of LTA Zeolite: A Theoretical Study. *Comput. Mater. Sci.* **2021**, *196*, 110557. [CrossRef]
10. Valtchev, V.; Majano, G.; Mintova, S.; Pérez-Ramírez, J. Tailored Crystalline Microporous Materials by Post-Synthesis Modification. *Chem. Soc. Rev.* **2013**, *42*, 263–290. [CrossRef]
11. Wheatley, P.S.; Chlubná-Eliášová, P.; Greer, H.; Zhou, W.; Seymour, V.R.; Dawson, D.M.; Ashbrook, S.E.; Pinar, A.B.; McCusker, L.B.; Opanasenko, M.; et al. Zeolites with Continuously Tuneable Porosity. *Angew. Chem.-Int. Ed.* **2014**, *53*, 13426–13430. [CrossRef]
12. Zvereva, I.A.; Shelyapina, M.G.; Chislov, M.; Novakowski, V.; Malygina, E.; Rodríguez-Iznaga, I.; Hernández, M.A.; Petranovskii, V. A Comparative Analysis of Natural Zeolites from Various Cuban and Mexican Deposits: Structure, Composition, Thermal Properties and Hierarchical Porosity. *J. Therm. Anal. Calorim.* **2022**, *147*, 6147–6159. [CrossRef]
13. Barthomeuf, D. Zeolite Acidity Dependence on Structure and Chemical Environment. Correlations with Catalysis. *Mater. Chem. Phys.* **1987**, *17*, 49–71. [CrossRef]
14. Mihályi, R.M.; Lázár, K.; Kollár, M.; Lónyi, F.; Pál-Borbély, G.; Szegedi, Á. Structure, Acidity and Redox Properties of MCM-22 Ferrisilicate. *Microporous Mesoporous Mater.* **2008**, *110*, 51–63. [CrossRef]
15. Catizzone, E.; Migliori, M.; Mineva, T.; Van Daele, S.; Valtchev, V.; Giordano, G. New Synthesis Routes and Catalytic Applications of Ferrierite Crystals. Part 2: The Effect of OSDA Type on Zeolite Properties and Catalysis. *Microporous Mesoporous Mater.* **2020**, *296*, 109988. [CrossRef]
16. Vogt, E.T.C.; Whiting, G.T.; Dutta Chowdhury, A.; Weckhuysen, B.M. Zeolites and Zeotypes for Oil and Gas Conversion. In *Advances in Catalysis*; Jentoft, F.C., Ed.; Academic Press: Amsterdam, The Netherlands, 2015; Volume 58, pp. 143–314.
17. Shi, J.; Wang, Y.; Yang, W.; Tang, Y.; Xie, Z. Recent Advances of Pore System Construction in Zeolite-Catalyzed Chemical Industry Processes. *Chem. Soc. Rev.* **2015**, *44*, 8877–8903. [CrossRef] [PubMed]
18. Mohamed, M.M. Catalytic Properties of Fe Ion-Exchanged Mordenite toward the Ethanol Transformation: Influence of the Methods of Preparation. *J. Mol. Catal. A Chem.* **2003**, *200*, 301–313. [CrossRef]
19. Kotolevich, Y.; Zepeda-Partida, T.; Yocupicio-Gaxiola, R.; Antúnez-Garcia, J.; Pelaez, L.; Avalos-Borja, M.; Vázquez-Salas, P.J.; Fuentes-Moyado, S.; Petranovskii, V. Influence of the Valence of Iron on the NO Reduction by CO over Cu-Fe-Mordenite. *Catalysts* **2023**, *13*, 484. [CrossRef]
20. López-Bastidas, C.; Smolentseva, E.; Petranovskii, V.P.; Machorro, R. Plasmon Spectra of Binary Ag-Cu Mixtures Supported in Mordenite. *Plasmon. Des. Mater. Fabr. Charact. Appl. XIV* **2016**, *9921*, 992130. [CrossRef]
21. Giroir-Fendler, A.; Denton, P.; Boreave, A.; Praliaud, H.; Primet, M. The Role of Support Acidity in the Selective Catalytic Reduction of NO by C_3H_6 under Lean-Burn Conditions. *Top. Catal.* **2001**, *16–17*, 237–241. [CrossRef]
22. Sun, Q.; Wang, N.; Bai, R.; Hui, Y.; Zhang, T.; Do, D.A.; Zhang, P.; Song, L.; Miao, S.; Yu, J. Synergetic Effect of Ultrasmall Metal Clusters and Zeolites Promoting Hydrogen Generation. *Adv. Sci.* **2019**, *6*, 1802350. [CrossRef]
23. Sazama, P.; Moravkova, J.; Sklenak, S.; Vondrova, A.; Tabor, E.; Sadovska, G.; Pilar, R. Effect of the Nuclearity and Coordination of Cu and Fe Sites in β Zeolites on the Oxidation of Hydrocarbons. *ACS Catal.* **2020**, *10*, 3984–4002. [CrossRef]
24. de Carvalho, M.C.N.A.; Passos, F.B.; Schmal, M. The Behavior of Cu/ZSM-5 in the Oxide and Reduced Form in the Presence of NO and Methanol. *Appl. Catal. A Gen.* **2000**, *193*, 265–276. [CrossRef]
25. Chen, H.; Malki, E.M.E.; Wang, X.; Sachtler, W.M.H. Mono- and Multinuclear Oxo-Cations in Zeolite Cavities. In *Catalysis by Unique Metal Ion Structures in Solid Matrices*; Centi, G., Wichterlová, B., Bell, A.T., Eds.; NATO Science Series; Springer: Dordrecht, The Netherlands, 2001; Volume 13, pp. 75–84.
26. Čapek, L.; Kreibich, V.; Dědeček, J.; Grygar, T.; Wichterlová, B.; Sobalík, Z.; Martens, J.A.; Brosius, R.; Tokarová, V. Analysis of Fe Species in Zeolites by UV-VIS-NIR, IR Spectra and Voltammetry. Effect of Preparation, Fe Loading and Zeolite Type. *Microporous Mesoporous Mater.* **2005**, *80*, 279–289. [CrossRef]
27. Shamzhy, M.; Opanasenko, M.; Concepción, P.; Martínez, A. New Trends in Tailoring Active Sites in Zeolite-Based Catalysts. *Chem. Soc. Rev.* **2019**, *48*, 1095–1149. [CrossRef] [PubMed]
28. Schoonheydt, R.A. Transition Metal Ions in Zeolites: Siting and Energetics of Cu^{2+}. *Catal. Rev. Sci. Eng.* **1993**, *35*, 129–168. [CrossRef]
29. Chal, R.; Gérardin, C.; Bulut, M.; VanDonk, S. Overview and Industrial Assessment of Synthesis Strategies towards Zeolites with Mesopores. *ChemCatChem* **2011**, *3*, 67–81. [CrossRef]
30. Mensah, J.; Yan, P.; Rawal, A.; Lee, A.F.; Wilson, K.; Robinson, N.; Johns, M.L.; Kennedy, E.; Stockenhuber, M. Catalytic Cracking of 1,3,5-Triisopropylbenzene and Low-Density Polyethylene over Hierarchical Y Zeolites and Al-SBA-15. *ChemCatChem* **2024**, *16*, e202300884. [CrossRef]
31. Christensen, C.H.; Johannsen, K.; Schmidt, I.; Christensen, C.H. Catalytic Benzene Alkylation over Mesoporous Zeolite Single Crystals: Improving Activity and Aelectivity with a New Family of Porous Materials. *J. Am. Chem. Soc.* **2003**, *125*, 13370–13371. [CrossRef]
32. Abdulridha, S.; Jiao, Y.; Xu, S.; Zhang, R.; Ren, Z.; Garforth, A.A.; Fan, X. A Comparative Study on Mesoporous Y Zeolites Prepared by Hard-Templating and Post-Synthetic Treatment Methods. *Appl. Catal. A Gen.* **2021**, *612*, 117986. [CrossRef]
33. Chu, N.; Wang, J.; Zhang, Y.; Yang, J.; Lu, J.; Yin, D. Nestlike Hollow Hierarchical MCM-22 Microspheres: Synthesis and Exceptional Catalytic Properties. *Chem. Mater.* **2010**, *22*, 2757–2763. [CrossRef]

34. Milina, M.; Mitchell, S.; Crivelli, P.; Cooke, D.; Pérez-Ramírez, J. Mesopore Quality Determines the Lifetime of Hierarchically Structured Zeolite Catalysts. *Nat. Commun.* **2014**, *5*, 3922. [CrossRef]
35. Grey, C.P. Nuclear Magnetic Resonance Studies of Zeolites. In *Handbook of Zeolite Science and Technology*; Auerbach, S., Carrado, K., Dutta, P., Eds.; CRC Press: New York, NY, USA, 2003; pp. 267–331.
36. Klinowski, J. Nuclear Magnetic Resonance Studies of Zeolites. *Prog. Nucl. Magn. Reson. Spectrosc.* **1984**, *16*, 237–309. [CrossRef]
37. Zheng, M.; Chu, Y.; Wang, Q.; Wang, Y.; Xu, J.; Deng, F. Advanced Solid-State NMR Spectroscopy and Its Applications in Zeolite Chemistry. *Prog. Nucl. Magn. Reson. Spectrosc.* **2024**, *140–141*, 1–41. [CrossRef]
38. Shelyapina, M.G.; Yocupicio-Gaxiola, R.I.; Zhelezniak, I.V.; Chislov, M.V.; Antúnez-García, J.; Murrieta-Rico, F.N.; Galván, D.H.; Petranovskii, V.; Fuentes-Moyado, S. Local Structures of Two-Dimensional Zeolites—Mordenite and ZSM-5—Probed by Multinuclear NMR. *Molecules* **2020**, *25*, 4678. [CrossRef] [PubMed]
39. Shelyapina, M.G.; Krylova, E.A.; Mazur, A.S.; Tsyganenko, A.A.; Shergin, Y.V.; Satikova, E.; Petranovskii, V. Active Sites in H-Mordenite Catalysts Probed by NMR and FTIR. *Catalysts* **2022**, *13*, 344. [CrossRef]
40. Klinowski, J. Recent Advances in Solid-State Nmr of Zeolites. *Annu. Rev. Mater. Sci.* **1988**, *18*, 189–218. [CrossRef]
41. Asgar Pour, Z.; Koelewijn, R.; El Hariri El Nokab, M.; van der Wel, P.C.A.; Sebakhy, K.O.; Pescarmona, P.P. Binder-Free Zeolite Beta Beads with Hierarchical Porosity: Synthesis and Application as Heterogeneous Catalysts for Anisole Acylation. *ChemCatChem* **2022**, *14*, e202200518. [CrossRef]
42. Wang, Z.; Jiang, Y.; Lafon, O.; Trébosc, J.; Kim, K.D.; Stampfl, C.; Baiker, A.; Amoureux, J.-P.; Huang, J. Brønsted Acid Sites Based on Penta-Coordinated Aluminum Species. *Nat. Commun.* **2016**, *7*, 13820. [CrossRef]
43. Ravi, M.; Sushkevich, V.L.; van Bokhoven, J.A. Towards a Better Understanding of Lewis Acidic Aluminium in Zeolites. *Nat. Mater.* **2020**, *19*, 1047–1056. [CrossRef]
44. Kanellopoulos, J.; Gottert, C.; Schneider, D.; Knorr, B.; Prager, D.; Ernst, H.; Freude, D. NMR Investigation of Proton Mobility in Zeolites. *J. Catal.* **2008**, *255*, 68–78. [CrossRef]
45. Shelyapina, M.G.; Nefedov, D.Y.; Antonenko, A.O.; Valkovskiy, G.A.; Yocupicio-gaxiola, R.I.; Petranovskii, V. Nanoconfined Water in Pillared Zeolites Probed by ^{1}H Nuclear Magnetic Resonance. *Int. J. Mol. Sci.* **2023**, *24*, 15898. [CrossRef]
46. Bornes, C.; Fischer, M.; Amelse, J.A.; Geraldes, C.F.G.C.; Rocha, J.; Mafra, L. What Is Being Measured with P-Bearing NMR Probe Molecules Adsorbed on Zeolites? *J. Am. Chem. Soc.* **2021**, *143*, 13616–13623. [CrossRef] [PubMed]
47. Bornes, C.; Sardo, M.; Lin, Z.; Amelse, J.; Fernandes, A.; Ribeiro, M.F.; Geraldes, C.; Rocha, J.; Mafra, L. ^{1}H-^{31}P HETCOR NMR Elucidates the Nature of Acid Sites in Zeolite HZSM-5 Probed with Trimethylphosphine Oxide. *Chem. Commun.* **2019**, *55*, 12635–12638. [CrossRef] [PubMed]
48. Lewis, J.D.; Ha, M.; Luo, H.; Faucher, A.; Michaelis, V.K.; Román-Leshkov, Y. Distinguishing Active Site Identity in Sn-Beta Zeolites Using ^{31}P MAS NMR of Adsorbed Trimethylphosphine Oxide. *ACS Catal.* **2018**, *8*, 3076–3086. [CrossRef]
49. Zasukhin, D.S.; Kasyanov, I.A.; Kolyagin, Y.G.; Bulygina, A.I.; Kharas, K.C.; Ivanova, I.I. Evaluation of Zeolite Acidity by ^{31}P MAS NMR Spectroscopy of Aadsorbed Phosphine Oxides: Quantitative or Not? *ACS Omega* **2022**, *7*, 12318–12328. [CrossRef] [PubMed]
50. Gunther, W.R.; Michaelis, V.K.; Griffin, R.G.; Roman-Leshkov, Y. Interrogating the Lewis Acidity of Metal Sites in Beta Zeolites with ^{15}N Pyridine Adsorption Coupled with MAS NMR Spectroscopy. *J. Phys. Chem. C* **2016**, *120*, 28533–28544. [CrossRef] [PubMed]
51. Wang, C.; Dai, W.; Wu, G.; Guan, N.; Li, L. Application of Ammonia Probe-Assisted Solid-State NMR Technique in Zeolites and Catalysis. *Magn. Reson. Lett.* **2022**, *2*, 28–37. [CrossRef]
52. Biaglow, A.I.; Gorte, R.J.; Kokotailo, G.T.; White, D. A Probe of Brønsted Site Acidity in Zeolites: ^{13}C Chemical Shift of Acetone. *J. Catal.* **1994**, *148*, 779–786. [CrossRef]
53. Yu, Z.; Wang, Q.; Chen, L.; Deng, F. Brønsted/Lewis Acid Sites Synergy in H-MCM-22 Zeolite Studied by 1H and 27Al DQ-MAS NMR Spectroscopy. *Cuihua Xuebao/Chin. J. Catal.* **2012**, *33*, 129–139. [CrossRef]
54. Yakimov, A.V.; Sushkevich, V.L.; van Bokhoven, J.A.; Copéret, C. Probing Acid Sites in MOR Zeolite Using Low-Temperature ^{13}C Solid-State NMR Spectroscopy of Adsorbed Carbon Monoxide. *J. Phys. Chem. C* **2022**, *126*, 3681–3687. [CrossRef]
55. Bonardet, J.L.; Gédéon, A.; Springuel-Huet, M.A.; Fraissard, J. NMR of Physisorbed ^{129}Xe Used as a Probe to Investigate Molecular Sieves. *Mol. Sieves–Sci. Technol.* **2006**, *5*, 155–248. [CrossRef]
56. Weiland, E.; Springuel-Huet, M.A.; Nossov, A.; Gédéon, A. ^{129}Xenon NMR: Review of Recent Insights into Porous Materials. *Microporous Mesoporous Mater.* **2016**, *225*, 41–65. [CrossRef]
57. Boventi, M.; Mauri, M.; Simonutti, R. ^{129}Xe: A Wide-Ranging NMR Probe for Multiscale Structures. *Appl. Sci.* **2022**, *12*, 3152. [CrossRef]
58. Driehuys, B.; Cates, G.D.; Miron, E.; Sauer, K.; Walter, D.K.; Happer, W. High-Volume Production of Laser-Polarized ^{129}Xe. *Appl. Phys. Lett.* **1996**, *69*, 1668–1670. [CrossRef]
59. Walker, T.G.; Happer, W. Spin-Exchange Optical Pumping of Noble-Gas Nuclei. *Rev. Mod. Phys.* **1997**, *69*, 629–642. [CrossRef]
60. Comment, A.; Jannin, S.; Hyacinthe, J.N.; Miéville, P.; Sarkar, R.; Ahuja, P.; Vasos, P.R.; Montet, X.; Lazeyras, F.; Vallée, J.P.; et al. Hyperpolarizing Gases via Dynamic Nuclear Polarization and Sublimation. *Phys. Rev. Lett.* **2010**, *105*, 018104. [CrossRef]
61. Krjukov, E.V.; O'Neill, J.D.; Owers-Bradley, J.R. Brute Force Polarization of ^{129}Xe. *J. Low Temp. Phys.* **2005**, *140*, 397–408. [CrossRef]

62. Barskiy, D.A.; Tayler, M.C.D.; Marco-Rius, I.; Kurhanewicz, J.; Vigneron, D.B.; Cikrikci, S.; Aydogdu, A.; Reh, M.; Pravdivtsev, A.N.; Hövener, J.B.; et al. Zero-Field Nuclear Magnetic Resonance of Chemically Exchanging Systems. *Nat. Commun.* **2019**, *10*, 3002. [CrossRef]
63. Burueva, D.B.; Eills, J.; Blanchard, J.W.; Garcon, A.; Picazo-Frutos, R.; Kovtunov, K.V.; Koptyug, I.V.; Budker, D. Chemical Reaction Monitoring Using Zero-Field Nuclear Magnetic Resonance Enables Study of Heterogeneous Samples in Metal Containers. *Angew. Chem.-Int. Ed.* **2020**, *59*, 17026–17032. [CrossRef]
64. Tayler, M.C.D.; Ward-Williams, J.; Gladden, L.F. NMR Relaxation in Porous Materials at Zero and Ultralow Magnetic Fields. *J. Magn. Reson.* **2018**, *297*, 1–8. [CrossRef]
65. Tayler, M.C.D.; Ward-Williams, J.; Gladden, L.F. Ultralow-Field Nuclear Magnetic Resonance of Liquids Confined in Ferromagnetic and Paramagnetic Materials. *Appl. Phys. Lett.* **2019**, *115*, 072409. [CrossRef]
66. Valiullin, R.; Kärger, J.; Cho, K.; Choi, M.; Ryoo, R. Dynamics of Water Diffusion in Mesoporous Zeolites. *Microporous Mesoporous Mater.* **2011**, *142*, 236–244. [CrossRef]
67. Mehlhorn, D.; Valiullin, R.; Kärger, J.; Cho, K.; Ryoo, R. Exploring the Hierarchy of Transport Phenomena in Hierarchical Pore Systems by NMR Diffusion Measurement. *Microporous Mesoporous Mater.* **2012**, *164*, 273–279. [CrossRef]
68. Krylova, E.A.; Shelyapina, M.G.; Nowak, P.; Harańczyk, H.; Chislov, M.; Zvereva, I.A.; Privalov, A.F.; Becker, M.; Vogel, M.; Petranovskii, V. Mobility of Water Molecules in Sodium- and Copper-Exchanged Mordenites: Thermal Analysis and ^{1}H NMR. *Microporous Mesoporous Mater.* **2018**, *265*, 132–142. [CrossRef]
69. Mantle, M.D.; Ainte, M.; York, A.P.E.; Bentley, M.; Gladden, L.F. A Simple ^{1}H PFG NMR Method to Determine Intracrystalline Molecular Self-Diffusivities for Weakly Adsorbing Hydrocarbon Gases in Microporous Materials. *Catal. Today* **2024**, *431*, 114561. [CrossRef]
70. Mitchell, J.; Broche, L.M.; Chandrasekera, T.C.; Lurie, D.J.; Gladden, L.F. Exploring Surface Interactions in Catalysts Using Low-Field Nuclear Magnetic Resonance. *J. Phys. Chem. C* **2013**, *117*, 17699–17706. [CrossRef]
71. Robinson, N.; Bräuer, P.; York, A.P.E.; D'Agostino, C. Nuclear Spin Relaxation as a Probe of Zeolite Acidity: A Combined NMR and TPD Investigation of Pyridine in HZSM-5. *Phys. Chem. Chem. Phys.* **2021**, *23*, 17752–17760. [CrossRef] [PubMed]
72. D'Agostino, C.; Bräuer, P.; Zheng, J.; Robinson, N.; York, A.P.E.; Song, L.; Fan, X. Adsorbate/Adsorbent Interactions in Microporous Zeolites: Mechanistic Insights from NMR Relaxation and DFT Calculations. *Mater. Today Chem.* **2023**, *29*, 101443. [CrossRef]
73. Webber, J.B.W.; Livadaris, V.; Andreev, A.S. USY Zeolite Mesoporosity Probed by NMR Cryoporometry. *Microporous Mesoporous Mater.* **2020**, *306*, 110404. [CrossRef]
74. Fleury, M.; Pirngruber, G.; Jolimaitre, E. Probing Diffusional Exchange in Mesoporous Zeolite by NMR Diffusion and Relaxation Methods. *Microporous Mesoporous Mater.* **2023**, *355*, 112575. [CrossRef]
75. Burduhos Nergis, D.D.; Vizureanu, P.; Ardelean, I.; Sandu, A.V.; Corbu, O.C.; Matei, E. Revealing the Influence of Microparticles on Geopolymers' Synthesis and Porosity. *Materials* **2020**, *13*, 3211. [CrossRef]
76. Bernin, D.; Topgaard, D. NMR Diffusion and Relaxation Correlation Methods: New Insights in Heterogeneous Materials. *Curr. Opin. Colloid Interface Sci.* **2013**, *18*, 166–172. [CrossRef]
77. Chizhik, V.I.; Chernyshev, Y.S.; Donets, A.V.; Frolov, V.V.; Komolkin, A.V.; Shelyapina, M.G. *Magnetic Resonance and Its Applications*; Springer International Publishing: Cham, Switzerland, 2014; ISBN 9783319052984.
78. Freeman, R.; Hill, H.D.W. Fourier Transform Study of NMR Spin-Lattice Relaxation by "Progressive Saturation". *J. Chem. Phys.* **1971**, *54*, 3367–3377. [CrossRef]
79. Wei, R.; Dickson, C.L.; Uhrín, D.; Lloyd-Jones, G.C. Rapid Estimation of T_1 for Quantitative NMR. *J. Org. Chem.* **2021**, *86*, 9023–9029. [CrossRef] [PubMed]
80. Kingsley, P.B. Methods of Measuring Spin-Lattice (T_1) Relaxation Times: An Annotated Bibliography. *Concepts Magn. Reson.* **1999**, *11*, 243–276. [CrossRef]
81. Fujara, F.; Kruk, D.; Privalov, A.F. Solid State Field-Cycling NMR Relaxometry: Instrumental Improvements and New Applications. *Prog. Nucl. Magn. Reson. Spectrosc.* **2014**, *82*, 39–69. [CrossRef]
82. Hahn, E.L. Spin Echoes. *Phys. Rev.* **1950**, *80*, 580–594. [CrossRef]
83. Carr, H.Y.; Purcell, E.M. Effects of Diffusion on Free Precession in Nuclear Magnetic Resonance Experiments. *Phys. Rev.* **1954**, *94*, 630–638. [CrossRef]
84. Meiboom, S.; Gill, D. Modified Spin-Echo Method for Measuring Nuclear Relaxation Times. *Rev. Sci. Instrum.* **1958**, *29*, 688–691. [CrossRef]
85. Stejskal, E.O.; Tanner, J.E. Spin Diffusion Measurements: Spin Echoes in the Presence of a Time-dependent Field Gradient. *J. Chem. Phys.* **1965**, *42*, 288–292. [CrossRef]
86. Gibbs, S.J.; Johnson, C.S. A PFG NMR Experiment for Accurate Diffusion and Flow Studies in the Presence of Eddy Currents. *J. Magn. Reson.* **1991**, *93*, 395–402. [CrossRef]
87. Wu, D.H.; Chen, A.; Johnson, C.S. An Improved Diffusion-Ordered Spectroscopy Experiment Incorporating Bipolar-Gradient Pulses. *J. Magn. Reson. Ser. A* **1995**, *115*, 260–264. [CrossRef]
88. Morris, G.A. Diffusion-Ordered Spectroscopy. *eMagRes* **2009**, *2009*, 1–13. [CrossRef]
89. Chang, I.; Fujara, F.; Geil, B.; Hinze, G.; Sillescu, H.; Tölle, A. New Perspectives of NMR in Ultrahigh Static Magnetic Field Gradients. *J. Non. Cryst. Solids* **1994**, *172*, 674–681. [CrossRef]

90. Velasco, M.I.; Franzoni, M.B.; Chávez, F.V.; Acosta, R.H. Characterization of Structure and Functionality of Porous Materials. *J. Magn. Reson. Open* **2023**, *14–15*, 100099. [CrossRef]
91. Song, Y.Q.; Venkataramanan, L.; Hürlimann, M.D.; Flaum, M.; Frulla, P.; Straley, C. T_1-T_2 Correlation Spectra Obtained Using a Fast Two-Dimensional Laplace Inversion. *J. Magn. Reson.* **2002**, *154*, 261–268. [CrossRef] [PubMed]
92. Mitchell, J.; Gladden, L.F.; Chandrasekera, T.C.; Fordham, E.J. Low-Field Permanent Magnets for Industrial Process and Quality Control. *Prog. Nucl. Magn. Reson. Spectrosc.* **2014**, *76*, 1–60. [CrossRef] [PubMed]
93. Washburn, K.E.; Callaghan, P.T. Tracking Pore to Pore Exchange Using Relaxation Exchange Spectroscopy. *Phys. Rev. Lett.* **2006**, *97*, 25–28. [CrossRef]
94. Fleury, M.; Soualem, J. Quantitative Analysis of Diffusional Pore Coupling from T_2-Store-T_2 NMR Experiments. *J. Colloid Interface Sci.* **2009**, *336*, 250–259. [CrossRef]
95. Mitchell, J.; Griffith, J.D.; Collins, J.H.P.; Sederman, A.J.; Gladden, L.F.; Johns, M.L. Validation of NMR Relaxation Exchange Time Measurements in Porous Media. *J. Chem. Phys.* **2007**, *127*, 234701. [CrossRef]
96. Gao, Y.; Blümich, B. Analysis of Three-Site T_2-T_2 Exchange NMR. *J. Magn. Reson.* **2020**, *315*, 106740. [CrossRef]
97. Jeener, J.; Broekaert, P. Nuclear Magnetic Resonance in Solids: Thermodynamic Effects of a Pair of Rf Pulses. *Phys. Rev.* **1967**, *157*, 232–240. [CrossRef]
98. Spiess, H.W. Deuteron Spin Alignment: A Probe for Studying Ultraslow Motions in Solids and Solid Polymers. *J. Chem. Phys.* **1980**, *72*, 6755–6762. [CrossRef]
99. Bloembergen, N.; Purcell, E.M.; Pound, R.V. Relaxation Effects in Nuclear Magnetic Resonance Absorption. *Phys. Rev.* **1948**, *73*, 679–712. [CrossRef]
100. McCall, D.W.; Douglass, D.C.; Anderson, E.W. Molecular Motion in Polyethylene. II. *J. Chem. Phys.* **1959**, *30*, 1272–1275. [CrossRef]
101. Pfeifer, H. Nuclear Magnetic Resonance and Relaxation of Molecules Adsorbed on Solids. In *NMR—Basic Principles and Progress*; Diehl, P., Fluck, E., Kosfeld, R., Eds.; Springer: Berlin/Heidelberg, Germany, 1972; pp. 53–153, ISBN 978-3-642-65312-4.
102. Skripov, A.V.; Shelyapina, M.G. Nuclear Magnetic Resonance. In *Neutron Scattering and Other Nuclear Techniques for Hydrogen in Materials*; Fritzsche, H., Huot, J., Fruchart, D., Eds.; Springer International Publishing: Cham, Switzerland, 2016; pp. 337–376, ISBN 978-3-319-22792-4.
103. Zimmerman, J.R.; Brittin, W.E. Nuclear Magnetic Resonance Studies in Multiple Phase Systems: Lifetime of a Water Molecule in an Adsorbing Phase on Silica Gel. *J. Phys. Chem.* **1957**, *61*, 1328–1333. [CrossRef]
104. Chizhik, V.I.; Rykov, I.A.; Shelyapina, M.G.; Fruchart, D. Proton Relaxation and Hydrogen Mobility in Ti-V-Cr Alloys: Improved Exchange Model. *Int. J. Hydrogen Energy* **2014**, *39*, 17416–17421. [CrossRef]
105. Lalowicz, Z.T.; Birczyński, A.; Krzyziak, A. Translational and Rotational Dynamics of Molecules Confined in Zeolite Nanocages by Means of Deuteron NMR. *J. Phys. Chem. C* **2017**, *121*, 26472–26482. [CrossRef]
106. Kuhn, A.; Kunze, M.; Sreeraj, P.; Wiemhöfer, H.D.; Thangadurai, V.; Wilkening, M.; Heitjans, P. NMR Relaxometry as a Versatile Tool to Study Li Ion Dynamics in Potential Battery Materials. *Solid State Nucl. Magn. Reson.* **2012**, *42*, 2–8. [CrossRef]
107. Habasaki, J.; Len, C.; Ngai, K.L. *Dynamics of Glassy, Crystalline and Liquid Ionic Conductors. Experiment, Theories, Simulations*; Springer: Cham, Switzerland, 2017; Volume 132, ISBN 978-3-319-42389-0.
108. Shelyapina, M.G.; Nefedov, D.Y.; Kostromin, A.V.; Silyukov, O.I.; Zvereva, I.A. Proton Mobility in Ruddlesden–Popper Phase $H_2La_2Ti_3O_{10}$ Studied by ^{1}H NMR. *Ceram. Int.* **2019**, *45*, 5788–5795. [CrossRef]
109. Slichter, C.P. *Principles of Magnetic Resonance*; Springer: Berlin/Heidelberg, Germany, 1990; ISBN 978-3-662-09441-9.
110. Callaghan, P.T.; Jolley, K.W.; Lelievre, J. Diffusion of Water in the Endosperm Tissue of Wheat Grains as Studied by Pulsed Field Gradient Nuclear Magnetic Resonance. *Biophys. J.* **1979**, *28*, 133–142. [CrossRef]
111. Nowak, A.K.; Den Ouden, C.J.J.; Pickett, S.D.; Smit, B.; Cheetham, A.K.; Post, M.F.M.; Thomas, J.M. Mobility of Adsorbed Species in Zeolites: Methane, Ethane, and Propane Diffusivities. *J. Phys. Chem.* **1991**, *95*, 848–854. [CrossRef]
112. Prodinger, S.; Berdiell, I.C.; Cordero-Lanzac, T.; Bygdnes, O.R.; Solemsli, B.G.; Kvande, K.; Arstad, B.; Beato, P.; Olsbye, U.; Svelle, S. Cation-Induced Speciation of Port-Size during Mordenite Zeolite Synthesis. *J. Mater. Chem. A* **2023**, *11*, 21884–21894. [CrossRef] [PubMed]
113. Shelyapina, M.G.; Zvereva, I.A.; Yafarova, L.V.; Bogdanov, D.S.; Sukharzhevskii, S.M.; Zhukov, Y.M.; Petranovskii, V. Thermal Analysis and EPR Study of Copper Species in Mordenites Prepared by Conventional and Microwave-Assisted Methods. *J. Therm. Anal. Calorim.* **2018**, *134*, 71–79. [CrossRef]
114. Egorov, A.V.; Egorova, M.I.; Mizyulin, D.A.; Shelyapina, M.G. Water Structure and Dynamics in Microporous Mordenite from Molecular Dynamics Simulation. *Appl. Magn. Reson.* **2024**, *55*, 805–818. [CrossRef]
115. Mitra, P.P.; Sen, P.N.; Schwartz, L.M. Short-Time Behavior of the Diffusion Coefficient as a Geometrical Probe of Porous Media. *Phys. Rev. B* **1993**, *47*, 8565–8574. [CrossRef]
116. Valiullin, R.; Skirda, V. Time Dependent Self-Diffusion Coefficient of Molecules in Porous Media. *J. Chem. Phys.* **2001**, *114*, 452–458. [CrossRef]
117. Sen, P.N. Time-Dependent Diffusion Coefficient as a Probe of Permeability of the Pore Wall. *J. Chem. Phys.* **2003**, *120*, 9871–9876. [CrossRef]
118. Vyvodtceva, A.V.; Shelyapina, M.G.; Privalov, A.F.; Chernyshev, Y.S.; Fruchart, D. ^{1}H NMR Study of Hydrogen Self-Diffusion in Ternary Ti-V-Cr Alloys. *J. Alloys Compd.* **2014**, *614*, 364–367. [CrossRef]

119. Shelyapina, M.G.; Dost, A.V.; Skryabina, N.E.; Privalov, A.F.; Vogel, M.; Fruchart, D. Effect of Zr_7Ni_{10} Additive on Hydrogen Mobility in $(TiCr_{1.8})_{1-x}V_x$ (x = 0.2, 0.4, 0.6, 0.8): An ^{1}H NMR SFG Study. *Int. J. Hydrogen Energy* **2020**, *45*, 7929–7937. [CrossRef]
120. Callaghan, P.T. *Translational Dynamics and Magnetic Resonance. Principles of Pulsed Gradient Spin Echo NMR*; Oxford University Press: Oxford, UK, 2011; ISBN 9780199556984.
121. Hagslätt, H.; Jönsson, B.; Nydén, M.; Söderman, O. Predictions of Pulsed Field Gradient NMR Echo-Decays for Molecules Diffusing in Various Restrictive Geometries. Simulations of Diffusion Propagators Based on a Finite Element Method. *J. Magn. Reson.* **2003**, *161*, 138–147. [CrossRef]
122. Sen, P.N. Time-Dependent Diffusion Coefficient as a Probe of Geometry. *Concepts Magn. Reson. Part A Bridg. Educ. Res.* **2004**, *23*, 1–21. [CrossRef]
123. Price, W.S. *NMR Studies of Translational Motion: Principles and Applications*; Cambridge University Press: Cambridge, UK, 2009; ISBN 9780511770487.
124. Shelyapina, M.G.; Vyvodtceva, A.V.; Klyukin, K.A.; Bavrina, O.O.; Chernyshev, Y.S.S.; Privalov, A.F.; Fruchart, D. Hydrogen Diffusion in Metal-Hydrogen Systems via NMR and DFT. *Int. J. Hydrogen Energy* **2015**, *40*, 17038–17050. [CrossRef]
125. Suh, K.J.; Hong, Y.S.; Skirda, V.D.; Volkov, V.I.; Lee, C.Y.; Lee, C.H. Water Self-Diffusion Behavior in Yeast Cells Studied by Pulsed Field Gradient NMR. *Biophys. Chem.* **2003**, *104*, 121–130. [CrossRef] [PubMed]
126. Beckert, S.; Stallmach, F.; Toufar, H.; Freude, D.; Kärger, J.; Haase, J. Tracing Water and Cation Diffusion in Hydrated Zeolites of Type Li-LSX by Pulsed Field Gradient NMR. *J. Phys. Chem. C* **2013**, *117*, 24866–24872. [CrossRef]
127. Tsutsumi, K.; Kawai, T.; Yanagihara, T. Adsorption Characteristics of Hydrophobic Zeolites. *Stud. Surf. Sci. Catal.* **1994**, *83*, 217–224. [CrossRef]
128. Kawai, T.; Tsutsumi, K. Evaluation of Hydrophilic-Hydrophobic Character of Zeolites by Measurements of Their Immersional Heats in Water. *Colloid Polym. Sci.* **1992**, *270*, 711–715. [CrossRef]
129. Catuzo, G.L.; Santilli, C.V.; Martins, L. Hydrophobic-Hydrophilic Balance of ZSM-5 Zeolites on the Two-Phase Ketalization of Glycerol with Acetone. *Catal. Today* **2021**, *381*, 215–223. [CrossRef]
130. Pissis, P.; Daoukaki-Diamanti, D. Dielectric Studies of Molecular Mobility in Hydrated Zeolites. *J. Phys. Chem. Solids* **1993**, *54*, 701–709. [CrossRef]
131. Higgins, F.M.; De Leeuw, H.; Parker, S.C. Modelling the Effect of Water on Cation Exchange in Zeolite A. *J. Mater. Chem.* **2002**, *12*, 124–131. [CrossRef]
132. Maurin, G.; Bell, R.G.; Devautour, S.; Henn, F.; Giuntini, J.C. Modeling the Effect of Hydration in Zeolite Na^+-Mordenite. *J. Phys. Chem. B* **2004**, *108*, 3739–3745. [CrossRef]
133. Buntkowsky, G.; Breitzke, H.; Adamczyk, A.; Roelofs, F.; Emmler, T.; Gedat, E.; Gru, B.; Limbach, H.; Shenderovich, I.; Vyalikh, A.; et al. Structural and Dynamical Properties of Guest Molecules Confined in Mesoporous Silica Materials Revealed by NMR. *Phys. Chem. Chem. Phys.* **2007**, *9*, 4843–4853. [CrossRef] [PubMed]
134. Hansen, E.W.; Sto, M.; Schmidt, R. Low-Temperature Phase Transition of Water Confined in Mesopores Probed by NMR. Influence on Pore Size Distribution. *J. Phys. Chem.* **1996**, *100*, 2195–2200. [CrossRef]
135. Alba-Simionesco, C.; Coasne, B.; Dosseh, G.; Dudziak, G.; Gubbins, K.E.; Radhakrishnan, R.; Sliwinska-Bartkowiak, M. Effects of Confinement on Freezing and Melting. *J. Phys. Condens. Matter* **2006**, *18*, R15–R68. [CrossRef] [PubMed]
136. Waugh, J.; Fedin, E. Determination of Hindered Rotation Barriers in Solids. *Sov. Phys. Solid State* **1963**, *4*, 1633–1636.
137. Leherte, L.; Andre, J.-M.; Derouane, E.G.; Vercauteren, D.P. What Does Zeolitic Water Look like?: Modelization by Molecular Dynamics Simulations. *Int. J. Quantum Chem.* **1992**, *42*, 1291–1326. [CrossRef]
138. Porter, A.J.; McHugh, S.L.; Omojola, T.; Silverwood, I.P.; O'Malley, A.J. The Effect of Si/Al Ratio on Local and Nanoscale Water Diffusion in H-ZSM-5: A Quasielastic Neutron Scattering and Molecular Dynamics Simulation Study. *Microporous Mesoporous Mater.* **2023**, *348*, 112391. [CrossRef]
139. Paczwa, M.; Sapiga, A.A.; Olszewski, M.; Sergeev, N.A.; Sapiga, A.V. Spin-Lattice Relaxations Study of Water Mobility in Natural Natrolite. *J. Struct. Chem.* **2016**, *57*, 319–324. [CrossRef]
140. Kasperovich, V.S.; Shelyapina, M.G.; Khar'Kov, B.; Rykov, I.; Osipov, V.; Kurenkova, E.; Ievlev, A.V.; Skryabina, N.E.; Fruchart, D.; Miraglia, S.; et al. NMR Study of Metal-Hydrogen Systems for Hydrogen Storage. *J. Alloys Compd.* **2011**, *509*, S804–S808. [CrossRef]
141. Shelyapina, M.G.; Nefedov, D.Y.; Antonenko, A.O.; Hmok, H.; Egorov, A.V.; Egorova, M.I.; Ievlev, A.V.; Yocupicio-Gaxiola, R.I.; Petranovskii, V.; Antúnez-García, J.; et al. Dynamics of Guest Water Molecules in Pillared Mordenite Studied by 1H NMR Relaxation. *Appl. Magn. Reson.* **2023**, *54*, 915–928. [CrossRef]
142. Panich, A.M.; Sergeev, N.A.; Paczwa, M.; Olszewski, M. ^{1}H NMR Study of Water Molecules Confined in Nanochannels of Mordenite. *Solid State Nucl. Magn. Reson.* **2016**, *76*, 24–28. [CrossRef]
143. Sergeev, N.A.; Paczwa, M.; Olszewski, M.; Panich, A.M. 23Na and 27Al NMR Study of Structure and Dynamics in Mordenite. *Appl. Magn. Reson.* **2017**, *48*, 115–124. [CrossRef] [PubMed]
144. Katsiotis, M.S.; Fardis, M.; Al Wahedi, Y.; Stephen, S.; Tzitzios, V.; Boukos, N.; Kim, H.J.; Alhassan, S.M.; Papavassiliou, G. Water Coordination, Proton Mobility, and Lewis Acidity in HY Nanozeolites: A High-Temperature ^{1}H and ^{27}Al NMR Study. *J. Phys. Chem. C* **2015**, *119*, 3428–3438. [CrossRef]
145. Godefroy, S.; Korb, J.P.; Fleury, M.; Bryant, R.G. Surface Nuclear Magnetic Relaxation and Dynamics of Water and Oil in Macroporous Media. *Phys. Rev. E—Stat. Phys. Plasmas Fluids Relat. Interdiscip. Top.* **2001**, *64*, 021605. [CrossRef] [PubMed]

146. Mitchell, J.; Webber, J.B.W.; Strange, J.H. Nuclear Magnetic Resonance Cryoporometry. *Phys. Rep.* **2008**, *461*, 1–36. [CrossRef]
147. Korb, J.P. Nuclear Magnetic Relaxation of Liquids in Porous Media. *New J. Phys.* **2011**, *13*, 035016. [CrossRef]
148. Stallmach, F.; Pusch, A.K.; Splith, T.; Horch, C.; Merker, S. NMR Relaxation and Diffusion Studies of Methane and Carbon Dioxide in Nanoporous ZIF-8 and ZSM-58. *Microporous Mesoporous Mater.* **2015**, *205*, 36–39. [CrossRef]
149. D'Agostino, C.; York, A.P.E.; Bräuer, P. Host-Guest Interactions and Confinement Effects in HZSM-5 and Chabazite Zeolites Studied by Low-Field NMR Spin Relaxation. *Mater. Today Chem.* **2022**, *24*, 100901. [CrossRef]
150. Zou, R.; Chansai, S.; Xu, S.; An, B.; Zainal, S.; Zhou, Y.; Xin, R.; Gao, P.; Hou, G.; D'Agostino, C.; et al. Pt Nanoparticles on Beta Zeolites for Catalytic Toluene Oxidation: Effect of the Hydroxyl Groups of Beta Zeolite. *ChemCatChem* **2023**, *15*, e202300811. [CrossRef]
151. Forster, L.; Kashbor, M.M.M.; Railton, J.; Chansai, S.; Hardacre, C. Low-Field 2D NMR Relaxation and DRIFTS Studies of Glucose Isomerization in Zeolite Y: New Insights into Adsorption Effects on Catalytic Performance. *J. Catal.* **2023**, *425*, 269–285. [CrossRef]
152. Zhang, P.; Lu, S.; Li, J.; Chang, X. 1D and 2D Nuclear Magnetic Resonance (NMR) Relaxation Behaviors of Protons in Clay, Kerogen and Oil-Bearing Shale Rocks. *Mar. Pet. Geol.* **2020**, *114*, 104210. [CrossRef]
153. Ridwan, M.G.; Kamil, M.I.; Sanmurjana, M.; Dehgati, A.M.; Permadi, P.; Marhaendrajana, T.; Hakiki, F. Low Salinity Waterflooding: Surface Roughening and Pore Size Alteration Implications. *J. Pet. Sci. Eng.* **2020**, *195*, 107868. [CrossRef]
154. Mukhametdinova, A.; Habina-Skrzyniarz, I.; Kazak, A.; Krzyżak, A. NMR Relaxometry Interpretation of Source Rock Liquid Saturation—A Holistic Approach. *Mar. Pet. Geol.* **2021**, *132*, 105165. [CrossRef]
155. Yuan, Y.; Rezaee, R. Comparative Porosity and Pore Structure Assessment in Shales: Measurement Techniques, Influencing Factors and Implications for Reservoir Characterization. *Energies* **2019**, *12*, 2094. [CrossRef]
156. Petrov, O.V.; Furó, I. NMR Cryoporometry: Principles, Applications and Potential. *Prog. Nucl. Magn. Reson. Spectrosc.* **2009**, *54*, 97–122. [CrossRef]
157. Jackson, C.L.; McKenna, G.B. The Melting Behavior of Organic Materials Confined in Porous Solids. *J. Chem. Phys.* **1990**, *93*, 9002–9011. [CrossRef]
158. Strange, J.H.; Rahman, M.; Smith, E.G. Characterization of Porous Solids by NMR. *Phys. Rev. Lett.* **1993**, *71*, 3589–3591. [CrossRef]
159. Jehng, J.-Y.; Sprague, D.T.; Halperin, W.P. Pore Structure of Hydrating Cement Paste by Magnetic Resonance Relaxation Analysis and Freezing. *Magn. Reson. Imaging* **1996**, *14*, 785–791. [CrossRef]
160. McConnell, H.M. Reaction Rates by Nuclear Magnetic Resonance. *J. Chem. Phys.* **1958**, *28*, 430–431. [CrossRef]
161. Monteilhet, L.; Korb, J.P.; Mitchell, J.; McDonald, P.J. Observation of Exchange of Micropore Water in Cement Pastes by Two-Dimensional T_2—T_2 Nuclear Magnetic Resonance Relaxometry. *Phys. Rev. E-Stat. Nonlinear Soft Matter Phys.* **2006**, *74*, 061404. [CrossRef]
162. Robinson, N.; Xiao, G.; Connolly, P.R.J.; Ling, N.N.A.; Fridjonsson, E.O.; May, E.F.; Johns, M.L. Low-Field NMR Relaxation-Exchange Measurements for the Study of Gas Admission in Microporous Solids. *Phys. Chem. Chem. Phys.* **2020**, *22*, 13689–13697. [CrossRef]
163. Elgersma, S.V.; Sederman, A.J.; Mantle, M.D.; Gladden, L.F. Measuring the Liquid-Solid Mass Transfer Coefficient in Packed Beds Using T_2-T_2 Relaxation Exchange NMR. *Chem. Eng. Sci.* **2022**, *248*, 117229. [CrossRef]
164. Elgersma, S.V.; Zheng, Q.; Avrantinis, N.; Sederman, A.J.; Mantle, M.D.; Gladden, L.F. Quantifying Liquid-Solid Mass Transfer in a Trickle Bed Using T_2-T_2 Relaxation Exchange NMR. *Appl. Magn. Reson.* **2023**, *54*, 1423–1443. [CrossRef]

MDPI AG
Grosspeteranlage 5
4052 Basel
Switzerland
Tel.: +41 61 683 77 34

Molecules Editorial Office
E-mail: molecules@mdpi.com
www.mdpi.com/journal/molecules

Academic Open
Access Publishing

mdpi.com

ISBN 978-3-7258-7089-9